University of Louisville

ThinkIR: The University of Louisville's Institutional Repository

12-2013

Developing advanced mathematical models for detecting abnormalities in 2D/3D medical structures.

Ahmed Abd-Elrahman Elnakib
University of Louisville

DEVELOPING ADVANCED MATHEMATICAL MODELS FOR DETECTING ABNORMALITIES IN 2D/3D MEDICAL STRUCTURES

By

Ahmed Abd-Elrahman Elnakib
M.Sc., ECE, Mansoura University, 2007

A Dissertation
Submitted to the Faculty of the
J. B. Speed School of the University of Louisville
in Partial Fulfillment of the Requirements
for the Degree of

Doctor of Philosophy

Department of Electrical and Computer Engineering
University of Louisville
Louisville, Kentucky

December 2013

DEVELOPING ADVANCED MATHEMATICAL MODELS FOR DETECTING ABNORMALITIES IN 2D/3D MEDICAL STRUCTURES

By

Ahmed Abd-Elrahman Elnakib
M.Sc., ECE, Mansoura University, 2007

A Dissertation Approved on

December 5th, 2013

---

by the Following Reading and Examination Committee:

Ayman El-Baz, Ph.D., Dissertation
Director

Tamer Inanc, Ph.D., Co-Advisor

Manuel Casanova, Ph.D.

Olfa Nasraoui, Ph.D.

Karla Welch, Ph.D.

Cindy Harnett, Ph.D.

DEDICATION

This dissertation is dedicated to my mother, my father, and my wife for their love,

patience, and support during the completion of this endeavor.

ACKNOWLEDGMENTS

In the Name of Allah, the most beneficent, the most merciful. All deepest thanks are due to Allah, the compassionate for the uncountable gifts given to me.

I would like to express my sincere gratitude to Professor El-Baz, my dissertation advisor, for the immeasurable amount of support and guidance he has provided throughout this study. He gave me the opportunity to work in his distinguished research group and provided me with an exciting working environment that facilitate many opportunities to develop new ideas and working on promising applications. Dr. El-Baz is always willing to give, share, and appreciate. I knew that I could always expect full credit for my accomplishments. He always supported me with novel ideas that helped me to publish my works in the top international conference and journal papers. It is worthy to mention that Professor El-Baz is a great advisor as well as a good friend who helps any Ph.D. student who works with him in high energy level. I cannot thank him enough, and shall remain grateful for all he has done.

I would like to thank Professor Garth Beache of the Department of Radiology of University of Louisville Hospital for spending much of his valuable time guiding my work in automatic detection of cardiac damage tissue and automatic segmentation of heart cavity and other cardiac structures, commenting on its quality, and for many suggestions on how to make the tools developed more applicable in the setting of medical research and clinical use.

ABSTRACT

DEVELOPING ADVANCED MATHEMATICAL MODELS FOR DETECTING

ABNORMALITIES IN 2D/3D MEDICAL STRUCTURES

Ahmed Abd-Elrahman Elnakib

December 05, 2013

Detecting abnormalities in two-dimensional (2D) and three-dimensional (3D) medical structures is among the most interesting and challenging research areas in the medical imaging field. Obtaining the desired accurate automated quantification of abnormalities in medical structures is still very challenging. This is due to a large and constantly growing number of different objects of interest and associated abnormalities, large variations of their appearances and shapes in images, different medical imaging modalities, and associated changes of signal homogeneity and noise for each object. The main objective of this dissertation is to address these problems and to provide proper mathematical models and techniques that are capable of analyzing low and high resolution medical data and providing an accurate, automated analysis of the abnormalities in medical structures in terms of their area/volume, shape, and associated abnormal functionality.

This dissertation presents different preliminary mathematical models and techniques that are applied in three case studies: (*i*) detecting abnormal tissue in

the left ventricle (LV) wall of the heart from delayed contrast-enhanced cardiac magnetic resonance images (MRI), (*ii*) detecting local cardiac diseases based on estimating the functional strain metric from cardiac cine MRI, and (*iii*) identifying the abnormalities in the corpus callosum (CC) brain structure—the largest fiber bundle that connects the two hemispheres in the brain—for subjects that suffer from developmental brain disorders. For detecting the abnormal tissue in the heart, a graph-cut mathematical optimization model with a cost function that accounts for the object's visual appearance and shape is used to segment the the inner cavity. The model is further integrated with a geometric model (i.e., a fast marching level set model) to segment the outer border of the myocardial wall (the LV). Then the abnormal tissue in the myocardium wall (also called dead tissue, pathological tissue, or infarct area) is identified based on a joint Markov-Gibbs random field (MGRF) model of the image and its region (segmentation) map that accounts for the pixel intensities and the spatial interactions between the pixels. Experiments with real in-vivo data and comparative results with ground truth (identified by a radiologist) and other approaches showed that the proposed framework can accurately detect the pathological tissue and can provide useful metrics for radiologists and clinicians.

To estimate the strain from cardiac cine MRI, a novel method based on tracking the LV wall geometry is proposed. To achieve this goal, a partial differential equation (PDE) method is applied to track the LV wall points by solving the Laplace equation between the LV contours of each two successive image frames over the cardiac cycle. The main advantage of the proposed tracking method over traditional texture-based methods is its ability to track the movement and rotation of the LV wall based on tracking the geometric features of the inner, mid-, and outer walls of the LV. This overcomes noise sources that come from scanner and heart motion.

To identify the abnormalities in the CC from brain MRI, the CCs are aligned using a rigid registration model and are segmented using a shape-appearance model. Then, they are mapped to a simple unified space for analysis. This work introduces a novel cylindrical mapping model, which is conformal (i.e., one to one transformation and bijective), that enables accurate 3D shape analysis of the CC in the cylindrical domain. The framework can detect abnormalities in all divisions of the CC (i.e., splenium, rostrum, genu and body). In addition, it offers a whole 3D analysis of the CC abnormalities instead of only area-based analysis as done by previous groups. The initial classification results based on the centerline length and CC thickness suggest that the proposed CC shape analysis is a promising supplement to the current techniques for diagnosing dyslexia.

The proposed techniques in this dissertation have been successfully tested on complex synthetic and MR images and can be used to advantage in many of today's clinical applications of computer-assisted medical diagnostics and intervention.

TABLE OF CONTENTS

CHAPTER

APPENDIX

LIST OF TABLES

LIST OF FIGURES

LIST OF ALGORITHMS

CHAPTER I

INTRODUCTION

Early detection of abnormalities in human organs is very important for the diagnosis of human diseases and can lead to better treatment outcomes. The goal of this work is to detect abnormalities in medical structures and to investigate extracting automated and accurate metrics that can quantify these abnormalities. Medical reports show that the early detection of heart diseases (e.g., left ventricle dysfunction and ischemic heart disease, a case study in this dissertation), and brain disorders (e..g, dyslexia, a case study in this dissertation) can assist the clinicians to afford better treatment and leads to increase the survival rate of patients with these diseases. Medical imaging represents a noninvasive way to reveal these abnormalities and has been emerged as a basic component in current medical diagnostic tools. Nowadays, it has been effectively used to assist clinicians and radiologists in diagnosis, therapy decisions, and surgery operations.

Recent advances in medical image modalities, including magnetic resonance imaging (MRI), computed tomography (CT), and ultrasound (US), enable the acquisition of images for almost all types and sizes of different structures with acceptable degrees of contrast and resolution. A wide scope of abnormalities have been extensively explored in different research areas, such as detecting cancerous cells in different medical structures, identifying dead tissues in different organs, and detecting brain abnormalities in subjects with brain disorders. The process of detecting these abnormalities from medical images involves developing advanced

mathematical models for the appearance and shapes of the structures and their abnormalities and providing efficient algorithms towards accurate abnormality detection and quantification. Various aspects of these mathematical models and algorithms have been extensively explored for many years in a host of publications. However, obtaining the desired accurate automated abnormality detection and quantification is still very challenging due to a large and constantly growing number of abnormalities in medical structures, large variations of their properties in images, different metrics used to quantify each abnormality, different medical imaging modalities, and associated changes of signal homogeneity, variability, and noise for each modality. The main objective of this dissertation is to address these problems and present proper mathematical models and techniques in order to provide an accurate, automated detection and quantification of abnormalities using medical imaging. **Since all the work presented in this dissertation mainly deals with medical images, below, the different types of modalities that are used to capture medical images are overviewed.**
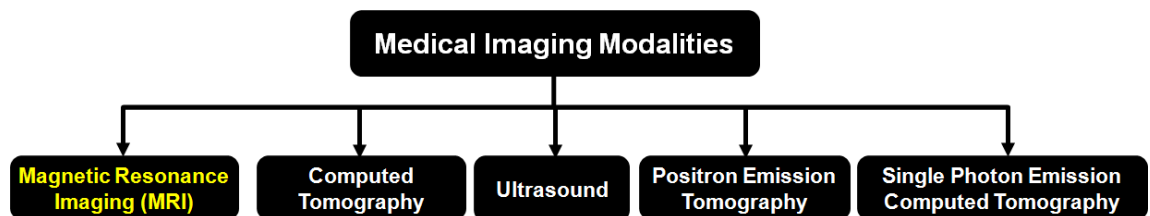
FIGURE 1: Classes of medical image modalities. This dissertation mainly deals with MRI (written with yellow font).

A.   MEDICAL IMAGING

A constant growing number of image modalities with different imaging capture parameters has been recently developed in order to capture and visualize the constantly growing number of different medical structures with acceptable

resolution and contrast. Each of these modalities (see e.g., Figure 1, Figure 2, and Figure 3) has its own mechanism of providing relevant physiological information of the organ being imaged as well as its own advantages and limitations. Medical images can be classified based on their modalities (Figure 1) or based on the type of information that they provide (i.e., the structure or the function of the organ being imaged, see Figure 3). **Since all the work presented in this dissertation mainly deals with magnetic resonance images, the details of the different techniques of magnetic resonance images are presented below.**

1.   Magnetic Resonance Imaging (MRI)

MRI is a medical imaging modality that is based on the same principles of nuclear magnetic resonance (NMR) spectroscopy [12]. MRI has become the most powerful and central non-invasive tool for clinical diagnosis of diseases [13]. The fundamental principle of MRI is based on the use of a strong static magnetic field in which the hydrogen nuclei (single proton) of water molecules in human tissues are aligned parallel to that field. Then, an external radio frequency (RF) pulse (wave) is applied to the unpaired magnetic spins (proton) aligned in the static magnetic field, making them spin in different directions [14]. The interaction between the RF and proton spins leads to periodic absorption and emission of energy. When the protons relax back to their lower energy (equilibrium) state, they release detectable signals (energy) that are spatially encoded and are used to construct the MR image. Different types of tissues (muscle, fat, cerebral spinal fluid, etc.) send back measurably different types of tissue-specific signals following the application of the same RF pulse. The contrast of an MR image is strongly dependent on the way the image is acquired. Different components of the scanned area can be highlighted using different pulse sequences: a preselected strength, shape, and timing of defined RF and gradient pulses (external fields). Generally, MRI can be
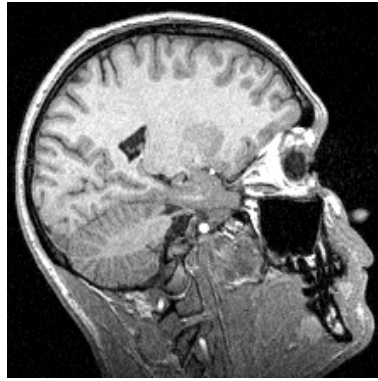
(a)

(b)

(c)
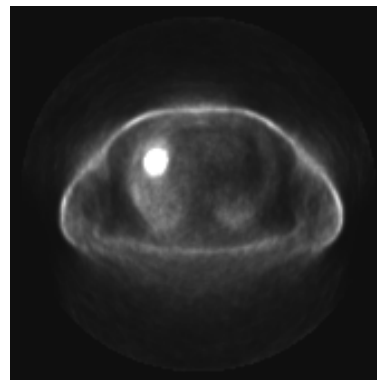
(d)
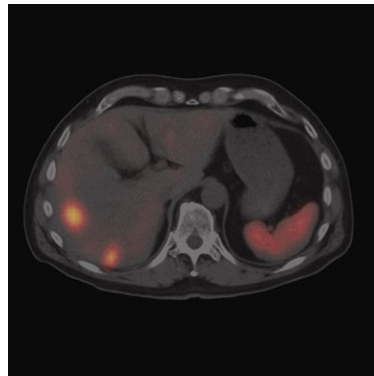
(e)

FIGURE 2: Different types of medical images: (a) magnetic resonance imaging (MRI) of the brain, (b) computed tomography (CT) image of the kidney, (c) ultrasound (US) image of the fetus, (d) positron emission tomography (PET) image of the lung, and (e) single photon emission computed tomography (SPECT) image of the liver.
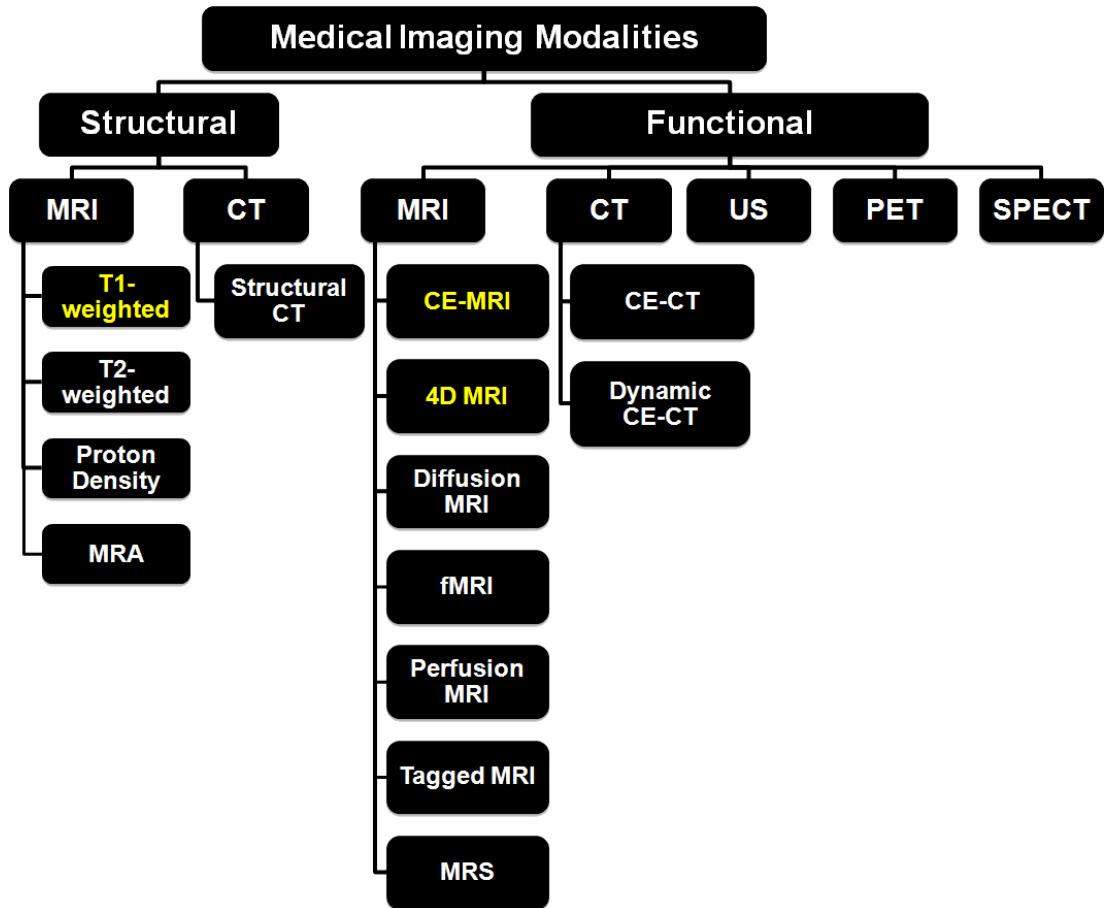
FIGURE 3: Categories of medical image modalities based on the type of information that they provide about the organ being imaged, i.e., structural or functional imaging. MRI, CT, US, PET, SPECT, MRA, CE-MRI, fMRI, MRS, CT-CE stand for magnetic resonance imaging, computed tomography, ultrasound, positron emission tomography, single photon emission computed tomography, magnetic resonance angiography, contrast-enhanced MRI, functional MRI, magnetic resonance spectroscopy, and contrast-enhanced CT, respectively. This dissertation mainly deals with the categories that are written in yellow.

used to acquire planner 2D images (Figure 5), 3D volumes (Figure 6), or sequences of 3D volumes. Most commonly-known specialized MRI techniques are shown in Figure 4. **The following sections focus on the MRI techniques that are used throughout this dissertation (i.e., structural MRI to image the brain and CE-MRI and 4D MRI to image the heart).**
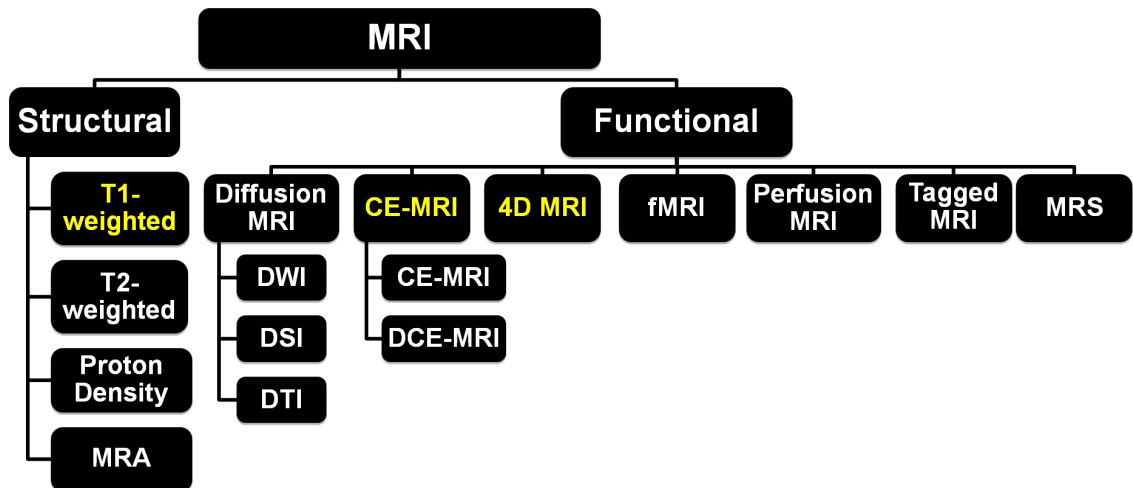
FIGURE 4: Different specialized MRI acquisition techniques. MRA, DWI, DSI, DTI, CE-MRI, DCE-MRI, fMRI, MRS, stand for magnetic resonance angiography, diffusion-weighted imaging, diffusion spectrum imaging, diffusion tensor imaging, contrast-enhanced MRI, dynamic CE-MRI, functional MRI, and magnetic resonance spectroscopy, respectively. The dissertation mainly deals with the categories that are written in yellow.

FIGURE 5: 2D MR image of the knee. Courtesy of [2]

a. Structural MRI: Structural MRI involves the MRI techniques that show the anatomy of human structures or body tissues, such as T-weighted, T2-weighted, proton density (PD), and magnetic resonance angiography (MRA). Since MRA, a MRI exam for imaging the vascular anatomy, is out of the scope of this dissertation,
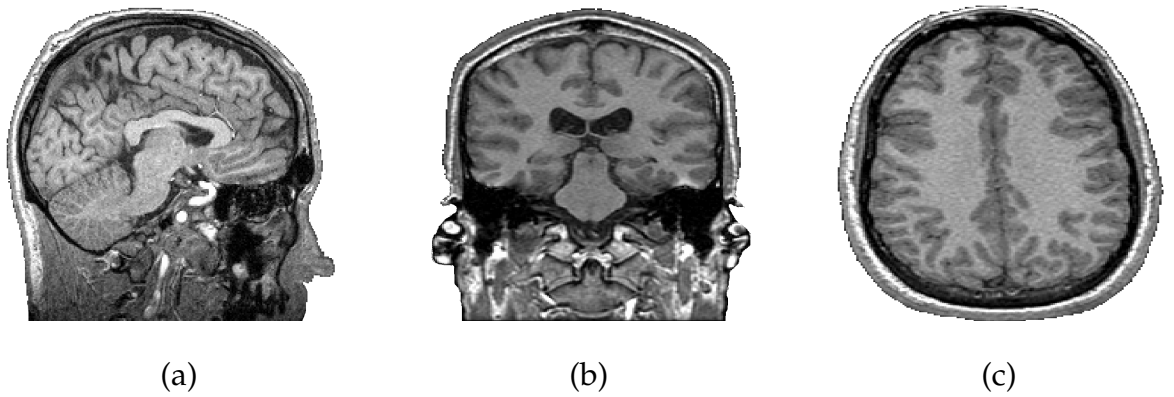
FIGURE 6: Typical 3D MRI of the brain, captured in three views: (a) sagittal plane, (b) coronal plane, and (c) axial plane.

this section will focus on illustrating the other three types. The amount of energy (or signal strength) on each of these three types primarily depends on the magnetic relaxation properties of body atomic nuclei. The time of the relaxation process (i.e., the time taken by nuclei to return to their baseline states after applying the RF pulse) is known as longitudinal relaxation time (T1) or transverse relaxation time (T2), based on the orientation of the component with respect to the magnetic field. Every tissue in the human body has its own T1 and T2 values, which depend on the concentration of protons in the tissue in the form of water and macromolecules. T1-weighted MRI is the commonly-run clinical MRI scan that emphasizes T1-contrast, i.e., most of the contrast between tissues is due to differences in tissue T1 values. Thus, it is the best MRI method for demonstrating anatomical details. T2-weighted scans are another basic type that emphasizes T2 contrast. Usually, T2-weighted is used when it is required to show high contrast between fluid, abnormalities (e.g., tumors, inflammation, trauma), and the surrounding tissues. Therefore, it is the best MRI method for pathological details. In practice, T1- and T2-weighted images provide complementary information, so both are important for characterizing abnormalities. Finally, the proton density (spin density) weighted scans try to have no contrast from either T1 or T2. The only signal change is due to differences in the amount of available spins (hydrogen nuclei in water). The main advantage of

the PD-weighted images is the increase in contrast between fluid and non-fluid tissues. However, PD-weighted images usually show less contrast resolution than T1- and T2-weighted images. This is due to the fact that the difference in hydrogen concentration (proton density) of soft tissues is relatively small.

The main strength of MRI is that it offers the best soft tissue contrast among all image modalities. Moreover, it is a dynamic technology that can be optimized to tailor the imaging study to the anatomical part of interest and to the disease process being studied. In this regard, MRI offers different degrees of dynamic optimization. For example, the imaging plane can be optimized to the anatomical area being studied (axial, coronal, sagittal, see Figure 6), and multiple oblique planes can be captured with equal ease. In addition, as described above, the signal intensities of the imaged tissues can be controlled by selecting the type of the scan: either proton density, T1-weighted, or T2-weighted [13, 15, 16] (see, Figure 7). Moreover, for a given type of scan, a pulse sequence is designed and imaging parameters are optimized to produce the desired image contrast (see Figure 8).

| (a) | (b) | (c) |
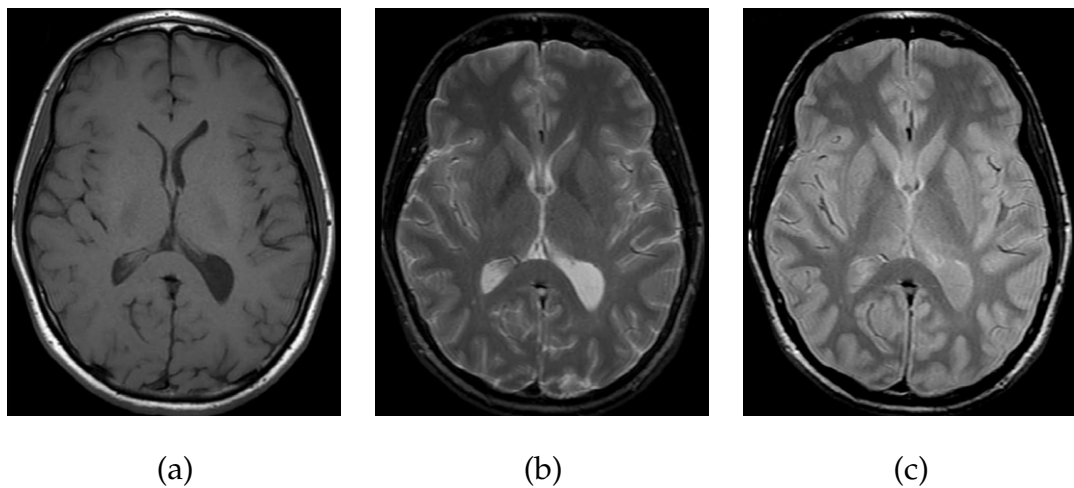
FIGURE 7: Examples of MRI brain scans: (a) T1-weighted, (b) proton density, and (c) T2-weighted images. The images have very different image contrasts that reveal specific information about various structures in the brain.
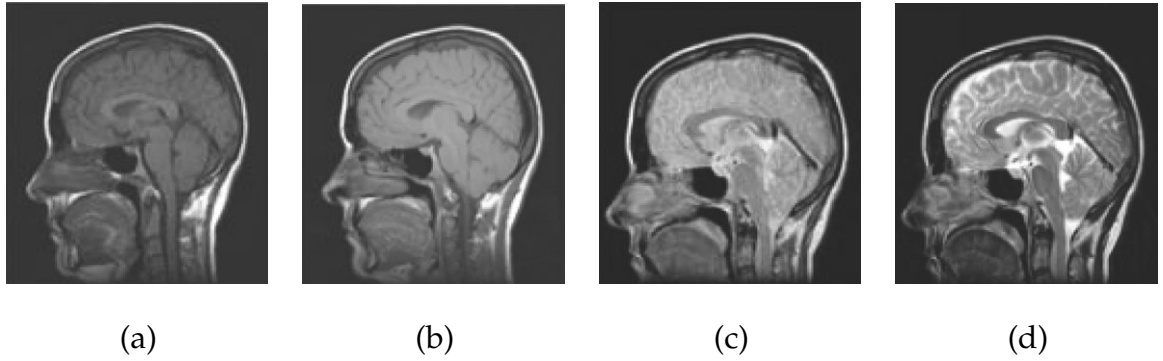
FIGURE 8: MRI scans of the brain using different pulse sequences and scanning parameters: (a)&(b) two T1-weighted images captured using different scanning parameters and (c)&(d) two T2-weighted images captured using different scanning parameters. Courtesy of [3].

b. Contrast-enhanced MRI (CE-MRI): Although structural MRI provides excellent soft tissue contrast, it lacks functional information. Contrast-enhanced MRI (CE-MRI) is a special MR technique that has the ability to provide superior information of the anatomy, function, and metabolism of target tissues [17]. The technique involves the acquisition of MR images with high temporal resolution before, during, and at several times after the administration of a contrast agent into the blood stream. In CE-MRI, the signal intensity in target tissue changes in proportion to the contrast agent concentration in the volume element of measurement, or voxel. CE-MRI is commonly used to enhance the contrast between different tissues, particularly normal and pathological. Typical examples of CE-MRI time series data of the kidney, heart, and prostate are shown in Figure 9.

CE-MRI has gained considerable attention due to the lack of ionizing radiation, and increased spatial resolution. It has been extensively used in many clinical applications, including detection of pathological tissue in the myocardium and early detection of acute renal rejection [18]. Unlike structural MRI where the contrast mainly depends on the intrinsic magnetic relaxation times T1 and T2, CE-MRI technique employs the administration (oral, rectal, intravesical, or intravenous) of
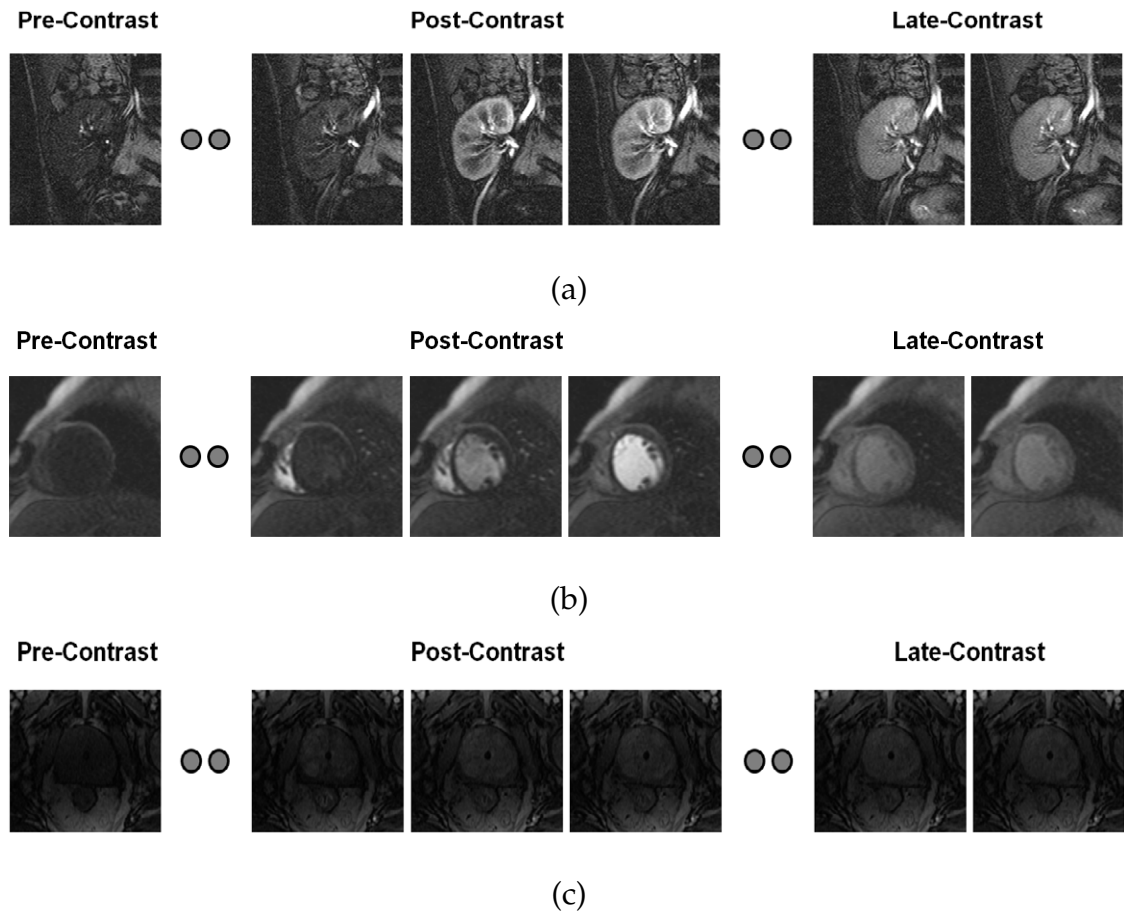
FIGURE 9: CE-MRI images taken at different time points post the adminstration of the contrast agent showing the change of the contrast as the contrast agent perfuse into the tissue beds for (a) kidney, (b) heart, and (c) prostate.

contrast agents prior to the medical scan. The main role of the use of the contrast agents is to increase the image contrast of anatomical structures (e.g., blood vessels) that are not easily visualized by the alteration of the magnetic properties of water molecules in their vicinity. This in turns improves the visualization of tissues, organs, and physiological processes. In clinical practice, several types of contrast agents are in use and their choice is based on the imaging modality. In particular, for MRI there are several types of contrast agents such as paramagnetic agents, superparamagnetic agents, extracellular fluid space (ECF) agents, and tissue (organ)-specific agents, see Figure 10.

```
                    ┌─────────────────────────┐
                    │   MRI Contrast Agents    │
                    └─────────────────────────┘
        ┌──────────────┬────────────┴──────────────┬──────────────┐
┌───────────────┐ ┌──────────────────┐ ┌──────────────────┐ ┌──────────────────┐
│  Paramagnetic │ │ Super-paramagnetic│ │ Extracellular Fluid│ │  Tissue (Organ)-  │
│               │ │                   │ │      Space        │ │  specific Agents  │
└───────────────┘ └──────────────────┘ └──────────────────┘ └──────────────────┘
    ┌───────────┐      ┌───────────┐
    │ Gadolinium│      │ Iron Oxide│
    └───────────┘      └───────────┘
    ┌───────────┐
    │ Manganese │
    └───────────┘
```
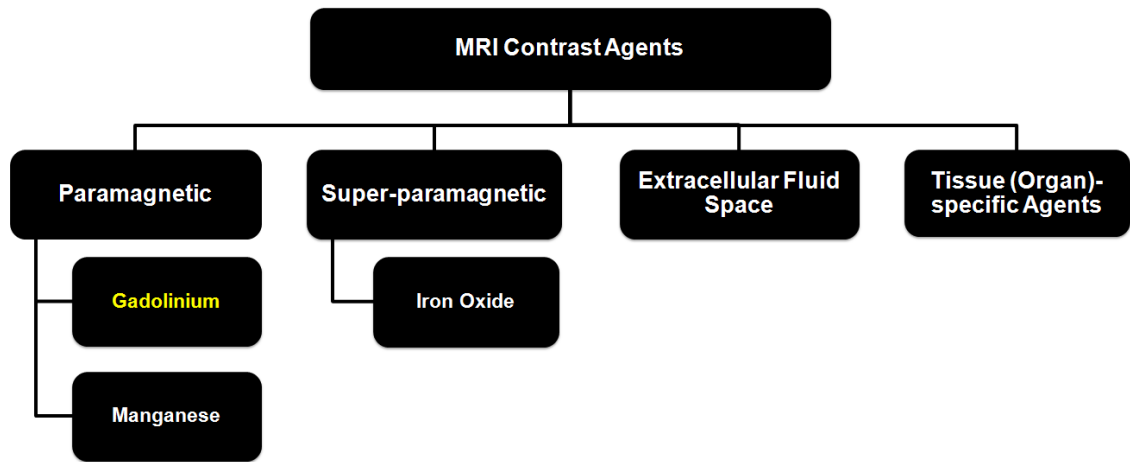
FIGURE 10: Different types of contrast agents used in MRI medical scans. In this dissertation, Gadolinium-based (written in yellow) CE-MRI is used to detect the pathological tissue from the left ventricle (LV) wall of the heart.

The most successful MRI contrast agents that have been widely investigated are gadolinium-based. Gadolinium, a rare metal, is a non-toxic paramagnetic contrast agent that enhances the detected MR signal and produces high contrast images of soft tissues by decreasing T1 relaxation times of water protons in living tissue in the vicinity of the paramagnetic contrast agent. Gadolinium-based CE-MRI has been extensively used in cardiovascular, oncological, and neurological imaging applications.

c. Four-dimensional (4D) MRI: Recent advances and scanning techniques of MRI allow the capture of 4D MRI images of the human structures. 4D MRI represents sequences of 3D volumes that are captured on different time instances. To acquire the 4D MRI, dedicated scanning techniques should be developed to scan the human structure of interest with a sufficient speed to cover the change in the anatomy with time. 4D MRI images have the ability to provide both functional and anatomical information about the human structure being imaged. Recently, they have been used in many applications, e.g., to show how the anatomy changes and provide the functionality of the heart during the cardiac cycle. An example of using 4D MRI of the heart is shown in Figure 11.
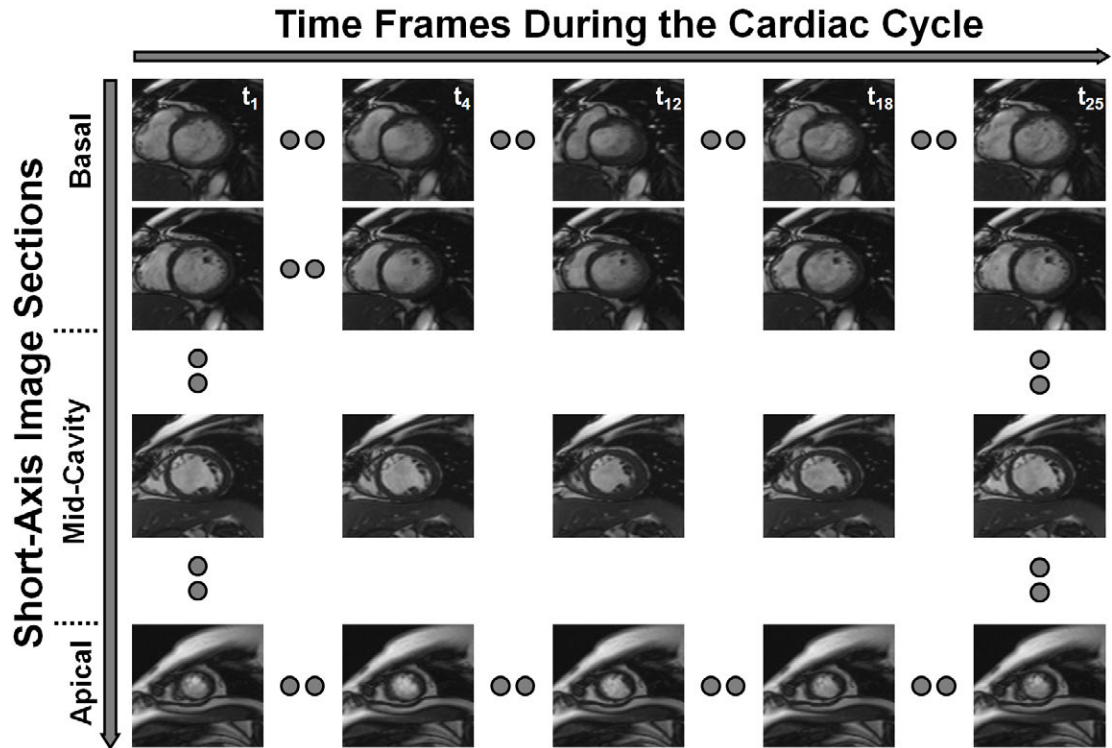
FIGURE 11: Typical 4D (3D plus time) cardiac MRI data. Images are acquired at different sections covering the heart (from basal to apical), and each section consists of a time series of 25 images over the cardiac cycle. Cine CMRI has the ability to show how the anatomy changes and provide the functionality of the heart during the cardiac cycle.

In total, potential advantages of MRI include that MRI does not involve exposure to any harmful radiation, can be repeated sequentially over time, and has the ability to generate cross-sectional images in any plane (including oblique planes). Additionally, MRI provides superior resolution with far better contrast (the ability to distinguish the differences between two arbitrarily similar but not identical tissues) compared with other medical image modalities [13]. Finally, MRI plays an important role in assessing tumors' locations and extent, directing biopsies, planning proper therapy, and evaluating therapeutic results [19].

On the other hand, MRI imaging modality has its own disadvantages: (i) MRI data acquisition is a relatively long and complex process–for each scan the

imaging parameters and the pulse sequence need to be fixed; (ii) MRI is not suitable for patients with metal implants due to its magnetic nature; (iii) MRI suffers from sensitivity to noise and image artifacts; (iv) MRI signals are dependent on the imaging sequence used and can become non-linear beyond certain concentrations leading to errors in extracted physiology; (v) MRI scanning processes may be uncomfortable for some people because it can produce claustrophobia. Recent improvements in MRI design aim to aid claustrophobic patients by using more open magnet designs and shorter exam times. However, there is often a trade-off between image quality and open design.

B. QUANTIFYING ABNORMALITIES IN MRI

Using MRI, several types of abnormalities in human structures can be revealed. In general, these abnormalities can be quantified based on different types of metrics, e.g., areal/volumetric, shape-based metrics, and/or functional metrics. A taxonomy of the different metrics are shown in Figure 12.

Volumetric metrics are of great clinical importance in diagnostics of diseases and deciding the need for therapies or proper medications. For example, they can be used to investigate the progress of tumors by estimating the corresponding change in the volume of tumors over periodic scans. The shape features are severely used to define certain diseases or pathologies associated in different medical structures. For example, the shape of lung nodules can be used as a discriminatory feature to distinguish malignant and benign nodules. Functional features are used to determine the status and functionality of different structures and can conclude patient enhancement. The goal of this work is to detect abnormalities in medical structures and to investigate extracting automated and accurate metrics that can quantify these abnormalities. In particular, this dissertation addresses two
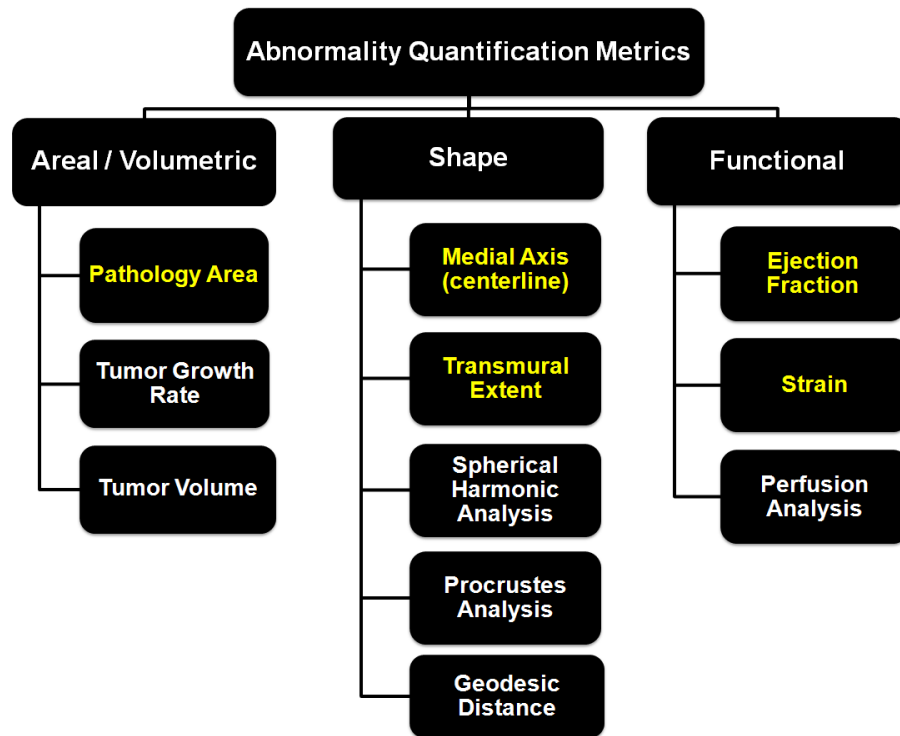
FIGURE 12: Taxonomy of abnormality quantification metrics showing examples for each category. The dissertation deals with the metrics written in yellow.

case studies for abnormality detection and quantification. The first case study is to detect the abnormal tissue in the left ventricle (LV) wall of the heart from cardiac magnetic resonance images in order to quantify the LV dysfunction. The second case study is to detect local cardiac diseases based on functional strain estimation from cine MRI. The third case study is to identify the shape abnormalities in the the corpus callosum (CC) brain structure—the largest fiber bundle that connects the two hemispheres in the brain—for the subjects that suffer from dyslexia using brain MRI. **Since the main interest of this dissertation is to extract accurate metrics to quantify abnormalities in these three case studies, the next section will detail the different types of quantification metrics for each case study.**

1.   Quantification of the LV Dysfunction

Different metrics can be extracted to quantify the LV dysfunction using MRI, such as the area of pathological tissue, the transmural extent, and the functional indexes (e.g., functional strain and the ejection fraction (EF)). Measuring the area of pathological tissue in the LV (see Figure 13) is important to assist the cardiologists in the diagnosis of the LV dysfunction and ischemic heart disease. However, for reliable size measurement, the pathological tissue has to be accurately delineated within the LV wall from the adjacent undamaged tissue. **Accurate identification of the pathology is a challenge due to image noise, limited resolution, and imprecise boundaries.**
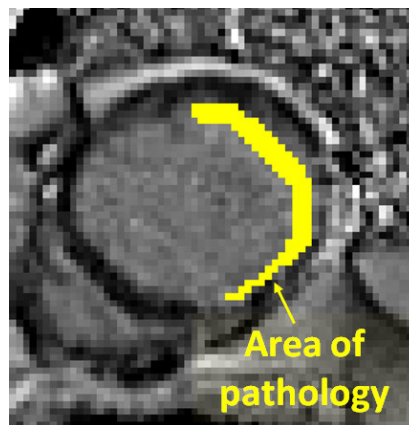
FIGURE 13: Area of pathological tissue in the LV wall, delineated in yellow, in a typical Gadolinium-based CE-MRI of the heart.

The transmural extent (or transmurality) is one of the candidate shape metrics that has been explored to quantify the myocardial viability. Transmurality is defined as the fraction of pathological tissue's extension across the myocardial wall. A previously investigated procedure for estimating the transmural extent (e.g., used in [20, 21]) extends a fixed number of radial lines from the inner to the outer contour of the LV (see Figure 14(a)). After segments of the pathological tissue along each line are determined, the transmural extent is estimated as the average
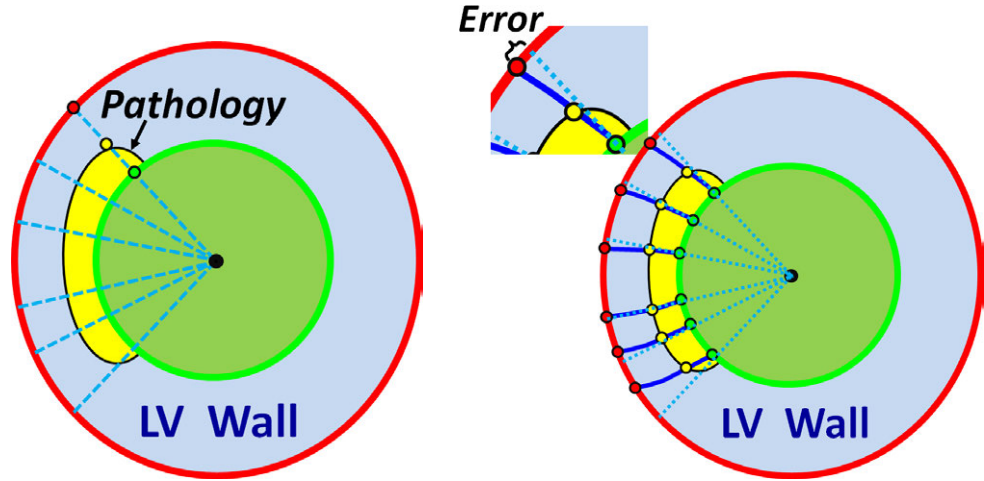
FIGURE 14: (a) The standard radial approach for the estimation of the transmural extent of pathological tissue in the LV wall and (b) the deviations of the radial method from the co-located corresponding pixel pairs.

pathological tissue's extent relative to these lines. As illustrated in Figure 14 (b), this, so-called radial method, is in principle inaccurate in establishing point-to-point correspondences and geometrically inconsistent in estimating the transmural extent. **Therefore, a more accurate shape-based analysis for estimating the transmural extent should be investigated.**

2. Detection of Local and Global Cardiac Diseases

Functional indexes can help cardiologists to accurately quantify the heart status and detect local and global cardiac diseases, e.g., the EF metric and the functional strain. The EF is a clinically relevant and well-documented global indicator of the LV function in terms of the total cavity volume (the LV volume variation over time):

$$EF = \frac{EDV - ESV}{EDV} = 1 - \frac{ESV}{EDV} \tag{1}$$

where ESV and EDV are the end systolic (the smallest cavity area) and the end diastolic (the greatest cavity area) volumes, respectively.

To estimate the EF, the LV cavity volume-time data at each image slice is used. Following the delineation of the cavity contour at each time point (image frame) of the cardiac cycle, the corresponding cavity areas are computed and a curve representing the physiology over the cardiac cycle is constructed. Then, the Simpson's rule is used to estimate the total LV volume by summing the contributions of enclosed areas from the individual image slices. From the total ventricular function curve, the EDV and ESV can be automatically extracted (see Figure 15 (a)) and hence calculate the EF.

(a)   (b)
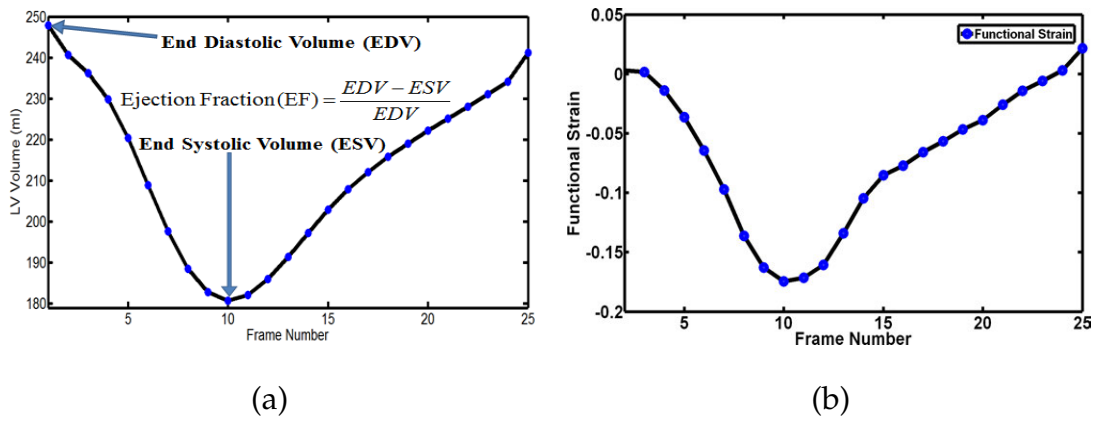
FIGURE 15: (a) Ventricular function curve (obtained by summing the cavity areas over the heart) over the cardiac cycle, being used to estimate the EF, and (b) corresponding functional strain of the heart over cardiac cycle.

On the other hand, the functional strain is one of the important quantification metrics of the cardiac status. Local cardiac diseases (such as coronary atherosclerosis) and global conditions (such as heart failure and diabetes) result in wall dysfunction that manifests on strain slopes during the contraction and expansion phases of the cardiac cycle [22]. Therefore, accurate strain estimation is important for the early detection of these diseases (see Figure 15 (b)). Traditionally, the functional strain is estimated by using the tagged images that lead to errors between

the estimated indexes due to the inter-slice variability between the different image modalities. **There is a need to develop approaches that can estimate more correlated functional indexes to completely characterize the heart status.**

(a) (b)
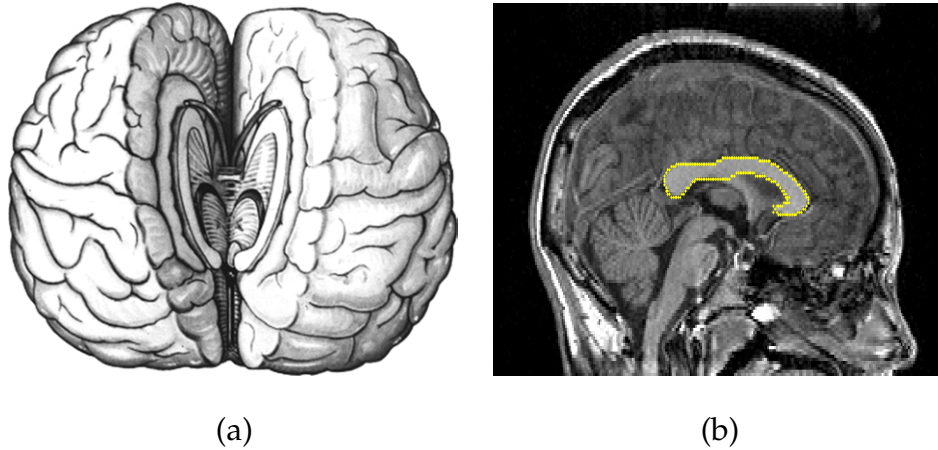
FIGURE 16: The corpus callosum (CC) brain structure: (a) 3D illustration and (b) a typical MR brain image with the CC delineated in yellow.

3. Identification of the CC Shape Abnormalities in Dyslexic Brains

The CC is the largest fiber bundle in the brain that is responsible for passing sensory, motor and cognitive information between homologous regions in the two cerebral hemispheres (see Figure 16). Since human reading skills are highly affected by the impaired communication between the hemispheres, the analysis of the CC for dyslexic subjects is extensively explored [23–26]. The CC centerline length (CLL) is a candidate metric to quantify the shape differences between the normal and dyslexic subjects (see Figure 17). Unfortunately, the existing techniques for extracting CC centerlines suffer from at least one of the following shortcomings: (*i*) they are computationally expensive, (*ii*) suffer from lack of robustness, and (*iii*) are sensitive to boundary noise. **There is a need to develop more accurate approaches to accurately extract the centerline in order to characterize the shape differences between normal and dyslexic subjects.**
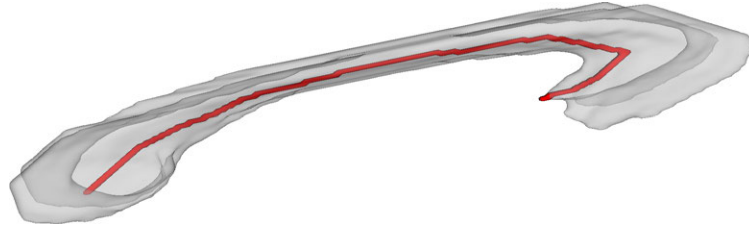
FIGURE 17: 3D visualization of the CC centerline.

C. THE NEED FOR THIS WORK

The current abnormality detection and quantification metrics suffer from the following limitations:

- The area and volumetric measurements are:

  - Subject to errors coming from spatial smoothing, spatial registration, and segmentation of structures.

  - Sensitive to image noise, limited resolution, and imprecise object boundaries.

- Current radial estimation method for the transmural extent of pathological tissue in the LV wall suffers from geometric inconsistency in estimating the point-to-point correspondences between the inner and outer boundaries.

- Most of the current approaches for extracting CC centerline are computationally expensive, suffer from lack of robustness, and/or are sensitive to boundary noise.

- The functional strain is estimated by using the tagged images whereas the EF metric is estimated from cine cardiac MRI. This leads to errors between the estimated indexes due to the inter-slice variability between the different image modalities.

To overcome these limitations, comprehensive mathematical models and advanced techniques are provided to analyze medical images and provide an accurate automated detection and quantification of abnormalities in medical structures. These mathematical models include three novel segmentation models. The first model is a graph-cut optimization model that integrates the appearance and shape of the object of interest for the purpose of segmentation. Experiments, presented in Chapter III, confirm that this approach shows superior results in segmenting the inner cavity of the heart. The second model is a fast marching level set that evolves from an initial boundary with a speed function formed based on the intensity, spatial interaction, and object shape. Experiments, presented in Chapter III, confirm the high capabilities of this approach to evolve from the inner cavity and stop by the outer boundaries of the LV of the heart, providing an accurate segmentation of the outer contour of the LV wall. The third segmentation approach makes full use of the intensity and spatial interaction descriptors, in a joint Markov Gibbs random field (MGRF) model of the image signals and their region map, to identify the pathological tissue in the LV wall. The intensity, spatial interaction, and shape descriptor are further extended in 3D (Chapter VII) to segment the 3D CC structure from the brain. The preliminary results of the proposed segmentation approaches confirm the benefits of these models and encourage applying them in other applications.

In addition to the proposed segmentation models, this work proposes an accurate model to estimate the transmural extent, an important metric to quantify the myocardial wall of the heart. The model is based on solving the PDE Laplace equation to collocate the correspondence between two contours. Phantom validation shows that the PDE Laplace-based method outperforms the current methods in estimating the transmural extent.

Moreover, a novel method for estimating the strain from cine MRI is presented. Unlike current methods that depend on the intensity and spatial information to track the wall motion, the proposed method sticks to the geometry of the heart to track its motion. To achieve this goal, this method applied a PDE method to track the LV wall points by solving the Laplace equation between the LV contours of each two successive image frames over the cardiac cycle. The main advantage of the proposed tracking method over traditional texture-based methods is its ability to track the movement and rotation of the LV wall based on tracking the geometrical features of the inner, mid-, and outer walls of the LV. This overcomes noise sources that come from scanner and heart motion.

Furthermore, an automated level-set-based model is presented to extract the CC centerline from brain MRI. The key idea of this model is to propagate wavefronts from the splenium with a fast speed. Then, the trajectory of wavefront points that have the maximum positive curvature and are located at the maximum distance from the object boundary represents the extracted centerline. Experiments show good dyslexia diagnostic results based on using this model.

Finally, a novel mapping model to establish correspondences between two 3D surfaces is proposed. Surfaces are mapped to a unified cylindrical domain for analysis. The model has been used to detect the abnormalities in the CC brain structure between the dyslexic and normal brains by analyzing the CCs in the cylindrical domain. This mapping leads to detect abnormalities in all divisions of the CC (i.e., splenium, rostrum, genu, and body) and offers a whole 3D analysis of the CC abnormalities instead of only area based as done by other groups.

D. DISSERTATION ORGANIZATION

This dissertation consists of eight chapters. The following remarks summarize the scope of each chapter:

Chapter II overviews the existing computational methods for identifying left ventricle heart pathologies.

Chapter III illustrates the proposed framework for the segmentation of the inner cavity and outer border of the myocardial (LV) wall using graph-cut optimization of a cost function that accounts for the object visual appearance and shape.

Chapter IV illustrates the proposed framework for LV pathology identification and quantification based on a joint MGRF of image and its region map that accounts for the pixel intensities and the spatial interactions between the pixels.

Chapter V illustrates the proposed framework for estimating the functional strain from cine cardiac MRI based on tracking the geometric features of the inner-, mid-, and outer-walls of the LV.

Chapter VI overviews the existing MRI-based systems for detecting brain abnormalities that are associated with dyslexia. The chapter covers the findings in the literature for detecting dyslexia-associated abnormalities in structural MRI, diffusion tensor imaging (DTI), and functional MRI (fMRI).

Chapter VII explains the proposed framework for detecting abnormalities in the CC brain structure based on a novel cylindrical mapping of the CC surface that offers a whole 3D analysis of the CC abnormalities and reveals 3D discriminant features for dyslexia diagnosis.

Chapter VIII concludes the work and outlines the future work.

CHAPTER II

COMPUTATIONAL METHODS FOR IDENTIFYING LEFT VENTRICLE (LV) HEART PATHOLOGIES: A SURVEY

Characterizing the workings of the heart and detecting left ventricle (LV) wall pathologies are very important for diagnosing ischemic heart disease and heart failure. Heart failure is the most important cause of morbidity and mortality in adult cardiovascular disease, affecting 6 million USA patients annually. If not diagnosed and treated early, these patients have a relentless time course to premature death.

Recent advances in cardiac MRI (CMRI), enable the detection of the LV wall pathologies and estimation of different quantification metrics that characterize the working of the heart. Examples of these metrics include the area of pathological tissue in the LV wall, the transmural extent of pathology, and other indexes such as wall thickening, functional strain, and the ejection fraction (EF) metrics. Several computational methods have been proposed in the literature in order to estimate these metrics based on using different CMRI acquisition techniques, such as cardiac-enhance CMRI (CE-CMRI) and cine CMRI. This chapter overviews these computational methods, focusing on the metrics extracted using CE-CMRI and cine CMRI (see Figure 18).

To estimate these metrics, a general framework for analyzing CMRI in order to quantify the LV wall pathologies is demonstrated in Figure 19. The framework consists of two processing steps: the segmentation of the LV wall and estimation of
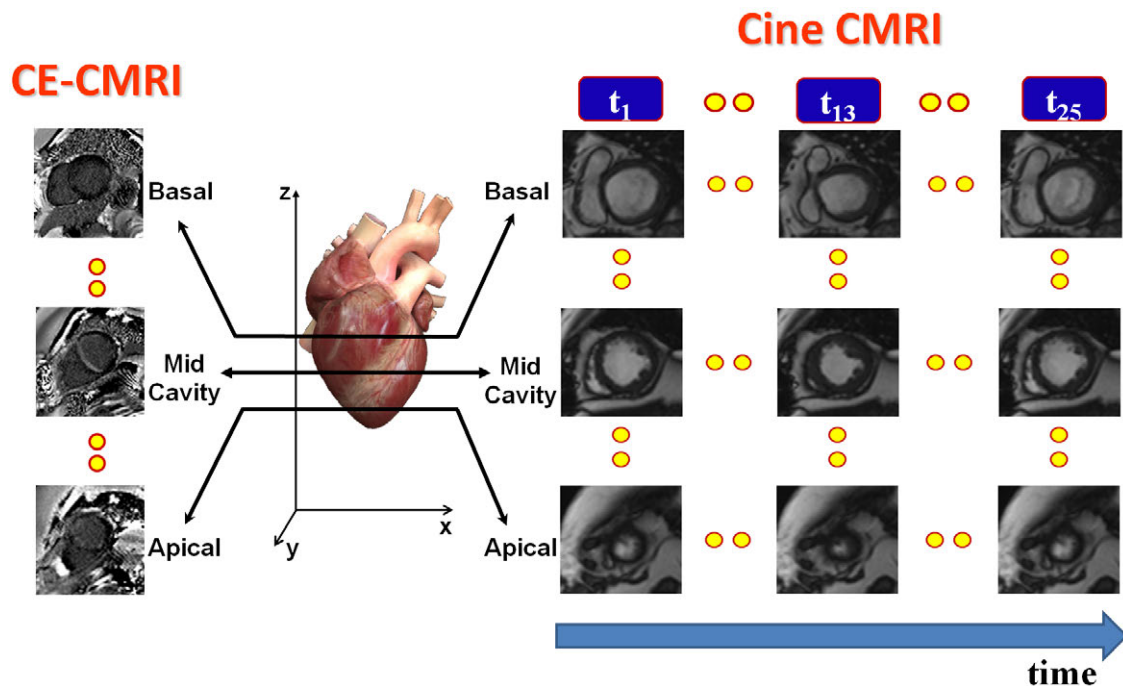
FIGURE 18: CMRI data showing the cross sections of the heart from basal to apical. Left: CE-CMRI, commonly used to enhance the contrast between different tissues, particularly normal and pathological; and right: cine-CMRI, each section consists of a time series of 25 images over the cardiac cycle. Cine CMRI has the ability to show how the anatomy changes and provide the functionality of the heart during the cardiac cycle.

the different metrics used to assess the LV dysfunction and related heart diseases. **This section will discuss the computational methods used for each of these processing steps.**

A. SEGMENTATION OF THE LV WALL

Accurate segmentation of the LV borders from CMRI is of great importance for the reliable assessment of myocardial viability and diagnostics of ischemic heart disease and LV dysfunction [27]. However, the segmentation is a

challenge [28] due to: (*i*) the existence of large variabilities in LV appearances from patient to patient and within the subsequent images of the same patient; (*ii*) the large shape variations of target boundaries; and (*iii*) other problems arising from broken or discontinuous object boundaries, large image noise, and inhomogeneities. **This section will overview the different computational methods that address the segmentation of the LV wall from CE-CMRI and cine CMRI.**
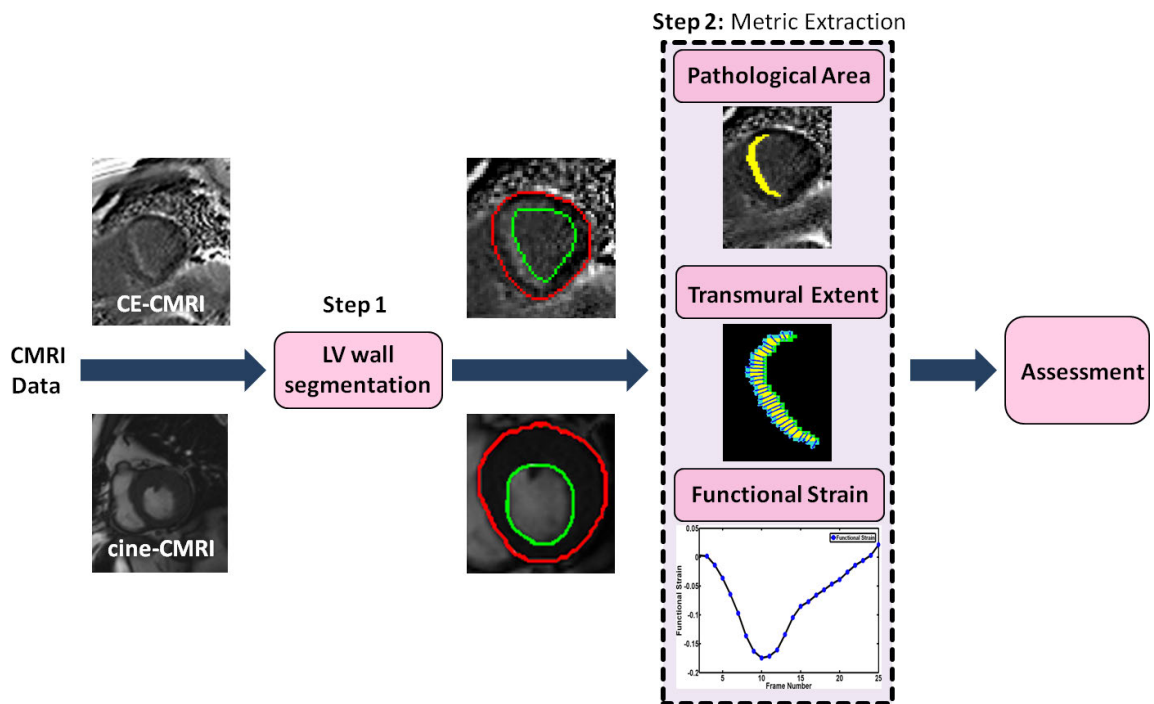
FIGURE 19: A general framework to analyze CMRI. The framework consists of two steps: the segmentation of the LV wall and the estimation of candidate metrics for quantifying the LV wall pathologies.

1. Segmentation of the LV Wall from CE-CMRI

Most research studies manually segmented the LV wall from CE-CMRI (see Figure 20) in order to use the segmentation to delineate the pathological tissues and provide the quantification metrics, e.g., in [29–36]. However, the segmentation is observer dependent and time consuming. Very limited number of research studies
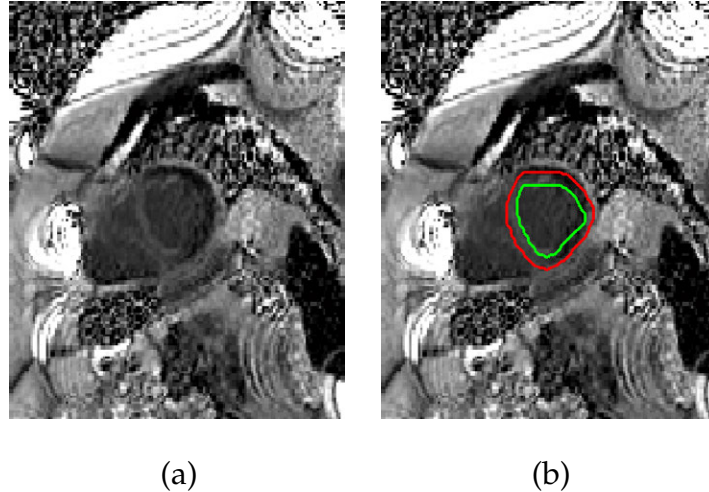
FIGURE 20: Example of the delineation of the LV wall from CE-CMRI of the heart. (a) The original image, and (b) the inner and outer borders of the LV wall are delineated in green (inner) and red (outer).

used semi-automated or automated methods to segment of the LV wall. For example, Hennemuth et al. [37] used a general purpose semi-automated segmentation method proposed by Schenk et al. [38], where the LV wall is segmented interactively using a live-wire-algorithm [38]. Elagouni et al. [39] proposed a framework for pathological tissue segmentation where the LV wall is segmented using a segmentation method proposed by Ciofolo et al. [40]. In this method, the LV wall is segmented based on 2D geometric template deformation and shape prior. A registration step is applied to align the shape prior to the LV wall segmentation contours obtained using the deformable geometric template. However, such a registration step is computationally expensive and time-consuming. Table 1 presents the different methodologies for LV wall segmentation from CE-CMRI. A limited number of research studies have addressed the segmentation problem of the LV wall from CE-CMRI. Most of these methods are (*i*) computationally expensive and/or (*ii*) based on semi-automated or general purpose segmentation frameworks. **Therefore, there is a need to develop more dedicated methods for accurate segmentation of the LV wall from CE-CMRI.**

TABLE 1: Methodologies for segmentation of the LV wall from CE-CMRI. For each study, the number of subjects, the segmentation method, the automation level, and the performance are reported.

Study	Data	Method	Performance
Hennemuth et al. [37]	21 Subjects	• Live-wire segmentation [38] • Semi-automatic	• Not reported
Elagouni et al. [39]	11 Subjects	• 2D geometric template deformation and shape prior [40] • Automatic	• Average distance errors between manual and automatic contours are 2.2±0.6 mm for endocardium and 2.0±0.8 mm for epicardium

2. Segmentation of the LV Wall from Cine CMRI

Traditionally, the segmentation of the LV contours from cine-CMRI is performed manually [41, 42]. However, it is prohibitively time consuming, labor-intensive, and is prone to intra- and inter-observer variability [43]. To avoid the manual procedure shortcomings, several semi-automated and automated techniques have been proposed for the delineation of the LV wall.

Semi-automated Methods: Many semi-automated techniques for the extraction of the LV wall borders have been proposed [44–50]. For example, Ben Ayed et al. [44, 45] proposed a semi-automated approach for the segmentation of the LV using a variational deformable model-based approach to minimize an energy functional containing a similarity overlap constraint, measured by the Bhattacharyya

coefficient. A semi-automated framework to extract the myocardium was proposed by Li et al. [46]. Their framework employed two energy functionals, each represented by a weighted sum of edge-, region-, and shape-based features, for segmenting the endo- and the epi-cardiums. Chen et al. [48] proposed a hybrid semi-automated framework to segment the LV wall borders using variational level sets. The myocardium is separated from the background, in a user defined region-of- interest (ROI), based on the difference in their intensity distributions. The deformable model evolution was derived by minimizing an energy function consisting of regional and edge-based information. Pednekar et al. [49] proposed an intensity-based segmentation approach that uses circular Hough transform to estimate the LV borders in CMR images. Uzümcü et al. [50] proposed a semi-automated method that is based on a multidimensional dynamic programming (DP), which is applied to a parametric shape model instead of applying it directly to image data. Please see Petitjean and Dacher [51] for a more comprehensive review of semi-automated methods for cardiac image segmentation.

Automated Methods: The challenging problem of the LV wall borders segmentation has also been addressed using automated techniques [52–69]. In particular, O'Brien et al. [70] proposed a model-based technique for the LV segmentation on cardiac MR image. An active shape model (ASM) was employed for statistical modeling of the LV shape, and separate models for spatial and temporal variation were used. Cousty et al. [71] proposed a segmentation framework based on discrete mathematical morphology and spatiotemporal watershed transform to segment the endocardium and the epicardium separately. Zhang et al. [52] proposed a segmentation approach based on a combination of an ASM and an active appearance model (AAM) to segment the LV wall using short- and long-axes CMR data. A refinement step followed by using a reversed 3D ASM model to achieve better cardiac motion tracking as well as improved shape details. Andreopoulos et al. [72] achieved LV segmentation using statistical models of shape and appearance. Their method employed a fitting of a 3D AAM on short axis cardiac MR images followed

by hierarchical 2D + time ASM to refine segmentation. Jolly et al. [53] proposed an automated framework based on deformable registration for the LV segmentation. Candidate contours of each slice are obtained in the average image of the co-aligned time frames using the shortest paths, and a minimal surface is built to generate the final contours. Kurkure et al. [54] proposed a hybrid segmentation approach that integrates intensity- and texture-based information for the extraction of the myocardium, LV blood pool, and other adjacent structures, e.g., lungs and liver. A DP-based boundary detection method was used to delineate the LV myocardial contours. Cocosco et al. [56] proposed an automated approach for the segmentation of the LV on cardiac images based on binary classification within a predefined ROI to segment the blood pool. Lynch et al. [57] presented an automated level-set scheme for the segmentation of CMR data using prior knowledge of the temporal deformation of the myocardium. Liang et al. [58] proposed an automated approach using the radial GVF [73] and the Hough transform to segment the LV contours. Zhuang et al. [59] proposed a framework to propagate the labels in a heart atlas to the CMR images for ventricle segmentations based on image registration. Their method employed anatomical information from the atlas as priors to constrain the registration. To improve the quality of segmentations obtained by the AAMs on CMR data, Zambal et al. [60] combined a set of local 2D AAMs with a global shape model. Their method propagates the position and size of the basal slices to apical ones and keeps the global shape characteristics plausible. Lynch et al. [61] presented a coupled level-set segmentation of the LV of the heart using a priori information. Two fronts representing the epi- and endo-cardium boundaries of the LV were evolved using both gradient- and region-based information. The segmentation is supervised with a coupling function and a probabilistic model built from training instances. An approach relying on morphological operations is proposed by Katouzian et al. [62]. For endo-cardium segmentation, the edge detection is performed and the pupillary muscles are excluded via a convex-hull method. The epicardial boundary is delineated through a threshold decomposition

opening approach. Jolly et al. [63, 64] introduced an automated LV segmentation technique to extract the myocardium using Gaussian mixture models and Dijkstra active contours. Lynch et al. [65] introduced an automated framework for the segmentation of the LV of the heart using clustering and cardiac anatomy knowledge. Lelieveldt et al. [66] proposed a multiview AAM for the segmentation of multiple views in long- and short-axis CMR images. Fu et al. [67] developed a wavelet-based image enhancement technique to enhance the LV wall border profiles as the pre-processor for a DP-based automatic border detection algorithm. A variational coupled level set approach that combined boundary and region-based information to segment the LV borders was introduced by Paragios [74]. They presented an anatomical module to constrain the relative positions of the endocardium and epicardium interfaces and to enforce an intensity consistency over the temporal cycle. State-of-the-art automated techniques for cardiac image segmentation are detailed in the recent review by Petitjean and Dacher [51]. Table 2 summarizes the different methodologies for LV wall segmentation from cine-CMRI, presenting the number of evaluation datasets and the achieved performance for each method.

To summarize, the segmentation of cine CMR images has been the subject of extensive research in the last few years. Several semi-automated and automated segmentation methods have been developed. However, the known methods have the following limitations: *(i)* some techniques require intensive manual training; *(ii)* most of them are computationally expensive; *(iii)* parametric shape-based approaches depend on the existence of good texture features in cardiac images and perform poorly on some slices due to noise and lack of well-defined features; and *(iv)* the accuracy of the knowledge-based approaches (e.g., deformable models that are based on shape priors) depends on the size of the training data and the accuracy of the alignment.

TABLE 2: Methodologies for segmentation of the LV wall from cine-CMRI. For each study, the number of subjects, the segmentation method, the automation level, and the performance are reported.

Study	Data	Method	Performance
Ayed et al. [44]	10 datasets	• Deformable model • Semi-automatic	• Average Dice similarity coefficient (DSC) between manual and semi-automatic inner and outer contours are 0.93 ± 0.02 and 0.94 ± 0.01, respectively
Li et al. [46]	25 images	• Energy minimization based on edge, region, and shape-based features • Semi-automatic	• Average DSC between manual and semi-automatic contours are 0.87 ± 5.2
Chen et al. [48]	5 subjects, 294 images	• Level-set • Semi-automatic	• Average DSC between manual and semi-automatic contours are 0.89 ± 3.5

Table 2: Continued.

Pednekar et al. [49]	14 subjects, 294 images	• Threshold-based + Hough transform • Semi-automatic	• Bland-Altman analysis shows good agreement between the semi-automated technique and manual segmentation
Uzmcu et al. [50]	20 subjects	• Dynamic programming + parametric shape model • Semi-automatic	• Average border positioning errors for all slices are 1.77 ± 0.57 mm for epicardial and 1.86 ± 0.59 mm for endocardial contours
O'Brien et al. [70]	33 datasets	• Active shape model (ASM) • Semi-automatic	• Average volumetric point-to-curve errors between the method and manual segmentation are 1.98 ± 0.13 mm for epicardial and 1.87 ± 0.21 mm for endocardial contours, using a set of 10 (out of 33) training datasets

Table 2: Continued.

Cousty et al. [71]	18 subjects	• Mathematical morphology + watershed transform • Semi-automatic	• Mean point to surface errors are 1.51 ± 0.38 mm for the endocardial border and 1.81 ± 0.43 mm for the epicardial border
Zhang et al. [52]	50 subjects	• ASM + AAM • Automatic	• Average border positioning error was 1.89 mm for epicardial and 2.52 mm for endocardial contours; average DSC between manual and automatic contours are 0.90 and 0.91 for epicardial and endocardial contours, respectively
Andreopoulos et al. [72]	33 subjects	• ASM + AAM • Automatic	• Inner/outer error (mean distance between annotated landmarks and segmented contours) are 1.43 ± 0.49 mm/1.51 ± 0.48 mm

Jolly et al. [53]	19 datasets	• Deformable registration of contours • Automatic	• Root mean square distance between ground truth and automatic contours is 2.7 mm, Average DSC is 0.89
Kurkure et al. [54]	357 images	• Dynamic programming based on intensity and texture information • Automatic	• Average DSC between automatic and manual segmentation is 0.86 ± 0.12
Cocosco et al. [56]	32 datasets	• Binary classification • Automatic	• Resulting quantitative cardiac functional parameters using automated method show good agreement with manual quantification of clinical datasets
Lynch et al. [57]	6 datasets	• Level-set • Automatic	• Average DSC is 0.81 ± 0.16 for all data analyzed

Table 2: Continued.

Zhuang et al. [59]	8 datasets	• Atlas-based image registration • Automatic	• DSC for myocardium segmentation is 0.75. The average surface distance, including the endocardial surface and epicardial surface of the ventricles, is 0.7 ± 1.0 mm
Zambal et al. [60]	32 datsets	• 2D AAM and 3D shape model • Automatic	• The average point-to-surface error with respect to expert annotation is 1.96 mm
Lynch et al. [61]	4 datasets	• Coupled level-set • Automatic	• The average point-to-surface errors with respect to expert annotation are 0.477 mm and 1.149 mm for endocardium and epicardium, respectively
Jolly et al. [63]	9 subjects, 482 images	• Gaussian mixture model + Dijkstra active contour • Automatic	• The average error distance is less than 1 pixel

Table 2: Continued.

Lynch et al. [65]	25 datasets	• Clustering based on cardiac anatomy knowledge • Automatic	• Root mean square distance errors are 4.765 and 3.75 for endo- and epi-cardium
Lelieveld et al. [66]	29 subjects	• AAM • Automatic	• Point-to-curve border positioning errors are 41.7 ± 0.8 pixels for the two-chamber view, 1.5 ± 0.7 pixels for the four-chamber view and 1.4 ± 0.7 pixels for the short-axis contours
Fu et al. [67]	10 subjects, 160 images	• Dynamic programming border detection + wavelet-based enhancement approach • Automatic	• Statistical t-test based on Hausdorff distance implies that the segmentation is closer to the manually drawn borders
Paragios [74]	Not reported	• Coupled level-set • Automatic	• Not reported

B. METRICS FOR QUANTIFYING LV WALL PATHOLOGIES

After segmenting the LV wall from CMRI, different quantification metrics that characterize the working of the heart can be extracted. From CE-CMRI the area of pathological tissue in the LV wall and the transmural extent of pathology can be estimated. From cine CMRI, wall thickening, functional strain, and EF metrics can be calculated. Figure 21 summarizes the different quantification metrics that can be extracted from CE-CMRI and cine CMRI. Below, the current computational methods to calculate these metrics are illustrated.
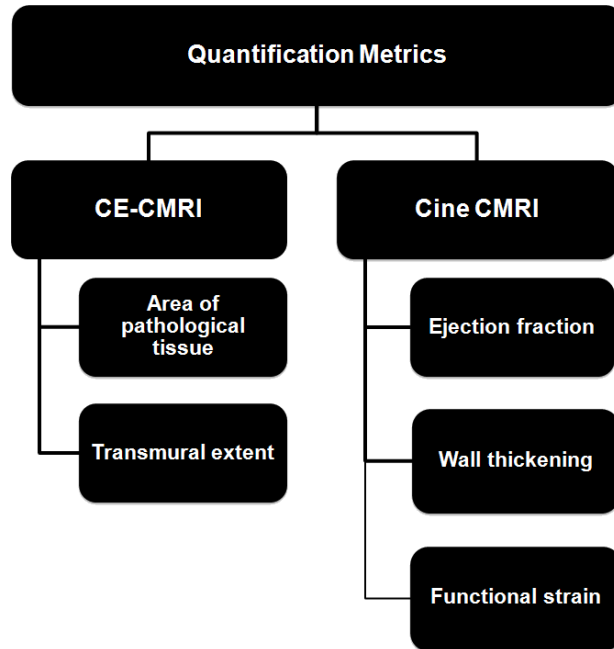
FIGURE 21: Taxonomy of quantification metrics that can be extracted from CE-CMRI and cine CMRI.

1. Area of Pathological Tissue

Assessment of myocardial viability through identifying ischemically damaged tissue is of great clinical importance as the standard means of diagnosing and monitoring irreversible myocardial sequelae of ischemic heart disease, as well as

guiding optimal therapies for individual patients [27]. The infarcted myocardium, after administering a gadolinium contrast agent, appears hyper-enhanced compared to the normal myocardium on late (15-25 min) acquisitions [75–79] (see Figure 22). Extensive research has been conducted on the use of late CE-CMRI, which allows for estimating the transmural extent of damaged myocardium with high spatial resolution [75–79], to delineate the pathological tissue and extract useful metrics for indexing myocardial injury.

(a)   (b)
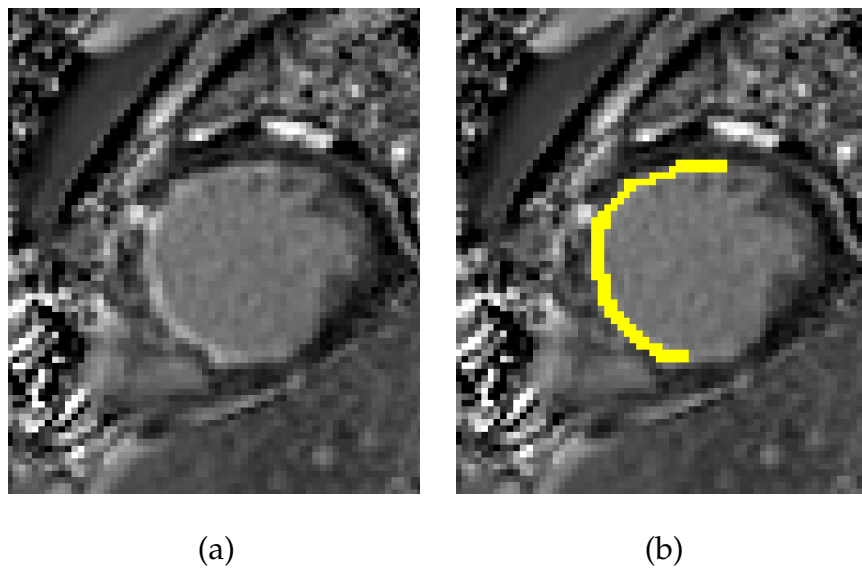
FIGURE 22: (a) Original CE-MRI of the heart and (b) the pathological area is delineated in yellow.

Measuring the area of pathological tissue in the LV (see Figure 22) is important to assist the cardiologists in the diagnosis of the LV dysfunction and ischemic heart disease. For reliable size measurement, the pathological tissue has to be accurately delineated within the LV wall from the adjacent undamaged tissue. Accurate identification is a challenge due to image noise, limited resolution, and imprecise boundaries. While the pathological tissue can be outlined manually to determine its area, such a measurement is time-consuming and operator-dependent. Automated or semi-automated myocardial viability assessment overcomes these drawbacks, but most of these techniques use simple, heuristic intensity thresholds to

detect the pathological tissue. Previous definitions of abnormality empirically set a threshold at more than two [29] or three [30] standard deviations above the average intensity in a remote (presumedly healthy) myocardial region. A user-specified threshold was employed by Setser et al. [31] to distinguish between viable and nonviable myocardium. Amado et al. [32] used the full-width at half-maximum (FWHM) criterion [80] to identify the pathological tissue: a seed point in the hyperenhanced region is provided manually, and the pathological tissue includes, by definition, all the pixels with the intensities exceeding 50% of the seed intensity, which propagate from the seed point.

A recent study by Neizel et al. [33] with a group of 62 patients demonstrated that infarct segmentation using a visual, user-specified threshold is better correlated with manually traced infarcts than the FWHM approach. Beek et al. [34] compared the FWHM approach with the simple thresholding method, using various thresholds, in predicting segmental recovery after therapy. Unlike the study by Neizel et. al. [33], this comparison documented no significant difference between the accuracy of the two approaches in a group of 38 patients with chronic ischemic myocardial dysfunction. Tao et al. [35] extended the gray-level-histogram-based threshold selection used by Otsu et. al. [81], to initially determine the infarct area, with an augmented assessment to reduce the false positive (FP) and false negative (FN) errors based on connectivity filtering and region growing. Heiberg et al. [36] augmented the intensity thresholding with a level-set-based regulation to exclude small noisy regions. Hennemuth et al. [37] used the image intensity profile to initiate a watershed-based segmentation. Connected component analysis, to fill holes and exclude small noisy regions was further used to refine this segmentation. Recently, Elagouni et al. [39] analyzed the LV wall intensities to generate a fuzzy segmentation map, characterizing the membership degree for each pixel. After thresholding and morphological cleaning of the fuzzy map, the area of pathology was delineated by region analysis. **The main concern with these meth-**

ods is that they do not adequately account for spatial interactions between the myocardium pixels and are quite sensitive to imperfect myocardium contours and image noise.

TABLE 3: Methodologies for pathology identification using CE-CMRI. For each study, the number of patients, the LV wall segmentation method, the pathology identification method, and the performance are reported.

Study	# Data	Method		Performance
		LV Wall	Pathology Identification	
Kim et al. [29]	26	Manual outline	Threshold based: two standard deviation above the average	• Visually acceptable
Fieno et al. [30]	24	Manual outline	Threshold based: three standard deviation above the average	• Visually acceptable
Setser et al. [31]	18	Manual outline	A user-specified threshold	• Results shows good agreement with observer delineation
Amado et al. [32]	13	Manual outline	segmented based on FWHM region	• Bland-Altman analysis shows good agreement between the FWHM approach and postmortem data

Heiberg et al. [36]	40	Manual outline	Intensity thresholding with a level-set-based regulation	• The difference in infarct size between semi-automatic quantification and the mean of three observers was 6.19±6.6 ml (mean±SD)
Hennemuth et al. [37]	21	Segmented based on a semi-automatic live-wire	Watershed-based segmentation and Connected component analysis	• Bland-Altman analysis shows better agreement between the manual and the automatic segmentations than between the manual and the Fieno et al. [30] method
Neizel et al. [33]	62	Manual outline	Compared visual user-specified threshold with FWHM Region growing	• User-specified threshold-based method is better correlated with manually traced infarcts than the FWHM approach
Beek et al. [34]	38	Manual outline	Compared the FWHM approach with the simple thresholding method	• Results reported no significant difference between the accuracy of the two approaches

Tao et al. [35]	20	Manual outline	Gray-level-histogram-based threshold selection + connectivity filtering and region growing	• DSC values are 0.83 ± 0.07 and 0.79 ± 0.08 between the automatic identification and the manual tracing from observer 1 and observer 2
Elagouni et al. [39]	11	Segmented based on a deformable template	Fuzzy segmentation map	• Extracted metrics using automated segmentation showed agreement with those extracted using semi-automatic expert delineations

2. Transmural Extent

After the identification of the pathological tissue in the LV wall, it is important to extract useful metrics to quantify these pathologies. The transmural extent (or transmurality) is one of the candidate shape-based metrics that has been explored to quantify the myocardial viability. Transmurality is defined as the fraction of pathological tissue's extension across the myocardial wall (see Figure 23). A previously investigated procedure for estimating the transmural extent (e.g., used in [20, 21]) extends a fixed number of radial lines from the inner to the outer contour of the LV (see Figure 14(a)). After segments of the pathological tissue along

each line are determined, the transmural extent is estimated as the average pathological tissue's extent relative to these lines. As illustrated in Figure 14 (b), this, so-called radial method, is in principle inaccurate in establishing point-to-point correspondences and geometrically inconsistent in estimating the transmural extent. The alternate centerline method estimates the transmural extent by generating a fixed number of lines that are perpendicular to the computed centerline between the inner and outer contours of the LV wall. Similarly, after identifying the pathological tissue along each line, the transmural extent is defined as the average pathological tissue's extent relative to these lines. The centerline method was historically used for wall motion regional assessment [82], and subsequently for wall thickening analysis [83], and for transmural extent estimation [84]. Unlike the radial method, the centerline method does not depend on the choice of the centroid or the coordinate system of lines [85], but is affected by inner and outer contour imperfections and image noise. **As previously mentioned, a more accurate shape-based analysis for estimating the transmural extent should be investigated.**
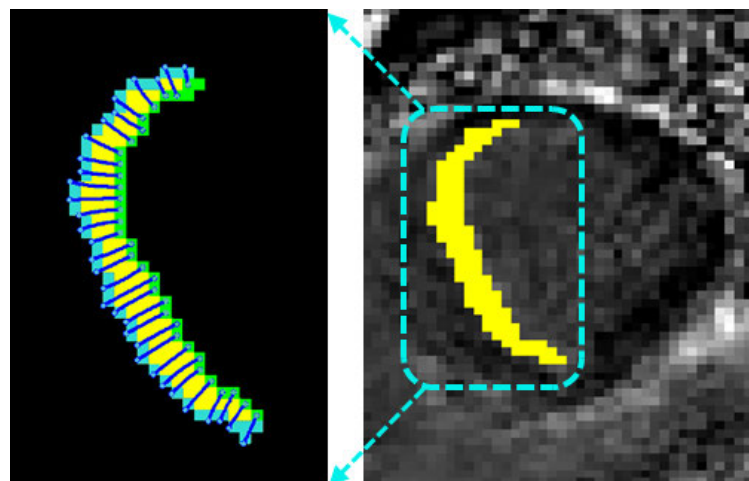
FIGURE 23: Illustration of the transmural extent of the pathological tissue in the LV wall. Right: CE-CMRI of the heart with the pathological area delineated in yellow, and left: an enlarged section of the pathology showing the extent of the pathology as the blue lines connecting the edges of the pathology.

3. Functional Strain

Functional strain is one of the important quantification metrics of the cardiac status. Local cardiac diseases (such as coronary atherosclerosis) and global conditions (such as heart failure and diabetes) result in wall dysfunction that manifests on strain slopes during the contraction and expansion phases of the cardiac cycle [22] (see Figure 24). Therefore, accurate strain estimation is important for the early detection of these diseases.
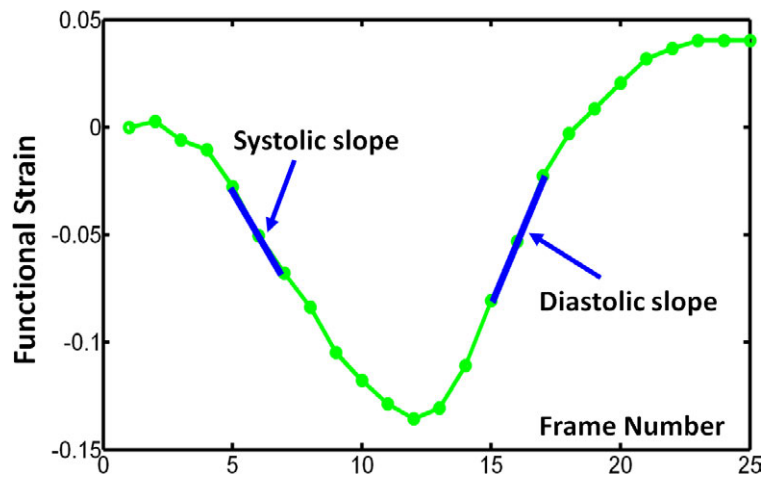
FIGURE 24: Functional strain curve showing the systolic and diastolic strain slopes during the contraction and expansion phases of the cardiac cycle.

In the literature, functional strain is estimated based on nonrigid registration using ultrasound images [86, 87] or motion analysis using tagged MRI [88–92] (see Figure 25). Current studies calculate the heart displacement and strain parameters from ultrasound images by estimating the motion of the heart using spatio-temporal elastic registration. For example, Ledesma-Carbayo et al. [86] used a spatio-temporal elastic registration algorithm for motion reconstruction from two-dimensional ultrasound sequences of the heart. A B-spline transformation model is used to model the motion and deformation of the myocardium through the cardiac cycle. The spatio-temporal deformation field that represents the heart motion

is found by minimizing an image similarity criterion and is further used to obtain the displacement and the strain parameters. Elen et al. [86] extended the work in [86] to 3D and applied an automated intensity-based nonrigid spatio-temporal registration for 3D ultrasound images to estimate the heart motion. The 3D deformation field between different image frames is found by maximizing the mutual information of corresponding voxel intensities. The main concern with using ultrasound images for estimating the functional strain is that they are low contrast. Moreover, the registration is always computationally expensive and involve pixel/voxel errors. Therefore, other modalities should be investigated to afford more accurate estimation of the functional strain parameters.

Strain estimation methods using tagged MRI are more common. These methods can be categorized as spatial- or spectral-domain techniques. The former estimates the whole tissue motion and strain by identifying spatial locations of the tag lines in an image and using either model-based or model-free interpolation and differentiation [88, 89]. Because spatial methods track actual pixels throughout the image, they require substantial image preprocessing and segmentation, and therefore are often computationally expensive. On the other hand, the spectral analysis harmonic phase (HARP) method computes phase images from sinusoidal tagged MR images by bandpass filtering in the Fourier domain [90–92]. Unfortunately, the spectral tracking failed in cases of a high rate motion between successive frames, through plane motion, or boundary points [93]. Moreover, to completely quantify the status of the heart, other performance indexes are needed (e.g., global index and wall thickness from cine CMRI). However, the derived indexes from cine and tagged CMRI suffer from inter-slice variability since they are extracted from different cross-sections and different image modalities.

To avoid the inter-slice variability, recent trends estimate the strain from cine CMRI (e.g., [94–97]). Most of these methods depend on texture features to track
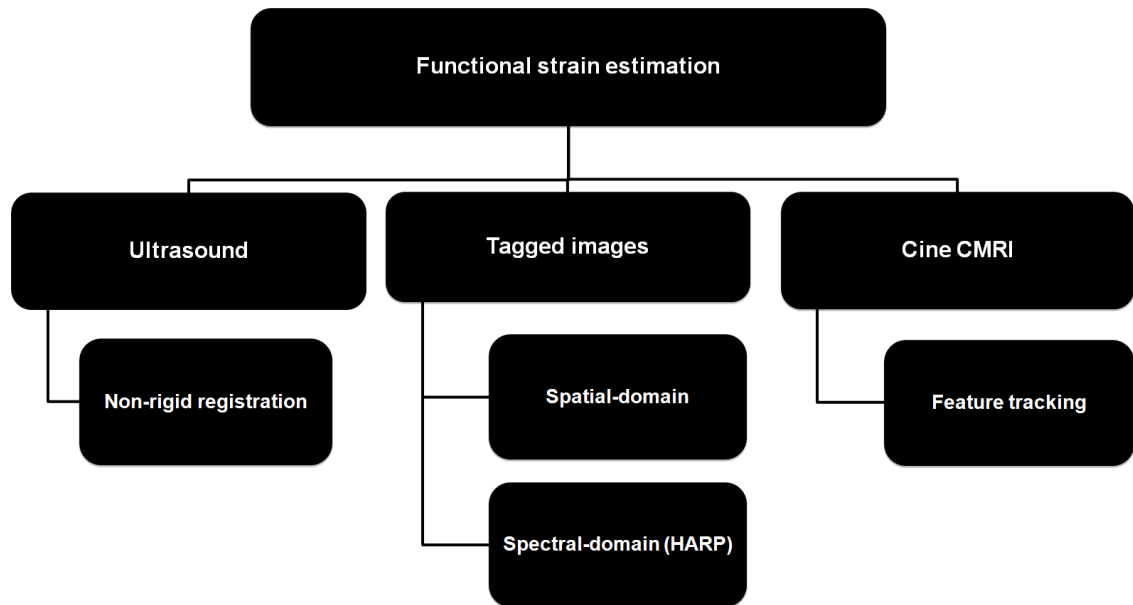
FIGURE 25: Taxonomy of function strain estimation methods from ultrasound images, tagged MRI, and cine CMRI.

predefined points on the inner and outer LV wall. For example, Maret et al. [94] used a feature tracking method to estimate the strain and other indexes from cine CMRI and showed that it can be used for the detection of the transmural scar. Hor et al. [95] correlated between the estimated strains from tagged MRI (using HARP method) and from cine CMRI (using tracking) in a population with a wide range of cardiac dysfunction. Their study showed that the circumferential strain estimation can be performed from the cine CMRI without the need for additional tagged images. Since the current tracking methods are based on image features, such as the pixels' intensity and their spatial features, they suffer from the following limitations: (*i*) they are not sufficient to accurately track the LV points due to the lack of texture information inside the wall, (*ii*) they are not able to track all the LV wall points, and (*iii*) the intensity and spatial information inside the wall (e.g., at the mid-wall) remains unchanged, which leads to inaccurate strain estimation at the mid-wall. **Therefore, there is a need for developing more efficient techniques for accurate strain estimation.**

C.   LIMITATIONS OF CURRENT APPROACHES

The current approaches for the quantification of the LV dysfunction suffer from the following limitations:

- The segmentation of the LV wall in most of the known frameworks is not sufficiently accurate and reliable because:

  - Image intensities for the goal objects and their backgrounds vary greatly across subjects and time.

  - Parametric shape models become unsuitable for discontinuous objects due to a small number of distinct cardiac landmarks.

  - Deformable models without adequate appearance and shape priors fail under excessive image noise, poor resolution, diffuse boundaries, or occluded shapes.

- Current approaches for sizing the area of the pathological tissue in the LV wall do not adequately account for spatial interactions between the myocardium pixels and are quite sensitive to imperfect myocardium contours and image noise.

- Current radial shape-based approach for transmural extent estimation suffers from geometric inconsistency in estimating the point-to-point correspondences between the inner and outer boundaries, while the centerline method suffers from imperfect inner and outer contours, especially for noisy images.

- Current tracking methods are based on image features, such as the pixels' intensity and their spatial features; they suffer from the following limitations:

  - They are not sufficient to accurately track the LV points due to the lack of texture information inside the wall.

– They are not able to track all the LV wall points.

– The intensity and spatial information inside the wall (e.g., at the mid-wall) remains unchanged, which leads to inaccurate strain estimation at the mid-wall.

To overcome the aforementioned limitations, an augmented, automatic framework to analyze the CE-CMR images is proposed. The framework is based on the segmentation of the inner cavity and outer border of myocardial (LV) wall using graph-cut optimization of a cost function that accounts for the object visual appearance and shape. **The details of the proposed segmentation method are presented in Chapter III**. To delineate the pathological tissue in the LV wall, the image is modeled as a joint Markov-Gibbs random field (MGRF) that accounts for not only the 1st-order visual appearance (based on the pixel-wise intensities), but also incorporates the 2nd-order spatial interactions between the pixels. Then, the transmural extent is estimated using a geometrically motivated approach, based on a partial differential equation (PDE) that accurately co-locates the corresponding pixel pairs. **The details of the proposed methods for sizing the area of the pathological tissue and for estimating the transmural extent are presented in Chapter IV**. To estimate the strain from cine CMRI, a novel method is proposed based on tracking the LV wall geometry. Unlike current methods that depend on the intensity and spatial information to track the wall motion, this method sticks to the geometry of the heart to track its motion. To achieve this goal, the application of the proposed PDE method is extended to track the LV wall points by solving the Laplace equation between the LV contours of each two successive image frames over the cardiac cycle. **The details of the proposed method for estimating the strain from cine CMRI are presented in Chapter V**.

CHAPTER III

SEGMENTATION OF LV WALL FROM CE-CMRI

To identify the pathological tissue in the left ventricle (LV) wall, an accurate segmentation of the LV wall borders is a mandatory step. In this chapter, a novel automatic framework for the segmentation of the LV wall from contrast-enhanced cardiac magnetic resonance imaging (CE-CMRI) is proposed. The framework consists of two main steps. First, the inner cavity of the LV is segmented from the surrounding tissues based on finding the maximum a posteriori (MAP) estimation of a new energy function using a graph-cuts-based optimization algorithm. The proposed energy function consists of three descriptors: 1st-order visual appearance descriptors of the CE-CMR image, a 2D spatially rotation-variant 2nd-order homogeneity descriptor, and a LV inner cavity shape descriptor. Second, the outer contour of the LV is segmented by generating an orthogonal wave, starting from the LV inner contour, by solving an Eikonal partial differential equation with a new speed function that combines the prior shape and current visual appearance models of the LV wall. The proposed framework was tested on *in-vivo* CE-CMR images and validated with manual expert delineations of the LV borders. Experiments and comparison results on real CE-CMR images confirm the robustness and accuracy of the proposed framework over the existing ones.

A. BASIC ANALYSIS STAGES

Accurate segmentation of the LV borders from CE-CMR images is of great importance for the reliable assessment of myocardial viability and diagnostics of ischemic heart disease and LV dysfunction [27]. However, the segmentation in most of the known frameworks is not sufficiently accurate and reliable because image intensities for the goal objects and their backgrounds vary greatly across subjects and time. Parametric shape models become unsuitable for discontinuous objects due to a small number of distinct cardiac landmarks, and deformable models without adequate appearance and shape priors fail under excessive image noise, poor resolution, diffuse boundaries, or occluded shapes. To overcome these limitations, an automatic framework to analyze CE-CMR images is proposed. The proposed framework (*i*) segments the inner cavity of the LV from the surrounding tissues based on a learned soft inner cavity shape model and an identifiable joint MGRF model of CE-CMR image and "object–background" region maps, and (*ii*) segments the outer contour of the LV by evolving an orthogonal wave from the inner contour by solving an Eikonal partial differential equation with a new speed function that combines the prior shape and current visual appearance models of the LV wall.

1. LV Inner Cavity Segmentation

The segmentation of the inner cavity of the LV is a challenge due to the dynamic heart motion and the image artifacts from blood circulation within the ventricular cavity. This stage proposes a powerful approach for inner cavity segmentation based on a learned soft inner cavity shape model and an identifiable joint MGRF model of CE-CMR image and "object–background" region maps.

a.   Joint MGRF model of the inner cavity and background: The joint-MGRF model fundamentally relates the joint probability of an image and its object - background region map to geometric structure and to the energy of repeated patterns within the image [98, 99]. The basic theory behind such models is that they assume that the signals associated with each pixel depend on the signals of the neighboring pixels, and thus explicitly take into account their spatial interactions, and other features, such as shape.

Let $\mathbf{Q} = \{0, \ldots, Q - 1\}$, $\mathbf{L} = \{\text{ob}, \text{bg}\}$, and $\mathbf{U} = [0, 1]$ be a set of Q integer gray levels, a set of object ("ob") and background ("bg") labels, and a unit interval, respectively. Let a 2D arithmetic grid $\mathbf{R} = \{(x, y) : x = 0, 1, \ldots, X - 1; y = 0, 1, \ldots, Y - 1\}$ support grayscale CE-CMR image $\mathbf{g} : \mathbf{R} \rightarrow \mathbf{Q}$, their binary region maps $\mathbf{m} : \mathbf{R} \rightarrow \mathbf{L}$, and probabilistic shape model $\mathbf{s} : \mathbf{R} \rightarrow \mathbf{U}$. The shape model allows for registered (aligned) CE-CMR images. The co-registered CE-CMR images and their region maps $\mathbf{m}$ are modeled with a joint MGRF model as follows [100, 101]:

$$P(\mathbf{g}, \mathbf{m}) = P(\mathbf{g}|\mathbf{m})P(\mathbf{m}) \tag{2}$$

combining a 2nd-order MGRF $P(\mathbf{m})$ of region labels for a spatially homogeneous evolving region map $\mathbf{m}$ and a 1st-order conditionally independent random field $P(\mathbf{g}|\mathbf{m})$ of image intensities given the map. The map model $P(\mathbf{m}) = P_{\text{s}}(\mathbf{m})P_{\text{h}}(\mathbf{m})$ has two independent parts: a subject-specific dynamical shape prior, which is a spatially variant independent random field of region labels $P_{\text{s}}(\mathbf{m})$, and a 2nd -order MGRF model $P_{\text{h}}(\mathbf{m})$ of a spatially homogeneous evolving map $\mathbf{m}$ for the image.

As shown in Figure 26, the proposed method focuses on accurate identification of spatial interactions in $P_{\text{h}}(\mathbf{m})$, pixel-wise distributions of intensities in $P(\mathbf{g}|\mathbf{m})$, and prior distribution of the shape of the inner cavity in $P_{\text{s}}(\mathbf{m})$ for co-aligned CE-MR images. The probabilistic shape model $\mathbf{s}$ is learned from a set of co-aligned training images. To perform the initial inner cardiac cavity segmen-
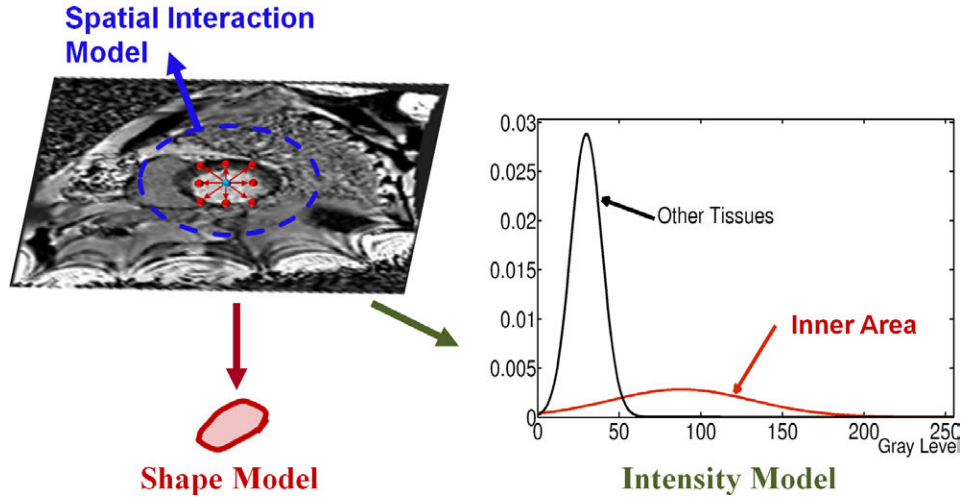
FIGURE 26: Aligning a joint MGRF model to a shape prior.

tation, every given CE-CMR image is aligned to a selected reference image. The shape model provides the pixel-wise object and background probabilities being used, together with the conditional image intensity model $P(\mathbf{g}|\mathbf{m})$, to build an initial region map. The final segmentation is performed by optimizing the identified joint MGRF model of the CE-CMR image and its region map using global graph-cuts.

b. Spatial interaction in the inner cavity of the LV: A generic MGRF of region maps accounts only for pairwise interaction between each region label and its neighbors [100, 101].Generally, the interaction structure and Gibbs potentials are arbitrary and can be identified from the training data. For simplicity, the interaction structure is restricted to the nearest pixels only (i.e., to the 8-neighborhood) and assume, by symmetry considerations, that the potentials depend only on the intra- or inter-region position of each pixel pair (i.e., whether the labels are equal or not) but are independent of its relative orientation. Under these restrictions, it is similar to the conventional auto-binomial (Potts) model and differs only in that the potentials are estimated analytically.

The 8-neighborhood (Figure 27) has two types of symmetric pairwise inter-

actions specified by the absolute distance a between two pixels in the CE-CMR slice ($a = 1$, and $\sqrt{2}$, respectively): (*i*) the closest pairs with the inter-pixel coordinate offsets $\mathbf{N}_1 = \{(\pm 1, 0), (0, \pm 1)\}$; and (*ii*) the farther diagonal pairs with the offsets $\mathbf{N}_{\sqrt{2}} = \{(1, \pm 1), (-1, \pm 1)\}$. The potentials of each type are bi-valued because only the coincidence of the labels is taken into account: $\mathbf{V}_a = \{V_{a,\mathrm{eq}}; V_{a,\mathrm{ne}}\}$ where $V_{a,\mathrm{eq}} = V_a(l, l')$ if $l = l'$ and $V_{a,\mathrm{ne}} = V_a(l, l')$ if $l \neq l'$; $a \in \mathbf{A} = \{1, \sqrt{2}\}$. Then the MGRF model of region maps is as follows:

$$P_{\mathrm{h}}(\mathbf{m}) \propto \exp \sum_{(x,y) \in \mathbf{R}} \sum_{a \in \mathbf{A}} \sum_{(\xi, \eta) \in \mathbf{N}_a} V_a(m_{x,y}, m_{x+\xi, y+\eta}) \qquad (3)$$

To identify the MGRF described in Equation (2), approximate analytical maximum likelihood estimates are formed in line with [100, 101] as follows:

$$V_{a,\mathrm{eq}} = -V_{a,\mathrm{ne}} = 2\left(f_{a,\mathrm{eq}}(\mathbf{m}) - \frac{1}{2}\right) \qquad (4)$$

where $f_{a,\mathrm{eq}}(\mathbf{m})$ denotes the relative frequency of the equal label pairs in the equivalent pixel pairs $\{((x, y), (x + \xi, y + \eta)): (x, y) \in \mathbf{R}; (x + \xi, y + \eta) \in \mathbf{R}; (\xi, \eta) \in \mathbf{N}_a\}$.
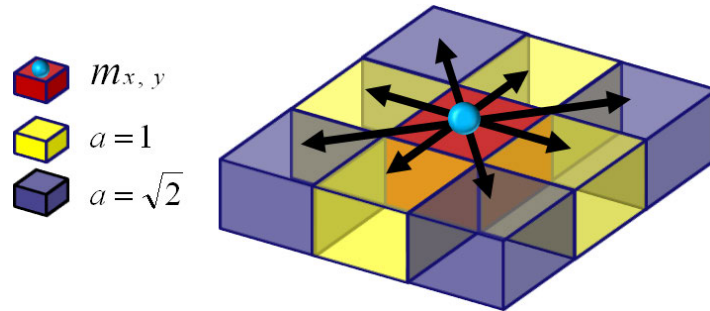
FIGURE 27: A2^{nd}-order MGRF neighborhood system.

c.   Conditional intensity model for CE-CMR slice: A simple random field of conditionally independent intensities is used to model the CE-CMR slice, given a region map:

$$P(\mathbf{g}|\mathbf{m}) = \prod_{(x,y) \in \mathbf{R}} p_{m_{x,y}}(g_{x,y})$$

where the pixel-wise probability distributions for the inner cardiac contour and its background, $p_\lambda = [p_\lambda(q) : q \in \mathbf{Q}]$; $\lambda \in \mathbf{L}$, are estimated during the segmentation process. To separate p_{ob} and p_{bg}, the mixed empirical distribution of all the pixel intensities is approximated with a linear combination of discrete Gaussians (LCDG)[1] [101–103].

The LCDG assignment separates the object from the background[2] more accurately than a more conventional mixture of only the positive Gaussians (e.g., [106]) and can account for non-linear intensity variations, such as those caused by patient weight and data acquisition factors. The LCDG has two dominant positive DGs that represent modes associated with the object (i.e., inner cavity) and background, respectively, in the empirical intensity distribution for the CE-CMR image to be segmented. To approximate more closely this distribution, the LCDG also contains a number of positive and negative subordinate DGs:

$$p_{\mathrm{LCDG}}(q) = \sum_{j=1}^{C_{\mathrm{p}}} w_{\mathrm{p},j} \psi(q|\rho_{\mathrm{p},j}) - \sum_{j=1}^{C_{\mathrm{n}}} w_{\mathrm{n},j} \psi(q|\rho_{\mathrm{n},j}) \tag{5}$$

where the index $\alpha \in \{\mathrm{p}, \mathrm{n}\}$ specifies whether the DG is positive or negative, C_α is the number of such components, and $\rho_{\alpha,j}$ and $w_{\alpha,j}$ denote the weight and parameters of each individual DG $\Psi_{\rho_{\alpha,j}}$; $j = 1, \ldots, c_\alpha$, respectively. The LCDG of Equation (5), including the numbers C_{p} and C_{n} of its components, is identified using the expectation-maximization (EM)-based algorithm introduced in [100–103, 107–112].

d. Probabilistic model of the inner cavity shape: Most of the recent works on image segmentation use level-set based representations of shapes: an individ-

---

[1]A Discrete Gaussian (DG) $\Psi_\rho = (\psi(q|\rho) : q \in \mathbf{Q})$ with $\rho = (\mu, \sigma^2)$ is defined as $\psi(q|\rho) = \Phi_\rho(q + 0.5) - \Phi_\rho(q - 0.5)$ for $q = 1, \ldots, Q - 2$, $\psi(0|\rho) = \Phi_\rho(0.5)$, , and $\psi(Q - 1|\rho) = 1 - \Phi_\rho(Q - 1.5)$ where $\Phi_\rho(q)$ is the cumulative Gaussian function with the mean μ and the variance σ^2.

[2]LCDG model is also applicable for images with more than two classes. The number of mixture components can be automatically estimated from the image using the modified Akiake information criterion [104, 105].

ual shape is outlined by a set of boundary pixels at the zero-level of a certain distance function, and a given shape is approximated with the closest linear combination of the training shapes. The main drawback of this representation is that the space of signed distances is not closed with respect to linear operations. As a result, linear combinations of the distance functions may relate to invalid or even physically impossible boundaries.

To circumvent this limitation, a soft probabilistic inner cavity shape model is used

$$P_{\mathbf{s}}(\mathbf{m}) = \prod_{(x,y) \in \mathbf{R}} S_{m_{x,y}}$$

where $S_{m_{x,y}}$ is the empirical probability that the pixel (x, y) belongs to the inner cavity given the map. The proposed framework exploits three shape priors (built at the learning stage) for the basal, mid-ventricular and apical levels. Each soft template is constructed following Algorithm 1.

Algorithm 1 Shape Prior Construction

- Co-align a set of training CE-CMR images (shown in the top row of Figure 28) using rigid registration with mutual-information as a similarity measure [113] as shown in the middle row of Figure 28.

- Manually segment the object (the inner cavity) from the aligned sets as shown in the bottom row of Figure 28.

- Estimate the pixel-wise probabilities by counting how many times each pixel (x, y) was segmented as the object as shown in Figure 29.

---

e. Optimization of the joint MGRF model using the graph-cut algorithm: After accurately identifying the joint MGRF model of the CE-CMR image, the inner cavity segmentation problem is formed as a search for the MAP region map $\mathbf{m}$ in all the possible configurations of this joint MGRF model. The MAP region map is
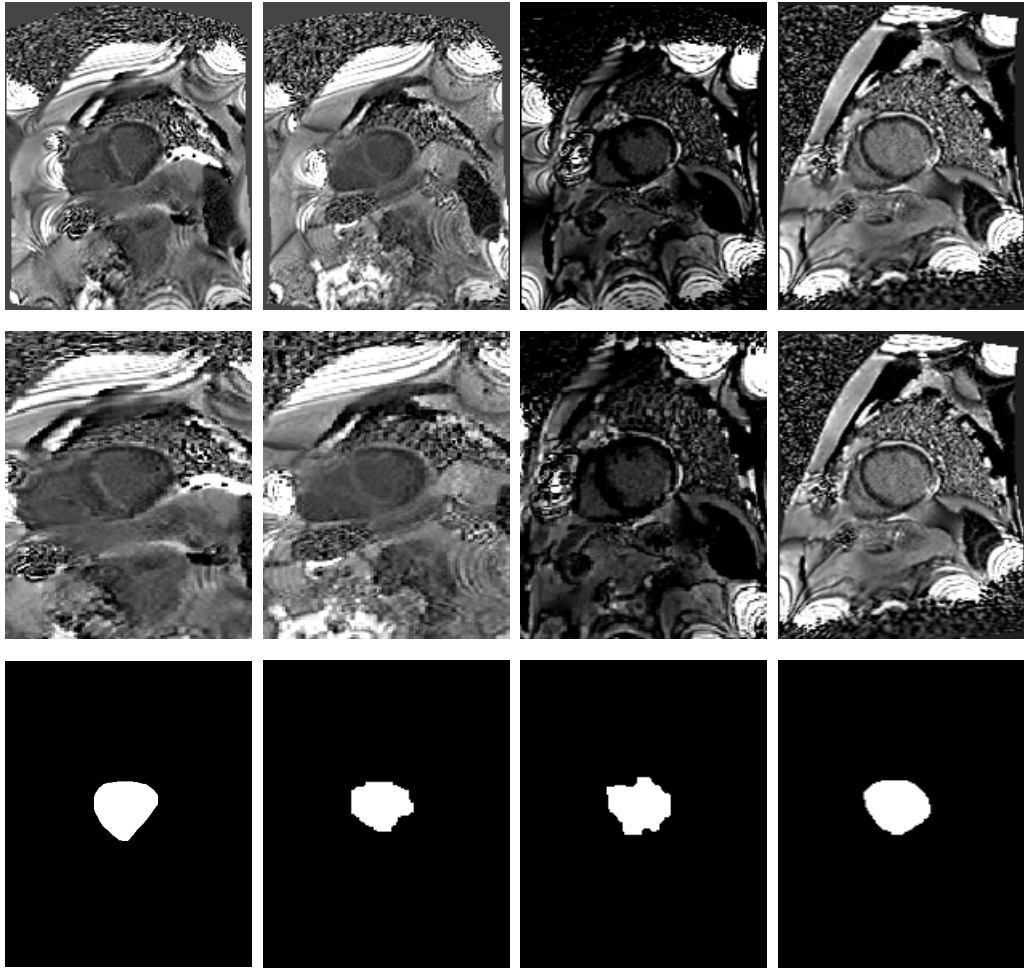
FIGURE 28: Inner cavity shape prior reconstruction: top row- database samples; middle row- affine mutual-information-based registration ; and bottom row- manual segmentation.

(a)	(b)	(c)	(d)
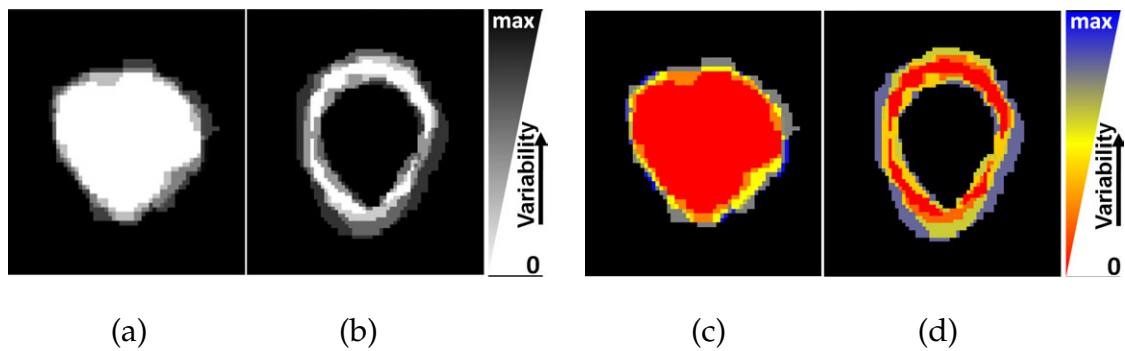
FIGURE 29: (a) & (b) Gray-coded inner and LV wall shape priors. (c) & (d) Another way for visualization using color-map.

found by maximizing the interaction energy of the joint MGRF model. A new energy function E is formulated to accurately model the CE-CMR image. This new function is formed as the logarithmic function of the probability distribution of the joint MGRF model given in Equation (2):

$$E(\mathbf{m}) = \log(P(\mathbf{g}|\mathbf{m})) + \log(P_h(\mathbf{m})) + \log(P_s(\mathbf{m})) \tag{6}$$

The search problem is an exhausting task and should be done in an efficient and precise way. A graph-cut based algorithm (i.e., the two-terminal Min-Cut/Max-Flow algorithm [114]) is applied for such a task due to its powerful capability to end up with the optimal global region map [115], which is obtained by maximizing E (i.e., minimizing $-E$ using graph-cut). The two-terminal graph-cut with positive edge weights is constructed as follows (see Figure 30 for more illustration):
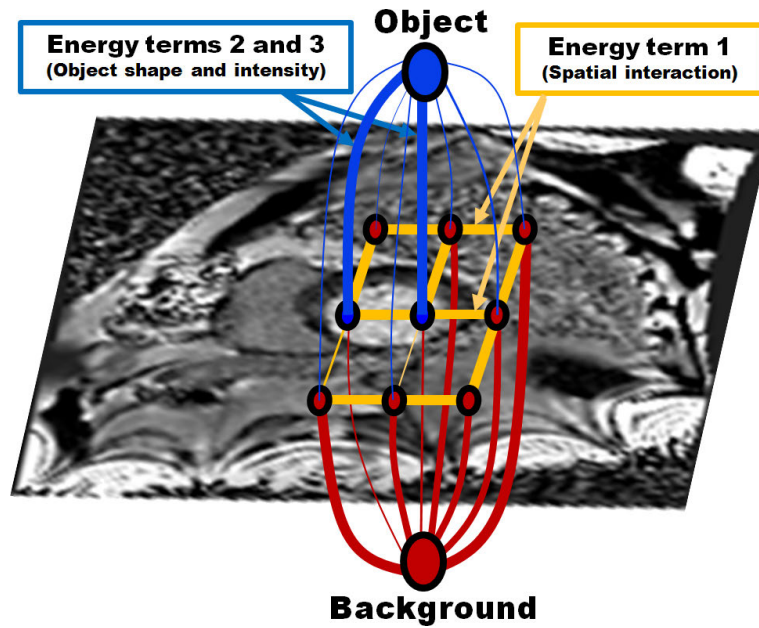
FIGURE 30: Constructed two terminal graph-cuts: terminal-links (in blue and red) account for both the 1st-order visual appearance descriptors of the CE-CMR image and the inner cavity shape, and neighbor-links (in orange) penalize for the spatially invariant 2nd-order homogeneity descriptor of the CE-CMR image (the thicker links denote greater affinity between corresponding nodes or terminals).

Algorithm 2 Graph-Cut Construction

- Define the terminal-links by accounting for both the 1st-order visual appearance descriptors of the CE-CMR image and the inner cavity shape descriptor (i.e., $-\log(P(\mathbf{g}|\mathbf{m})) - \log(P_{\mathrm{s}}(\mathbf{m}))$).

- Define the neighbor-links by penalizing for the spatially invariant 2nd-order homogeneity descriptor of the CE-CMR image (i.e., $-\log(P_{\mathrm{h}}(\mathbf{m}))$).

---

2. LV Outer Contour Segmentation

The goal of the LV outer contour segmentation method is to suppress the effect of gray level inhomogeneity and lack of the edges of the LV wall in order to enhance the segmentation accuracy. To achieve this goal, the outer border of the LV wall is extracted by a robust wave-propagation based search (see Figure 31). An orthogonal wave is emitted from the inner border ($t = 0$) towards the external border of the LV wall (i.e., a fast marching level-set [116–118]). Every point on the emitted wave is classified to be wall or background based on three descriptors: shape prior of the LV wall (see Figure 32), 1st-order visual appearance descriptors of the LV wall, and a 2nd-order spatial interaction homogeneity descriptor. Note that the proposed segmentation approach follows the same methodologies as in Section III.A.1 to estimate three descriptors of the LV wall. The whole search algorithm for the outer border of the LV wall is described in Algorithm 3.

3. Performance Evaluation of the Proposed Segmentation Algorithms

Dice similarity coefficient (DSC): The segmentation performance is evaluated by using the DSC metric [120] that estimates the overlap between the experimentally segmented region and ground truth (GT) segmentation. Let $|\mathbf{C}|$, $|\mathbf{G}|$, and $|\mathbf{g}|$ denote areas (by the number of pixels) of the segmented object $\mathbf{C}$ (i.e., in-
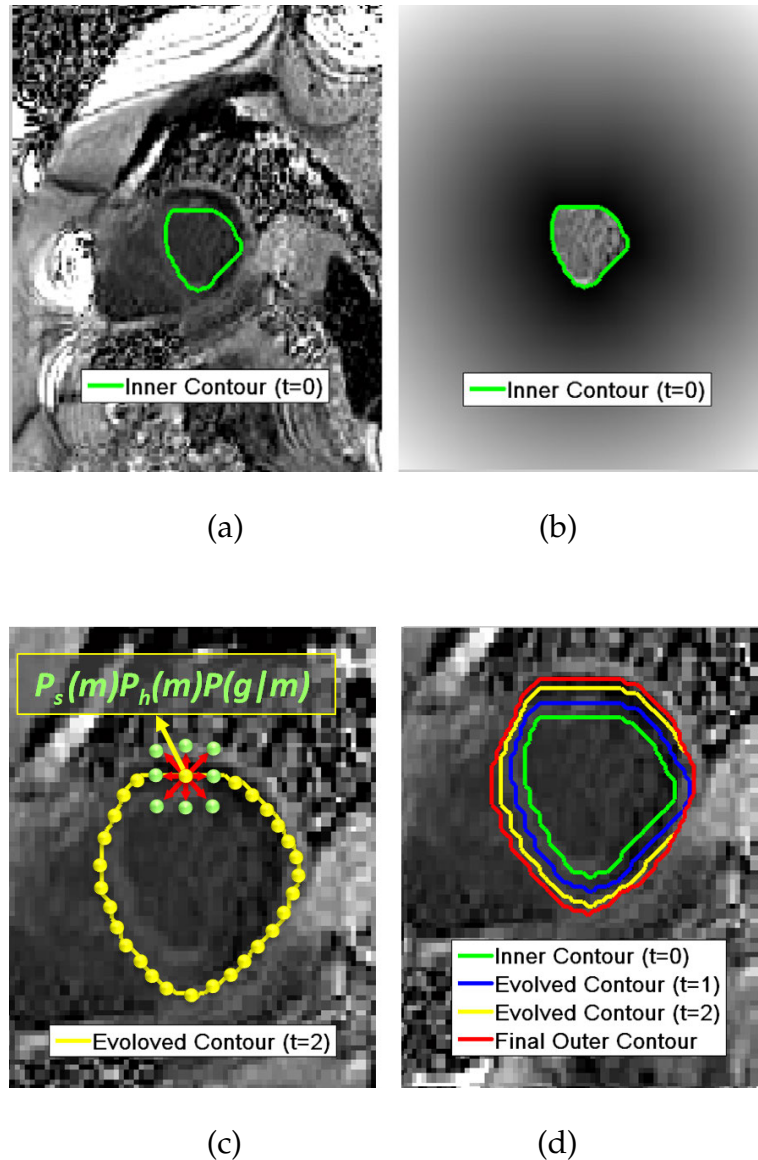
FIGURE 31: Outer contour segmentation: (a) inner edge of the LV wall at time (t=0), (b) normalized minimum Euclidian distance between every point in the outer area of the LV inner cavity and the LV inner edge, (c) an emitted wave at time (t=2) where every point is classified to be wall or background using a Bayesian classifier based on three descriptors, and (d) samples of the propagating waves from the inner edge of the LV at different time instants; the red contour represents the final segmentation of the outer contour of the LV.

Algorithm 3 Segmentation of the Epicardium Contour of the Myocardium

1. Find the inner edge of the LV wall (see Figure 31(a)).

2. Find the normalized minimum Euclidian distance $D(x, y)$ between every point (x, y) in the outer area of the LV inner cavity and the LV inner edge (see Figure 31(b)) by solving the Eikonal equation

$$|\nabla T(x, y)| F(x, y) = 1 \tag{7}$$

where $T(x, y)$ is the time at which the front crosses the point (x, y) and $F(x, y)$ is the speed function [119]; the solution uses the fast marching level-set at unit speed function $F(x, y) = 1$.

3. Propagate an orthogonal wave from the inner edge of the LV points by solving Equation (7) using the fast-marching level-set at the speed function $F(x, y) = exp(-\beta D(x, y))$, where β is a constant to control the evolution of the generated wave. For a smooth evolution $\beta < 1$.

4. Classify every point on the emitted wave to be wall or background using a Bayesian classifier based on the three descriptors as illustrated in section III.A.1 (see Figure 31(c)).

5. Iteratively repeat 3 and 4 until no change occurs in the position of the generated wave; the final area represents the segmentation of the outer contour of the LV (see Figure 31(d)).

ner or outer areas), its GT **G**, and the CE-CMR data **g**, respectively. Then the true positive TP $= |\mathbf{C} \cap \mathbf{G}|$ is the overlapping between **C** and **G**; the false positive FP $= |\mathbf{C} - \mathbf{C} \cap \mathbf{G}|$, and the false negative FN $= |\mathbf{G} - \mathbf{C} \cap \mathbf{G}|$. The DSC is defined as (see Figure 33):

$$\text{DSC} = \frac{2 \times \text{TP}}{2 \times \text{TP} + \text{FP} + \text{FN}} \tag{8}$$
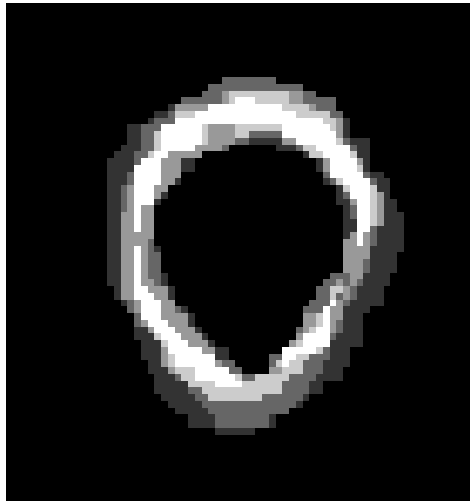
FIGURE 32: Gray coded myocardium wall shape prior at the mid-ventricular level.
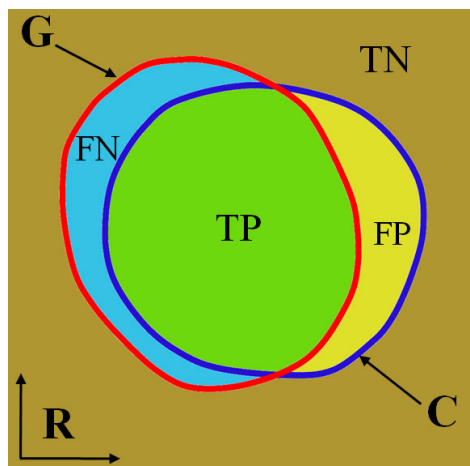
FIGURE 33: Image segmentation performance is evaluated by the Dice similarity coefficient (DSC). The true positive (TP) is the overlap between the segmented object (C) and the GT (G); the false positive (FP) is the difference between the segmented object and the TP, and the false negative (FN) is the difference between the GT and the TP. The DSC measures the similarity between the segmented object and the GT: the closer the DSC to "1", the better the segmentation.

The DSC measures the agreement between the segmentation and the GT; the closer the DSC to unity ("1"), the better the segmentation. Dice similarity of

the proposed segmentation method was compared to well-established approaches, using the two-tailed Student's t-test for paired data. P-value of less than 0.05 is considered statistically significant.

B. EXPERIMENTAL RESULTS

The proposed framework was tested on 14 datasets collected from six patients who had suffered chronic heart attacks (at least four months prior), with clinically documented ejection fraction dysfunction, and who subsequently underwent an experimental myocardial regeneration therapy, as part of an institutionally approved trial. All images were obtained using a Siemens 1.5T Espree system (Siemens Medical Solutions, USA Inc), with multichannel phased array reception coils [121]. Late (at 15 to 25 min) gadolinium contrast agent enhanced (0.2 mM/kg) acquisitions, using both conventional inversion time chosen acquisitions and phase sensitive inversion recovery. To ensure adequate signal-to-noise ratios, the typical spatial resolution was $2.08 \times 2.08 \times 8.0 \, \text{mm}^3$. Typically 10-14 image cross-sections were obtained to cover the LV. To test the proposed method, a total of 168 images were examined. To evaluate the segmentation accuracy of the proposed framework, the "ground truth (GT)" delineations of the inner and outer contours were given by an expert (a radiologist) for five datasets; a total of 55 images.

The results of the proposed segmentation approaches for inner and outer borders are illustrated in Figure 34 and Figure 35. To highlight the advantage of integrating the shape prior with the intensity and spatial interaction information in the joint MGRF probabilistic model, the inner cavity region is segmented based on the intensity only (Figure 36(b)), and based on the intensity and the spatial interaction information (Figure 36(c)). It is clear that counting only on intensity and spatial interaction information will not lead to accurate segmentation due to the
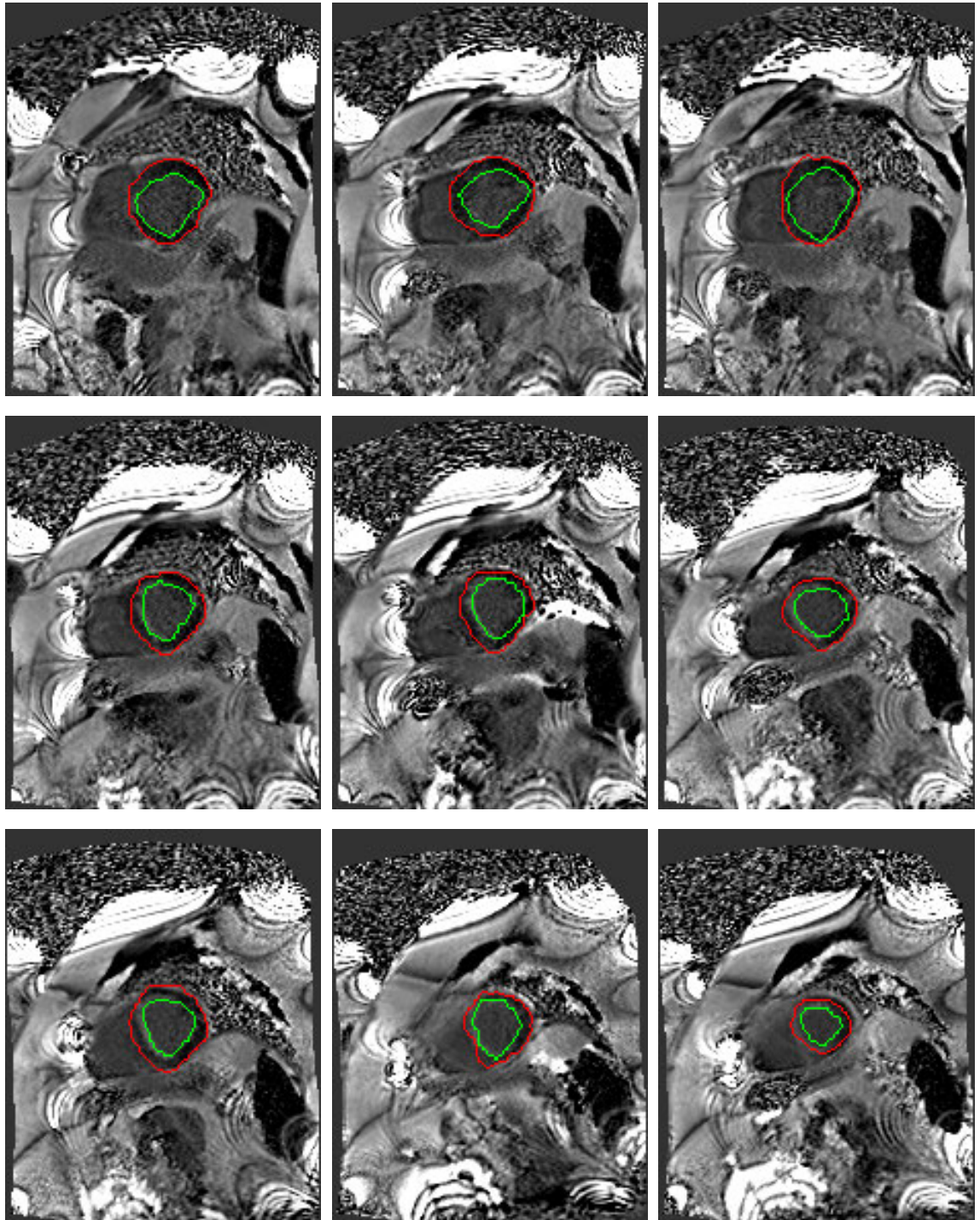
FIGURE 34: Segmentation results of the inner and outer contours for CE-CMR images of one data subject.

gray-levels inhomogeneities. Figure. 36(d) shows how the segmentation result is enhanced after integrating the shape prior. These results highlight the advantages of the proposed segmentation approach.
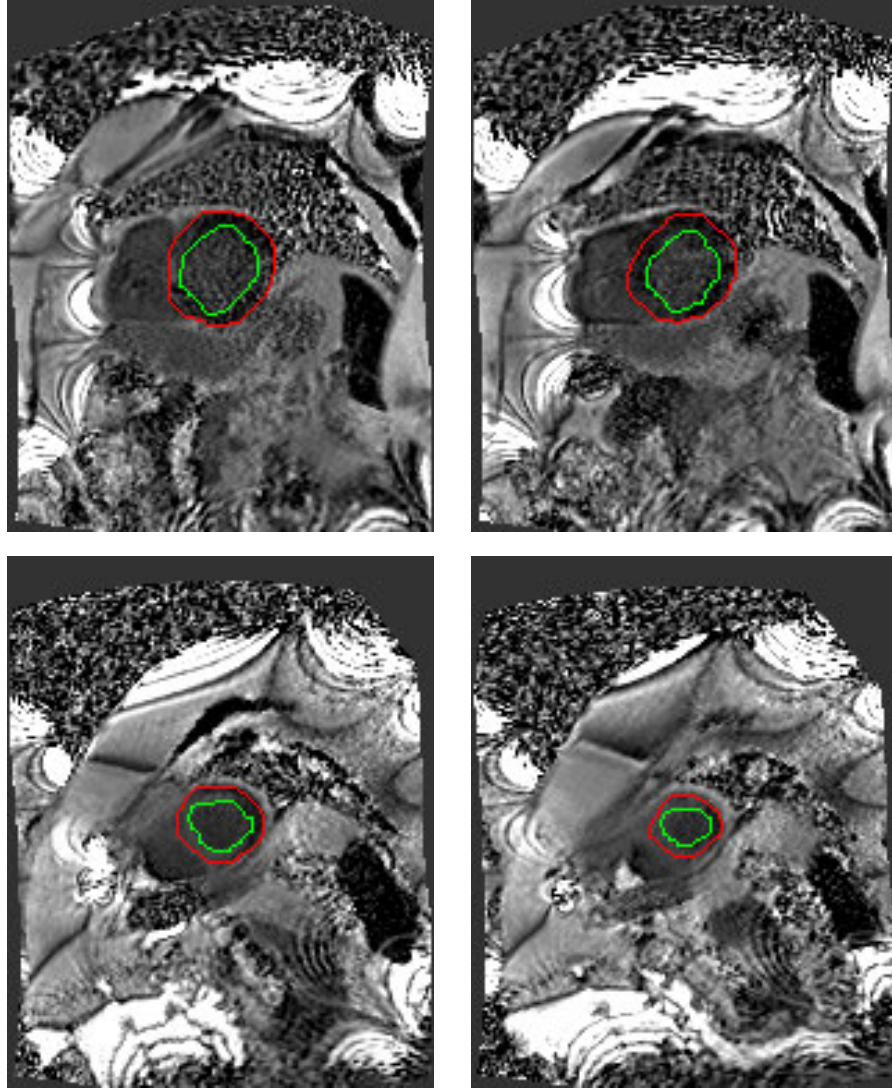
FIGURE 35: More segmentation results for sample image cross-sections from different datasets.

Figure 37 and Figure 38 show visual comparative segmentation results for the proposed approach versus the level-sets based segmentation approach proposed in [1] for the segmentation of the inner cavity and of the outer region of the LV wall, respectively. Table 4 summarizes the comparative segmentation results for the five data sets (55 images) with the known GT (manual segmentation by an
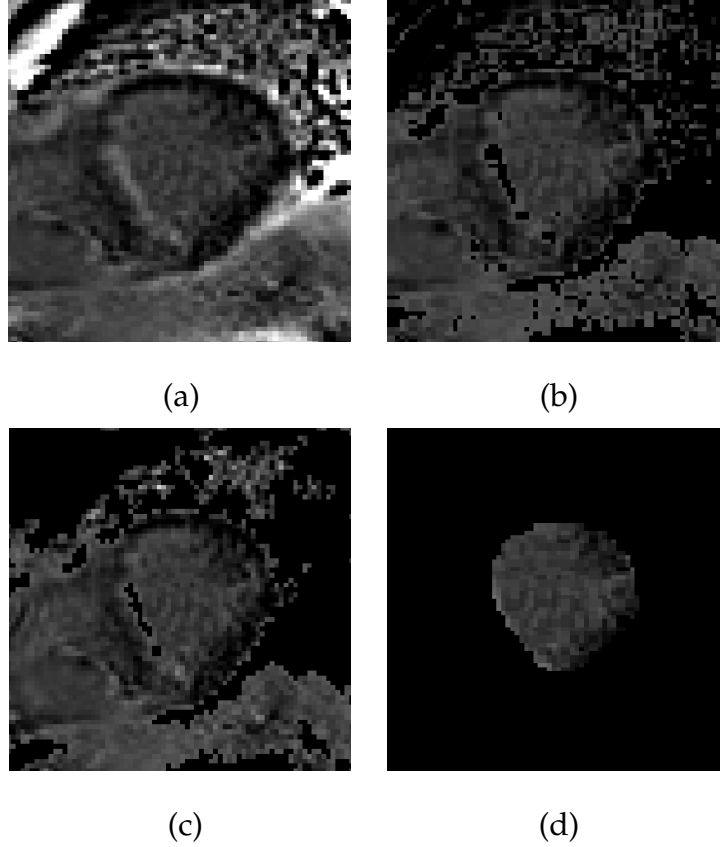
FIGURE 36: Inner cavity segmentation: (a) original slice, and segmentation (b) using intensity model alone, (c) using intensity and spatial interaction models, and (d) after integrating shape model.

expert). As presented in the table, the proposed segmentation approaches for inner and outer borders of the LV wall show better performance than the level-set shape-based approach of Tsai et al. [1], as evidenced by larger DSCs approaching the ideal value 1 (DSC metric is calculated as illustrated in Section III.A.3). Moreover, the differences in the mean DSC between the proposed segmentation and Tsai et. al approach are statistically significant according to the unpaired t-test (the two-tailed P values for the segmentation of the inner and outer borders are less than or equal to 0.0001 and 0.003, respectively). These results highlight the advantage of the proposed segmentation approaches.

(a)   (b)
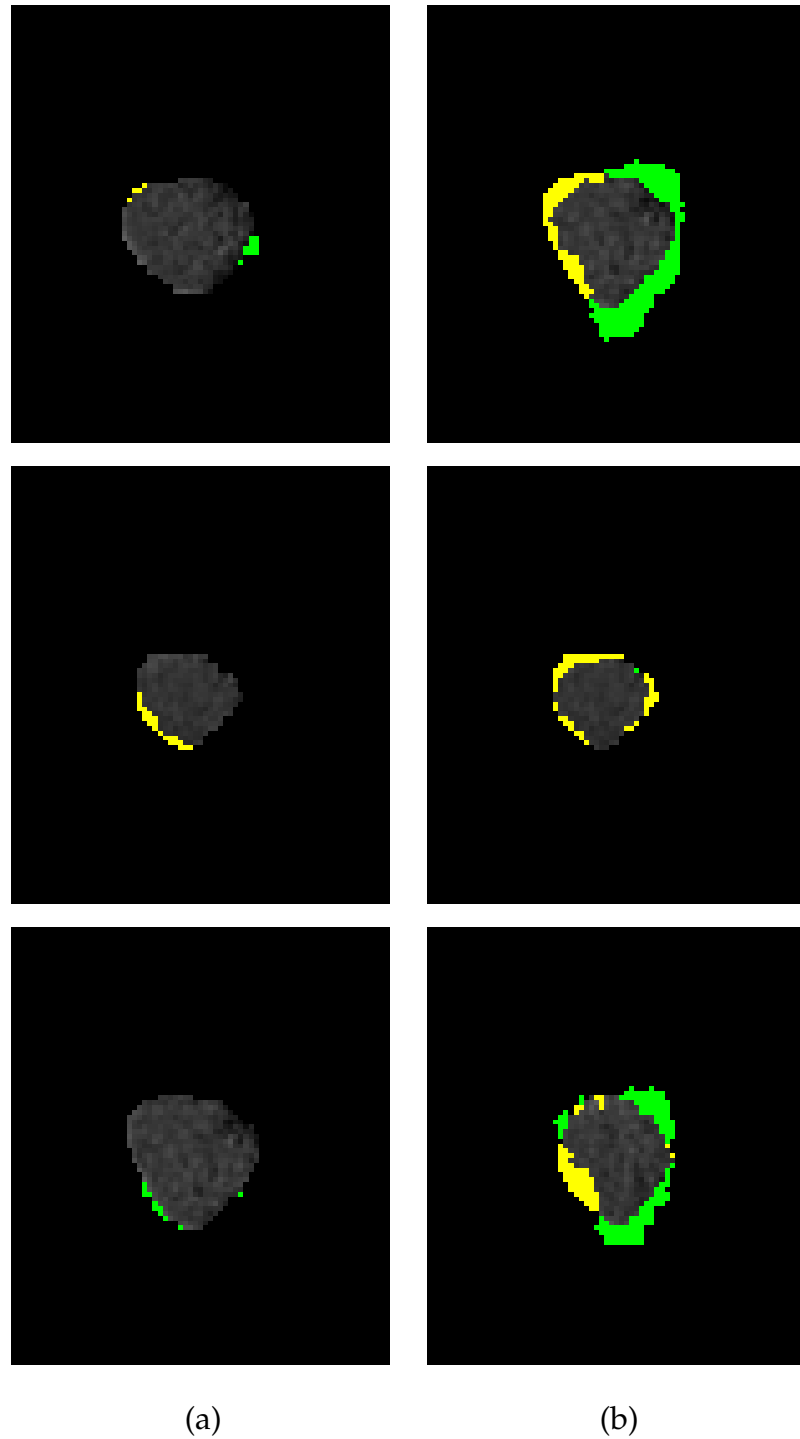
FIGURE 37: Comparative segmentation results for the LV wall inner cavity for the proposed approach (a) versus the level-sets based segmentation [1] (b) for different sample images. Yellow represents the missed segmented points (FN) and green represents the introduced segmented points that were not on the GT (FP).

(a)   (b)
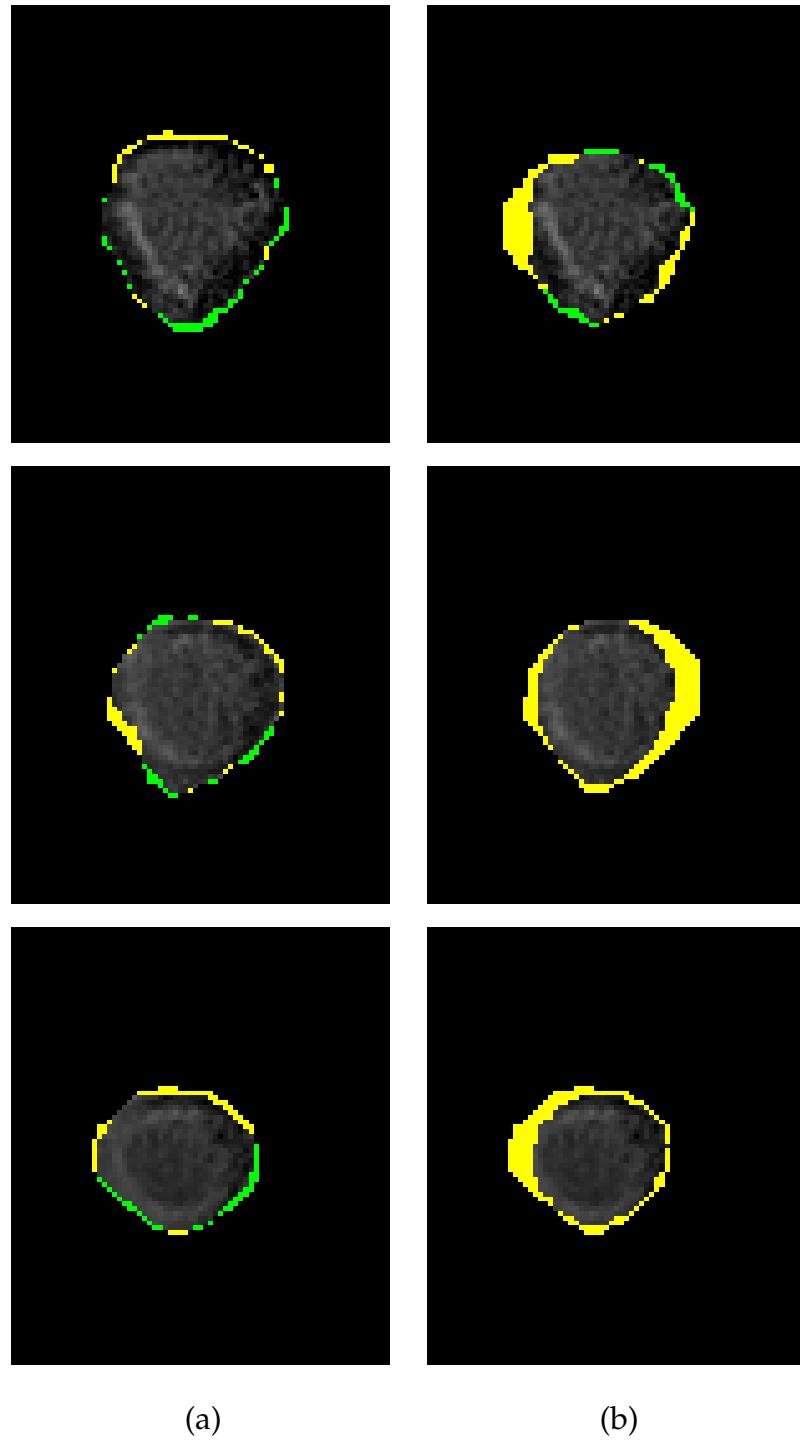
FIGURE 38: Comparative segmentation results for the outer region of the LV wall for the proposed approach (a) versus the level-sets based segmentation [1] (b) for different sample images. Yellow represents the FN points and green represents the FP points.

TABLE 4: Dice similarity coefficients (DSC) between the proposed segmentation and the ground truth (GT) in comparison to the level-sets based segmentation approach in [1].

	Inner		Outer	
	Proposed Method	**[1]**	**Proposed Method**	**[1]**
Minimum DSC	0.85	0.75	0.80	0.34
Maximum DSC	0.99	0.93	0.96	0.91
Mean DSC	0.94	0.83	0.92	0.81
Standard Deviation	0.045	0.055	0.047	0.157
P-value	$< 10^{-4}$		0.003	

C. SUMMARY

In total, a fully-automated segmentation framework for segmenting the LV wall is presented based on three image descriptors: the gray level intensity, the shape information, and the spatial information descriptors. For segmenting the LV inner cavity, these descriptors are embedded into a new energy function that is globally optimized using graph cuts. For segmenting the LV outer borders, the three descriptors are used to control the speed of an orthogonal wave starting from the LV inner borders. The results suggest that the proposed approach can precisely segment CE-CMR images. In addition, the results confirm the robustness of the proposed methods against the complex shape variations of the LV. The developed segmentation framework is very suitable for segmenting the anatomical structures that have noise and inhomogeneity problems. The work presented in this chapter has been published in the international conference of image processing (ICIP) [122]. The next chapter investigates the identification of the pathological tissue in the LV wall based on the accurate segmentation of the wall borders.

CHAPTER IV

SIZING THE PATHOLOGICAL TISSUE IN THE LV WALL USING CE-CMRI

A novel automatic framework for detecting and quantifying viability from cardiac-enhanced magnetic resonance imaging (CE-CMRI) is proposed. The framework identifies the pathological tissues in a segmented left ventricle (LV) wall (the segmentation of LV wall is presented in Chapter III) based on a joint Markov-Gibbs random field (MGRF) model that accounts for the 1st-order visual appearance of the myocardial wall (in terms of the pixel-wise intensities) and the 2nd-order spatial interactions between pixels. The pathological tissue is quantified based on two metrics: the percentage area in each segment with respect to the total area of the segment (area metric), and the trans-wall extent of the pathological tissue (shape metric). In this work, the transmural extent is estimated using point-to-point correspondences based on the geometrical features that are extracted from the solution of the Laplace partial differential equation. Transmural extent was validated using a simulated phantom. Fourteen datasets (168 images) were tested and validated against manual expert delineation of the pathological tissue, outlined by two observers. Mean Dice similarity coefficient (DSC) values of 0.90 and 0.88 were obtained for the observers, approaching the ideal value, 1. The Bland Altman statistic of infarct volumes estimated by manual versus the MGRF estimation revealed little bias difference, and most values falling within the 95% confidence interval, suggesting good agreement. The DSC measure documented statistically significant superior segmentation performance for the proposed MGRF method versus established intensity-based methods (greater DSC, and smaller standard

69

deviation). The proposed Laplace method showed good operating characteristics across the full range of extent of transmural infarct, outperforming conventional methods. Phantom validation and experiments on patient data confirmed the robustness and accuracy of the proposed framework.

A.   INTRODUCTION

Assessment of myocardial viability through identifying ischemically damaged tissue is of great clinical importance as the standard means of diagnosing and monitoring irreversible myocardial sequelae of ischemic heart disease, as well as guiding optimal therapies for individual patients [27]. The infarcted myocardium, after administering a gadolinium contrast agent, appears hyper-enhanced compared to the normal myocardium on late (15-25 min) acquisitions [75–79]. Extensive research has been conducted on the use of late CE-CMR images, which allow for estimating the transmural extent of damaged myocardium with high spatial resolution [75–79], to delineate the pathological tissue and extract useful metrics for indexing myocardial injury. In this chapter, two candidate metrics have been explored to quantify myocardial viability: the percentage of the segmented pathological tissue with respect to the total area of the myocardial wall, and the transmural extent of this tissue relative to the full LV wall thickness. A review of the current methods to estimate the area and the transmural extent of pathology are presented in Sections II.B.1 and II.B.2, respectively.

As discussed in Chapter I, the current methods for identifying ischemically damaged tissue have the following aggregate limitations: (*i*) the pathological tissue identification does not adequately account for spatial interactions between the myocardium pixels; (*ii*) many of these methods are quite sensitive to imperfect myocardium contours and image noise; and (*iii*) the radial transmural extent esti-

mation suffers from geometric inconsistency in estimating the point-to-point correspondences between the inner and outer boundaries, while the centerline method suffers from imperfect inner and outer contours, especially for noisy images.

To overcome these drawbacks, an augmented, automatic framework is proposed to analyze the CE-CMR images. To delineate the pathological tissue in the LV wall, the image is modeled as a joint MGRF that accounts for not only the 1st-order visual appearance (based on the pixel-wise intensities), but also incorporates the 2nd-order spatial interactions between the pixels. Next, area and shape metrics are estimated to quantify the infracted region. The shape metric (i.e., the transmural extent) is estimated using a geometrically motivated approach, based on a partial differential equation (PDE) that accurately co-locates the corresponding pixel pairs. This distance metric, as shown in Figure 39(b), overcomes the geometric inconsistency of the often-used radial procedure, as shown in Figure 39(c).
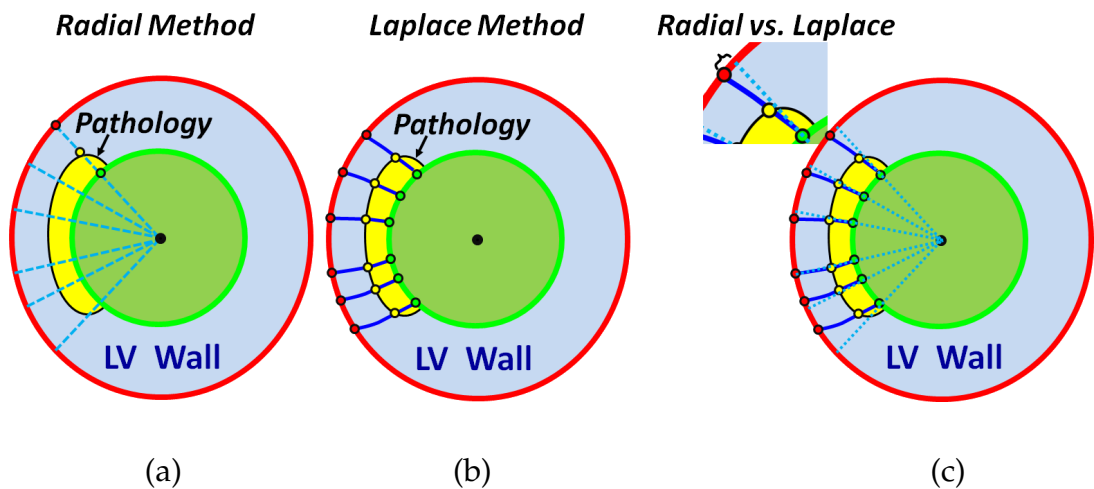
FIGURE 39: Illustration of estimating the transmural extent of pathological tissue in the LV wall: (a) standard radial approach, (b) proposed Laplace PDE-based approach, and (c) deviations of (a) from the co-located corresponding pixel pairs of (b).

B. BASIC ANALYSIS STAGES

This chapter details the identification and quantification of damaged myocardial tissue on CE-CMR images (steps 2 and 3 of the proposed framework; see Figure 40). Myocardium contour segmentation (step 1) was previously discussed in Chapter III.
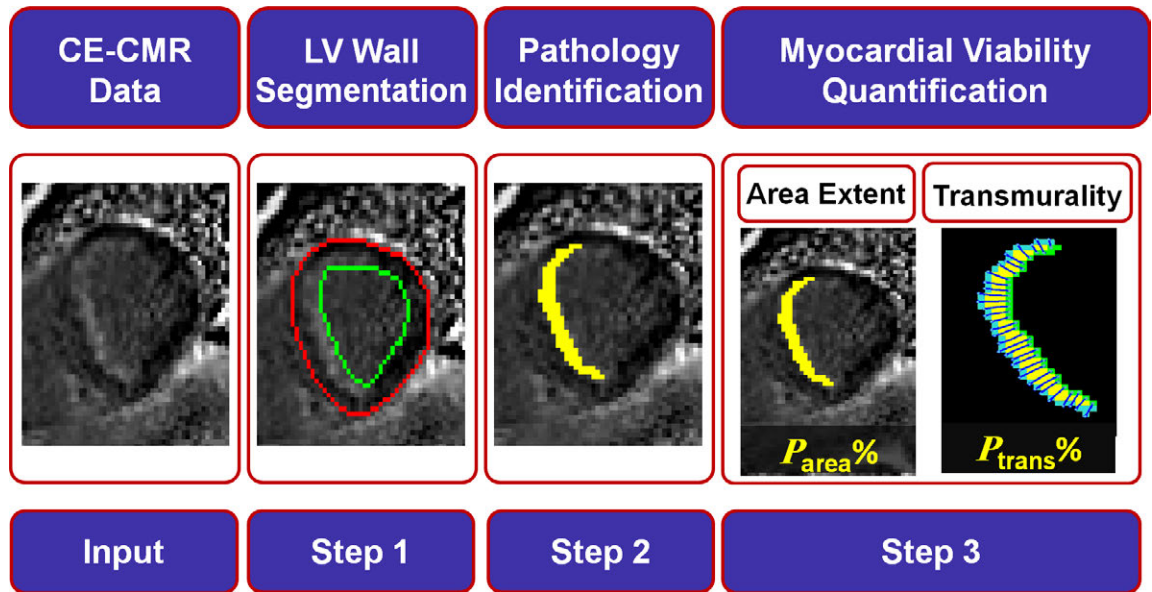
FIGURE 40: Basic processing steps of the proposed framework for analyzing CE-CMR images: LV wall segmentation, pathology identification, and myocardial viability quantification in terms of the area extent and transmurality metrics.

1. Identification of the Pathological Tissue in the LV Wall

For the challenging task of delineating the pathological tissue in the LV wall, a powerful approach is proposed based on applying a joint MGRF model to the CE-CMR image signals and the region map labels (i.e., object and background) that accounts for the intensity and the spatial interactions between the pixels of pathological tissue. The main novelty of this joint MGRF segmentation compared to the

conventional thresholding methods, with heuristic or user-selected thresholds, is two-fold. First, an initial proper threshold is found automatically by accurate identification of pixel-wise object and background intensity distributions. Second, the initial region map is refined by identifying the 2nd-order spatial interactions. For the initial segmentation, the mixed 1st-order intensity distribution for the image is separated into the conditional object and background components, which are used to build an initial region map. To optimize the final region map, the iterative conditional mode (ICM) relaxation approach [123] is used to search for a local maximum of the joint image-map probability by maximizing sequentially the pixel-wise conditional probabilities of region map labels. At each step the approach minimizes the MGRF energy for each pixel in the entire image. This minimization step is repeated until there is no further decrease in the MGRF energy, thereby establishing a stopping criterion.

The intensity and the spatial interaction descriptors for the pathological tissue and the background (other tissue in the LV wall) are estimated using the same methodologies described in Sections III.A.1.a and III.A.1.b, respectively. The whole search algorithm for identifying the pathological tissue in the LV wall is described in Algorithm 4.

2. Myocardial Viability Quantification

After accurately segmenting the pathological tissues, two potential metrics have been derived to quantify the myocardial viability: the geographic extent (area) of the pathological tissue, and the transmural extent (transmurality). These metrics have been previously explored as indexes of myocardial viability. In particular, the transmurality has been well-documented as a predictor of clinical outcomes using CE-CMR data [124].

Algorithm 4 Segmentation of the Pathological Tissues of the Heart

---

1. For the bounded myocardial wall for each CE-CMR image, obtain the intensity model, namely the marginal intensity distributions of the pathological tissue and its background, by the LCDG-based approximation of the mixed empirical intensity probability distribution using the corresponding EM-based algorithms [102].

2. Use the estimated intensity model to get the initial segmentation of the pathological tissues, i.e., form an initial region map of pathological tissues.

3. Estimate the log-likelihood MGRF energy of the image and its initial region map.

4. Use the ICM relaxation algorithm [123] to estimate the final map (segmentation of pathological tissues) that maximizes the MGRF energy .

---

a. The percentage area P_{area} of the pathological tissue: The percentage area P_{area} of the pathological tissue is estimated for each segment i in the 17-segment model (Figure 41) [4]; $i \in \{0, .., 17\}$, as follows (see Figure 42):

$$P_{\text{area}}(\text{segment } i) = \frac{\text{Area of pathological tissue in the segment } (A_i)}{\text{Area of myocardium wall segment } (B_i)} \times 100\% \quad (9)$$

b. The transmural extent of the pathological tissues (P_{trans}): The transmural extent of the pathological tissues (transmurality) is the fraction of the pathological tissue's extension across the myocardial wall [125]. Inaccurate geometric point-to-point correspondences and inconsistencies in the resulting transmural extent affect its traditional estimation as illustrated in Section IV.A (Figure 39). In this work, a PDE-based approach is proposed to co-locate the corresponding pixel pairs between the inner and outer contours of the LV wall, and between the inner and outer edges of the pathological tissue (Figure 43). These correspondences are found by solving the 2nd-order linear Laplace PDE for a scalar potential field Υ [18, 126–129].
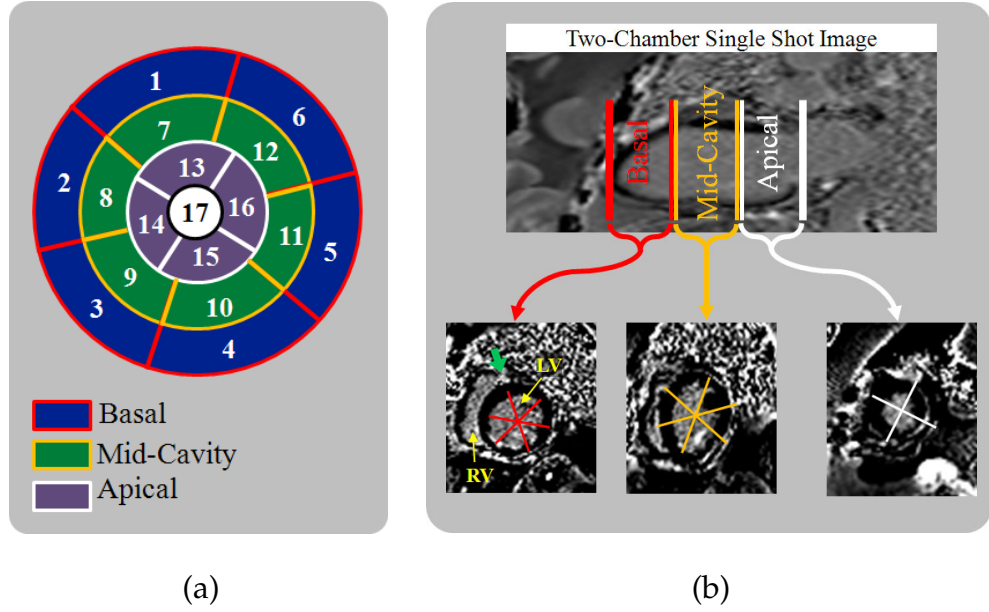
FIGURE 41: The myocardial 17-segment model [4]: (a) the circumferential polar plot and (b) the locations of the segments for basal (left), mid-cavity (middle), and apical (right) image sections. The segment numbering starts contour-clockwise from the anatomical landmark indicated by the green arrow in the basal section, namely, the anterior insertion of the right ventricle wall on the left ventricle wall.

Laplace's equation is a 2nd-order linear PDE for a scalar field. It arises in a variety of applications including fluid mechanics, electromagnetism, potential theory, solid mechanics, heat conduction, geometry, probability, etc. Mathematically, the planer Laplace PDE equation takes the form:

$$\nabla^2 \Upsilon = \frac{\partial^2 \Upsilon}{\partial^2 x^2} + \frac{\partial^2 \Upsilon}{\partial^2 y^2} = 0 \tag{10}$$

Generally, the solution of the Laplace equation between two boundaries, such as $\mathbf{B_a}$ and $\mathbf{B_b}$ in Figure 44, can be envisioned as resulting in intermediate equipotential surfaces (dashed lines in Figure 44) and streamlines that connect the boundaries. The desired point-to-point correspondences between the boundaries are established by the streamlines, orthogonal to all the equipotential surfaces (vi-
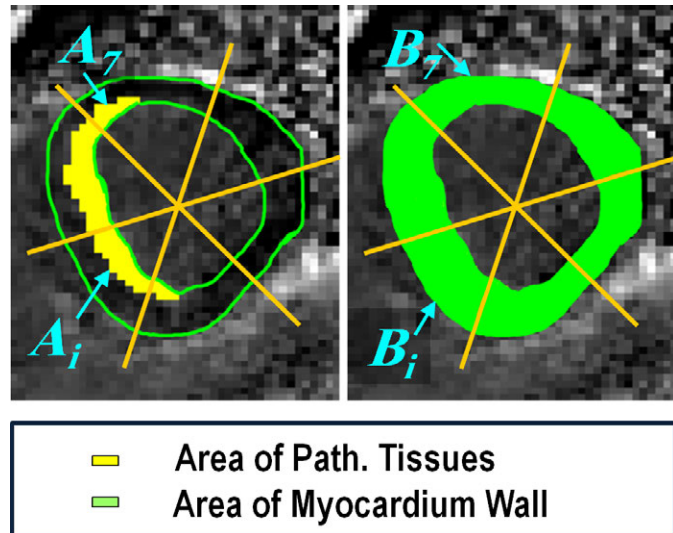
FIGURE 42: Estimation of the percentage area of myocardial injury ($P_{\texttt{area}}$): A_i is the area of injury in segment i and B_i is the total area of the segment. For each segment, $P_{\texttt{area}}$ is the percentage of the area of the injury in the segment (A_i) with respect to the total area of the segment (B_i).
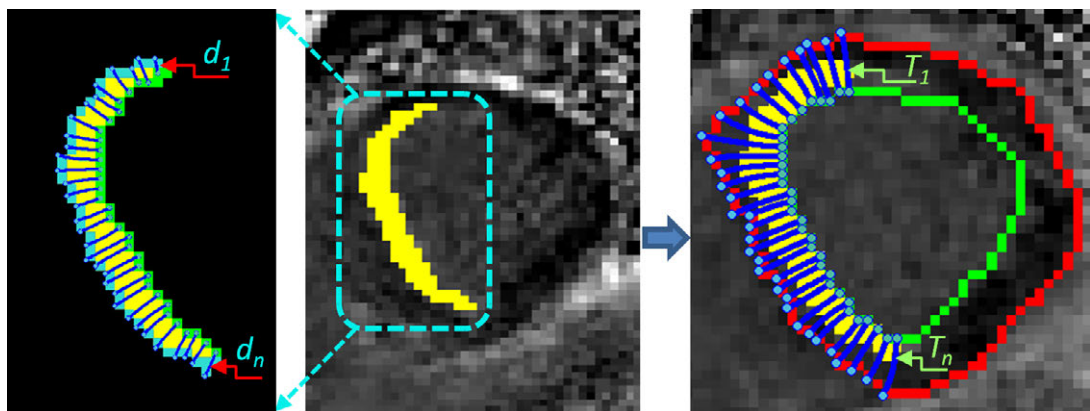
FIGURE 43: Estimation of the transmural extent of myocardial injury. The pathological tissue in the LV wall is identified in the middle image. The Laplace correspondence is shown in the right image between the inner and outer borders of the LV wall (T_j), and in the left image between the inner and outer borders of the pathological tissue (d_j). For each segment, $P_{\texttt{trans}} = \text{mean}(dj/Tj)$ for all the lines inside the segment.

sualized by the line connecting the points $\mathbf{B}_{ai}$ and $\mathbf{B}_{bi}$ in Figure 44). The correspondences between the borders of the pathological tissue and between the contours of the LV wall, found by solving the Laplace PDE (see Figure 43), are used in the proposed estimation of the transmural extent. The transmural extent for each segment in the 17-segment model is estimated as the average ratio between the segment's pathology extent (d) and the segment's wall thickness (T):

$$P_{\text{trans}} (\text{segment } i) = \left(\frac{1}{n} \sum_{j=1}^{n} \frac{d_j}{T_j} \right) \times 100\%$$

where n is the number of lines in the segment i that connect the estimated corresponding pairs.
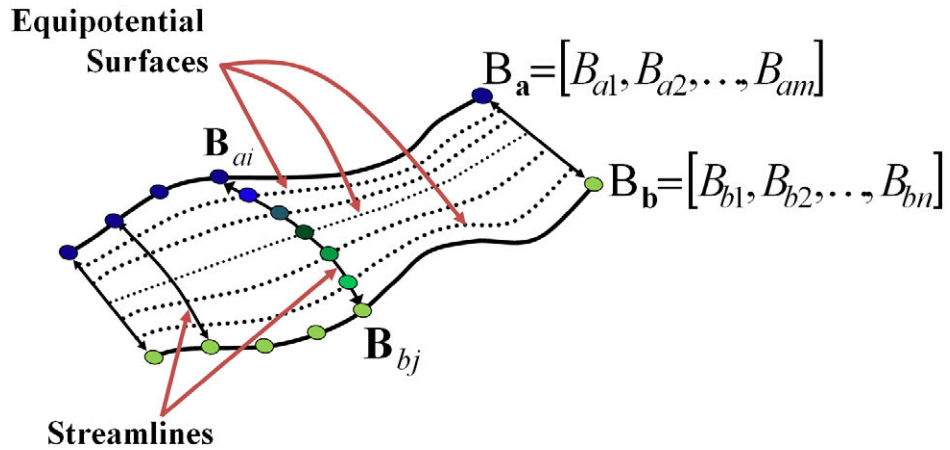
FIGURE 44: Schematic illustration of correspondences by a potential field. The solution of the Laplace PDE between the two boundaries $\mathbf{B_a}$ and $\mathbf{B_b}$ results in intermediate equipotential surfaces (dashed lines), and orthogonal streamlines that connect both the boundaries. The streamlines (e.g. the line connecting the points $\mathbf{B}_{ai}$ and $\mathbf{B}_{bi}$) establish the point-to-point correspondences between the boundaries.

C. PERFORMANCE EVALUATION AND VALIDATION

1. Evaluation of the Proposed Segmentation Algorithm

The segmentation performance is evaluated using two metrics, the DSC metric [120] and the Bland Altman analysis. The **DSC** metric estimates the overlap between the experimentally segmented region and ground truth (GT) segmentation (Figure 45). It is calculated as illustrated in Section III.A.3. The **Bland Altman analysis** assesses the degree of agreement between two methods of clinical measurement [130]. To indicate an agreement, the bias (mean difference of the clinical measurement between the two methods) should be near zero; also most of the data points should fall within 95% limits of agreement (±1.96 Standard Deviation (SD) around the bias). The Bland Altman statistic is computed to compare the computed volume of infarcted tissue (total number of voxels scaled by the resolution and the slice thickness) using the proposed automatic method versus the GT, as determined by two experienced observers.
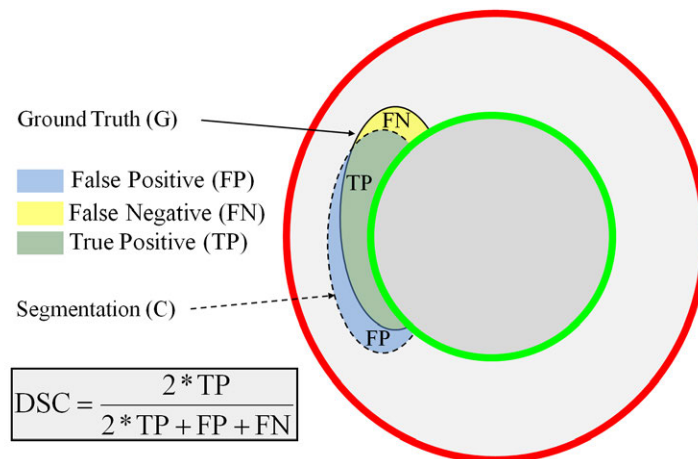
FIGURE 45: Image segmentation performance is evaluated by the Dice Similarity Coefficient (DSC).

2. Validation the Proposed Method of Estimating Transmural Extent using a Simulated Phantom

To validate the proposed transmural extent method, a realistic synthetic phantom with varying injury transmural extent was constructed and tested using the proposed Laplace PDE-based method versus two alternate standards (the radial method and the centerline method [82]). A phantom is constracted with elliptical symmetry (to represent the heart in cross-section), and considered uniform thickness of infarct throughout for practicality of computation. Total wall thickness was used as 12 mm to correspond to a realistic normal heart wall dimension, and a realistic inner LV wall edge extracted from actual patient image data. To account for the fact that a real infarct can have nonuniform thickness throughout a region, varying thicknesses (from 2mm to 10mm to correspond from small to very large infarcts) were considered. Particularly, ranges less than 25% (small), 25 to 50% (intermediate), and more than 50% (large) of the wall are physiologically meaningful ranges of the transmural extent of injury, as previously documented by Kim et al. [124]. For idealized transmural resolution, an in-plane spatial resolution of 1 mm $\times$ 1 mm is used to obtain a sufficient number of pixels across the wall. This phantom is illustrated in Figure 46, where Figure 46(a) shows the full phantom illustrating uniform size injury, and Figure 46(b) is a schematic depicting the proposed approach to account for varying thicknesses across the infarct, particularly at the step between the different thicknesses, as indicated by the dashed arrows.

Figure 47(a) illustrates the transmural extent estimation using the radial method with lines extended from the center of the LV inner cavity. Figure 47(b) illustrates the centerline estimation method with lines perpendicular to the centerline, defined as joining the midpoints of the known simulated full wall thickness. Figure 47(c) illustrates the proposed Laplace PDE-based estimation of the trans-
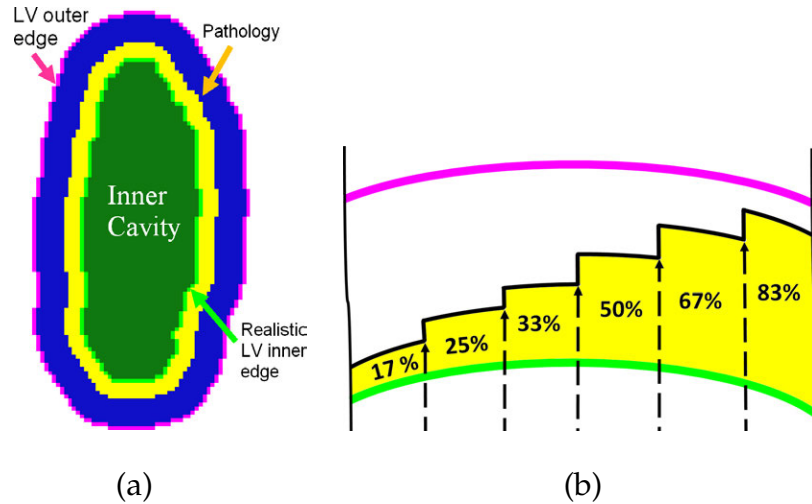
FIGURE 46: Validation of the proposed method for transmural extent estimation using simulated phantoms with a realistic inner LV wall edge: (a) a representative phantom with elliptical symmetry and uniform thickness of infarct, (b) an approach to account for the fact that a real infarct can have nonuniform thickness throughout a region: varying thicknesses were considered, from 17 % to 83% to correspond from small to large infarcts, particularly at the step between the different thicknesses as indicated by the dashed black arrows.
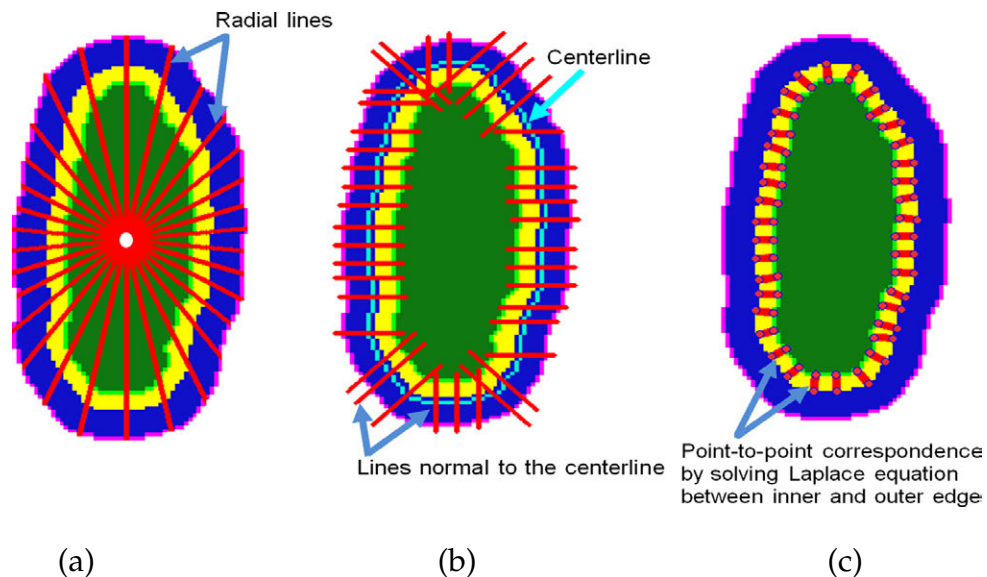
FIGURE 47: Illustration of the different methods, i.e., the radial method (a), the centerline method (b), and the Laplace method (c), used to estimate the transmural extent on a simulated phantom.

mural extent, where the streamlines via the equipotential surfaces connect each corresponding pair of points, at the inner- and outer-edges of pathology. For all the three methods, the average of the line-wise transmural extents is used.

D. EXPERIMENTAL RESULTS

The proposed framework was tested on 14 datasets collected from six patients who had suffered chronic heart attacks (at least four months prior), with clinically documented ejection fraction dysfunction, and who subsequently underwent an experimental myocardial regeneration therapy, as part of an institutionally approved trial. All images were obtained using a Siemens 1.5T Espree system (Siemens Medical Solutions, USA Inc), with multichannel phased array reception coils [121]. Late (at 15 to 25 min) gadolinium contrast agent enhanced (0.2 mM/kg) acquisitions, using both conventional inversion time chosen acquisitions and phase sensitive inversion recovery. To ensure adequate signal-to-noise ratios, the typical spatial resolution was $2.08 \times 2.08 \times 8.0$ mm^3. Typically 10-14 image cross-sections were obtained to cover the LV. To test the proposed method, a total of 168 images were examined. To evaluate the segmentation accuracy of the proposed framework, the "ground truth (GT)" delineations of pathological tissues in each image were given by an expert (a radiologist).

1. Delineation of Pathological Tissues

To assess the myocardial viability, first the pathological tissue. are identified Typical results of the proposed joint MGRF-based estimation, compared to the GT manual expert delineation are shown in Figure 48. Table 5 presents the DSC values between the proposed automatic segmentation and the GT, for two independent

observers, Ob1 and Ob2. The agreement between this GT and the proposed segmentation was confirmed using the paired t-test, for each of the observers (P-value 0.487). In addition, the Bland Altman analysis [130] comparing estimated infarct volumes for the MGRF segmentation versus manual delineation by two independent experienced observers revealed bias (mean difference) near zero, with most of the data points falling within the 95% confidence limits of agreement, reflecting good agreement with GT (see Figure 49 (a) and (b)). The DSC and the Bland Altman analyses confirm the robustness and reproducibility of the proposed framework.

The DSC was also used to compare the proposed framework with two established segmentation approaches namely, the 2σ [29] and 3σ [30] threshold techniques. As shown in Table 5, the proposed approach outperforms both of these techniques, as evidenced by the DSC approaching the ideal value of 1, and having the smallest standard deviation. Furthermore, a statistically significant difference is documented between the proposed approach and the 2σ- and the 3σ-threshold techniques. The reported results in table 5 agrees with the work of Amado et al. [32] in that the performance of the simple intensity methods gets worse as one goes to higher σ cut-offs.

TABLE 5: Performance of the proposed pathological tissue segmentation versus the established 2σ- and 3σ-threshold methods on the 14 datasets (168 images) in terms of the DSC metric compared with the ground truth (GT), for two experienced observers Ob1 and Ob2. SD stands for the standard deviation.

	Proposed Approach		2σ-threshold [29]		3σ-threshold [30]	
Observer (Ob)	Ob1	Ob2	Ob1	Ob2	Ob1	Ob2
DSC Mean	0.90	0.88	0.73	0.76	0.52	0.61
DSC SD	0.056	0.057	0.088	0.078	0.113	0.162
P-value (versus Proposed approach)	$< 10^{-4}$	$< 10^{-4}$	$< 10^{-4}$	$< 10^{-4}$	$< 10^{-4}$	$< 10^{-4}$

| Original Data | Ground Truth Pathology Identification | Our Estimation |
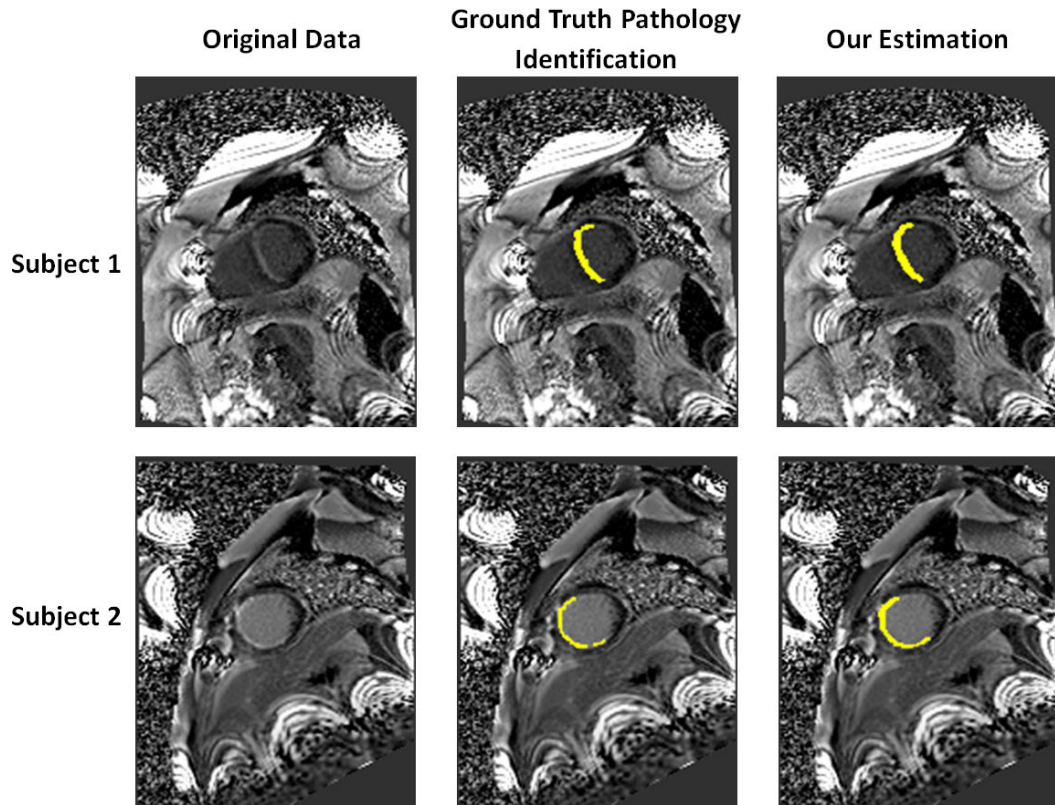
FIGURE 48: Sample results for the proposed pathological tissue identification compared with the manual expert ground truth (GT) for a representative image section from two subjects.

2. Validation of the Transmural Extent using Synthetic Phantoms

Two key metrics for quantifying the myocardial viability: the percentage area of pathological tissue and the transmural extent were explored. To validate the proposed framework, varying transmural injury extents were simulated using a simulated phantom. Figure 39 illustrates theoretic geometric errors of the established radial method. Table 6 summarizes estimates for the proposed method versus the two established methods, where idealized infarcts of transmural extents (encompassing less than 25%, 25 to 50%, and more than 50% of the wall) were chosen for their previously documented physiological relevance [35] (see Fig 46). As shown in Table 6, the Laplace method provides the closest absolute estimates of the known GT, over all ranges of infarct. Moreover, the computed errors in estimat-
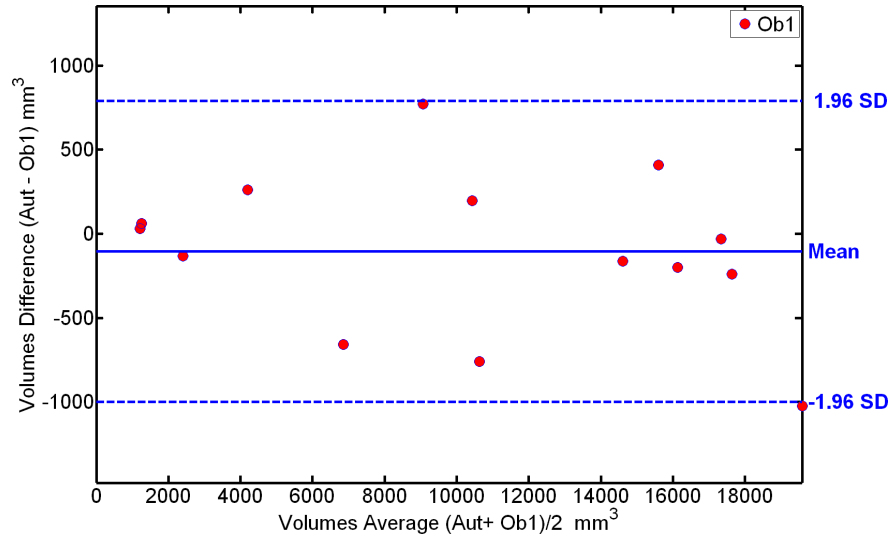
(a)
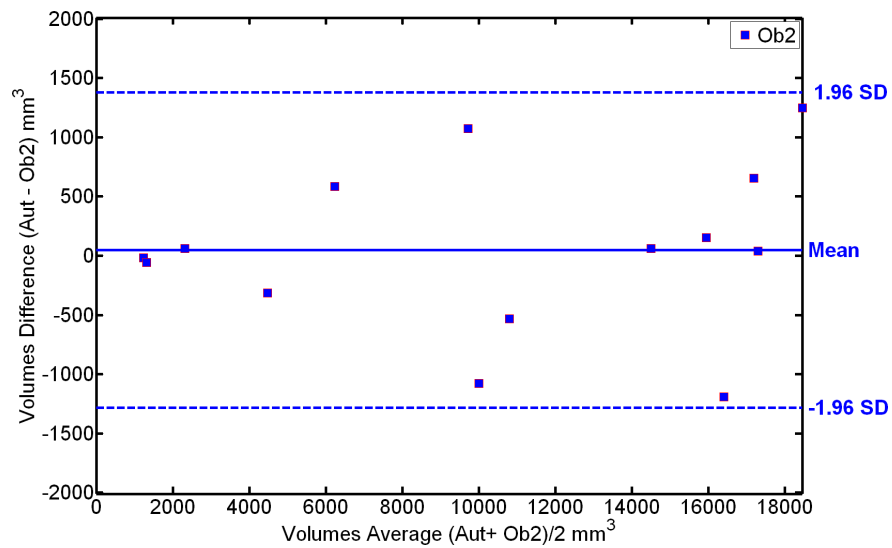
(b)

FIGURE 49: Bland Altman plots for the 14 datasets presented in this study. The clinical parameter, infarct volume, is estimated using the proposed automatic segmentation (Aut) versus manual delineations by two observers, Ob1 (a) and Ob2 (b). For good agreement, the mean of the volume difference between the two methods should be near zero, and data points should fall within the 95% confidence interval (i.e., between 1.96 SD and -1.96 SD).

ing the transmural extent using the proposed method are all less than 3%, while they approach 25% for the radial method, and 7% for the centerline method. These differences were statistically significant (see Table 6).

3. Clinically Meaningful Effects

The ability of the proposed framework for the detection and quantification of damaged tissue has been initially explored to index clinically meaningful changes. Figure 50 visually illustrates the changes in the injured myocardium, processed using the MGRF method, for a representative patient, one year after treatment. Table 7 presented the reported extracted two parameters for myocardium viability quantification for this patient over one year of treatment. Table 8 summarizes the overall extracted two parameters for myocardium viability quantification for all datasets enrolled in this study (i.e., 14 datasets from six patients). Figure 51 and Figure 52 show the potential of the two metrics to document changes with treatment, that were consistent with improvements in patient status, as documented by clinical indexes. This lends encouragement for the proposed framework to detect meaningful effects in treatment and physiological studies.

An important feature is that the proposed framework is not tied to a specific image resolution, given that the pathological tissue size is typically of similar dimension or greater than the scanner pixel size, and depends on the pathology size only implicitly, via the MGRF model learned. One should expect that the higher the scanner resolution (essentially the finer the nearest neighbor grid), the more the interactions between the pixel labels will be taken into account. It is conceivable that the finer the scale at which the pathology is examined (attained via higher scanner resolution), more sophisticated nearest neighborhood interactions may need to be taken into account.

TABLE 6: Transmural extent estimation using the three methods (i.e., radial and centerline standards, and the proposed proposed Laplace method) on a synthetic simulated phantom with varying transmural infarct. All simulated results have been computed using double precision (16 decimal places with error equal to 1.224×10^{-16}). The final results were approximated to three decimal points to reflect an idealized precision for estimating the transmural extent.

Transmural Extent	Metric	Laplace	Radial	Centerline
2 mm (17%)	Extent (mm)	1.954	2.493	2.126
	Error (mm)	0.046	0.493	0.126
	Error%	**2.300**	**24.664**	**6.292**
3 mm (25%)	Extent (mm)	2.987	3.711	3.179
	Error (mm)	0.013	0.711	0.179
	Error %	**0.450**	**23.712**	**6.562**
4 mm (33%)	Extent (mm)	3.974	4.861	4.250
	Error (mm)	0.026	0.861	0.250
	Error %	**0.652**	**21.518**	**6.245**
6 mm (50%)	Extent (mm)	6.021	7.265	6.304
	Error (mm)	0.021	1.265	0.304
	Error %	**0.348**	**21.092**	**5.060**
8 mm (66%)	Extent (mm)	7.981	9.548	8.342
	Error (mm)	0.019	1.548	0.342
	Error %	**0.236**	**19.353**	**4.272**
10 mm (83%)	Extent (mm)	10.047	11.912	10.422
	Error (mm)	0.047	1.912	0.422
	Error %	**0.047**	**19.118**	**4.219**
P-value (Error % versus Laplace)			$< 10^{-4}$	$< 10^{-4}$
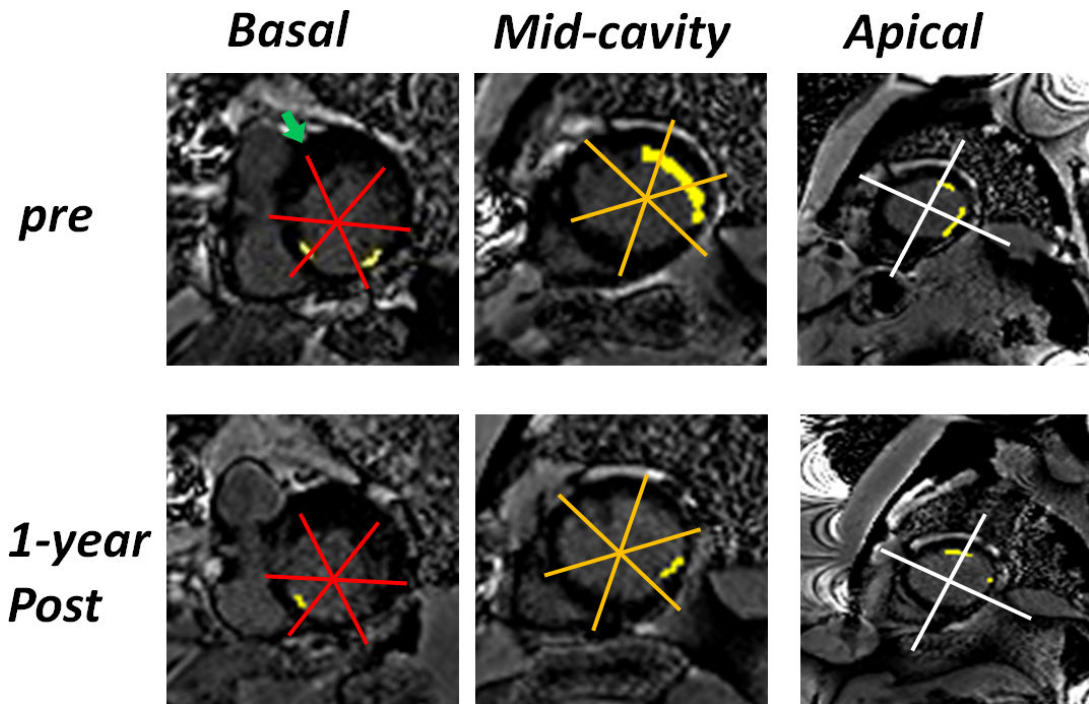
FIGURE 50: Changes in the injured myocardium, processed using the MGRF method, for a representative patient , one year after treatment.

E. DISCUSSION

The overall motivation of this work is that while qualitative assessment of the extent of damaged myocardial tissues is often adequate for routine clinical applications, efficient and accurate quantitative estimation is desirable for research, and to help elucidate mechanisms (e.g. in testing new therapies). Current methods based on heuristic or user-selected thresholds do not account for the textures of the segmented pixels, and, further most of them require user interaction. Therefore, a fully automated quantification of the myocardial viability may represent an advance.

TABLE 7: The extracted two parameters for myocardium viability quantification (i.e., P_{area} and P_{trans}) for one patient over one year treatment.

Segment	P_{area} Pre	P_{area} Post	P_{trans} Pre	P_{trans} Post
# 1	0.0	0.0	0.0	0.0
# 2	0.0	0.0	0.0	0.0
# 3	2.4	2.2	2.0	1.4
# 4	6.4	4.3	6.2	2.9
# 5	0.0	0.0	0.0	0.0
# 6	0.0	0.0	0.0	0.0
# 7	0.0	2.7	0.0	0.3
# 8	0.0	0.0	0.0	0.0
# 9	2.2	0.0	0.8	0.0
# 10	4.6	4.7	3.8	2.7
# 11	27.4	12.8	20.3	10.5
# 12	19.1	2.6	10.1	1.3
# 13	5.8	0.0	2.7	0.0
# 14	0.9	1.2	0.2	0.03
# 15	9.0	2.4	9.0	2.5
# 16	15.9	0.0	6.9	0.0
# 17	0.0	0.0	0.0	0.0
Overall	4.5	2.4	3.1	1.3

1. Pathological Tissue Identification

The proposed framework presents a powerful new approach for identifying the pathological tissue based on a joint MGRF model of the pathological (object) and healthy (background) tissue. In addition to a more accurate selection of an

TABLE 8: Summary of the overall extracted two parameters for myocardium viability quantification for all datasets enrolled in this study (i.e., 14 datasets from six patients) after six months (post 1) and one year (post 2) treatment.

Subject	P_{area}			P_{trans}		
	Pre	Post 1	Post 2	Pre	Post 1	Post 2
# 1	6.5	5.2	2.0	5.3	3.6	1.3
# 2	18.4	14.4	14.1	14.8	11.3	9.7
# 3	4.5	2.4	–	3.1	1.3	–
# 4	11	8.6	–	5.0	3.8	–
# 5	2.1	1.1	–	0.8	0.5	–
# 6	10.9	9.2	–	3.6	3.5	–
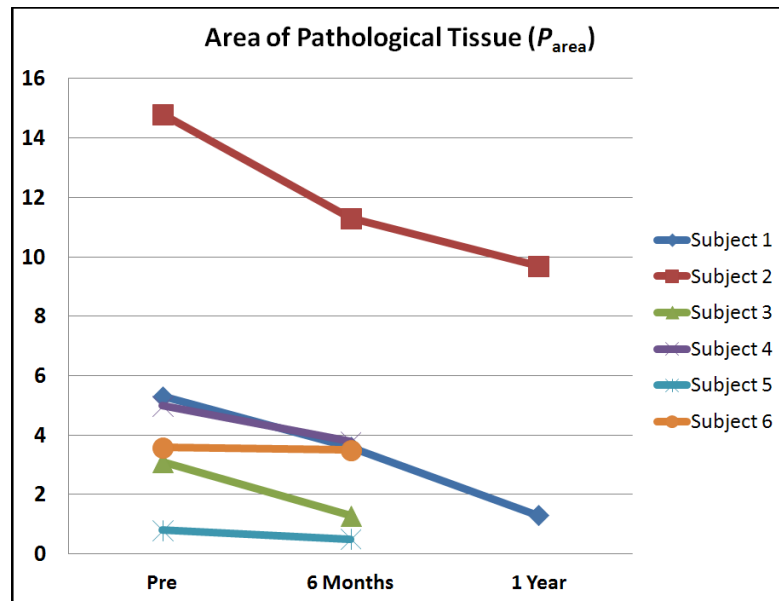
FIGURE 51: Summary of overall P_{area} for six patients before treatment (pre), after six months, and after one year treatment.
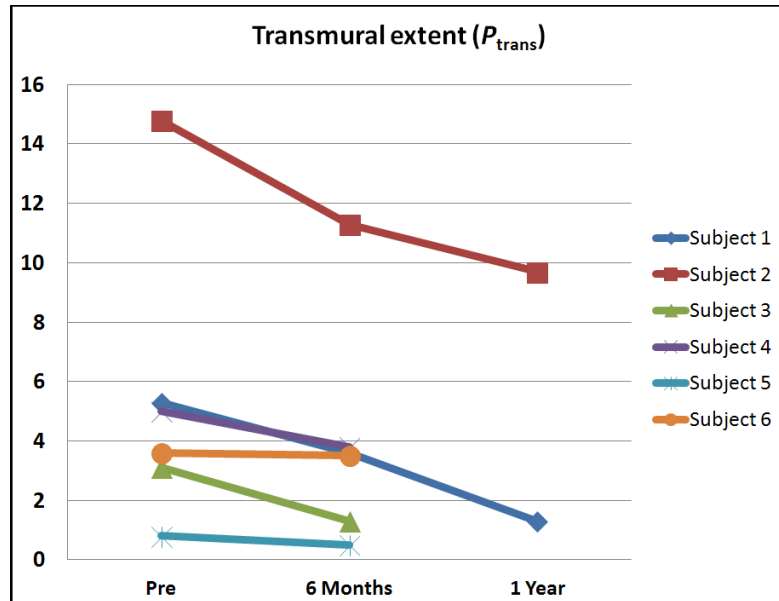
FIGURE 52: Summary of overall $P_{\texttt{trans}}$ for six patients before treatment (pre), after six months, and after one year treatment.

intensity threshold to separate the pathological and normal tissues, it accounts for the textures of the segmented pixel groups via the spatial interaction between the neighboring pixels. The MGRF model effectively discards noisy pixels, and results in a more smooth and connected segmentation. In this study, DSC analysis documented good interobserver agreement in the ability of the MGRF method to correspond to the GT (see Table 5). Also, as shown in Table 5, the proposed framework outperforms the standard 2σ- and 3σ-threshold based techniques, as evidenced by DSC analysis. In addition, there is a good agreement with GT for computing clinical quantities such as infarct volumes, as documented using the Bland-Altman statistic (see Figure 49).

2.   Transmural Evaluation

Two myocardial viability metrics were explored; the percentage area of pathological tissue, and the transmural extent that have been well documented to predict patient outcomes [124]. The seminal study of Kim et. al [124] has established

pathophysiologically meaningful ranges of transmural extent of infarcts, namely transmurality of less than 25% (essentially clinically small infarct) and more than 50% (clinically large infarct). It would appear that it is for infarcts of intermediate extent, in the 25% to 50% transmural extent range, for which improved characterization and better understanding of mechanisms would be of greatest benefit. In this regard, Table 6 shows that the percentage error for the radial and centerline methods manifest an approximate decreasing monotonic function as infarct transmural extent increases. For the proposed Laplace method, the behavior departs from monotonicity. While largest corresponding to the smallest transmural infarct decreases considerably, but remains approximately flat, for intermediate and large extent infracts. This behavior is explained, at least in part, by the fact that the absolute error is small (approximately less than 0.05 mm) for all values examined, and thus is of importance mainly for the small transmural infarcts. Thus the Laplace method has a superior operating characteristic in the range of values corresponding to the intermediate size infracts, compared to the radial or centerline methods.

In terms of practicality of computations, the present Matlab implementation using an Intel quad-core processor (3.2GHz each), with 16 GB of memory, and a 1 TB hard drive with RAID technology required approximately three minutes for identifying pathological tissue in a dataset encompassing 12 cross-sections, and less than one minute for computing the two quantification metrics for all the segments of the myocardial 17-segment model. The processing time on a typical desktop with a dual-core processor (2.1 GHz each), and 4 GB of memory was approximately eight minutes and less than one minute, for identifying pathological tissue and estimating the two quantification metrics, respectively. By implementing the proposed algorithms in the C/C++/C sharp programming environment, this time may be considerably reduced. The present analysis is explored to be extended from 2D images to 3D considerations, especially as relates to implementation of a 3-D MGRF [131].

F. SUMMARY

A fully-automated framework for quantification of myocardial viability is proposed. The framework presents a powerful approach for segmenting the pathological tissue from CE-CMR images. The approach takes into account the spatial interaction between the myocardium pixels to ensure the homogeneity of the segmented tissue. In addition, the proposed framework provides a method to accurately estimate the transmural extent of the pathological tissues in the LV wall and overcome the inconsistencies of the traditional estimation method. The estimated myocardial viability quantification parameters allow for both diagnosis and monitoring the patients. Phantom validation and experiments with CE-CMR images and manually segmented expert delineations confirm the robustness and the accuracy of the proposed approach. The work presented in this chapter has been published in the IEEE international symposium on biomedical imaging (ISBI) [132] and the international journal of cardiovascular imaging [127].

CHAPTER V

A NOVEL FRAMEWORK FOR ESTIMATING FUNCTIONAL STRAIN FROM CARDIAC CINE MRI

Functional strain is one of the important quantification metrics of the cardiac status. Local cardiac diseases (such as coronary atherosclerosis) and global conditions (such as heart failure and diabetes) result in wall dysfunction that manifests on strain slopes during the contraction and expansion phases of the cardiac cycle. Therefore, accurate strain estimation is important for the early detection of these diseases.

In this chapter, a novel method to estimate the strain from cine cardiac cine magnetic resonance imaging (CMRI) is proposed based on tracking the left ventricle (LV) wall geometry. Unlike current methods that depend on the intensity and spatial information to track the wall motion, the proposed method sticks to the geometry of the heart to track its motion. To achieve this goal, a three-step framework is presented. First, the LV wall borders are segmented using a level-set based deformable model guided by a stochastic force derived from a second order Markov-Gibbs random field (MGRF) model that accounts for the object shape and appearance features. Second, the mid-wall of the LV is found by estimating the centerline between the inner and outer segmented LV borders. Finally, a Laplace-based partial deferential equation (PDE) method is used to track the LV wall points over each two successive image frames over the cardiac cycle. The proposed method is the first Laplace-based strain estimation framework that uses Laplace equation to accurately track the myocardium points over the cardiac cycle

in such a way that overcomes noise sources, which come from scanner and heart motion. The proposed method shows the ability to track all the LV wall points and the cardiac motion even at the mid-wall. Moreover, it shows accurate results on simulated phantom images, with predefined point locations of the LV wall through the cardiac cycle. In addition, the same image modality is used (i.e., cine CMRI) to estimate the strain and other performance indexes (e.g., global index), more cor-related and accurate indexes can be obtained. In this chapter, three performance indexes, i.e., peak systolic strain change, systolic strain slope, and diastolic strain slope, are used to follow-up on a given treatment (e.g., stem cell therapy [133], the case study in this work).

A. PROPOSED FRAMEWORK

As shown in Figure 53, the proposed framework for strain estimation con-sists of four main processing steps. First, the LV wall is segmented from the cine CMR images. Second, the mid-wall is determined. Third, the points on the inner, mid-wall, and outer contours of the LV wall are tracked through the cardiac cycle. Finally, the circumferential and radial strains are estimated. This section will detail each of these processing steps.

1. LV Wall Segmentation

In the first step of the proposed framework, a segmentation method of the LV wall is implemented based on a validated geometric (level set-based) deformable model [134–138]. The evolution of the level set is controlled by three features, namely a probabilistic shape prior, the first-order pixel-wise image intensities, and a second-order Potts-MGRF spatial interaction model. These three features are
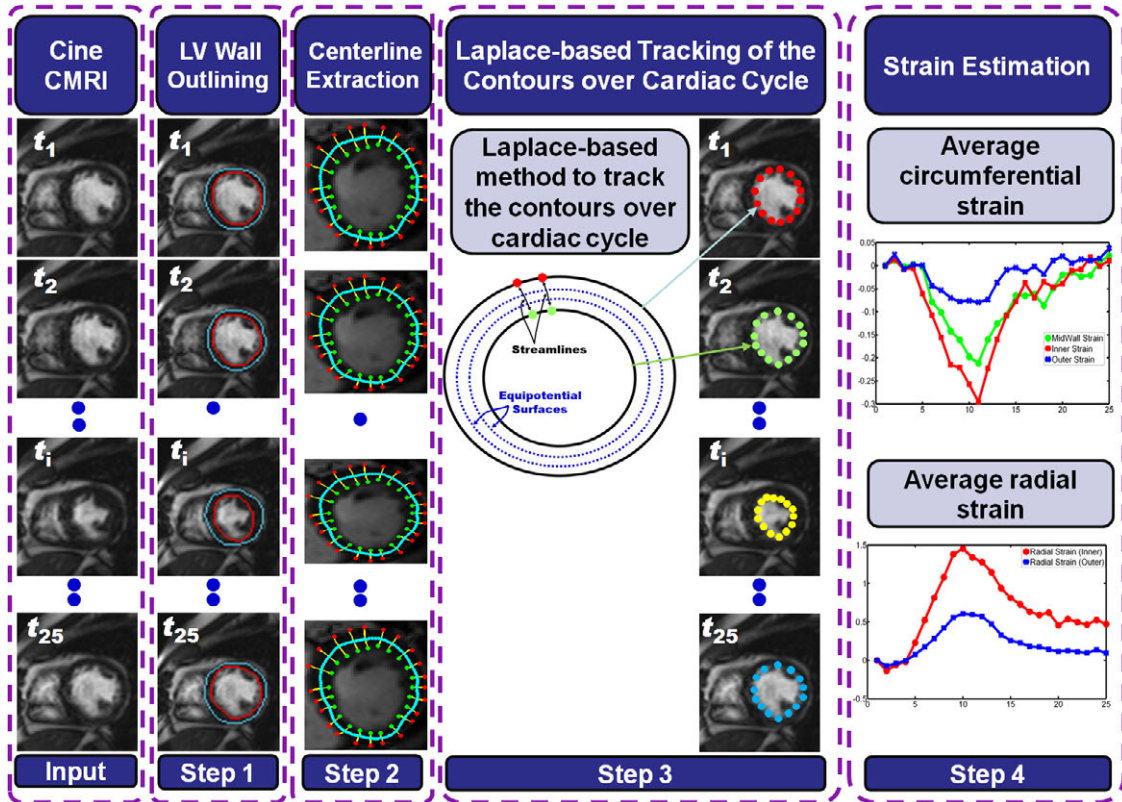
FIGURE 53: Basic processing steps for the proposed framework. The segmentation of the inner, mid- and outer walls of the LV is followed by geometrical tracking to estimate the circumferential and radial strain curves over the cardiac cycle.

used to construct a speed function that is subsequently used to evolve the deformable boundary. For more details on this method and the comparison with other segmentation approaches, please see [134–138].

2. LV Centerline (Midwall) Extraction

To delineate the centerline, a three-step approach is used to extract the midwall. First, the solution of the Laplace equation is found (Equation (10)) between the segmented inner and outer contours of the LV wall in order to get the paired correspondence points. Then, the points located equidistant from the boundary point-pairs are determined using the Euclidian distance. Finally, the mid-wall is

approximated using a closed spline fit for the identified points. This procedure is summarized as an algorithm:

Algorithm 5 Extraction of the Centerline of the Myocardium
---

1. Segment the inner and outer borders of the LV wall from the input cardiac data (see Figure 54(a)).

2. Solve the Laplace equation between the inner and outer borders to find the corresponding point pairs (see Figure 54(b)).

3. Determine the points located equidistant from the boundary point-pairs, estimated using Euclidian distance (see Figure 54(c)).

4. Determine the centerline (i.e., the mid-wall) using a closed spline fit for the identified points (see Figure 54(d)).

| (a) | (b) | (c) | (d) |
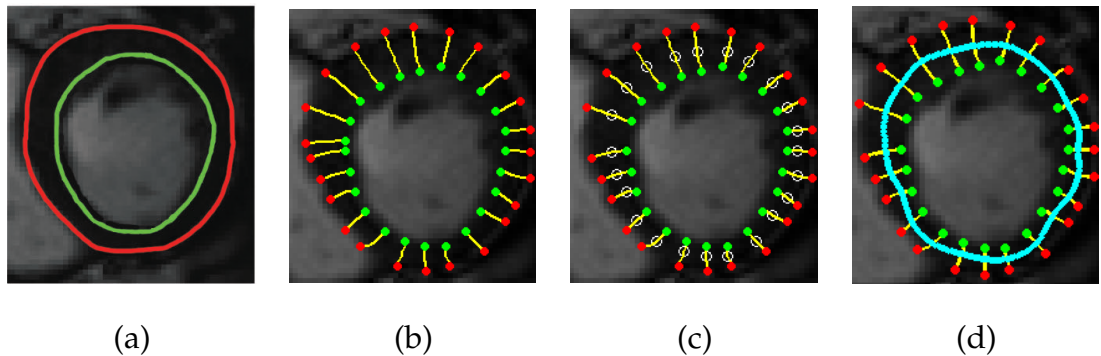
FIGURE 54: Illustration of the centerline extraction: (a) the inner (green) and outer (red) boundaries of the LV wall, (b) streamlines found by solving Laplace equation, (c) the identified centerline points (white open circles), and (d) the extracted centerline (blue).

3. Laplace-based Tracking

In order to estimate the strain function, points along myocardial contours are tracked over the cardiac cycle. A geometrically motivated method is used to determine the matching of myocardial points from time-frame to time-frame by
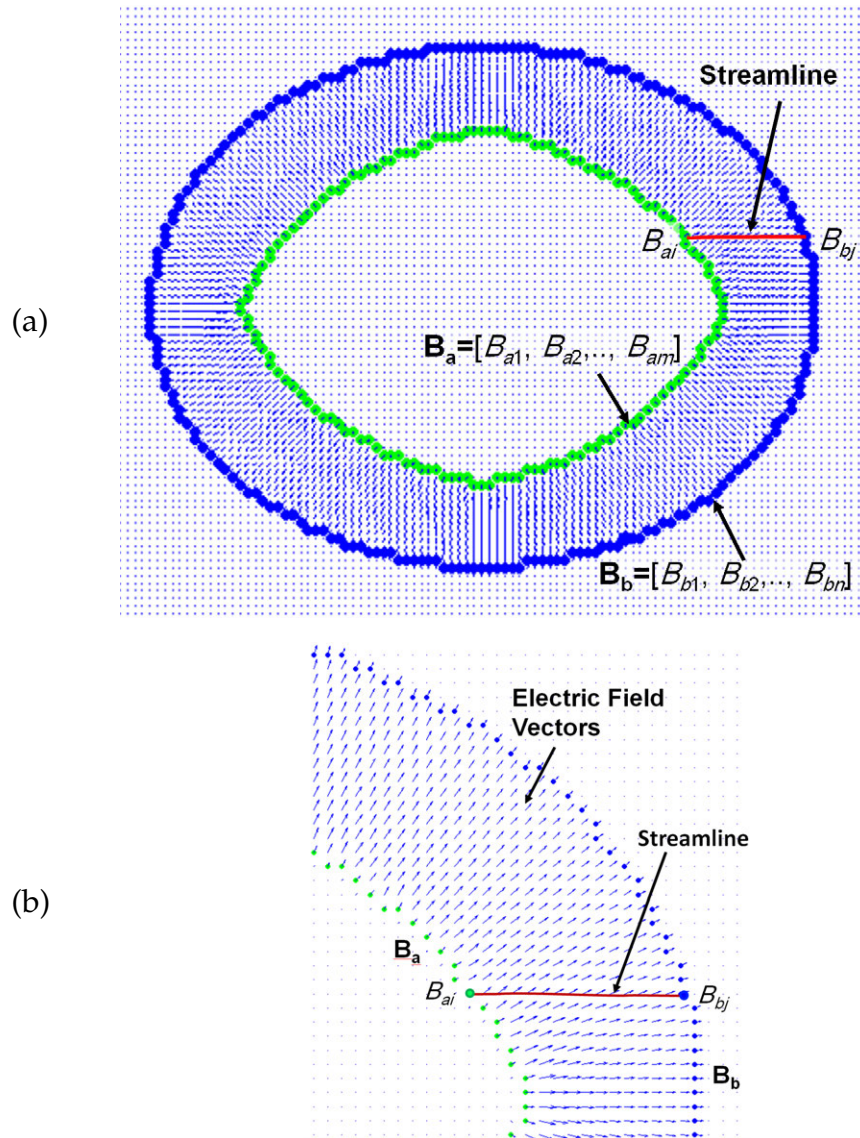
FIGURE 55: Co-allocating point-to-point correspondences by solving the Laplace equation between the different time points of a particular heart wall, for the purpose of tracking that wall over the time series. (a) The geometrical feature of the wall, i.e., the electric filed vectors in the area between two inclosed regions $\mathbf{B}_a$ (in blue) and $\mathbf{B}_b$ (in green), are used to find the point-to-point correspondences. (b) An enlarged section around the indicated streamline.

solving the Laplace equation (Equation (10)) between each two successive contours (see Figure 55). In this fashion, a material point can be tracked from one temporal frame to another. Figure 55 shows an illustration of how the solution of Laplace's

equation is used to determine the corresponding pixel pairs. A potential Υ is found in the interior area enclosed by both surfaces $\mathbf{B}_a$ and $\mathbf{B}_b$ in Figure 55 by solving the Laplace equation such that Υ is maximum at $\mathbf{B}_a$ and minimum at $\mathbf{B}_b$. Then, the electric field vectors (the geometrical features of the wall, the electric filed vectors $E_x = \frac{\partial \Upsilon}{\partial x}$ and $E_y = \frac{\partial \Upsilon}{\partial y}$, in the interior area between $\mathbf{B}_a$ and $\mathbf{B}_b$) are used to find the corresponding pixel pairs as shown in Figure 55. Algorithm 6 summarizes the steps used to track the LV contour on successive temporal frames.

Algorithm 6 Laplace-Based Contour Tracking over the Time Series

---

Step 1. Wall Borders Segmentation:

Segment the LV inner and outer walls from cine CMRI cross section image (e.g., by the approach in [134]).

Step 2. Centerline Estimation:

Find the centerline of the segmented LV wall using Algorithm 5.

Step 3. Laplace Tracking:

For each two successive image frames, track the border points on the inner, mid-, and outer wall edges throughout the cardiac cycle:

(a) Initial condition: set the maximum and minimum (zero) potential at the inner walls of the reference (current) image frame and the target (successive) image frame, respectively.

(b) Solve the Laplace equation to find the potentials between the respective inner wall borders.

(c) Compute the components of the electric field vectors E_x and E_y for the estimated potential in Step 3(b).

(d) Form the streamlines using the electric field vectors in Step 3(c), then track the point-to-point correspondences between respective inner borders.

(e) Repeat Step 3(a) to Step 3(d) for respective mid- and outer wall borders.

---

4. Strain Estimation

The estimation of strain is based on the Lagrangian strain calculation for finitely small displacement. Mathematically, the strain is estimated as [139]:

$$S_L = \begin{pmatrix} \varepsilon_{x_1} & \varepsilon_{x_1 x_2} \\ \varepsilon_{x_2 x_1} & \varepsilon_{x_2} \end{pmatrix} \tag{11}$$

Where ε_{x_1} and ε_{x_2} are the normal strain components (associated with the normal motion to the object borders), i.e., $\varepsilon_{x_1} = \frac{\Delta x_1}{x_1}$ and $\varepsilon_{x_2} = \frac{\Delta x_2}{x_2}$. $\varepsilon_{x_1 x_2}$ and $\varepsilon_{x_1 x_2}$ are the shear strain components (associated with the parallel motion to the object borders), i.e., $\varepsilon_{x_1 x_2} = \frac{\Delta x_1}{x_2}$ and $\varepsilon_{x_2 x_1} = \frac{\Delta x_2}{x_1}$. This work focuses on estimating the normal strain components (i.e., the circumferential (ε_{x_1}) and radial (ε_{x_2}) strains, Figure 56).

(a) (b)
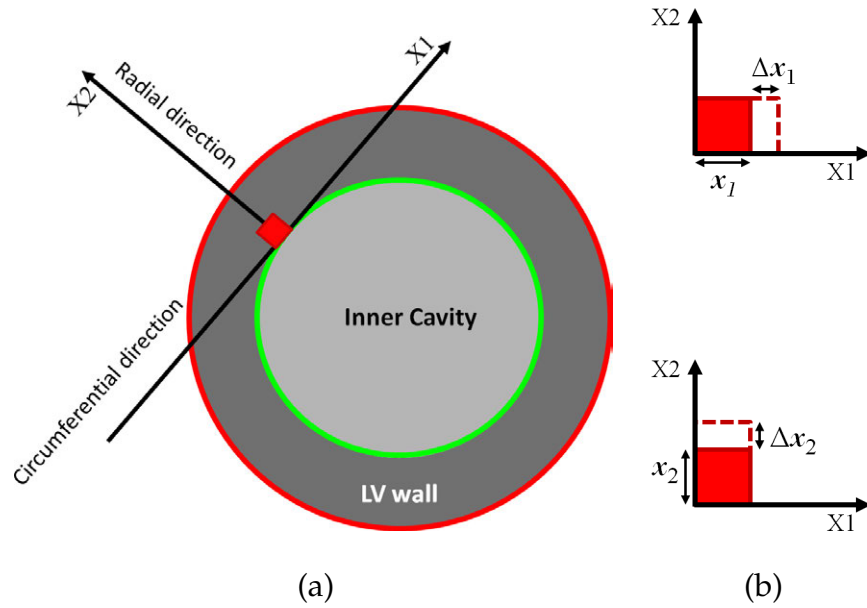
FIGURE 56: Estimation of radial and circumferential strains: (a) schematic illustration of the radial (X_2) and circumferential (X_1) directions for an element (e.g., the red square in the figure) on the LV wall and (b) illustration of the estimation of the normal strain components in the X_1 ($\varepsilon_{x_1} = \frac{\Delta x_1}{x_1}$) and X_2 ($\varepsilon_{x_2} = \frac{\Delta x_2}{x_2}$) directions.

To estimate the radial and circumferential strains through the cardiac cycle from the cine CMRI, Algorithm 7 is followed, which summarizes the processing steps for the proposed framework.

Algorithm 7 Strain Estimation Algorithm

Step 1. Contour Tracking:

Track the inner border, mid-wall, and outer border over the time series images based on the proposed Laplace-based tracking algorithm (Algorithm 6).

Step 2. Strain Estimation:

(a) Estimate the Lagrangian circumferential strains by tracking the fractional change in Euclidean distance between two adjacent reference correspondence points on the same border (i.e., inner, mid-wall, or outer border), see Figure 57.

(b) Estimate the mean radial strain (between inner and mid-wall or between mid-wall and outer wall, where the mid-wall was obtained using Algorithm 5) by tracking the fractional change in Euclidean distance between the two adjacent reference tracked points along the radial direction, see Figure 57.

B.   INDEXING FUNCTIONAL PARAMETERS

1.   Maximal Systolic Strain Change and Strain Slopes

The ability of the proposed framework for the quantification of myocardial wall dysfunction has been initially explored to index clinically meaningful changes. In this chapter, the systolic and diastolic circumferential strain slopes and peak systolic change (see Figure 58) derived from the cine CMRI are used as metrics to follow up treatment using stem cell therapy for the six patients enrolled in this study.
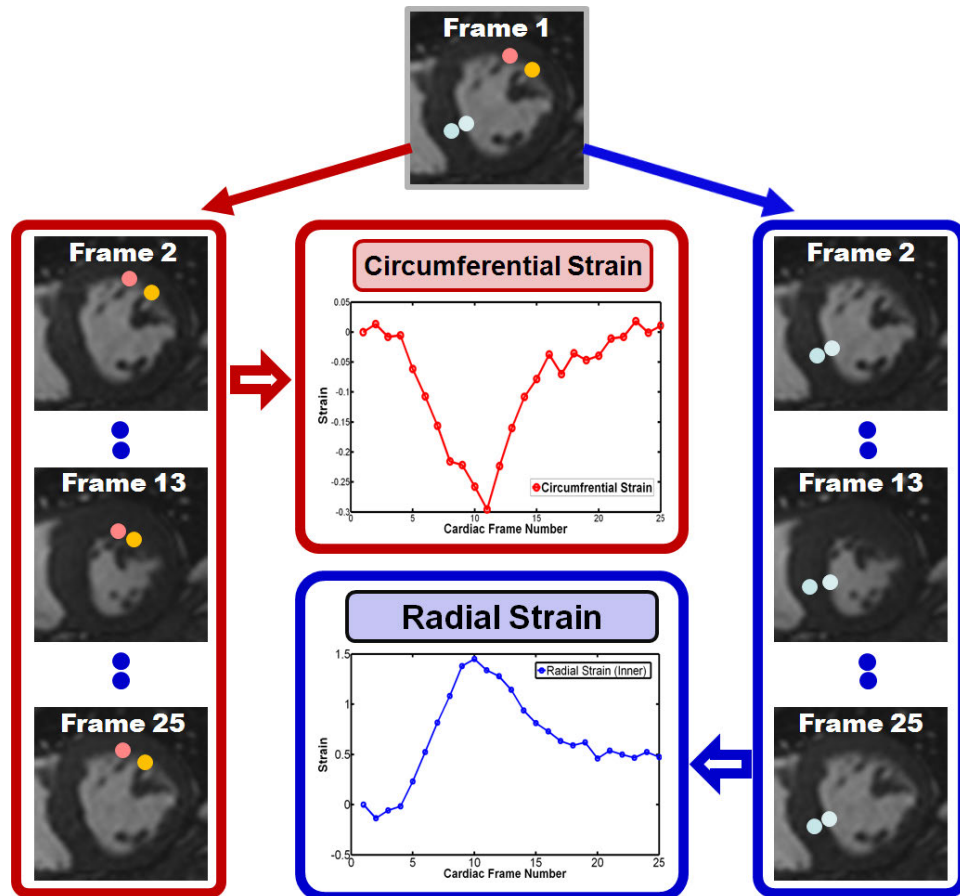
FIGURE 57: Illustration of the tracking process throughout the cardiac cycle to estimate the radial and circumferential strains.

2. Derivation of Maximal Systolic and Diastolic Contractile Function from Full Cardiac Cycle Data

A six-order polynomial fit of full cardiac cycle feature tracking derived strains was empirically used. From the fitted curve, the first and second derivative curves were computed. The systolic and diastolic strain slopes are estimated as the values of the first-order derivative curve points associated with the zero-crossing of the second-order derivative curve (see Figure 59). This combination objectively yielded the timing and magnitude of maximal change in strain (a parameter resembling ejection fraction), as well as the timing and magnitude of occurrence of greatest systolic and diastolic rate of strain (a parameter resembling strain rate).

101
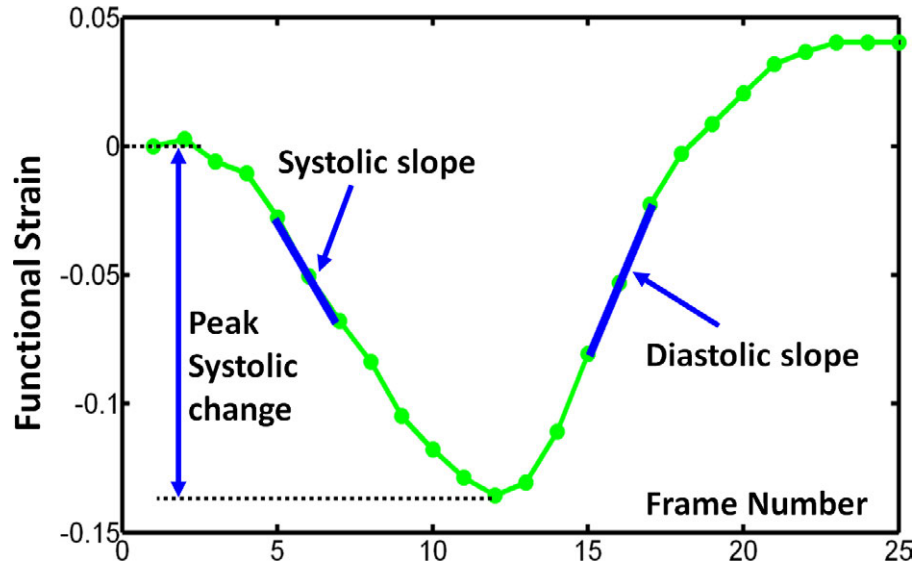
FIGURE 58: Three functional metrics are used to follow up treatment: the systolic and diastolic circumferential strain slopes and peak systolic change derived from the cine CMRI.
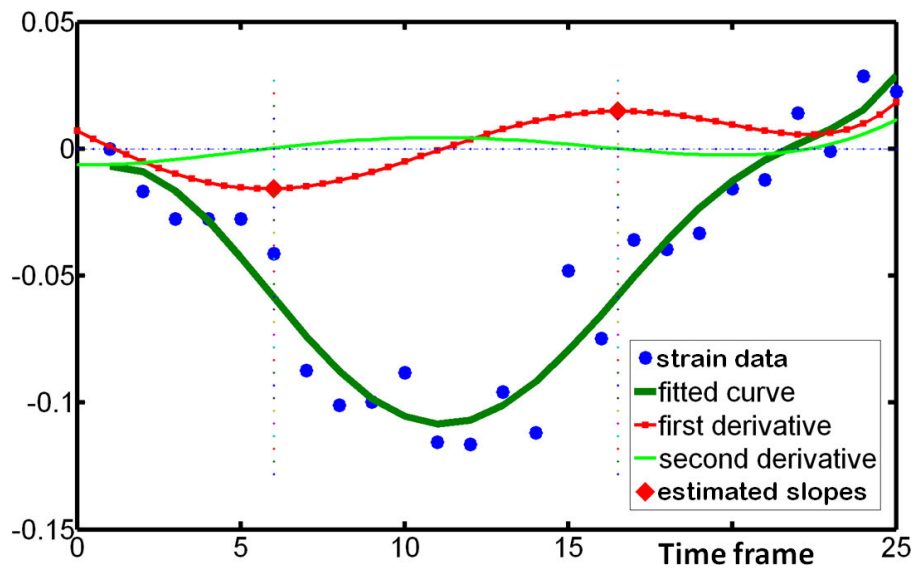
FIGURE 59: Automated estimation of functional strain metrics: a six-order polynomial fit of the strain data is used. From the fitted curve, the first- and second-order derivative curves were computed. The systolic and diastolic strain slopes are estimated as the values of the first-order derivative curve points (red rhombus) associated with the zero-crossing of the second-order derivative curve.

C. METHOD VALIDATION ON SYNTHETIC PHANTOMS

In order to validate the proposed framework for strain estimation, it has been tested using synthetic phantoms. The synthetic phantoms were constructed using a previously validated phantom [140] that generates the geometry of the heart borders over the cardiac cycle based on a descriptive mathematical model that accounts for the physiological features and the LV response during the cardiac cycle. A geometric transformation that covers shearing, rotation, translation, torsion, and compression of the LV is used in the model to describe the LV motion by mapping each location defined in the LV model to a corresponding spatial point at a certain time instant [141, 142]. Using this transformation, an inverse motion map is calculated analytically and is used to establish correspondences between two points at any two time instants. This allows for estimating ground truth (GT) strain values for validating the proposed method. A phantom constructed using this model is simulated to mimic the grey-level distribution of the cine CMRI images using the inverse mapping approach that was proposed in [101, 143] and is exemplified in Figure 60(a).

Effect of graded Rician noise on the synthetic phantom model: In order to evaluate the effect of noise on the accuracy of strain estimation, four corrupted phantoms were constructed with different levels of Rician noise, 0.15, 0.25, 0.35, and 0.45 (see Figure 60(b) and (c)). Note the noise is scaled such that 0 indicates no noise and a value of 1 indicates maximum noise corruption. The effect of the noise is to make determination of the wall boundaries, from which the strain is computed, less reliable. The proposed framework was tested using these four phantoms in order to test the robustness of the proposed strain estimation framework against noise.
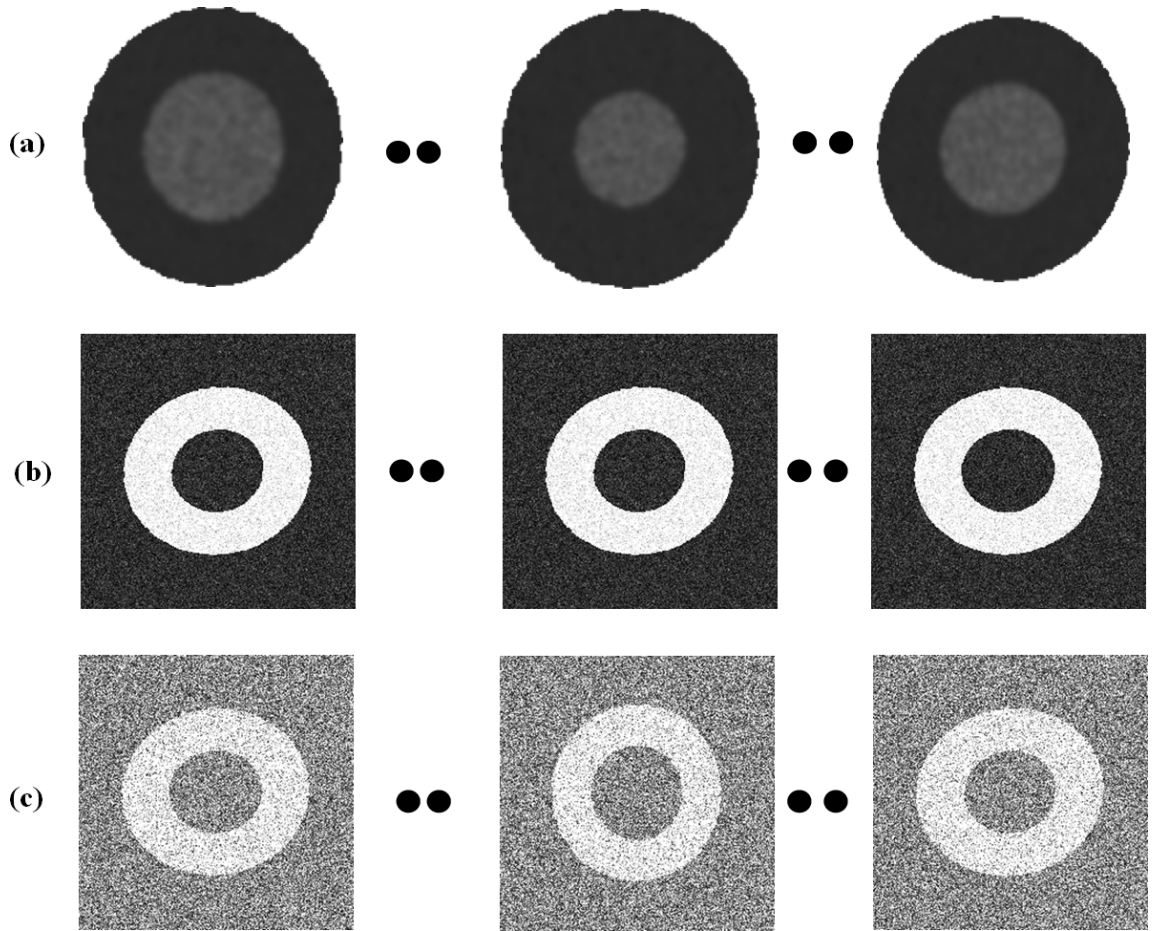
FIGURE 60: (a) Simulated phantom that generates deformation of the heart borders over the cardiac cycle, and corrupted phantoms with two representative levels of Rician noise; 0.15 (b), and 0.45 (c), respectively.

D. EXPERIMENTAL RESULTS

The proposed framework has been tested and validated on both in vivo cine CMRI data and a phantom model. The ability of the proposed framework to index the functional strain parameters was explored on both types of data. This section will present the reported results on phantom data as well as on in-vivo data.

1.   Validation on Synthetic Phantoms

Comparison of the proposed method to the ground truth strain curve: In order to validate the proposed strain estimation method, it is compared with the phantom model constructed on a mathematical model accounting for the physiological features and the LV response during the cardiac cycle (please, see Section V.C). The GT strain values for validating proposed method are estimated based on an analytically estimated inverse motion map that was used to establish correspondences between two points at any two time instants. The visual comparison (Figure 61) shows good agreement between the strain curves of the mid-wall determined using GT points obtained from the deformation of the phantom model and that obtained using the proposed framework. In addition, the mean percentage error between the estimated strain points and the GT points, calculated as the average percentage difference in the strain with respect to the GT, is 8.8%, which indicates good agreement.
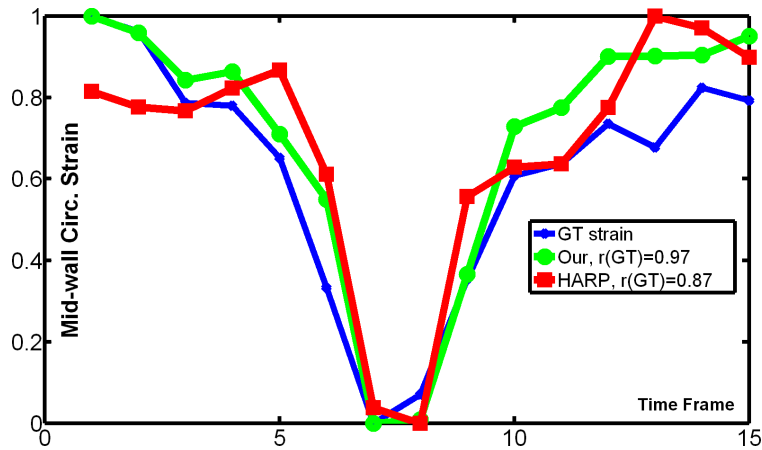
FIGURE 61: Comparison results between the proposed strain estimation and HARP methods with the truth points obtained from the deformation of the phantom model.

To highlight the advantage of the proposed method, the estimated strain parameters using the proposed method on the constructed phantom was compared with the strain parameters using the constructed phantom obtained by the com-

mercial HARP diagnosoft package, version 2.6 (*www.diagnosoft.com*) on a corre-sponding tagged phantom that has the same GT strains and is constructed with the same transformation model used for the proposed method. Figure 61 represents the estimated strains using the proposed method in comparison with the HARP method with respect to the GT strains. The reported correlation coefficients with repect to the GT ($r(\text{GT})$) for the proposed method and HARP method are 0.97 and 0.87, respectively. The reported mean percentage errors for the proposed method and HARP method with respect to the GT are 8.8% and 12.5%, respectively. As reported, the proposed strain estimation method is more close to the GT than the HARP method as evidenced by the higher correlation coefficient and lower mean percentage error values. This highlights the advantage of the proposed method.

Comparison of the proposed method to the ground truth for indexing the functional parameters: In addition to the comparison with the GT strain curve, the framework was tested for indexing functional parameters, i.e., the systolic and diastolic circumferential strain slopes, and the peak systolic change, derived from the cine CMRI. Five trials have been made to estimate the strain using different sets of points (each trial is done with the same points to be tracked). Then, the func-tional parameters are estimated from each trial. The propsoed model agrees with the GT for functional parameter estimation to within approximately 10% (calcu-lated as the range of the parameter values divided by their mean). The statistical t-test for estimating the functional parameters using the proposed feature track-ing method versus the GT for the five repeated trials report p-values of 0.11, 0.18, and 0.06 for indexing the peak systolic change, systolic strain slope, and diastolic strain slope, respectively. This indicates good agreement with the GT for index-ing the functional parameters, as evidenced by p-values greater than 0.05 (which indicates no statistical significance).

Robustness of the strain indexing in the presence of noise: In order to test the robustness of the proposed strain estimation framework against noise, the proposed framework was tested on four corrupted phantoms with different levels of Rician noise, 0.15, 0.25, 0.35, and 0.45 for indexing the functional parameters. As reported in Table 1, the functional parameters were typically within 25% (the range of parameter values divided by their mean) for a wide range of the examined noise values.

TABLE 9: Quantitative functional mid-wall circumferential strain results estimated using the simulated phantoms with different levels of Rician noise, for five repeated trials at each noise level, where the proposed framework is used to estimate the metrics. Note the noise is scaled such that 0 indicates no noise and a value of 1 indicates maximum noise corruption.

Noise Level	Peak Systolic Change %	Systolic strain slope	Diastolic strain slope
Uncorrupted	6.0±0.22	-0.021±0.001	0.028±0.040
0.15	6.0±0.14	-0.020±0.001	0.027±0.003
0.25	5.8±0.17	-0.024±0.001	0.031±0.010
0.35	5.5±0.24	-0.022±0.001	0.025±0.008
0.45	6.1±0.21	-0.023±0.002	0.024±0.004
Range	5.5 to 6.1	-0.020 to -0.024	0.024 to 0.031
(%)	(10.3 %)	(18.0 %)	(25 %)

Ability to track the movement and rotation of the heart: In order to get accurate estimation of the strain, the method should have the ability to track the LV wall movements within the cardiac cycle. Since the Laplace-based feature tracking method is a step-wise method, i.e., tracks the contour from one frame to the next (see step 3 in Algorithm 6), the movement of the LV wall can be tracked. Figure 62 visually shows the tracking of the LV inner contour points using the propsoed

method from end-diastolic to end-systolic over a representative phantom model that involves rotation. In addition, the mean distance error between the estimated points and the GT points, calculated as the average percentage difference in the Euclidian distance between the estimated points and the GT, is 3.26 mm, which is relatively small with respect to the LV wall dimensions. These results show the ability of the proposed method to accurately track the LV points even in the existence of high deformation and rotation of the LV wall during the cardiac cycle.
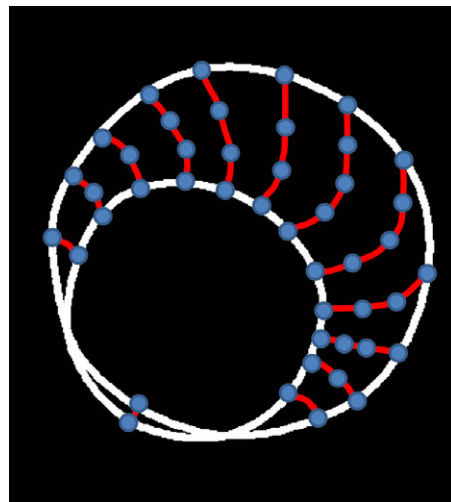
FIGURE 62: Tracking the inner LV contour points (blue points) using the proposed Laplace-based feature tracking algorithm from end-diastolic (the large contour) to end-systolic (the small contour) for a representative phantom model, showing the ability of the proposed method to track the rotation of the LV wall.

2. Experiments on In vivo Data

CMRI protocol: The proposed framework has been tested on 14 independent cine CMR data sets, obtained from six infarction patients. These patients had suffered chronic heart attacks (at least four months prior) with clinically documented ejection fraction dysfunction. Subsequently, they underwent an experimental myocardial regeneration therapy as part of an institutionally approved

trial [133]. Short-axis images were obtained using a 1.5 T Espree system, Siemens Medical Solutions, USA Inc., with phased array wrap-around reception coils. Breath-hold cine imaging was done using segmented True-FISP contrast. Typical parameters were: repetition time (TR): 4.16 ms; echo time (TE): 1.5 ms; flip angle: 80°, 1 average; k-space lines per segment: 12; in-plane resolution: 1.4×3.1 mm^2; and slice thickness: 8 mm. Typical 25 temporal image frames were obtained for each slice.

Physiology of the strain dependence: To estimate the strain and construct strain curves, Algorithm 7 is applied. Figures 63(a) and (b) illustrate the circumferential and radial strain results for one patient. As expected, the global ventricular volume curve of this patient is correlated with the estimated circumferential strain, whereas it is inversely correlated with the estimated radial strain, as shown in Figure 63(c). This is clearly manifested with the synchronization between the timing of occurrence of end systole of the ventricular volume curve and the timing of peak circumferential and radial strains. These results emphasize the correctness of the proposed strain estimation method.

Clinically meaningful effects: The ability of the proposed framework for the detection and quantification of damaged tissue has been initially explored to index clinically meaningful changes. Table 10 illustrates the potential of using these metrics to document changes with treatment that were consistent with improvements in patient status, as documented by clinical indexes. This lends encouragement for the proposed framework to detect and quantify meaningful effects in treatment and physiological studies.
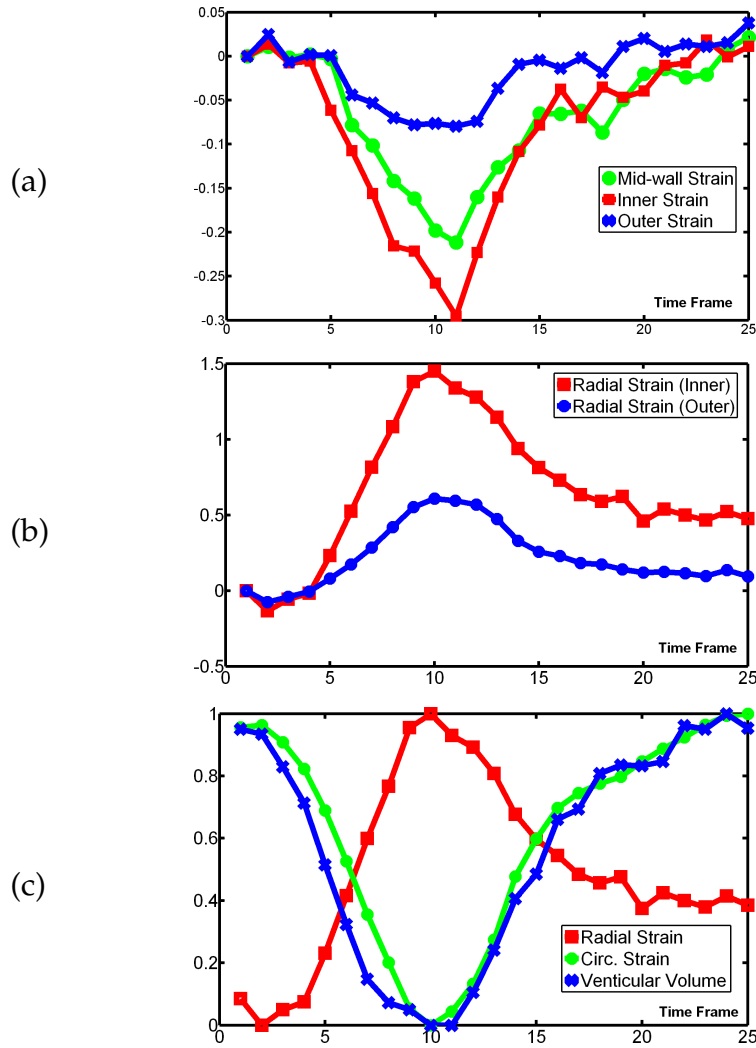
FIGURE 63: (a) Circumferential strains estimated at the inner wall, mid-wall and outer wall of the LV of one patient, plotted over the cardiac cycle. (b) Radial strains estimated between the inner and mid-wall (blue), and between the outer and mid-walls (red) of the LV of the same patient. (c) Relation between the average inner to mid-wall radial strain (solid circle), mid-wall circumferential strain (solid square), and the global ventricular volume curve, using normalized values between 0 and 1 for comparison. Note that the timing of the smallest cavity volume is coincident with peak radial strain and peak circumferential strain. Note also the peak systolic and peak diastolic slopes of the strain curve occur at the same optimum with respect to the timing of the ventricular volume curve.

TABLE 10: Results of the metrics that are used to follow up treatment using stem cell therapy for 14 datasets (from 6 patients) after 6 months (post 1) and one year (post 2) treatment. Larger peak systolic change and absolute slope values indicate an enhancement in the myocardial wall function.

	Peak Systolic Change			Systolic Strain Slope			Diastolic Strain Slope		
Subject	Pre	Post 1	Post 2	Pre	Post 1	Post 2	Pre	Post 1	Post 2
# 1	9.2 %	13.8 %	17.5 %	-0.010	-0.011	-0.018	0.014	0.017	0.020
# 2	2.8 %	5.2 %	7.2 %	-0.011	-0.012	-0.021	0.014	0.023	0.011
# 3	8.2%	9.9 %	–	-0.017	-0.020	–	0.021	0.015	–
# 4	13.6%	17.4 %	–	-0.021	-0.031	–	0.029	0.041	–
# 5	10.1%	22.4%	–	-0.023	-0.040	–	0.026	0.027	–
# 6	9.8%	10.6%	–	-0.015	-0.014	–	0.012	0.014	–

E. DISCUSSION

This chapter investigated the utility of conventional cine data to estimate the functional strain parameters at the inner, mid-, and outer LV walls for the characterization of myocardial function. Unlike traditional texture-based tracking methods, the proposed method is based on the geometrical features of the inner, mid- and outer walls of the LV. The proposed method showed the ability to track the movement and rotation of the heart. Hence, overcoming any noise that comes from heart motion and permitting accurate strain estimation.

1. Comparison of the Proposed Method to the Ground Truth and Other Methods

The mean percentage error between the strain points estimated using the proposed method and the GT points, obtained from the deformation of the phantom model, is 8.8%. This indicates that the accuracy for measuring the strain is

above 90%, which is promising. In addition, the proposed model agrees with the GT for indexing functional metrics to within approximately 10%. The statistical t-test between the proposed method versus the GT for five repeated trials report p-values of 0.111, 0.177, and 0.063 for indexing the peak systolic change, systolic strain slope, and diastolic strain slope, respectively. This indicates good agreement with the GT for indexing the functional parameters, as evidenced by p-values greater than 0.05 (which indicate no statistical significance). In addition, the proposed strain estimation method is more close to the GT than the HARP method as evidenced by the higher correlation coefficient and lower mean percentage error values with respect to the GT. The reason behind the superiority of the proposed method over the HARP technique is that the HARP method introduces large errors in the case of high rate motion. This problem is partially solved in the proposed method by tracking the heart motion based on the geometrical features of the inner, mid- and outer walls of the LV. This is documented with the small reported distance error between the tracked points using the propsoed model and the GT points in the case of heart motion (see Figure 62).

2. Robustness of the Strain Indexing Against Noise

For the simulated phantom data with respect to noise using the propsoed Laplace tracking method, the functional parameters were typically within 25% for a wide range of noise values examined. This is within the variability of functional parameters that can be observed related to breath-hold irreproducibility [144].

3. Reasonableness of the Physiological Indexing

For sample real patient data, a monotonic dependence of strain across the myocardial wall was obtained, with the greatest strain observed in the inner wall for both circumferential and radial strains [145]. In addition, the expected full cardiac cycle temporal strain dependence of circumferential strain versus radial strain was observed. Further, when comparing circumferential and radial strains to physiological events as plotted using a ventricular volume curve derived from cine data, the timing of physiological cardiac events–smallest cavity volume (end-systole), fastest systolic emptying (contraction), and fastest diastolic filling (relaxation)–were found to be temporally coincident. This would be expected since they characterize corresponding physiological events. In addition, the ability of functional indexes derived using the proposed Laplace-based tracking method is documented to index clinically meaningful change on sample clinical data.

4. Limitations

The proposed framework estimate the functional strain parameters from 3D (2D + time) sequences of thick-slice cine CMRI data. Future work includes the application of the algorithm on 4D (3D+time) thin-slice data in order to fully estimate all the strain components in 3D. This will be achieved by extending the proposed Laplace-based method in 3D in order to find the potential field between 3D surfaces.

F. Summary

A novel framework for strain estimation from cine CMRI is presented. The LV wall points are tracked throughout the cardiac cycle by applying a PDE method to track the LV points by solving the Laplace equation between the LV wall borders. The main advantage of the proposed tracking method over traditional texture-based methods is its ability to track the movement and rotation of the LV wall based on tracking the geometric features of the inner, mid-, and outer walls of the LV. This overcomes noise sources that come from scanner and heart motion. In addition, the strain estimation method shows accurate validation results on simulated phantoms with predefined point locations of the LV wall through the cardiac cycle. Moreover, the proposed method will allow an accurately estimate of the correlation coefficients between the strain index and other performance indexes derived from cine images, such as global (e.g., ejection fraction) and local (e.g., wall thickening) indexes. This will avoid the inter-slice variability problem since all indexes will be derived from cine CMRI data. The work presented in this chapter has been published in the international conference of image processing [146] and the international symposium on computational models for life science [147]. Future work includes extending this study to 4D (3D+time) and investigating the type of correlation between these indexes.

CHAPTER VI

MRI FINDINGS FOR DYSLEXIA: A SURVEY

Developmental dyslexia is a brain disorder that is associated with a disability to read, which affects both the behavior and the learning abilities of children. Recent advances in MRI techniques have enabled imaging of different brain structures and correlating the results to clinical findings. The goal of this chapter is to cover these imaging studies in order to provide a better understanding of dyslexia and its associated brain abnormalities. In addition, this survey covers the noninvasive MRI-based diagnostics methods that can offer early detection of dyslexia. This chapter focuses on three MRI techniques: structural MRI, functional MRI (fMRI), and diffusion tensor imaging (DTI). Structural MRI reveals dyslexia-associated volumetric and shape-based abnormalities in different brain structures (e.g., reduced grey matter volumes, decreased cerebral white matter gyrifications , increased corpus callosum (CC) size, and abnormal asymmetry of the cerebellum and planum temporale structures). fMRI reports abnormal activation patterns in dyslexia during reading operations (e.g., aggregated studies observed under-activations in the left hemisphere fusiform and supramarginal gyri and over-activation in the left cerebellum in dyslexic subjects compared with controls). Finally, DTI reveals abnormal orientations in areas within the white matter micro-structures of dyslexic brains (e.g., aggregated studies reported a reduction of the fraction anisotropy (FA) values in bilateral areas within the white matter). Herein, all of these MRI findings will be discussed focusing on various aspects of implemented methodologies, testing databases, as well as the reported findings.

Finally, the chapter addresses the correlation between the MRI findings in the literature, various aspects of research challenges, and future trends in this active research field.

A. INTRODUCTION

Developmental brain disorders are among the most interesting and challenging research areas in modern neuroscience. Dyslexia is an extremely complicated example of such a disorder that affects anywhere between 4% to 10% of the general population [148]. Dyslexia is characterized by the failure to develop age-appropriate reading skills in spite of a normal intelligence level and adequate reading instructions [149]. Perceptual problems in dyslexia seemingly result from an inability to retrieve correct verbal labels for phonemes [150], which makes it difficult to deconstruct words into constituent sounds and match written words to spoken language. Educational interventions that teach phoneme awareness have shown better results in dealing with reading disorders than other programs [151]. Although considerable progress has been made towards the identification of effective instructional practices, the knowledge regarding the underlying pathology and pathophysiological mechanisms remains fragmentary.

Case studies in dyslexia have suggested various flaws in the circuitry of the visual cortex and connectivity/synchronicity between different brain regions [152]. Research studies suggest that the alteration in connectivity between brain regions is basically derived from microscopic abnormalities in the minicolumn's basic ontogenetic pattern [153]. Minicolumns are the basic unit of function of the cerebral cortex each brain having hundreds of millions of them [154]. The areal expansion of the cerebral cortex across species (encephalization) presumably occurs through an increased number of minicolumns. Therefore, it is not surprising that

some of the gross changes observed in putative minicolumnopathies include variations in brain volume, gyrification, and size of the CC. Recent neuropathological case reports suggest the presence of a minicolumnopathy in dyslexia [155, 156]. Consistent with this observation, some structural MRI-based studies have shown that dyslexic patients have a reduced brain volume, decreased gyrification, and increased CC volume relative to total brain size [11]. This survey expands on these microscopic findings by describing reported MRI findings for dyslexia. The review aims to improve the understanding of possible causal abnormalities, their topography, and proposed MRI-based diagnostics methods.

Multiple studies have identified different brain structures (e.g., grey matter, white matter, cerebellum, planum temporale, and CC structures) involved in abnormal neural development associated with dyslexia [157] (see Figure 64). A general MRI-based dyslexia framework to detect such abnormalities is illustrated in Figure 65. The input of the framework is the MRI data (e.g., structural MRI, fMRI, or DTI). The first step of the framework is to remove the noise and enhance the images using image filtering and noise removal techniques. Second, the brain structure is selected either manually or using a specified segmentation technique for the target brain structure. Finally, different metrics can be derived from the selected brain structure to indicate an abnormality associated with dyslexia. An abnormality is identified if a candidate metric showed a significant difference between its reported values tested on two sample groups of normal and dyslexic subjects. The goal of this survey is to address these abnormalities and present the different metrics used to describe them using MRI techniques.

These brain abnormalities can be reported using different MRI techniques (e.g., structural MRI, fMRI, or DTI). Using structural MRI, the brain abnormalities can be described using different volumetric and shape metrics. For example, MRI studies reported altered brain volumes in the brain of dyslexic individuals found
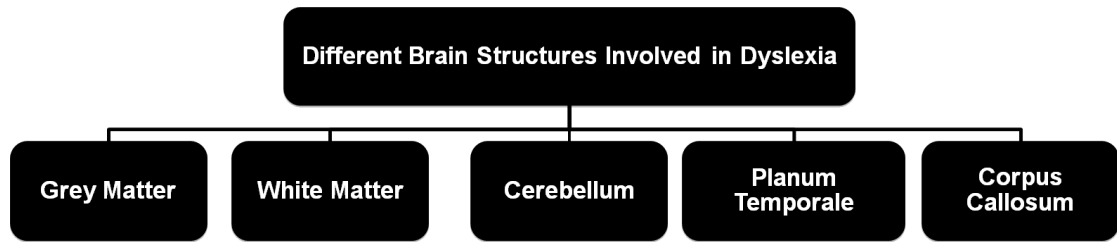
FIGURE 64: Different brain structures that are involved in dyslexia.
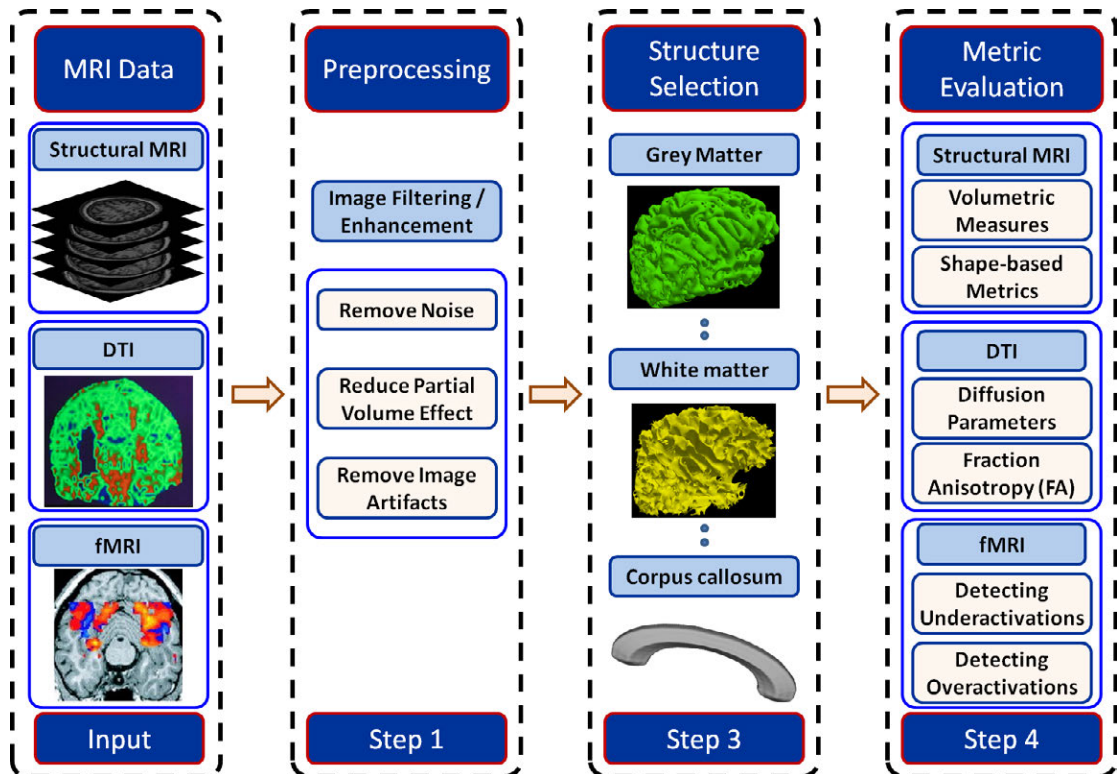
FIGURE 65: A general framework for analyzing MRI images in order to detect brain abnormalities associated with dyslexia.

on specific regions of the brain (e.g., in the grey matter, white matter, cerebellum, and CC structures). In addition, shape metrics have been derived from structural MRI, such as the reported abnormality in CC thickness and asymmetry of the cerebellum in dyslexic subjects with respect to controls. fMRI can provide measures for the under- or over-activations in dyslexic subjects compared with controls, when stimulated with different reading operations. Using DTI, the diffusion parameters, such as the fraction anisotropy (FA), are candidate metrics to describe the abnor-

malities associated with dyslexia. Figure 66 summarizes the different findings that can be obtained using different MRI techniques such as structural MRI, fMRI, and DTI. The following section will discuss all these findings including the various aspects of implemented methodologies and testing databases.
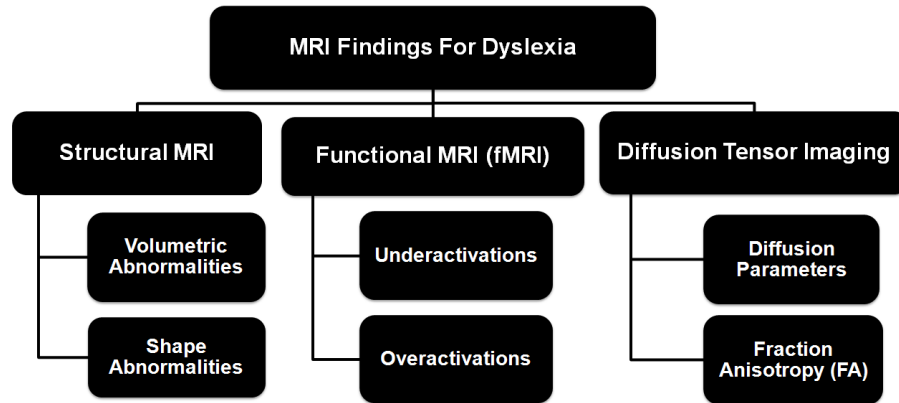
FIGURE 66: A taxonomy of the different findings that can be obtained using the different MRI techniques such as structural MRI, fMRI, and DTI.

B. STRUCTURAL MRI

Magnetic resonance imaging (MRI) is a medical imaging modality that is based on the principles of nuclear magnetic resonance (NMR) spectroscopy [12]. The main strength of MRI is that it offers the best soft tissue contrast among all image modalities. This makes MRI the most powerful noninvasive tool for clinical diagnosis and a very useful modality in imaging the brain anatomy [13]. Due to the structural MRI ability to image brain soft tissues with high contrast, it has been used extensively to reveal dyslexia-associated abnormalities in different brain structures as well as to derive volumetric and shape metrics to describe these abnormalities [158]. Below, the structural MRI findings for dyslexia are described for each brain structure that has been investigated, i.e., the grey matter, white matter, cerebellum, planum temporale, and CC (see Figure 67).
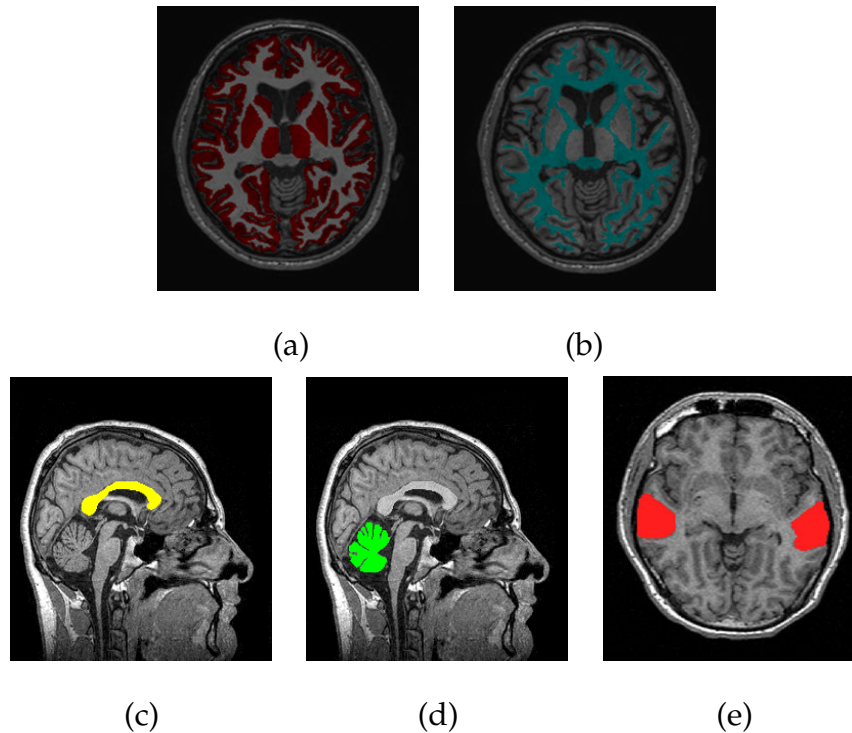
FIGURE 67: Different brain structures that are involved in dyslexia as appears in structural MRI: (a) grey matter (delineated in dark-red), (b) white matter (delineated in dark-cyan), (c) corpus callosum (delineated in yellow) , (d) cerebellum (delineated in green), and (e) Planum temporale (delineated in red).

1. The Grey Matter

The cerebral cortex or grey matter contains the nerve cells responsible for routing sensory and/or motor stimuli through the central nervous system (see Figure 68). One hypothesis suggests that the grey matter density in specific regions (e.g., reading areas) of the brains of dyslexic individuals is altered. Following this hypothesis, altered brain regions were identified with a voxel-based morphometry (VBM) [159–168] using software packages, such as BrainImage software [159] and statistical parametric mapping (SPM) software [160, 161, 163–168]. The idea behind the VBM approach is to normalize the brain stereotactically to a common space (e.g., an atlas with predefined anatomic subregions) and use voxel statistics to identify anatomical brain regions of altered grey matter density. Using

the VBM analysis, altered grey matter density was identified in the left temporal lobes [159], left and right fusiform gyrus, bilateral anterior cerebellum, and right supramarginal gyrus [160]. Brown et al. [161] reported decreased volumes of the gray matter in the left temporal lobe, bilaterally in the temporoparietooccipital juncture, frontal lobe, caudate, thalamus, and cerebellum of dyslexic brains. Brambati et al. [162] reported focal abnormalities in gray matter volume bilaterally in the planum temporale, inferior temporal cortex, and cerebellar nuclei. Silani et al. [163] identified altered grey and white matter density in the left middle and inferior temporal gyri and the left arcuate fasciculus. Eckert et al. [164] identified gray matter volume differences in the left and right lingual gyrus, left inferior parietal lobule, and cerebellum. Vinckenbosch et al. [165] reported reduced gray matter volumes in both temporal lobes of dyslexic brains, particularly in the middle and inferior temporal gyri of the left temporal lobe. In addition, the study reported increased gray matter density bilaterally in the precentral gyri. Hoeft et al. [166] reported reduced gray matter volume in the left parietal region in dyslexic brains. Steinbrink et al. [168] reported reduced gray matter volumes in the superior temporal gyrus of both hemispheres of dyslexic brains. Pernet et al. [169] reported alterations of the grey matter in the left superior temporal gyrus, occipital-temporal cortices, and lateral/medial cerebellum.

Schultz et al. [170] emphasized the role of sex and age when analyzing the brain abnormalities associated with dyslexia. Following this way of thinking, Evans et al. [171] investigated grey matter abnormalities associated with sex and age in dyslexia. They used a VBM approach to study the grey matter differences between four groups: 28 men (mean age 43 years), 26 women (mean age 34 years), 30 boys (mean age10 years), and 34 girls (mean age 10 years). For the first group (men), reduced grey matter volumes were reported in both the left middle/inferior temporal gyri and right postcentral/supramarginal gyri of the brains. In the second group (women), reduced grey matter volumes were reported in the right pre-
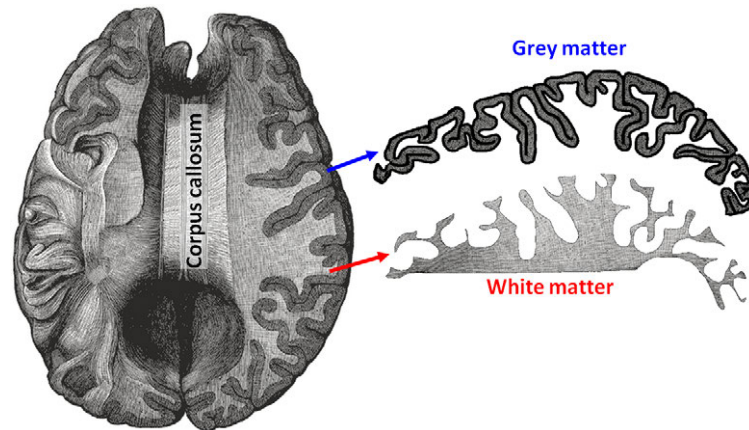
FIGURE 68: A visualization figure for the brain showing the grey matter, white matter, and corpus callosum structures.

cuneus and paracentral lobule/medial frontal gyrus. In boys, a reduced grey matter volume was reported in the left inferior parietal cortex (supramarginal/ angular gyri). Finally, differences in girls were seen within the right central sulcus and adjacent gyri, and the left primary visual cortex. The study suggested the importance of considering sex and age when analyzing grey matter abnormalities.

In addition, VBM analysis has been used to investigate other findings associated with dyslexia. For example, Jednoróg et al. [172] used a VBM approach to investigate the existence of anatomical markers associated with distinct cognitive impairments of dyslexia. VBM analysis has been applied to four groups: a group of 35 controls and three groups of dyslexic subtypes (total of 46 dyslexic children). These groups were classified based on the cognitive deficits: phonological, rapid naming, magnocellular/dorsal, and auditory attention shifting. VBM analysis revealed grey matter volume clusters specific to each studied group including areas of left inferior frontal gyrus, cerebellum, right putamen, and bilateral parietal cortex. Krafnick et al. [173] used VBM analysis to investigate possible volumetric changes in the grey matter following intensive reading intervention in dyslexic children, which resulted in significant gains in reading skills. The study on 11 dyslexic children showed that the intervention was accompanied by an increase in grey mat-

ter volume, reported in the left anterior fusiform gyrus/hippocampus, left pre-cuneus, right hippocampus and right anterior cerebellum. Raschle et al. [174] used VBM analysis to investigate if the structural alterations in the brain are present before reading is taught. This study, performed on 20 children, reported a reduc-tion in gray matter volumes in the left occipitotemporal, bilateral parietotempo-ral regions, left fusiform gyrus, and right lingual gyrus for pre-reading children with a family history of dyslexia compared to children without a family history of dyslexia. The study suggested that the reported brain alteration in dyslexia may be present at birth or develop in early childhood prior to reading onset.

Instead of examining the volumetric changes in the grey matter densities in the brain, several studies have investigated the shape abnormalities in the brain cortex associated with dyslexia [5, 175, 176]. For example, Nitzken et al. [5] used spherical harmonic (SH) analysis to detect the brain cortex variability between dyslexic and normal brains. The SHs (a linear combination of special basis func-tions) were used to represent the shape complexity of the 3D surface of the brain in controls and dyslexic individuals. The shape complexity of the brain was de-scribed using the estimated number of the SHs to delineate the brain cortex (see Figure 69). This number was used to classify the brains as normal or dyslexic. Their experiments suggest that the estimated number of the SHs is a promising supplement to the current screening methods for dyslexia. A study by Williams et al. [175], using the SH analysis in [31], observed that dyslexic brains exhibit less surface complexity than controls (see Figure 69). Altarelli et al. [176] analyzed the cortical thickness on the ventral occipitotemporal regions, due to their defined functional response to visual categories. The cortical thickness was estimated for each participant using Freesurfer software [177, 178]. The study reported a reduc-tion in the cortical thickness in the left hemisphere regions of dyslexic brain, which are responsive to words. Table 11 summarizes the current MRI-based systems for the detection of dyslexia-associated grey matter abnormalities.
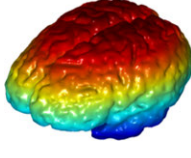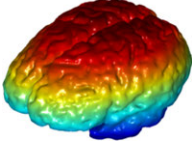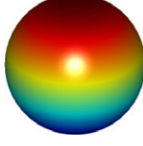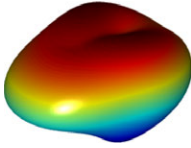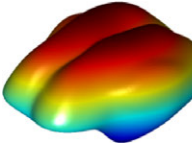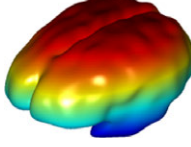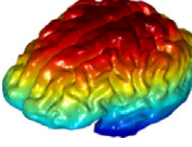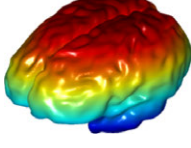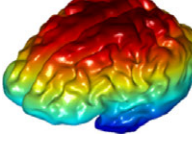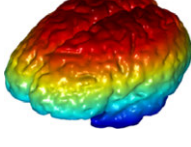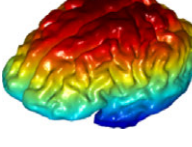
	Dyslexic	Control
Original Mesh		
1 SH		
5 SHs		
20 SHs		
40 SHs		
60 SHs		

FIGURE 69: Method proposed by Nitzken et al. [5] for the approximation of the 3D brain cortex shape for dyslexic and normal subjects.

TABLE 11: Image-based systems for the detection of dyslexia-associated grey matter abnormalities using structural MRI. For each study, the number of subjects, the method, and the study outcomes are reported.

Study	Data	Method	Findings
Eliez et al. [159]	30 subjects: 16 dyslexic and 14 control	Voxel-based morphometry (VBM)	• Altered grey matter density was reported in the left temporal lobes

Table 11: Continued.

Brown et **al. [161]**	30 subjects: 16 dyslexic and 14 control	Voxel-based morphometry (VBM)	• Reduced gray matter volumes were reported in dyslexic brains in the left temporal lobe, bilaterally in the temporoparietooccipital juncture, in the frontal lobe, caudate, thalamus, and cerebellum
Silani et **al. [163]**	64 subjects: 32 dyslexic and 32 control	Voxel-based morphometry (VBM)	• Altered grey matter density was reported in the left middle and inferior temporal gyri and the left arcuate fasciculus
Eckert et **al. [164]**	26 subjects: 13 dyslexic and 13 control	Voxel-based morphometry (VBM)	• Altered grey matter density was reported in the left and right lingual gyrus, left inferior parietal lobule, and cerebellum

Vinckenbosch et al. [165]	24 subjects: 10 dyslexic and 14 control	Voxel-based morphometry (VBM)	• Reduced gray matter volumes were reported in both temporal lobes of dyslexic brains, particularly in the middle and inferior temporal gyri of the left temporal lobe. Increased gray matter density was reported in the precentral gyri bilaterally
Kronbichler et al. [160]	28 subjects: 13 dyslexic and 15 control	Voxel-based morphometry (VBM)	• Altered grey matter density was reported in the left and right fusiform gyrus, bilateral anterior cerebellum, and right supramarginal gyrus
Steinbrink et al. [168]	16 subjects: 8 dyslexic and 8 control	Voxel-based morphometry (VBM)	• Reduced gray matter volumes were reported in the superior temporal gyrus of both hemispheres of dyslexic brains

Table 11: Continued.

Pernet et al. [169]	77 subjects: 38 dyslexic and 39 control	Voxel-based morphometry (VBM)	• Altered grey matter volumes were reported in the left superior temporal gyrus, occipital-temporal cortices, and lateral/medial cerebellum
Krafnick et al. [173]	11 dyslexic children	Voxel-based morphometry (VBM)	• Reading improvements are accompanied by an increase in grey matter volume, reported in the left anterior fusiform gyrus/hippocampus, left precuneus, right hippocampus and right anterior cerebellum

Table 11: Continued.

Raschle et al. [174]	20 children	Voxel-based morphometry (VBM)	• Reduced gray matter volumes were reported in the left occipitotemporal, bilateral parietotemporal regions, left fusiform gyrus and right lingual gyrus for pre-reading children with a family-history of dyslexia compared to children without a family-history of dyslexia
Nitzken et al. [5]	30 subjects: 16 dyslexic and 14 control	Analysis of cortex using spherical harmonics (SHs)	• The estimated number of the SHs, used to approximate the brain shape complexity, can be used as a discriminant feature to distinguish dyslexic brains from controls
Williams et al. [175]	47 subjects: 16 dyslexic and 31 control	Analysis of cortex using spherical harmonics (SHs)	• The study observed that dyslexic brains exhibit less surface complexity than controls

Table 11: Continued.

Evans et al. [171]	118 subjects: 59 dyslexic and 59 control	Voxel-based morphometry (VBM)	• The study reported reduction in the grey matter densities in specific regions based on sex and age
Jednorog et al. [172]	81 subjects: 46 dyslexic and 35 control	Voxel-based morphometry (VBM)	• VBM revealed grey matter volume clusters specific for three studied groups (classified based on the cognitive deficits) including areas of left inferior frontal gyrus, cerebellum, right putamen, and bilateral parietal cortex
Altarelli et al. [176]	29 subjects: 14 dyslexic and 15 control	Analysis of the cortical thickness using Freesurfer software [177]	• The study reported a reduction in thickness in dyslexic children compared with controls in the left hemisphere regions that are responsive to words

2. White Matter

The white matter of the brain connects different areas of the gray matter within the nervous system (see Figure 68). Several studies [6–8, 163, 179] have attempted to identify how the connectivity (i.e., the white matter) between different gray matter areas is related to dyslexia. Using VBM, white matter brain regions were identified to be associated with developmental dyslexia. For example, Silani et al. [163] used a VBM method to identify altered white matter density in the left middle and inferior temporal gyri and the left arcuate fasciculus.

Instead of examining the volumetric changes in the white matter densities in the brain, other studies have investigated the shape abnormalities in the white matter in dyslexic brains [6–8, 179]. For example, El-Baz et al. [6–8] quantified the differences between the shape of cerebral white matter (CWM) gyrifications for dyslexic and normal subjects, see Figure 70. The reported results showed statistical significant differences in the reported geometric characteristics of CWM gyrifications between normal and dyslexic subjects. Casanova et al. [179] analyzed the depth of the gyral white matter measured in an MRI series of 15 dyslexic adult men and 11 age-matched comparison subjects. Measurements were based upon the 3D Euclidean distance map inside the segmented cerebral white matter surface. Mean gyral white matter depth was 3.05 mm (SD ±0.30 mm) in dyslexic subjects and 1.63 mm (SD ±0.15 mm) in the controls. The results added credence to the growing literature suggesting that the attained reading circuit in dyslexia is abnormal. Otherwise, the anatomical substratum (i.e., corticocortical connectivity) underlying this inefficient circuit is normal. Table 12 summarizes the current MRI-based systems for the detection of dyslexia-associated white matter abnormalities.
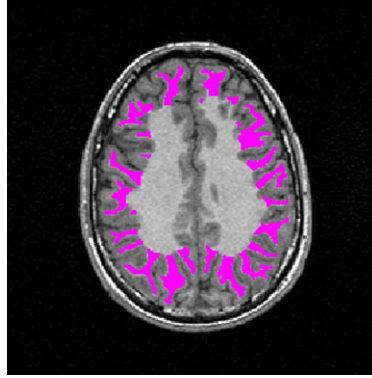
FIGURE 70: Extracted CWM gyrifications (pink) using the method proposed by El-Baz et al. [6–8]

TABLE 12: Image-based systems for the detection of dyslexia-associated white matter abnormalities using structural MRI. For each study, the number of subjects, the method, and the study outcomes are reported.

Study	Data	Method	Findings
Silani et al. [163]	64 subjects: 32 dyslexic and 32 control	Voxel-based morphometry (VBM)	• Altered white matter density was reported in the left middle and inferior temporal gyri and the left arcuate fasciculus
El-Baz et al. [6–8]	30 subjects: 16 dyslexic and 14 control	Shape analysis of the thickness of CWM gyrifications	• Results reported statistically significant differences in the reported geometric characteristics of CWM gyrifications between normal and dyslexic subjects

Table 12: Continued.

Casanova et al. [179]	26 subjects: 15 dyslexic and 11 control	Analysis of the depth of the gyral white matter	• Mean gyral white matter depth was 3.05 mm (SD ±0.30 mm) in dyslexic subjects and 1.63 mm (SD ±0.15 mm) in the controls

3.   Planum Temporale and Cerebellum

Other brain structures, such as the planum temporale [180, 181] and cerebellum [182, 183], have been studied to investigate their relation to developmental dyslexia. The planum temporale is a highly lateralized cortical region located posterior to the auditory cortex within the Sylvian fissure. It is a key anatomical component of Wernicke's area (see Figure 71), an area which is involved in the understanding of written and spoken language. This structure has shown a significant asymmetry between the two hemispheres of the brain and found to be larger in the left cerebral hemisphere than the right. Since earlier studies reported a disturbance in the leftward asymmetry in dyslexia [184], several quantitative methods for identifying planum temporale anomalies on the MRI of subjects with developmental dyslexia were developed. For example, Brambati et al. [162] used a VBM analysis to report focal abnormalities in gray matter volume bilaterally in the planum temporale. Larsen et al. [185] analyzed the size and symmetry of the planum temporale using MRI in two groups of normal and dyslexic subjects. The study observed a planum symmetry of around 70% among the dyslexic and around only 30% among the control subjects. Among two group of 19 dyslexic and 12 control subjects, Leonard et al. [186] used structural MRI to report asymmetry in the left-side temporal bank and the right-side parietal bank within both groups,

with the dyslexic brains showing larger asymmetries. The authors explained these exaggerated asymmetries as due to an observed shift of right planar tissue from the temporal to parietal bank in dyslexic individuals. The study also observed a higher incidence of cerebral anomalies bilaterally in dyslexic subjects. More recently, Bloom et al. [187] analyzed the symmetry of the planum temporale to identify possible anomalies in developmental dyslexia. They reported a significantly reduced leftward asymmetry in children with dyslexia.
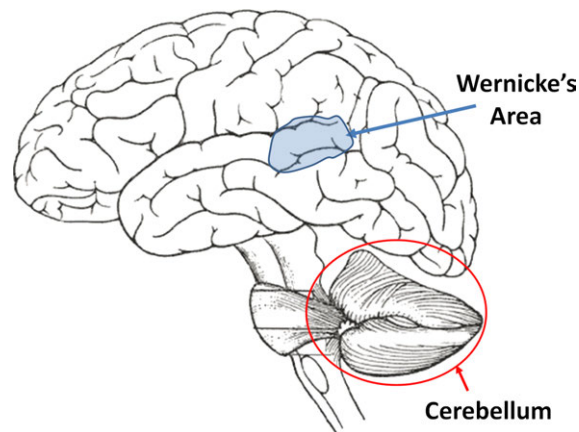
FIGURE 71: A visualization figure for the brain showing the cerebellum brain structure and the Wernicke's area that the planum temporale forming its heart

Although the studies [162, 185–187] showed abnormalities in the asymmetry of the planum temporale in dyslexic individuals, Rumsey et el. [188] analysis for the size and asymmetry of the planum temporale reported different findings. Their study was performed on 16 dyslexic subjects and 14 matched controls that had been previously analyzed using positron emission tomography (PET) during tasks for word recognition and phonological processing [189]. PET analysis showed functional abnormalities (differences in activation patterns) in temporal and parietal regions in dyslexic individuals, including the posterior portions of the superior temporal gyrus containing the planum temporale [189]. However, their analysis for the size and asymmetry of the planum temporale reported equivalent leftward asymmetries of the planum temporale in the two groups, i.e., the left side

is larger than the right side in around 70% to 80% of both groups. They suggested that the anomalous asymmetry of the planum temporale is not strongly associated with dyslexia and did not contribute to the reported functional abnormalities using PET analysis.

Other studies attempted to distinguish between dyslexic and control participants using volumetric features extracted from the cerebellum (see Figure 71). VBM analysis identified altered grey matter density in the cerebellum [160, 161, 164, 169]. For example, Brown et al. [161] reported decreased volumes of the gray matter in the cerebellum of dyslexic individuals. Kronbichler et al. [160] identified altered grey matter bilaterally in the anterior cerebellum. Pernet et al. [169] reported alterations of the grey matter in lateral/medial cerebellum. Based on manual tracing of the cerebellum region, Eckert et al. [190] reported reduced volume of the right anterior lobe of the cerebellum and pars triangularis bilaterally in dyslexic subjects. Using these volumes, 72% of the dyslexic subjects and 88% of the controls were correctly classified. Correlated with these findings, Fernandez et al. [191] also reported reduced volume of the anterior lobe of the cerebellum in dyslexic individuals based on manual tracing, which was aided by the cerebellar atlas published by Schmahmann et al. [192]. Table 13 summarizes the current MRI-based systems for the detection of dyslexia-associated abnormalities in the planum temporale and cerebellum. Due to the limited number of these studies, more research should be conducted to provide more accurate findings regarding a possible relation between the planum temporale and cerebellar anomalies to developmental dyslexia.

Other studies attempt to distinguish between dyslexic and control participants using volumetric features extracted from the cerebellum, the superior-most region of the central nervous system (see Figure 71). Using the VBM analysis, the altered grey matter density was identified in the cerebellum [160, 161, 164, 169].

For example, Brown et al. [161] reported decreased volumes of the gray matter in cerebellum of dyslexic brains. Kronbichler et al. [160] identified altered grey matter bilaterally in the anterior cerebellum. Pernet et al. [169] reported alterations of the grey matter in lateral/medial cerebellum. Based on manual tracing of the cerebellum region, Eckert et al. [190] reported reduced volume of the right anterior lobe of the cerebellum and pars triangularis bilaterally in dyslexic subjects. Using these volumes, 72% of the dyslexic subjects and 88% of the controls were correctly classified. Correlated with these findings, Fernandez et al. [191] also reported reduced volume of the anterior lobe of the cerebellum in dyslexic brains based on manual tracing, which was aided by the cerebellum atlas published by Schmahmann et al. [192]. Table 13 summarizes the current MRI-based systems for the detection of dyslexia-associated abnormalities in the planum temporale and cerebellum. Due to the limited number of these studies, more research should be conducted to provide more accurate findings regarding a possible relation between the planum temporale and cerebellum anomalies to developmental dyslexia.

TABLE 13: Image-based systems for the detection of dyslexia-associated abnormalities in the planum temporale and cerebellum using structural MRI. For each study, the number of subjects, the method, and the study outcomes are reported.

Study	Data	Method	Findings
Larsen et al. [185]	28 subjects: 19 dyslexic and 19 controls	Analysis of the size and symmetry of the planum temporale	• The results reported a planum symmetry of around 70% among the dyslexic and only around 30% among the control subjects

Leonard et al. [186]	31 subjects: 19 dyslexic and 12 controls	Analysis of the size and symmetry of the planum temporale	• Reported asymmetries in the left-side temporal bank and the right-side parietal bank within both groups were observed, with the dyslexic brains showing larger asymmetries
Rumsey et el. [188]	40 subjects: 16 dyslexic and 14 controls	Analysis of the size and symmetry of the planum temporale	• Equivalent leftward asymmetries of the planum temporale was reported in around 70% to 80% of both groups
Eckert et al. [190]	50 subjects: 32 dyslexic and 18 control	Volumetric measurements of brain regions and cerebellum based on manual tracing	• Reduced volume was observed in the right anterior lobe of the cerebellum and pars triangularis bilaterally of dyslexic brains. Using these volumes, 72% of the dyslexic subjects and 88% of the controls were correctly classified

Eckert et al. [164]	26 subjects: 13 dyslexic and 13 control	Voxel-based morphometry (VBM)	• Altered grey matter density was reported in the cerebellum
Kronbichler et al. [160]	28 subjects: 13 dyslexic and 15 control	Voxel-based morphometry (VBM)	• Altered grey matter density was reported bilaterally in the anterior cerebellum
Pernet et al. [169]	77 subjects: 38 dyslexic and 39 control	Voxel-based morphometry (VBM)	• Altered grey matter volumes were reported in the lateral/medial cerebellum
Bloom et al. [187]	55 subjects: 29 dyslexic and 26 controls	Analysis of the size and symmetry of the planum temporale	• A significant reduction of the leftward asymmetry in children with dyslexia was reported
Fernandez et al. [191]	39 subjects: 23 dyslexic and 16 control	Volumetric analysis of the cerebellum brain structure based on manual tracing	• Reduced volume of the anterior lobe of the cerebellum was observed in dyslexic brains

4. Corpus Callosum (CC)

The CC is the largest fiber bundle in the brain that is responsible for transferring sensory, motor and cognitive information between homologous regions of

the two cerebral hemispheres. Since human reading skills are highly affected by impaired communication between the hemispheres, the detection of CC abnormalities in dyslexia has been an area of research interest. To detect these abnormalities, several studies [23–26] traced the CC from a midsagittal MRI slice either manually [23–25] or with commercial software packages [26], and the statistical difference analysis has been applied to find out which part in the CC contributes significantly to identifying brains of dyslexic individuals.

Instead of using area metrics that are subject to errors associated with pixel-based measurement, shape-based approaches to detect the shape differences between the CC of normal and dyslexic subjects have been explored. Earlier works for dyslexia detection focused on the 2D analysis of the CC. For example, Plessen et al. [193] computed the mean shape of both dyslexic and normal CCs from the midsagittal slice of the CC and noticed that the CC body length is a discriminatory feature between the dyslexic and normal subjects.

To ensure a more accurate quantification of anatomical differences between the CC of dyslexic and control subjects, Casanova et al. [194] and Elnakib et al. [195] applied a 3D analysis method for the CC surface. To ensure a complete 3D analysis, the whole CC surface (traced from all the slices in which the CC appears) is mapped onto a cylinder, in such a way as to accurately compare various CCs of dyslexic and normal individuals. Validation on 3D simulated phantoms demonstrated the ability of the method in [194, 195] to accurately detect the shape variability between two 3D surfaces [9]. The study reported a generalized increase in size of the CC in dyslexia with a concomitant diminution at its rostral and caudal poles. In addition, they reported significant differences between 14 normal and 16 dyslexic subjects in all four anatomical divisions, i.e., the splenium, rostrum, genu and body of their CCs (see Figure 72). The 3D analysis of the CC surface resulted in a number of 3D features that can be used to discriminate between

dyslexic subjects and controls [9, 196]. In [196], Elnakib et al. reported significant differences between the CC centerlines (CCL) for 14 normal and 16 dyslexic subjects. They extended their work in [9] and used another feature- the centerline thickness (CCT) defined as the mean thickness for each CC cross section perpendicular to the centerline- to distinguish between normal and dyslexic subjects (see Figure 72). The combination of the two features (CCL and CCT) showed an increase in the accuracy from 75% (using the CLL alone)-88% (using CCT alone) to 94%. To summarize the current image-based systems for detection of dyslexia-associated abnormalities in CC brain structure, Table 14 provides a summary of these systems.

TABLE 14: Image-based systems for the detection of dyslexia-associated CC abnormalities. For each study, the number of subjects, the method, and the study outcomes are reported.
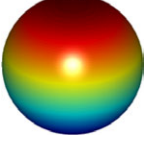
Study	Data	Method	Findings
Hynd et al. [23]	32 subjects: 16 dyslexic and 16 control	Area-based analysis of the CC in the mid-sagittal MRI brain slice	• The study reported a significantly smaller anterior region of interest (the genu) in the dyslexic children and significant correlations between reading achievement and the region-of-interest measurements for the genu and splenium

Rumsey et al. [24]	40 subjects: 21 dyslexic and 19 control	Area-based analysis of the CC in the mid-sagittal MRI brain slice	• The study reported a larger area of the posterior third of the CC in dyslexic men than in controls. No differences were reported in the anterior or middle CC
Robichon et al. [25]	28 subjects: 16 dyslexic and 12 control	Area- and morphological-based analysis of the CC in the mid-sagittal MRI brain slice	• The study reported a more circular and thicker shape of the dyslexics' CC and a larger average midsagittal surface in dyslexic men than in controls, in particular in the isthmus
Fine et al. [26]	68 readers	Area-based analysis of the CC in the mid-sagittal MRI brain slice	• Results suggested that better readers have larger midsagittal areas at the CC midbody
Plessen et al. [193]	40 subjects: 20 dyslexic and 20 control	Analysis of the CC shape in the mid-sagittal MRI brain slice	• The study reported a shorter CC length in the dyslexic group, localized in the posterior midbody/isthmus region

Table 14: Continued.

Elnakib et al. [196]	40 subjects: 16 dyslexic and 14 controls	3D shape analysis of the CC	• The study reported significant differences between the CC centerlines between normal and dyslexic subjects
Elnakib et al. [195]	40 subjects: 16 dyslexic and 14 controls	3D shape analysis of the CC	• The study reported significant differences between normal and dyslexic subjects in all four anatomical divisions, i.e., splenium, rostrum, genu and body of the CC
Casanova et al. [194]	40 subjects: 16 dyslexic and 14 controls	3D shape analysis of the CC	• The study reported a generalized increase in size of the CC in dyslexia with a concomitant diminution at its rostral and caudal poles
Elnakib et al. [9]	40 subjects: 16 dyslexic and 14 controls	3D shape analysis of the CC	• Combining two features, CCL and CCT, reported an increase in the accuracy from 75% (using the CLL alone)–88% (using CCT alone) to 94%

(a) (b)
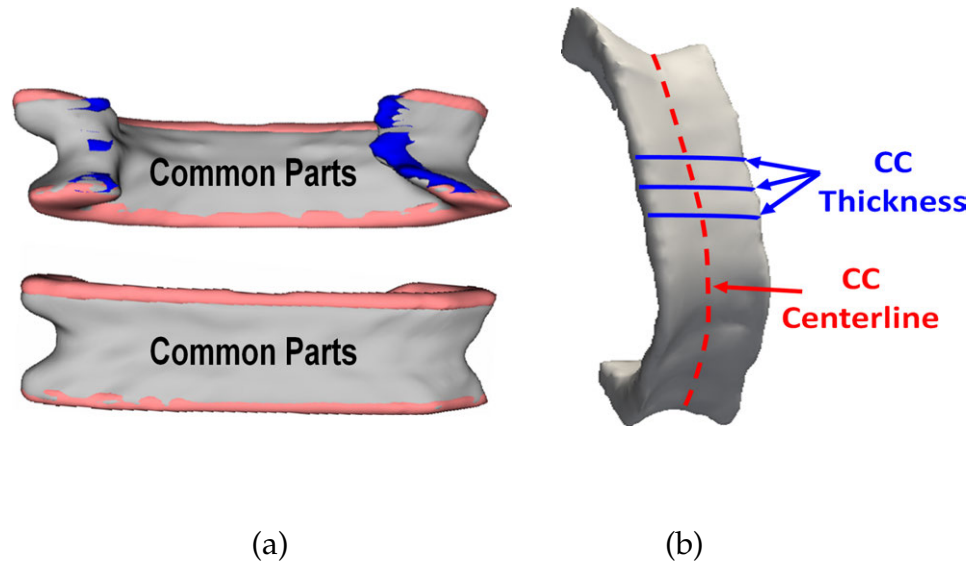
FIGURE 72: 33D shape analysis of the CC proposed by Elnakib et al. [9]: (a) color-coded anatomical differences between the CC for normal and dyslexic subjects: the common parts (gray), parts that exist in normal subjects and do not exist in dyslexic subjects (blue), and parts that exist in dyslexic subjects and do not exist in normal subjects (pink), (b) 3D CC features used to classify normal and dyslexic subjects: the centerline length (CLL) and the mean CC thickness (CCT), defined as the mean thickness for each CC cross section perpendicular to the centerline.

C. DIFFUSION TENSOR IMAGING (DTI)

DTI is another type of MRI that is based on the measurement of the Brownian motion of water molecules in tissue. DTI is a newly developed MRI technique to study in vivo tissue microstructure, e.g., the connectivity between different brain areas. This MRI modality allows the scientist to look at the network of nerve fibers. In addition, the analysis of DTI derives important features of the brain tissue, e.g., FA feature. The latter micro-structural feature reflects how the diffusion within a voxel depends on orientation, i.e., specifies the degree of diffusion directional-

ity. Due to these reasons, DTI has been investigated by neuroscientists to study a number of disorders (e.g., addiction, epilepsy, traumatic brain injury, and various neurodegenerative diseases) and to demonstrate subtle abnormalities in a variety of diseases, (e.g., stroke, multiple sclerosis, dyslexia, and schizophrenia) [197–199]. An example of brain nerves' connectivity bundle obtained from a 3D DTI data set is shown in Figure 73.
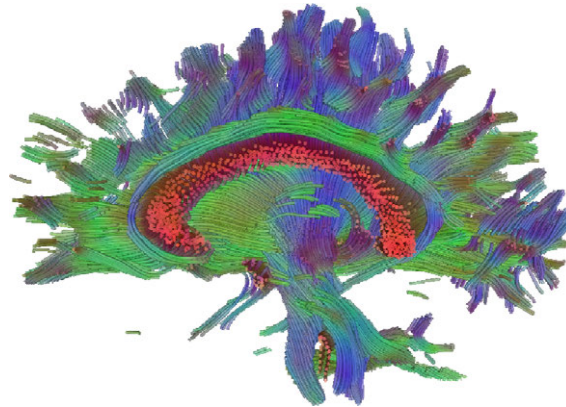
FIGURE 73: Colored streamlines represent likely paths of nerve fiber bundles. This data was extracted from a diffusion imaging data set. Courtesy of Schultz [10].

DTI was used extensively to determine regions related to dyslexia within the white matter [168, 200–207]. Klingberg et al. [200] applied a voxel-based approach based on the SPM software package to spatially smooth and normalize the brains to a common stereotactic space before analyzing the FA values. They reported that the FA scores decrease bilaterally in the temporal-parietal white matter in the subjects with reading difficulties. Correlated with these findings, Beaulieu et al. [208] used DTI to show that the brain connectivity in the white matter, regionally in the left temporo-parietal, is correlated with a wide range of reading abilities in young children (age, 8-12 years).

To avoid the potential influence of spatial smoothing and spatial registration associated with the voxel-based analyses (e.g., with the SPM software), Niogi et al. [201] determined a region of interest either manually or semi-automatically with user-selected seed pixels. They reported significant differences in the FA

scores within the left superior corona radiata and the left centrum semiovale comparing children with a reading disability and non-impaired children. Steinbrink et al. [168] reported a decreased FA in bilateral fronto-temporal and left temporo-parietal white matter regions (inferior and superior longitudinal fasciculus) in the dyslexic subjects. A correlation between white matter anisotropy and speed of pseudoword reading was observed. Richards et al. [202] reported alterations of the white matter microstructure in specific bilateral tracts within the frontal lobe, temporal lobe, occipital lobe, and parietal lobe. Carter et al. [203] reported a reduced FA in the left superior longitudinal fasciculus (SLF) and abnormal orientation in the right SLF in dyslexics. Odegard et al. [204] reported correlations between FA values and real word and pseudoword decoding in the left superior corona radiata (positive correlation) and the left posterior CC (negative correlation). Rimrodt et al. [209] reported reduced FA values in the left inferior frontal gyrus and left temporo-parietal white matter of dyslexic brains. Vandermosten et al. [205] reported a reduced FA in the left arcuate fasciculus of adults with dyslexia. In an extension of this work, Vandermosten et al. [206] reported a reduction in the white matter lateralization in both the posterior superior temporal gyrus and the arcuate fasciculus in the dyslexic readers. Hasan et al. [207] studied the utility of regional DTI measurements of the CC in understanding the neurobiology of reading disorders in a group of 50 childen: 24 dyslexics, 15 readers with comprehension or fluency problems, and 11 controls. They analyzed the diffusion attributes in the midsagittal cross-sectional CC subregions using DTI. The results reported a significant correlation of the callosal microstructural attributes, such as the mean diffusivity of the posterior middle sector of the CC, with measures of word reading and reading comprehension. In addition, reading group differences in FA, mean diffusivity and radial diffusivity were observed in the posterior CC. Table 15 summarizes the current DTI-based systems for the detection of dyslexia-associated white matter microstructure abnormalities.

TABLE 15: Image-based systems for the detection of dyslexia-associated white matter microstructure abnormalities using DTI. For each study, the number of subjects, the method, and the study outcomes are reported.

Study	Data	Method	Findings
Klingberg et al. [200]	17 subjects: 6 dyslexic and 11 control	A voxel-based approach based on the SPM software to define the regions and statistical analysis to analyze FA values	• The study reported reduced FA scores bilaterally in the temporal-parietal white matter in the subjects with reading difficulties
Beaulieu et al. [208]	32 subjects	A voxel-based approach based on the SPM software to define the regions and statistical analysis to analyze FA values	• The study reported that the brain connectivity in the white matter, regionally in the left temporo-parietal, is correlated with a wide range of reading abilities in young children
Niogi et al. [201]	31 subjects: 11 dyslexic and 20 control	Manual or semi-automated determination of the region of interest to analyze the FA values	• They reported significant differences in the FA scores within the left superior corona radiata and the left centrum semioval between children with a reading disability and non-impaired children

Table 15: Continued.

Steinbrink et al. [168]	16 subjects: 8 dyslexic and 8 control	Analysis of DTI data to examine white matter microstructure	• DTI reported reduced FA scores in the dyslexic group in bilateral fronto-temporal and left temporo-parietal white matter regions (inferior and superior longitudinal fasciculus)
Richards et al. [202]	21 subjects: 14 dyslexic and 7 control	Voxel-wise statistical analysis of the fractional anisotropy data using Tract-Based Spatial Statistics	• Alterations of the white matter microstructure were reported in the dyslexic group in specific bilateral tracts within the frontal lobe, temporal lobe, occipital lobe, and parietal lobe
Carter et al. [203]	13 subjects: 7 dyslexic and 6 control	Analysis of DTI data to examine white matter microstructure	• A reduced FA score was reported in the dyslexic group in the left superior longitudinal fasciculus (SLF) and an abnormal orientation was found in the dyslexic group in the right SLF

Odegard et al. [204]	17 subjects: 10 dyslexic and 7 control	Voxel-wise statistical analysis of the fractional anisotropy data using Tract-Based Spatial Statistics	• Correlations between FA values and real word and pseudoword decoding were reported in the left superior corona radiata (positive correlation) and the left posterior corpus callosum (negative correlation)
Rimrodt et al. [209]	31 subjects: 14 dyslexic and 17 control	Semi-automated analysis of DTI data to examine white matter microstructure	• Reduced FA scores were reported in the dyslexic subjects in left inferior frontal gyrus and left temporo-parietal white matter
Hasan et al. [207]	50 children: 24 dyslexic, 15 readers with comprehension or fluency problems, and 11 controls	Diffusion analysis of midsagittal cross-sectional CC subregions using DTI	• Reading group differences in FA, mean diffusivity, and radial diffusivity were observed in the posterior CC

Table 15: Continued.

Vandermosten et al. [205, 206]	40 subjects: 20 dyslexic and 20 control	Analysis of DTI data to examine white matter microstructure	• Reduced white matter lateralization was reported in the posterior superior temporal gyrus [206] and the arcuate fasciculus [205, 206] of the dyslexic group

D.   FUNCTIONAL MRI

Functional magnetic resonance imaging (fMRI) is a noninvasive MRI technique that is used to study the activated area of the brain after certain stimuli and to map changes of brain hemodynamics that correspond to mental operations. The technique has the ability to observe which structures participate in specific mental tasks [210]. Functional MRI acquires two images, one while the brain is in the resting state followed by another one after the brain has been stimulated in some way. The areas of brain activation are determined as any regions which are different between the two scans. Functional MRI allows radiologists to better understand brain organization and has the advantage of providing in-depth details of what is inside the brain.

In the literature, fMRI has played an important role in understanding the pathophysiology of dyslexia and analyzing the neural brain systems for reading [211]. It has been used extensively to analyze the activation areas of the brain associated with the reading process within groups of normal and dyslexic subjects. Rimrodt et al. [212] used fMRI to observe brain activation associated with sentence comprehension (SC) and word recognition (WR) in two groups of 14 dyslexic sub-

jects and 15 controls. Activation areas associated with the SC-WR contrast were reported in left inferior frontal and extrastriatal regions. The dyslexic group showed more activation than controls in the left middle/superior temporal gyri (areas associated with linguistic processing), bilateral insula, right cingulate gyrus, right superior frontal gyrus, and right parietal lobe (areas associated with attention and response selection). Baillieux et al. [213] used fMRI to analyze the activation patterns of 15 dyslexic children and seven matched control subjects during a semantic association task. The activation patterns showed significant differences in cerebral and cerebellar activation between the dyslexic and the control groups. Focal activation patterns were found in the control group bilaterally in the frontal and parietal lobes and the posterior regions of the two cerebellar hemispheres. In contrast, diffuse activation was reported on cerebral and cerebellar regions of dyslexic subjects. The authors suggested the association between dyslexia and deficits of information processing and transfer within the cerebellar cortex. Reilhac et al. [214] used fMRI to investigate functional abnormalities in dyslexic children with visual attention span disorder during a letter-string comparison task. A lower accuracy of detecting letter identity substitutions within strings was reported in dyslexic subjects. Compared to the control group, under-activation was detected in the left superior parietal lobules and the left ventral occipito-temporal area of dyslexic subjects, suggesting that these regions may participate in letter string processing. Olulade et al. [215] analyzed fMRI activation patterns of nine reading-disabled and 12 control subjects during the analysis of complex spatial material unrelated to the reading of text. To perform that, two spatial problem solving tasks were tested: a word reading-rhyming task and a spatial visualization-rotation task. Reduced activation was observed in bilateral occipital, parietal and middle frontal regions in the reading-disabled group during both spatial tasks. The authors suggested that the underlying neural abnormality in dyslexic brains may affect non-related reading processes. In addition, they suggested that this abnormality may be reflected on other left hemisphere brain areas that are not associated with text reading.

In addition, fMRI has been used extensively to analyze brain functionality in dyslexia during phonological processing [216–222]. For example, Shaywitz et al. [216] analyzed fMRI activation patterns of 26 dyslexic subjects and 23 control subjects during a phonological analysis task. Under-activation was observed in Wernicke's area, the angular gyrus, and striate cortex and over-activation was observed in the inferior frontal gyrus , suggesting a neural deficit in dyslexia. Shaywitz et al. [217] used fMRI to analyze the activation patterns of dyslexic children during tasks that required phonologic analysis (i.e., during pseudoword and realword reading tasks). The study was conducted on 70 dyslexic cildren and 74 controls. The dyslexic subjects reported deficits in the posterior brai regions, including regions in the parietotemporal and occipitotemporal sites. The activation magnitude in the left occipitotemporal region was positively correlated with the reading skill. In addition, younger dyslexic children exhibited lower activation in the left and right inferior frontal lobe compared with older dyslexic children. The authors suggested that dyslexic children have deficits in the neural systems involved in reading that become evident at a young age. Georgiewa et al. [218] analyzed the activation patterns of 9 dyslexic and 8 control children during nonoral reading of German words. Compared to the control group, fMRI reported hyper-activation in the left inferior frontal gyrus in the dyslexic group suggestive of abnormalities in phonological processing. The control subjects exhibited activation in the left middle temporal gyrus area, whereas this area showed disturbed activity in dyslexics. Groth et al. [219] used fMRI to study the auditory temporal and phonological processing in dyslexic individuals using a German vowel length discrimination task. Dyslexic subjects performed worse than controls in response to temporal processing, whereas they did not differ in response to phonological processing. The study suggested that dyslexia is associated with impairments in temporal processing. The group extended their study in [220] and showed that the dyslexic subjects, who performed low in response to temporal processing, showed decreased activation of the insular cortices and the left inferior frontal gyrus. These

results suggested a neural basis for the deficits in the temporal auditory processing for dyslexic subjects. Díaz et al. [221] analyzed fMRI activation patterns of 14 dyslexic subjects and 14 matched controls during a phonological task (attending to speech sound changes) and a speaker task (attending to changes in voice characteristics). For both tasks, the dyslexic subjects exhibited abnormal activation of the medial geniculate body of the auditory sensory thalamus. In addition, this activity was correlated with reading scores, suggesting that the dysfunction of the auditory thalamus may participate in dyslexia. Kovelman et al. [222] analyzed fMRI activation patterns of 12 dyslexic, 12 age-matched control children, and 10 Kindergarten controls, who were matched to dyslexic children based on standardized tests of phonological awareness. During an auditory word-rhyming task, both control groups, but not the dyslexic, showed activation in the left dorsolateral prefrontal cortex, suggesting that phonological awareness may depend on the proper function of this region.

Moreover, fMRI has been used to investigate the neural integration of letters and speech in the brains of dyslexic individuals [148, 223]. Blau et al. [148] analyzed fMRI activation patterns of 13 dyslexic and 13 control subjects during four conditions of either reading letters or understanding speech sounds: visual, auditory, congruent audiovisual speech stimuli, and incongruent audiovisual speech stimuli. The study revealed under-activation of the superior temporal cortex in the dyslexic group when integrating letter and speech sounds, suggesting a deficit in the neural integration of letters and speech in dyslexic brains. The group extended their work in [223] on 18 dyslexic children and 16 control children to study letter-speech sound integration in dyslexia. The study reported reduced neural integration of letters and speech sounds in the planum temporale/Heschl sulcus and the superior temporal sulcus in dyslexic subjects. The authors suggested that letter-speech sound integration contributes to learning to read but may be poorly developed in dyslexia.

Investigation of the pathophysiology of dyslexic brains using fMRI has been the focus of several research studies [224–226]. Demb et al. [225] used fMRI to analyze the pathophysiology of dyslexic brains in an experiment using visual stimuli. The primary visual cortex and extrastriatal areas showed reduced activations in dyslexic subjects, suggesting a deficit in the magnocellular pathway in the dyslexic brains. In [224], Eden et al. used fMRI to study visual motion processing on six dyslexic subjects and eight controls. During the presentation of stationary patterns, both groups showed same activation in the extrastriatal cortex and V5/MT area-a part of the magnocellular visual subsystem located in the extrastriatal visual area that has been previously characterized for visual motion processing [227]. During the presentation of moving stimuli, the V5/MT area was activated in the control but not the dyslexic group. Peyrin et al. [226] investigated neurobiological evidence from fMRI for the reported dissociation between phonological and visual attention span disorders in dyslexic children [228]. The study analyzed the activation patterns of two dyslexic subjects: one with a phonological disorder but preserved visual attention span abilities and the second with the reverse profile. fMRI reported a decreased activation in the left inferior frontal gyrus of the first subject during a phonological rhyme judgment task, whereas the second subject exhibited a normal level of activation in this region. In contrast, a decreased activation of the parietal lobules was reported in the second subject during a visual categorization task, whereas these regions were normally activated in the first subject. In spite of the limited number of the tested subjects, the study provided insights about a possible relation between distinct cognitive impairments and distinct brain dysfunctions in dyslexia.

The brain activation patterns in dyslexia have also been investigated during working memory tasks [229, 230]. Wolf et al. [229] used fMRI to investigate the functional neuroanatomy underlying cognitive dysfunction in dyslexia. To perform this task, the study analyzed the activation pattern of 12 dyslexic subjects and

13 controls during verbal working memory task. The dyslexic subjects were slower than the controls. In addition, they were less accurate as the demand of the working memory increased. During working memory subprocesses, the authors identified abnormal connectivity patterns in the dyslexic subjects in two brain networks: a "phonological" (associated with the recognition of verbal stimuli) network and an "executive" network (associated with the accuracy of the working memory task and the number of errors during a spelling test). The dyslexic subjects exhibited an increased connectivity pattern within the "phonological" network in the left prefrontal and inferior parietal regions. Within the "executive" network, the dyslexic subjects showed an increased functional connectivity in the left angular gyrus, the right superior parietal cortex, the left inferior frontal gyrus, the left hippocampal gyrus, and the right thalamus whereas they exhibited a decreased functional connectivity in the bilateral dorsolateral prefrontal cortex, the left cuneus, the left insula, the right inferior parietal lobule, and the right precuneus. The authors suggested that the working memory dysfunction in dyslexia may be due to an abnormal functional connectivity in dissociable brain networks that are related to "phonological" and "executive" working memory subprocesses. Beneventi et al. [230] analyzed fMRI activation patterns of 11 dyslexic subjects and 13 controls during a working memory task. Reduced activation was observed in the left superior parietal lobule and the right inferior prefrontal gyrus in the dyslexic group. As the working memory load increased, the control subjects, but not the dyslexic subjects, exhibited increased activation in the working memory area, suggesting abnormal deficit in the working memory in dyslexic brains.

Other fMRI studies have investigated the functional brain connectivity in specific brain regions in response to different processing tasks [231, 232]. For example, Pugh et al. [231] used fMRI to investigate the functional connectivity in dyslexic brains around the angular gyrus in the left hemisphere during print tasks that require phonological assembly. The study was conducted on 29 dyslexic and

32 control subjects. The functional connectivity exhibited strong patterns in both groups in print tasks that do not require phonological assembly. In tasks that depend on assembly, disruption in functional connectivity was observed in the left hemisphere in the dyslexic group, suggesting a neural deficit in dyslexia associated with phonological-processing. Van der Mark et al. [232] used fMRI to analyze the connectivity of the visual word form area (VWFA) [233], within the larger left occipitotemporal cortex, to its neighboring language regions. The study analyzed the activation patterns in 18 dyslexic children and 24 matched controls during a continuous reading task. In the control group, the VWFA area was functionally connected to the left frontal and parietal language areas, but not connected to adjacent posterior and anterior regions. In contrast, the dyslexic group showed functional disconnectivities between the VWFA area and left inferior frontal and left inferior parietal language areas. The authors suggested that the deficits in the functional connectivity between the VWFA area and major language areas may lead to problems in orthographic and phonological processing of visual word forms.

Several other studies have investigated the functional activation of dyslexic subjects before and after treatment using fMRI [234–236]. For example, Temple et al. [234] analyzed the functional activation of 20 dyslexic subjects and 12 normal subjects during phonological processing before and after a treatment program that was based on auditory processing and oral language training. In association with behavioral improvement in the oral language and reading performance in the dyslexic group after the treatment, fMRI revealed improved activation in the left temporo-parietal cortex and left inferior frontal gyrus such that it approximated the normal group. In addition, the right-hemisphere frontal and temporal regions and the anterior cingulate gyrus exhibited increased activation in the dyslexic group. The study reported a positive correlation between the ability of the oral language with the magnitude of activation in the left temporo-parietal cortex. Aylward et al. [235] analyzed the functional activation of 10 dyslexic subjects

and 11 normal subjects before and after 28 hours of comprehensive reading instruction. The study analyzed the brain functionality during two different reading tasks: a phoneme mapping task (i.e., mapping sounds to letters) and a morpheme mapping tasks (i.e., understanding the relation between suffixed words and their roots). Prior to instructional treatment, the left middle and inferior frontal gyri, right superior frontal gyrus, left middle and inferior temporal gyri, and bilateral superior parietal regions showed reduced activation in the dyslexic subjects during the phoneme mapping task. In addition, left middle frontal gyrus, right superior parietal, and fusiform/occipital region exhibited lower activation in the dyslexic subjects during the initial morpheme mapping task. After instructional treatment, the reading scores of the dyslexic subjects showed an improvement that was associated with an increase in the brain activation during both tasks whereas a decrease in the brain activation was observed in the normal group during both tasks in a way that they approximated the dyslexics' activation. The authors suggested that comprehensive reading instruction can lead to behavioral gains that may be evident on the brain activation patterns during reading tasks. Richards et al. [236] investigated the functional activation of dyslexic subjects before and after treatment using fMRI during a phoneme mapping task. After a three-week instructional treatment program, the regions that exhibited abnormal functional activation in the dyslexic subjects (i.e., in the left frontal gyrus) showed no differences between the dyslexic and normal groups. The authors suggested that instructional treatment may normalize the abnormal functional activation.

Other fMRI studies investigate abnormal neural systems of dyslexic brains in non-English readers [237–239]. For example, Wimmer et al. [237] investigated dyslexia among German readers using fMRI. During lexical route processes, under-activation was reported in the left ventral occipitotemporal region of the dyslexic subjects. During sublexical route processes, under-activation was reported in the left inferior parietal region and in the left inferior frontal region in the dyslexic sub-

jects. Over-activations was reported in visual occipital regions, premotor/motor cortex, and subcortical caudate and putamen in the dyslexic subjects. Both the dyslexic and the control subjects exhibited no activations in the posterior temporal regions, which have shown abnormalities in fMRI studies on English readers [240]. The authors suggested a possible different neural organization of reading processes between German and English dyslexic readers. Seki et al. [238] investigated the functional abnormalities in dyslexic Japanese using fMRI. The study analyzed the activation patterns of dyslexic subjects during a reading task of sentences constructed from Japanese phonograms (kana). The left middle temporal gyrus was significantly activated in the control subjects but was less activated in dyslexic subjects. Other activated regions were detected in individual dyslexic subjects. Two dyslexic subjects showed activation in the bilateral occipital cortex. Two other dyslexic subjects showed activation in the inferior part of the frontal regions. The last dyslexic subject exhibited activation in both the bilateral occipital cortex and the inferior part of precentral gyrus. Since other fMRI studies on readers of alphabetic languages showed activation in the superior and middle temporal gyri during semantic tasks [241, 242], the authors suggested that functional brain abnormality in dyslexia during reading tasks may not differ between languages [238]. Another study by Kita et al. [239] used fMRI to investigate abnormal brain functionality in Japanese dyslexic children. The study analyzed the activation patterns of 14 dyslexic children, 15 control children, and 30 control adults during a phonological manipulation task. The phonological task activated areas in the left inferior and middle frontal gyrus, left superior temporal gyrus, and bilateral basal ganglia. Among these areas, a hyperactivity and hypo-activity were observed in the basal ganglia and the left superior temporal gyrus, respectively, in the dyslexic group as compared to the two other groups. The authors suggested that the abnormal brain activity may have similarities and differences between dyslexic Japanese and other speaking alphabetical languages. Table 16 summarizes the current fMRI-based systems for detecting functional abnormalities in dyslexia.

TABLE 16: Image-based systems for the detection of dyslexia-associated functional abnormalities using fMRI. For each study, the number of subjects, the method, and the study outcomes are reported.

Study	Data	Method	Findings
Eden et al. [224]	14 subjects: 8 dyslexic and 6 control	Analysis of fMRI activation during visual motion processing	• During the presentation of stationary patterns, both groups show same activation in the extrastriatal cortex and V5/MT area. During the presentation of moving stimuli, the V5/MT area was activated in the control but not the dyslexic group
Demb et al. [225]	10 subjects: 5 dyslexic and 5 control	Analysis of fMRI activation using a visual stimuli experiment	• The primary visual cortex and areas in the extrastriatal cortex showed reduced activations in dyslexic subjects

Table 16: Continued.

Shaywitz et al. [216]	49 subjects: 26 dyslexic and 23 control	Analysis of fMRI activation during a phonological analysis task	• Under-activations were observed in Wernicke's area, the angular gyrus, and striate cortex. Over-activation was observed in the inferior frontal gyrus
Pugh et al. [231]	61 subjects: 29 dyslexic and 32 control	Analysis of functional connectivity around the angular gyrus in the left hemisphere during print tasks that require phonological assembly	• The functional connectivity exhibited strong patterns in both groups in print tasks that do not require phonological assembly. In tasks that depend on assembly, disruption in functional connectivity was observed in the left hemisphere in the dyslexic group

Table 16: Continued.

Seki et al. [238]	10 subjects: 5 dyslexic and 5 control	Analysis of fMRI activation of dyslexic Japanese during a reading task of sentences constructed from Japanese phonograms (kana)	• The left middle temporal gyrus was significantly activated in the control subjects but was less activated in the dyslexic subjects. Other activated regions were detected in particular dyslexic subjects
Georgiewa et al. [218]	17 subjects: 9 dyslexic and 8 control	Analysis of fMRI activation during non-oral reading of German words	• Compared to the control group, fMRI reported hyperactivation in the left inferior frontal gyrus in dyslexic group. The control subjects exhibited activation in the left middle temporal gyrus area, whereas this area showed disturbance activity in the dyslexic subjects

Table 16: Continued.

Shaywitz et al. [217]	144 subjects: 70 dyslexic and 74 control	Analysis of fMRI cerebral and cerebellar activation during tasks that required phonologic analysis	• The dyslexic subjects reported deficits in the posterior brai regions. The activation magnitude in the left occipitotemporal region was positively correlated with the reading skill. Younger dyslexic children exhibited lower activation in the left and right inferior frontal compared with older dyslexic children

Temple et al. [234]	32 subjects: 20 dyslexic and 12 control	Analysis of fMRI activation before and after instructional treatment using a phonological processing task	• fMRI, after treatment, revealed an improved activation in the left temporo-parietal cortex and left inferior frontal gyrus such that it get close to the normal group. In addition, the right-hemisphere frontal and temporal regions and the anterior cingulate gyrus exhibited an increased activation in the dyslexic group. The study reported a positive correlation between the ability of the oral language with the magnitude of activation in the left temporo-parietal cortex

Table 16: Continued.

Aylward et al. [235]	21 subjects: 10 dyslexic and 11 control	Analysis of fMRI activation before and after 28 hours of instructional treatment using two different reading tasks: a phoneme mapping task and a morpheme mapping tasks	• After instructional treatment, the brain activation during both tasks increased in the dyslexic group and decreased in the normal group such that they get close to each other
Richards et al. [236]	39 subjects: 18 dyslexic and 21 control	Analysis of fMRI activation during a phoneme mapping task before and after a 3-week instructional treatment program	• After treatment, the regions of abnormal functional activation in the dyslexic subjects (i.e., in the left frontal gyrus) showed no difference between the dyslexic and normal groups
Blau et al. [148]	39 subjects: 18 dyslexic and 21 control	Analysis of fMRI activation during four conditions for reading: visual, auditory, audiovisual congruent, and audiovisual incongruent	• Under-activation was observed in the superior temporal cortex in the dyslexic group when integrating letter and speech sounds

Table 16: Continued.

Rimrodt et al. [212]	29 subjects: 14 dyslexic and 15 control	Analysis of fMRI activation areas of the brain during a sentence comprehension and a word recognition tasks	• Dyslexic group showed more activation than controls in the left middle/superior temporal gyri (areas associated with linguistic processing), and in the bilateral insula, right cingulate gyrus, right superior frontal gyrus, and right parietal lobe (areas associated with attention and response selection)
Baillieux et al. [213]	22 subjects: 15 dyslexic and 7 control	Analysis of fMRI cerebral and cerebellar activation during a semantic association task	• Diffused activations were reported on the cerebral and cerebellar regions in the dyslexic subjects, whereas these areas showed focal activation in the controls

Table 16: Continued.

Wimmer et al. [237]	39 subjects: 20 dyslexic and 19 control	Analysis of fMRI activation among dyslexic German readers during lexical and sublexical route processes	• The authors reported a different neural organization of reading processes in German dyslexic readers than the reported one [240] for English readers
Wolf et al. [229]	25 subjects: 12 dyslexic and 13 control	Analysis of fMRI activation during verbal working memory task	• The authors identified abnormal connectivity patterns in the dyslexic subjects in two brain networks: a "phonological" (associated with the recognition of verbal stimuli) network and an "executive" network (associated with the accuracy of the working memory task and the number of errors during a spelling test)

Table 16: Continued.

Beneventi et al. [230]	24 subjects: 11 dyslexic and 13 control	Analysis of fMRI activation during a working memory task	• Reduced activations were observed in the left superior parietal lobule and the right inferior prefrontal gyrus in the dyslexic group. As the working memory load increased, the control, but not the dyslexic subjects, exhibited increased activation in the working memory area
Blau et al. [223]	34 subjects: 18 dyslexic and 16 control	Analysis of fMRI activation during four conditions for reading: visual, auditory, audiovisual congruent, and audiovisual incongruent	• Reduced neural integration of letters and speech sounds was reported in the planum temporale/Heschl sulcus and the superior temporal sulcus in the dyslexic subjects

Table 16: Continued.

Van der Mark et al. [232]	42 subjects: 18 dyslexic and 24 control	Analysis of fMRI connectivity around the visual word form area (VWFA) [233] during a continuous reading task	• Deficits in the functional connectivity between the VWFA area and major language areas were reported in the dyslexic group
Groth et al. [219]	40 subjects: 20 dyslexic and 20 control	Analysis of fMRI activation areas of the brain during auditory temporal and phonological processing	• Dyslexic subjects performed worse than controls in response to temporal processing, whereas they did not differ in response to the phonological processing
Steinbrink et al. [220]	40 subjects: 20 dyslexic and 20 control	Analysis of fMRI activation areas of the brain during auditory temporal and phonological processing	• In response to temporal processing, dyslexic subjects performed low and showed decreased activation of the insular cortices and the left inferior frontal gyrus

Peyrin et al. [226]	2 dyslexic subjects	Analysis of fMRI activation during two tasks: a phonological rhyme judgement task and a visual categorization task	• The fMRI of the two dyslexic children reported a dissociation between phonological and visual attention span disorders
Reilhac et al. [214]	24 subjects: 12 dyslexic and 12 control	Analysis of fMRI activation of dyslexic children with visual attention span disorder during a letter-string comparison task	• A lower accuracy of detecting letter identity substitutions within strings was reported in the dyslexic subjects. Under-activations were detected in the left superior parietal lobules and the left ventral occipito-temporal in the dyslexic subjects
Díaz et al. [221]	28 subjects: 14 dyslexic and 14 control	Analysis of fMRI activationduring a phonological task	• The dyslexic subject exhibited an abnormal activation in the medial geniculate body of the auditory sensory thalamus

Table 16: Continued.

Olulade et al. [215]	21 subjects: 9 dyslexic and 12 control	Analysis of fMRI activation during two spatial problem solving tasks: a word reading-rhyming task and a spatial visualization-rotation task	• Abnormal functional neurology was reported during spatial problem solving tasks
Kovelman et al. [222]	24 subjects: 12 dyslexic and 12 control	Analysis of fMRI activation during an auditory word-rhyming task	• Control subjects, but not the dyslexic, showed activations in the left dorsolateral prefrontal cortex
Kita et al. [239]	29 subjects: 14 dyslexic and 45 control	Analysis of fMRI activation during a phonological manipulation task	• The phonological task activated areas in the left inferior and middle frontal gyrus, left superior temporal gyrus, and bilateral basal ganglia. A hyper-activity and hypo-activity were observed in the basal ganglia and the left superior temporal gyrus, respectively, in the dyslexic group

E. DISCUSSION AND SUMMARY

Investigating dyslexia-associated brain abnormalities provides insights into the possible pathophysiological mechanisms of the condition. In addition, different neuroimaging modalities offer noninvasive ways for the early detection of dyslexia and for following the outcome of treatment interventions. In this chapter, an overview of more than 110 articles that appeared in the field is presented to address the methodologies and findings of the current MRI-based systems for detecting brain abnormalities associated with dyslexia. This chapter addresses the strengths and limitations of the current approaches as well as the current MRI-based methods for dyslexia diagnosis. This final section summarizes this work by addressing the correlation between the MRI findings in the literature and outlining the research challenges that face proposed MRI-based diagnostic methods. In addition, the suggested trends to solve these challenges are presented.

Several studies have addressed the correlation between MRI findings in dyslexia by using hybrid MRI techniques (e.g., fMRI supported with structural MRI) or applying meta-analysis on the existing MRI findings in dyslexia. For example, Menghini et al. [167] investigated possible correlation between fMRI and structural MRI findings associated with the reading process on a group on 10 dyslexic and 10 control subjects. A VBM approach reported reduced grey matter volumes in the right posterior superior parietal lobule and precuneus and in the right supplementary motor area in the brains of dyslexic individuals. The reported structural abnormalities are consistent with the reported fMRI changes in the activation areas of the brain during an implicit learning task. The results support that an impairment of implicit learning task might affect the ability of learning to read. Hoeft et al. [166] used both fMRI and VBM analysis to compare the structural and functional findings on a dyslexic with two judgment control groups: an age-matched group and a younger reading-matched group. They applied fMRI to

report the activated areas of the brain during visual word rhyme judgment compared with visual cross-hair fixation rest. Compared to the age-matched group, the dyslexic group reported hypo-activation in left parietal and bilateral fusiform cortices and hyper-activation in left inferior and middle frontal gyri, caudate, and thalamus. Compared to the reading-matched group, the dyslexic group reported hypo activation in left parietal and fusiform regions. The VBM analysis reported reduced gray matter volume in the hypo-activated areas, i.e., only in the left parietal region, suggesting the independence of this area on current reading ability. The results also suggested that the areas of hyper-activation may relate to the level of current reading ability and their independence of atypical brain morphology in dyslexia.

In addition, the correlation between DTI and structural findings has been investigated. Hoeft et al. [243] investigated the capabilities of integrating DTI and fMRI findings to detect future long-term improvement in reading skills. The study, conducted on 25 children with dyslexia, showed that the combination of right inferior frontal gyri activation (observed using fMRI analysis) and right superior longitudinal fasciculus white matter integrity (observed using DTI analysis) predicted with an accuracy of 72% which particular child would improve his/her reading skills 2.5 years later. In addition, the activation patterns across the whole brain during phonological processing has increased the prediction accuracy over 90%. They suggested that MRI findings can predict future behavioral outcomes. Steinbrink et al. [168] reported a decreased FA in bilateral fronto-temporal and left temporo-parietal white matter regions (inferior and superior longitudinal fasciculus) in German dyslexic individuals. A correlation between white matter anisotropy and speed of pseudoword reading was observed.

Moreover, meta-analyses on fMRI findings were applied to assess the consistency of reported findings [244, 245]. Maisog et al. [244] performed two activa-

tion likelihood estimation (ALE) meta-analyses, one to reveal the over-activations and the other to reveal the under-activations that are associated with dyslexia using either fMRI or PET. The first meta-analysis on six studies showed hyper-activity in right thalamus and anterior insula of dyslexic individuals. The second meta-analysis on nine studies showed dyslexia-associated under-activation in two left extrastriatal areas within the Brodmann area 37, precuneus, inferior parietal cortex, superior temporal gyrus, thalamus, and left inferior frontal gyrus and dyslexia-associated hypo-activity in the fusiform, postcentral, and superior temporal gyri. The authors suggested that reading tasks are more associated with the left-sided brain regions in control subjects and the right-sided brain regions in dyslexic subjects. The analysis did not support dyslexia-associated abnormalities in the cerebellum or the left frontal cortex, suggesting that these areas may be varied according to the study's design. Richlan et al. [245] performed an ALE meta-analysis of 17 studies (12 fMRI and 5 PET). The lowest under-activations were observed in inferior parietal, superior temporal, middle and inferior temporal, and fusiform regions of the dyslexics' left hemisphere. Over-activation in the primary motor cortex and the anterior insula in dyslexic subjects was associated with under-activation in the inferior frontal gyrus.

Meta-analyses of structural MRI studies (VBM studies) has also been reported, e.g., in [240, 246]. Richlan et al. [240] performed a coordinate-based meta-analysis on nine VBM studies [160–168]. Reduced gray matter volume was found in the right superior temporal gyrus and left superior temporal sulcus of dyslexic brains, consistently across studies. Correlated reading-related under-activation using fMRI was reported in the left superior temporal sulcus on a previous meta-analyses on functional brain abnormalities in dyslexic readers [247]. These results suggested a correlation between structural and functional MRI for imaging the brain abnormalities in dyslexia. To identify the basis of this correlation and possible overlaps between structural and functional abnormalities in the brains

of dyslexic individuals, Linkersdorfer et al. [246] performed two types of meta-analysis: an ALE meta-analysis on nine VBM studies [160–162, 164–166, 168, 174] and an ALE meta-analyses of imaging studies reporting functional under-activations (24 studies) or over-activations (11 studies) in dyslexia. The VBM meta-analysis reported six significant clusters of altered grey matter volumes in bilateral temporo-parietal and left occipito-temporal cortical regions and in the cerebellum bilaterally. Areas of overlap between the VBM meta-analysis results and the meta-analyses of functional under-activations and over-activations were reported in the fusiform and supramarginal gyri of the left hemisphere, and in the left cerebellum, respectively. These results provided evidence for consistent structural brain variations with functional abnormalities in left hemispheric regions. The rest of this section outlines the research challenges that face the MRI-based systems for detecting brain abnormalities associated with dyslexia and the suggested trends to solve these challenges.

1. Research Challenges

Several challenges and aspects face MRI-based systems for detecting the brain abnormalities associated with dyslexia. These challenges can be summarized as follows:

- The findings of structural MRI-based systems face the following challenges:

  - Volumetric approaches depend on the segmentation of anatomical structures (e.g., white matter, grey matter, corpus callosum, planum temporale, and cerebellum). The segmentation of these structures is challenging due to inhomogeneities of the named brain structures. This may affect the accuracy of voxel-based measurements and may thus produce inconsistent findings.

– A limited number of studies have addressed the role of the planum temporale and cerebellum in developmental dyslexia. More research work should be investigated to provide more accurate findings regarding a possible relation between these structures to developmental dyslexia.

– More sophisticated shape indexes should be developed to describe morphological variability of brain structures.

– 3D and longitudinal analysis techniques of brain structures are challenging and but necessary to better describe some of the reported brain abnormalities.

- DTI-based systems' findings face the following challenges:

  – More accurate indexes should be investigated to describe the connectivity of the white matter microstructure.

  – DTI-based approaches may help to determine the diffusion parameters of the white matter structure. However, supported structural MRI may be helpful to provide better insights regarding the white matter abnormalities.

  – Longitudinal analysis techniques of DTI images are challenging. However, they may help to better understand the connectivity of the white matter structure in dyslexia.

- The findings of fMRI-based systems face the following challenges:

  – fMRI helps to determine the abnormal activation patterns in dyslexia during different brain operations. However, supported structural MRI is needed to reveal if this abnormal brain functionality is due to a physical structural abnormality or due to the study's design.

  – Longitudinal analysis of fMRI findings are challenging and may help to better understand the abnormal functionality of dyslexic brains.

Therefore, there is a need to develop more efficient systems for obtaining more accurate findings about dyslexia.

2. Trends

To address the aforementioned challenges, recent trends for the detection of dyslexia associated abnormalities involve the following aspects:

- More powerful, sophisticated shape features of brain structures need further investigations. A recent trend describes the cortex shape by representing its 3D surface with a linear combination of spherical harmonics (SH) [5, 175, 248]. Another trend uses a cylindrical map to accurately detect the shape variability between two 3D surfaces [9, 194, 195] (e.g., between CCs of normal and dyslexic subjects). Also, the 3D geometric characteristics of CWM gyrifications between normal and dyslexic subjects has been recently employed [6–8, 179]. A suggested future work is to employ different types of shape features from different brain structures to achieve better detection and diagnosis of dyslexia

- Integrating the findings of different MRI techniques (e.g., fMRI, DTI, and structural MRI) is very challenging. Studies should investigate the correlation between these findings and the impact of fusing the information obtained from these different types of images. The functional information from fMRI, the shape and anatomical information from structural MRI, and the connectivity information from DTI may lead to a better description of the brain network in dyslexia and illustrate how it works.

- Analysis of MRI findings over long period of time throughout longitudinal studies may give more consistent findings and better insights about dyslexia.

In addition, longitudinal studies may help diagnose dyslexia at early stages and provide outcome measures of treatment.

The clinical importance of the detection of dyslexia-associated abnormalities in brain structures has been reflected upon over 110 publications. The challenges and trends presented in this section, suggest that investigating more efficient MRI-based systems for the detection of dyslexia-associated abnormalities in brain structures will remain a very active research area. Thus, more comprehensive studies are necessary for establishing the state-of-the-art MRI-based systems in this active research field.

CHAPTER VII

DYSLEXIA DIAGNOSTICS BY 3D SHAPE ANALYSIS OF CORPUS CALLOSUM

This chapter expands on the MRI findings presented in Chapter VI for early detection of dyslexia and attempt to investigate the role of the corpus callosum (CC) brain structure for dyslexia diagnosis. Here, a new approach is presented for the quantitative analysis of three-dimensional (3D) magnetic resonance images (MRI) of the brain that ensures a more accurate quantification of anatomical differences between the CC of dyslexic and control subjects. The proposed approach consists of three main processing steps: (*i*) segmenting the CC from a given 3D MRI using the learned CC shape and visual appearance; (*ii*) extracting the centerline of the CC; and (*iii*) cylindrical mapping of the CC surface for its comparative analysis. Validation on 3D simulated phantoms demonstrates the ability of the proposed approach to accurately detect the shape variability between two 3D surfaces. Experimental results revealed significant differences (at the 95% confidence level) between 14 normal and 16 dyslexic subjects in all four anatomical divisions, i.e., splenium, rostrum, genu and body of their CCs. Moreover, the initial classification results based on the centerline length and thickness of the CC suggest that the proposed CC shape analysis is a promising supplement to the current techniques for diagnosing dyslexia.

A. INTRODUCTION

Structural MRI studies revealed dyslexia-associated abnormalities in the different structures inside the brain, e.g., a reduced brain volume, a decreased gyrification, and an increased CC volume (see Chapter VI). This chapter expands on these findings by analyzing and quantifying the variability of the 3D CC surface in a group of dyslexic and control subjects. The CC is the largest fiber bundle connecting the left and right cerebral hemispheres in the human brain. The CC surface variations relate to alterations of the intra-hemispheric connectivity and thus provide a correlation to recent findings suggesting flaws in connectivity between different brain regions in dyslexia [152].

Detection of dyslexia has been investigated in a number of studies. Earlier works for dyslexia detection focused on the 2D analysis of the CC [23–26, 193], please see section VI.B.4 in Chapter VI. However, 3D shape analysis methods were considered for analyzing the shape differences between the CCs in other brain applications. To analyze shape differences between 3D surfaces, correspondences should be established between a selected set of landmarks that represent these surfaces or between all surface points. Shape descriptors such as shape context [249] or thin-plate spline (TPS) deforming energy [250] can be used to establish the correspondence between two sets of landmarks. The shape context is the local histogram of edge points in polar coordinates and can be estimated for the selected set of landmarks to match the reference template points of a similar shape context. Alternatively, correspondences can be found by minimizing a shape correspondence error, defined by the energy of deforming a target TPS to match the reference object shape. The major problem with representing a shape with a set of landmarks is that they may not sufficiently represent the surface shape, and finer details can be missed. To avoid this problem, mapping the whole surface to a template sphere or ellipsoid was considered using the minimum description length

(MDL) [251] or spherical harmonic (SH) descriptors. The problem of these mappings is that they only work well for sphere-like shapes, which is not the case for the CC. Other investigators used conformal mapping to flatten colon surface [252], surface matching using geodesic and local geometry to locate correspondences between two surface points [253], harmonic shape images to map a 3D surface patch with disc topology to a 2D domain and encode the shape information of the surface patch into the 2D image [254], harmonics differentials to unfold colon wall volume [255], and solving the Poisson equation to extract useful shape features of a closed 2D object [256].

In regard to the study of the CC shape abnormalities, the work presented in [257, 258] accounted not only for the midsagittal slice, but also for four adjacent slices on both sides to locate differences between normal and autistic subjects. He et al. [257] traced the CC from the nine slices using a semi-automated active contour methodology. A contour stitching technique was applied to create the 3D CC surfaces for each subject. The surfaces were aligned using 2D rigid-body registration on each 2D slice across subjects. A mean shape (template) was calculated from the aligned surfaces, and a statistical difference analysis was applied to the signed distance map from each subject surface to the template. Instead of using a signed distance map metric, Vidal et al. [258] utilized the CC thickness–the distance between uniformly spaced points on the CC surface to the CC medial line (i.e., the average curve between superior and inferior CC boundaries) –to localize regions of callosal thinning in autism. He et al. [259] used a statistical shape analysis to find the CC shape differences between patients with phenylketonuri and controls. A set of landmarks was sampled on a template shape, and then an initial correspondence between the template and the target shape is established based on the similarity of locations and normal directions. The landmarks on the target are then refined by an iterative TPS method. The corresponding set of landmarks was used directly for statistical shape analysis.

Current limitations and the proposed approach: To identify whether the abnormal neural development of the CC is associated with dyslexia, the 3D surfaces of the CC for normal and dyslexic subjects are directly compared. Earlier works have focused on analyzing a 2D midsagittal cross-section of the CC, although this is insufficient for detecting the whole anatomic variability of the CC. That the known approaches rely only on the 2D analysis of the CC is the main motivation behind the proposed approach. To ensure a complete 3D analysis, the whole CC surface (traced from all the slices in which the CC appears) is mapped onto a cylinder, in such a way as to compare, more accurately, various dyslexic and normal CCs. The proposed cylindrical mapping has been inspired by the functional conformal mapping [260], that was recently considered an efficient technique for surface matching and anatomic structures visualization [252]. Similar to the conformal mapping, it is a bijective (one-to-one) transformation and preserves angular relationships between the points.

The proposed framework consists of four steps (see Figure 74): (1) age correction using rigid registration, (2) 3D CC segmentation, (3) centerline extraction, and (4) 3D shape analysis. The framework will address the following:

- Previous studies [23–26, 193] have shown significant localized increases or decreases (dependent on region) in the midsagittal CC cross-section in dyslexic patients. The focus of this study was on further establishing the morphometric nature of this size variation, i.e., whether the reported size of variability was the result of focal or generalized changes.

- The proposed method can be used to analyze the boundaries of the region of interest while being invariant to translation, rotation, and scaling.

- Current shape analysis techniques based on a set of certain landmarks suffer from missing finer shape details whereas mapping the whole surface to a

template sphere or ellipsoid introduce extreme distortion for non-sphere-like shapes (e.g., the CC).

- The proposed method can provide a point-to-point shape descriptor of the CC through the cylindrical mapping.

- The length of the extracted centerline and the CC thickness, estimated as the mean thickness for each CC cross-section perpendicular to the centerline, can be used as discriminatory features to distinguish between normal and dyslexic brains.
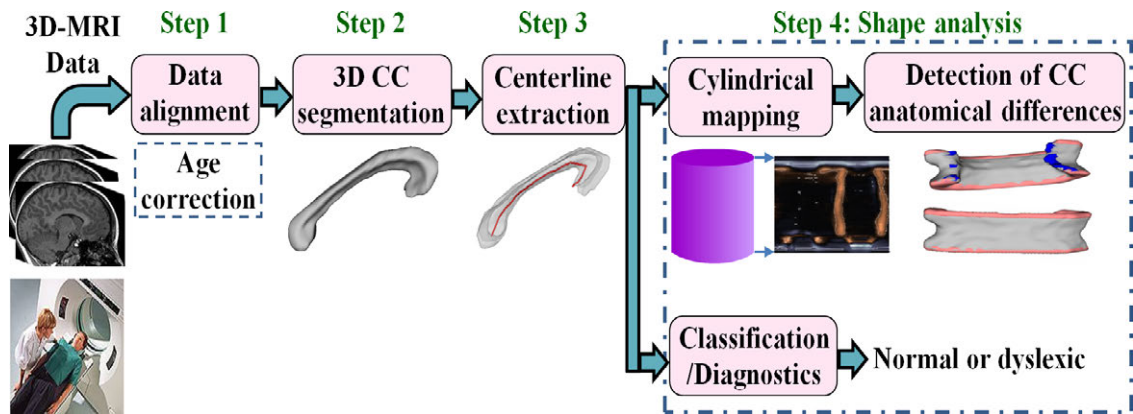
FIGURE 74: The proposed framework for analyzing 3D MR brain images.

Section VII.B briefly overviews the CC segmentation using a learned prior CC shape model and an identifiable joint Markov-Gibbs random field (MGRF) model of 3D registered MRI, and their 3D "object-background" region maps (step 1 and 2 of the proposed framework). Section VII.C illustrates the centerline extraction for the segmented CC by solving the Eikonal equation (step 3). In contrast to the known 2D solutions (e.g., in [116–118]) the proposed process evolves in the 3D space in order to detect 3D points of the maximal curvature. The shape analysis (step 4) including the cylindrical mapping of the CC after finding its centerline is described in Section VII.D. Performance evaluation and experimental results are presented in Section VII.E and Section VII.F. Discussion and conclusions are presented in Section VII.H.

B. 3D CORPUS CALLOSUM SEGMENTATION

The 3D CC segmentation is a challenging problem because it suffers from the diffusion of the CC gray levels, especially in its lateral boundaries, and from the sensitivity to image noise. Atlas based segmentation [261, 262] was utilized for 3D segmentation of the CC and other brain structures. However, its accuracy depends on the accuracy of the atlas-to-target registration. Accurate registration usually involves a nonrigid registration step, which is time consuming and source exhausting. Moreover, the atlas itself could suffer from possible insufficient representation of the whole image population.

To overcome these problems, the CC is segmented in a way that can address these shortcomings based on extending the joint MGRF model introduced in Section III.A.1, Chapter III, to account for the 3D features of the CC (i.e., the object appearance and shape). The object appearance is derived not only from the MRI gray level distribution but also from the spatial interactions between the MRI voxels in order to ensure the homogeneity of the segmentation and overcome noise effects (see Figure 75). The spatial interactions between the region labels are modeled by a 2nd-order translation and rotation variant probabilistic random field, of object / background labels, with analytical maximum likelihood estimates (MLE) of potentials [100, 101]. For simplicity, the interaction structure is restricted to the nearest voxels only, i.e., to the voxel's 26-neighborhood as shown in Figure 76. By symmetry considerations, the potentials are independent of relative orientation of each voxel pair and depend only on intra- or inter-region position (i.e., whether the labels are equal or not). Under these restrictions, it is the 3D extension of the conventional auto-binomial, or Potts model, differing only in that the potentials are estimated analytically.
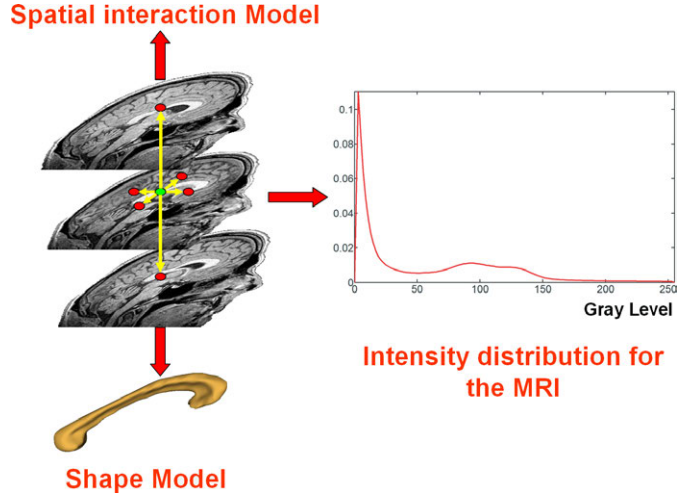
FIGURE 75: Joint Markov-Gibbs random field model of 3D MR images.

The 26-neighborhood has three types of symmetric pairwise interactions, as shown in Figure 76, specified by the absolute distance a between two voxels in the same and adjacent MRI slices ($a = 1$, $\sqrt{2}$, and $\sqrt{3}$, respectively): (*i*) the closest pairs with the inter-voxel coordinate offsets $\mathbf{N}_1 = \{(1,0,0),(0,1,0),(0,0,1)\}$, (*ii*) the diagonal pairs with the offsets $\mathbf{N}_{\sqrt{2}} = \{(0,1,\pm1),(1,0,\pm1),(1,\pm1,0)\}$, and (*iii*) the farthest diagonal pairs with the offsets $\mathbf{N}_{\sqrt{3}} = \{(1,\pm1,\pm1)\}$. The Gibbs potentials of each type are bi-valued because only label coincidence is accounted for: $\mathbf{V}_a = \{V_{a,\text{eq}}; V_{a,\text{ne}}\}$ where $V_{a,\text{eq}} = V_a(l,l')$ if $l = l'$ and $V_{a,\text{ne}} = V_a(l,l')$ if $l \neq l'$; $a \in \mathbf{A} = \{1, \sqrt{2}, \sqrt{3}\}$.

To enforce accurate lateral boundaries for the CC, the segmentation is guided by a probabilistic CC shape prior constructed from a set of rigid-aligned training datasets. Similar techniques have already been successful in segmenting various 2D MRI and CT objects (see e.g., [100, 116]), and the current algorithm has been modified to account for specific properties of the 3D CC. In this modification, a 3D shape is described by a probabilistic model rather than a more conventional distance map representation. As illustrated in Figure 77, The probabilistic shape
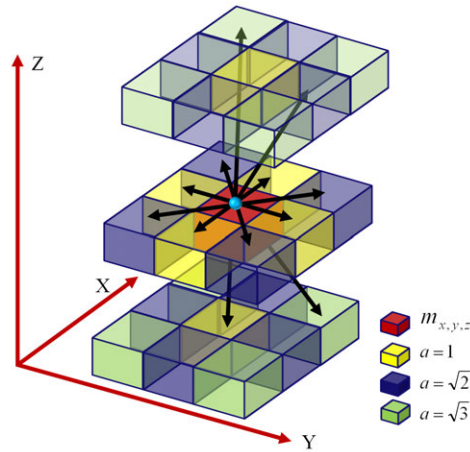
FIGURE 76: 3D 2nd order MRF neighborhood system. The reference voxel is shown in red.

model is constructed by co-aligning the training set of MRI by a rigid 3D registration using mutual information as a similarity measure [113] (Figure 77(b)); segmenting the CCs by hand from the aligned set (Figure 77(c)); and counting how many times each voxel was segmented as the CC (Figure 77(d)).
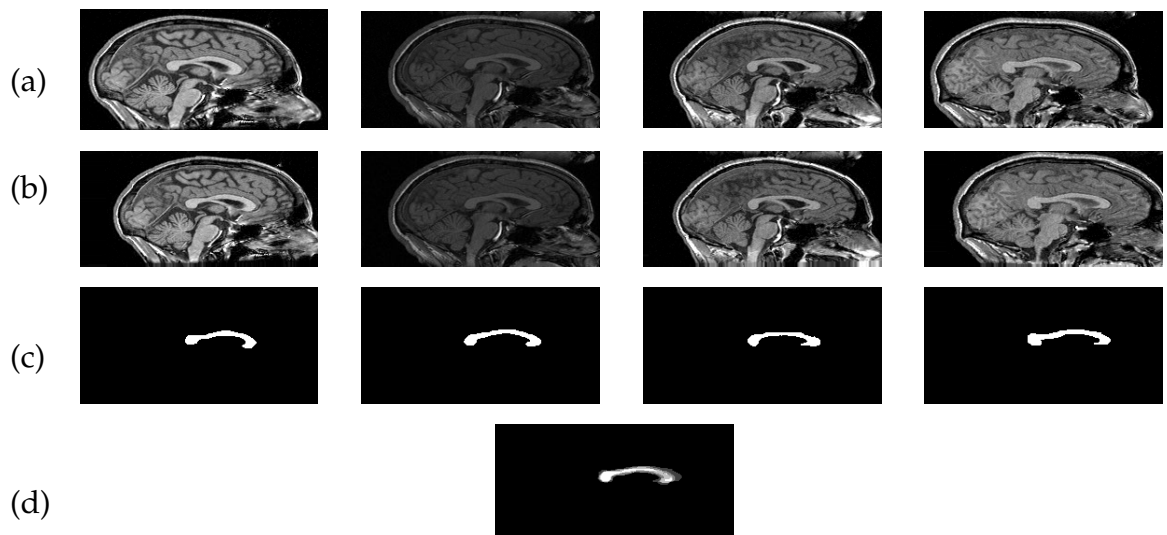
FIGURE 77: Shape reconstruction (2D illustrations): database samples (a), rigid mutual information based registration (b), manual segmentation (c), and a sagittal cross section in the estimated 3D voxel-wise probabilities of the CC shape.

In addition, the visual appearance of the CC to be segmented is modeled by approximating the 1D empirical marginal gray level distributions inside (object) and outside (background) with a linear combinations of sign-alternate discrete Gaussians (LCDG) [101–103]. The key steps for the CC segmentation are detailed in Algorithm 8.

Algorithm 8 Segmentation of the Corpus Callosum (CC) Brain Structure

---

1. Perform a rigid alignment of a given 3D MRI to an arbitrary CC prototype from the training set using mutual information as a similarity measure.

2. Estimate the conditional intensity model by identifying the bimodal LCDG.

3. Form an initial segmentation of the CC using the found conditional intensity model and the learned prior shape model.

4. Identify the MGRF model from the initial segmentation and update the conditional intensity model.

5. Perform the final Bayesian CC segmentation according to the updated joint MGRF model.

C. CENTERLINE EXTRACTION FROM THE CC

The existing approaches for extracting the centerline from 3D objects can be classified as distance transform methods [263, 264], topological thinning methods [265], and hybrid methods [266] for volumetric data and Voronoi-based methods [267] for polygonal data. Below, representative methods of each category are overviewed.

Zhou and Toga [263] proposed a voxel coding technique in which a discrete wave front propagates through the entire object starting from a manually selected reference point. The wave divides the object into a set of clusters which are approximately normal to the centerlines. Bitter et al. [264] proposed a penalized-distance algorithm to extract centerlines. Bouix et al. [266] extracted centerlines by thinning the object's medial surface, which is computed by thresholding the negative average outward flux of the gradient field of the distance map. Attali et al. [267] computed the medial surface of an object from a finite set of points by sampling its closed boundary and then pruning it based on geometric criteria to yield its centerline. Unfortunately, the existing techniques for extracting centerlines suffer from at least one of the following shortcomings: (*i*) their accuracy is dependent on the extraction of the medial surface, which is usually done using pruning methods; (*ii*) they are computationally expensive, (*iii*) suffer from lack of robustness, and (*iv*) sensitive to boundary noise. To overcome these problems, an automated level-set-based centerline extraction framework is presented to address those shortcomings. The key idea is to propagate wave-fronts from the splenium with a fast speed. Then, the trajectory of wavefront points that have the maximum positive curvature and are located at the maximum distance from the object boundary represents the extracted centerline.

Mathematically, the extraction of the centerline, connecting splenium (point A in Figure 78(a)) with rostrum (point B), is formulated in this work as a minimum-cost problem of finding the path minimizing the cumulative cost of traveling from the starting point A to the destination B. As defined in [268], if $W(x, y, z)$ is a cost function at any location (x, y, z) inside the CC, then the minimum cumulative cost at $B = (x', y', z')$ is

$$T(B) = \min_{C_{AB}} \int_0^L W(C(l))dl \qquad (12)$$

where L is the path length and C_{AB} is a set of all possible paths linking A to B

such that $C(0) = A$ and $C(L) = B$ are the starting and ending points of each path $C(l) \in C_{AB}$. The minimum cost path solving Equation (12) also satisfies the solution of the Eikonal equation:

$$|\nabla T(x, y, z)| F(x, y, z) = 1 \qquad (13)$$

where $T(x, y, z)$ is the time at which the front, evolving from the point A, crosses the point (x, y, z), and $F(x, y, z)$ is the speed function.

An approach to extract the centerline of the 3D CC is presented based on solving Equation (13) [9, 194–196, 269–273]. The main steps of the centerline extraction approach are detailed in Algorithm 9.
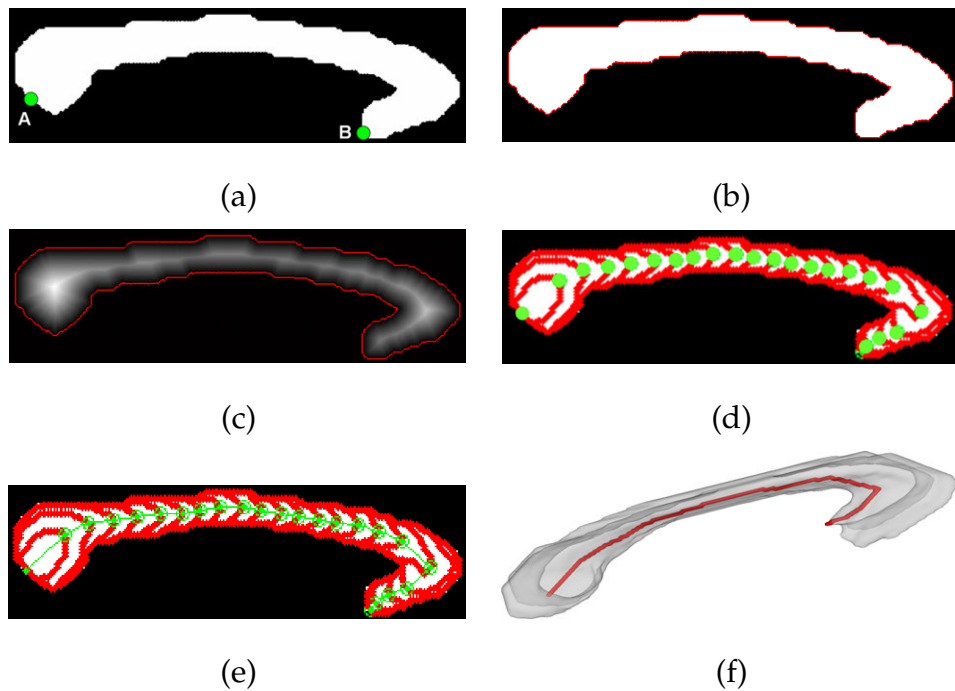
FIGURE 78: 2D Illustration for the steps of the proposed centerline algorithm: (a) a sagittal 2D cross-section on the 3D CC, (b) its estimated CC edges, (c) its normalized distance map, (d) the orthogonal wave propagated from the extracted centerline, (e) 2D extracted centerline, and (f) its 3D visualization.

Algorithm 9 Extraction of the Centerline of the CC
___

1. Find the boundary of the segmented CC by estimating its 3D edges (see Figure 78(b)).

2. Find the normalized minimum Euclidian distance $D(x, y, z)$ from every inner CC point (x, y, z) to the CC boundary (Figure 78(c)) by solving Equation (13) using the fast marching level-set at the unit speed function, $F(x, y, z) = 1$ [119].

3. Pick any splenium point as a starting point, A.

4. Propagate a wave, orthogonal to the centerline, from point A by solving Equation (13) using the fast marching level-set at the speed function $F(x, y, z) = 1 - \exp(-D(x, y, z))$ (Figure 78(d)).

5. For each propagating wave front, track the maximum curvature point (Figure 78(e,f)), which is considered at any time as the point corresponding to the starting point A. In the case of multiple relative maximal curvature points, select the one farthest from the CC boundary.

6. Terminate when the point of maximum curvature intersects the rostrum. This will be point B, and the trajectory of the maximum curvature is the centerline.

7. Repeat the process in the reverse direction, starting from B and terminating in the splenium, so as to eliminate any dependence on the somewhat arbitrary choice of A.
___

D. CYLINDRIC MAPPING TO EVALUATE CC VARIABILITY

The proposed method reveals differences between the dyslexic and normal CC by using cylindrical transformation. Before applying the cylindrical transformation, the extracted 3D CC is re-sliced by generating planes that are orthogonal to and equidistant along the CC centerline as shown in Figure 79(a,b). The re-slicing transforms 3D coordinates (x, y, z) of the voxels associated with each slice k into new coordinates (i, j, k), where (i, j) are the 2D coordinates on the corresponding slicing plane k. A boundary point (i, j) of each slice k is related to the surface of a cylinder with a fixed radius ρ as shown in Figure 80. The rectified centerline of the CC is superimposed onto the cylinder axis. Each boundary point (i, j, k) is superimposed to the corresponding polar angular location, θ, $\theta \in [0, 2\pi]$, on the cylinder by its representative distance r to the slice center (i_0, j_0, k). To account for the curvature of the CC surface, distances, r, are measured as the arc lengths of electric field lines inside a CC-shaped conducting surface with a point charge on the CC centerline axis (Figure 81).

Cross section at this plane

(a)   (b)
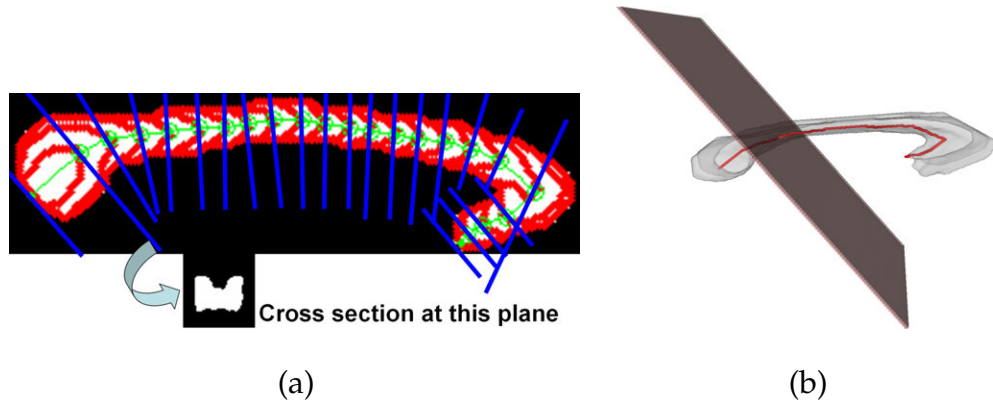
FIGURE 79: Illustrations of (a) 2D and (b) 3D re-slicing.

The proposed approach involves no parameterization, since the CC surface is simply mapped onto the cylindrical one. First, the CC surface is sliced to cross-sections, being perpendicular to the extracted centerline and having origins at the
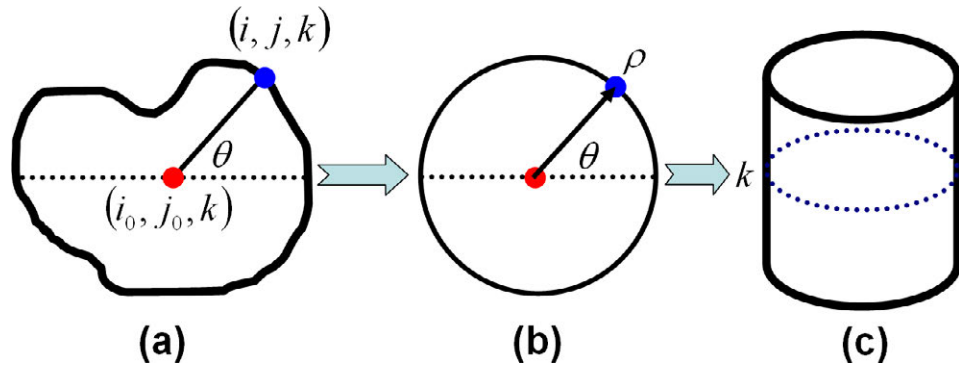
FIGURE 80: The proposed cylindric mapping: (a) a cross-section of the re-sliced CC, (b) the CC cross-section mapped onto a circle, (c) placing the circle onto the corresponding location in the cylinder.

points of the latter. All the surface points in each cross-section are mapped to the corresponding points at the cylindrical surface using rays with the same polar angles with respect to the origin. The mapping preserves the angular distances on the contour, so that the half of the contour (e.g. points located between $\theta = 0$ to $\theta = 180$) are always mapped to the half of the circle into locations with the same angles θ as shown in Figure 81.

The transformed surfaces were aggregated pointwise to provide mean CC shape maps r_{dyslexia} and r_{control}. The difference $\Delta r = r_{\text{dyslexia}} - r_{\text{control}}$, divided pointwise by their pooled standard error, yielded a statistical parametric map of unpaired t-test statistics with 28 degrees of freedom[3]. Regions of statistical significance were derived from the associated P-values using the method of Benjamini and Hochberg [274] with a false discovery rate $q* = 0.05$ (95%-confidence level).

---

[3]The degree of freedom for the unpaired t-test is the total sample size (14 normal subjects + 16 dyslexic subjects) minus 2.
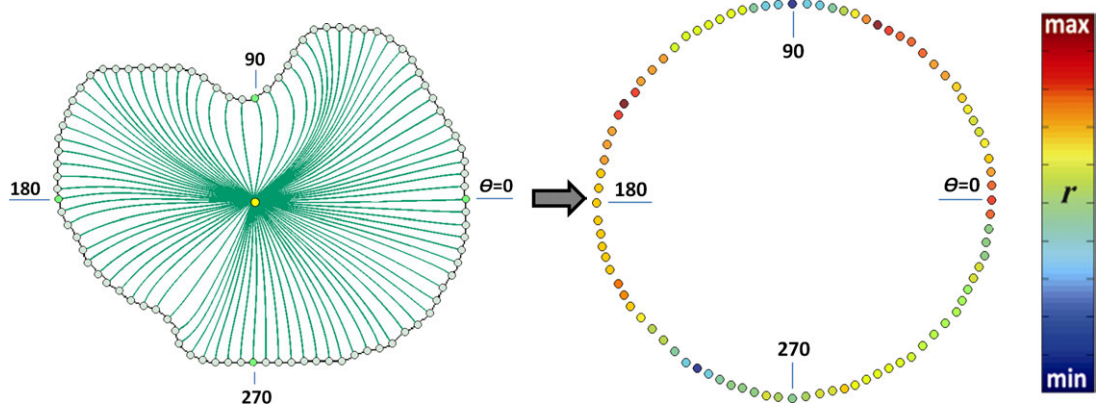
FIGURE 81: Left: A cross-section of the corpus callosum (CC) perpendicular to the centerline. Right: Mapping the cross section boundary points to the corresponding circle on the cylinder. Each point on the boundary is superimposed to the corresponding location on the circle, having the same angle θ, by its representative distance r to the CC centerline axis. The distance, r, is measured as the arc length of an electric field line inside the CC-shaped conducting surface with a point charge on the axis.

E.   PERFORMANCE EVALUATION

The proposed framework consists of two main processing steps, namely, the centerline extraction and the cylindrical mapping by estimating the arc-lengths of the electric field of a charged line located at the extracted centerline. To consider the discrete nature of the mapping, for each charged point on the centerline the arc-length of its electric field to the corresponding cross-section surface (containing the point charge and perpendicular to the centerline) is estimated. In this section, performance evaluations at each stage are illustrated, then the capability of the whole framework to detect the shape variability between two 3D surfaces is investigated using 3D simulated phantoms.

1. Centerline Extraction Evaluation on Synthetic Phantom

To validate the proposed methodology for extracting the 3D centerline of the CC, a simulated 3D phantom with a known centerline (known ground truth) was constructed. Then the proposed method was used to extract the 3D centerline and compared it to the known ground truth. Figure 82 shows two different views of the constructed 3D phantom, its known ground truth centerline, the proposed estimated centerline, and the proposed estimated centerline superimposed on the ground truth. To determine the accuracy of estimating the centerline, the middle slice that contains the centerline is analyzed; the percentage radial error is $0.466 \pm 0.387\%$ with respect to the CC thickness.

(a)	(b)	(c)	(d)
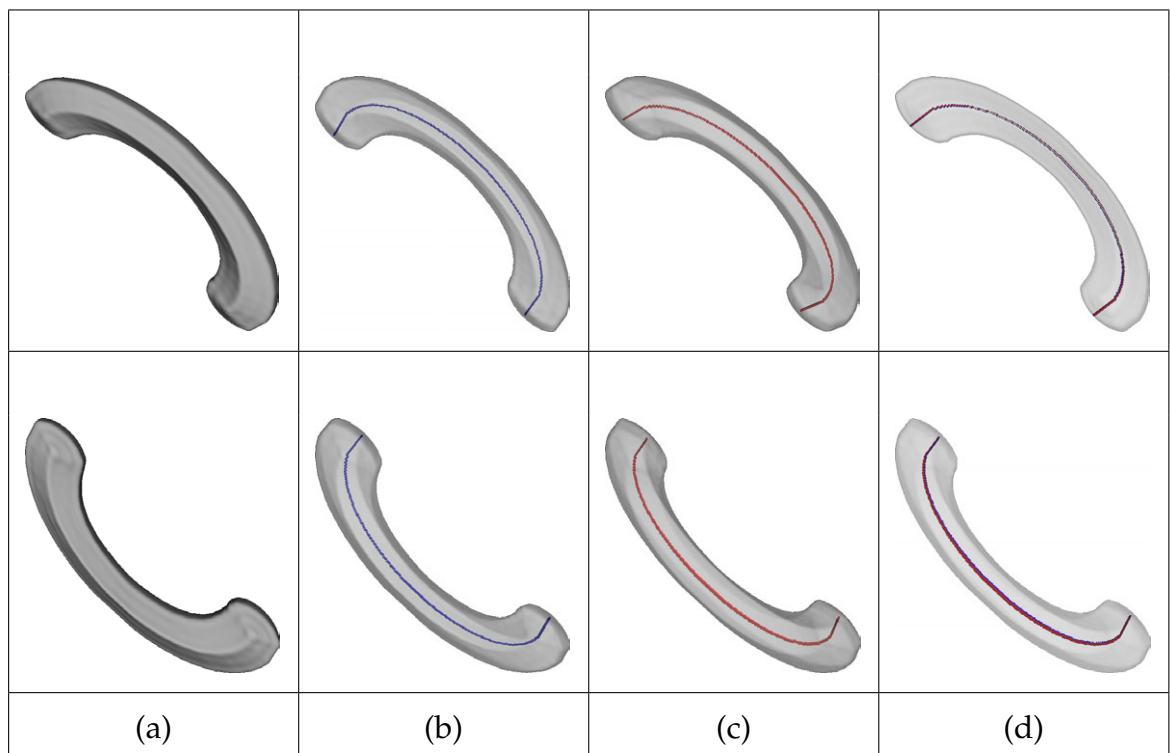
FIGURE 82: Validation results of 3D centerline extraction on a simulated phantom visualized on two different views (up and down rows): (a) the 3D phantom, (b) its known ground truth centerline, (c) the proposed estimated centerline, and (d) the proposed estimated centerline superimposed on the ground truth.
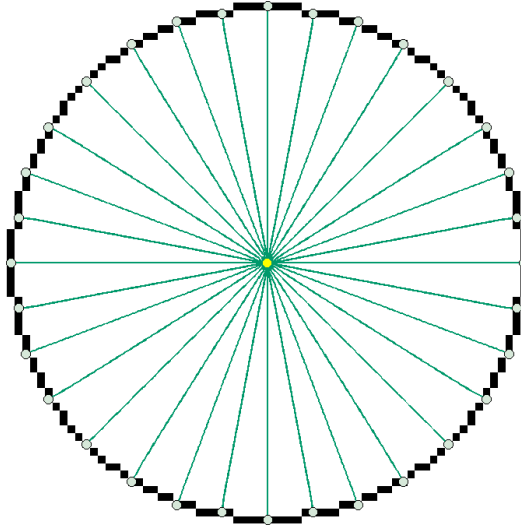
FIGURE 83: Validation of electric field establishing and arc-length estimation for a simulated phantom of a circle with a point charge at center.

2.   Validation of Electric Field Establishing and Arc-length Estimation on a Synthetic Phantom

The proposed approach for establishing the electric field and estimating the arc-length was validated on a simulated phantom image of a circular cross-section with a point charge at its center (see Figure 83). The exact electric field (ground truth) for this problem is established as straight lines in the radial direction. The error is measured for each point on the circle as the percentage difference between the estimated arc-length and the exact radius of the circle, achieving $0.86\% \pm 0.7815\%$ (mean±standard deviation (SD)) over all circle points.

3. Validation of Variability Detection between 3D Surfaces using Synthetic Phantoms

Since the preliminary results show a reduced length and a thicker body for the CC of dyslexic subjects, three synthetic 3D phantoms were constructed: a reference phantom, and short and thin phantoms with respect to the reference phantom (see Figure 84), in order to simulate the shape variability between the dyslexic and normal subject. To investigate the ability of the proposed approach to detect the shape variabilities between the dyslexic and normal CC shapes, it was tested on these synthetic phantoms. The unfolded cylindrical mapped sheets for the three phantoms (Figure 85) show that the proposed cylindrical mapping has successfully detected the shape variability between the reference and both the short and thin phantoms.

(a)   (b)   (c)
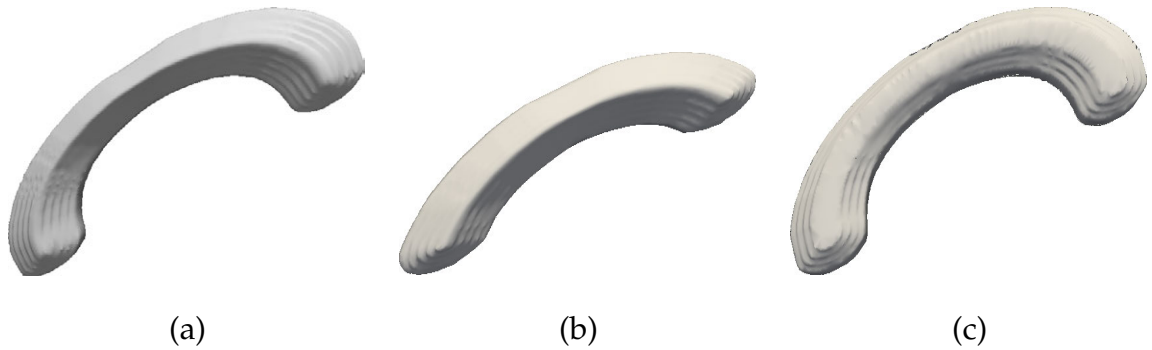
FIGURE 84: 3D simulated phantoms to test the ability of the proposed approach in detecting variability between 3D surfaces: (a) reference phantom, (b) short phantom, and (c) thin phantom.

In order to quantify the accuracy of shape variability detection, the inverse cylindrical mapping of the resulted sheets was applied. Let V_{Ref}, V_{Short}, and V_{Thin} denote the volumes of CC (number of voxels times the voxel volume) for the reference, short, and thin phantoms, respectively. Then, the volume of variability between the reference and short phantoms is $\frac{V_{\text{Ref}} - V_{\text{Short}}}{V_{\text{Ref}}} \times 100\%$, and between the reference and thin phantoms is $\frac{V_{\text{Ref}} - V_{\text{Thin}}}{V_{\text{Ref}}} \times 100\%$. The volumes of variability before

| | (a) | (b) | (c) |
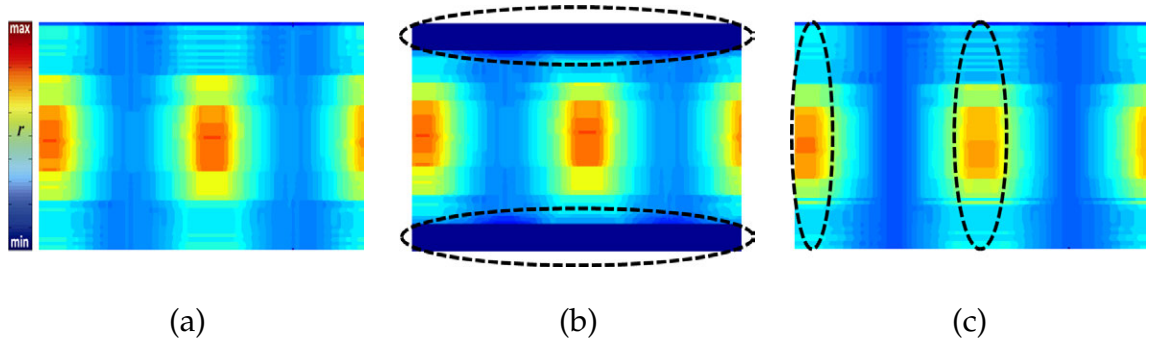
FIGURE 85: Unfolded cylindrical mapped sheets for (a) the reference, (b) short, and (c) thin simulated phantoms presented in Figure 84; dotted black lines point to the detected variability with respect to the reference phantom.

applying the cylindrical mapping (the ground truth) and after applying the cylindrical and inverse mapping (the detected volume) is callulated. Table 17 shows that the percentage errors in the detected volumes of variability with respect to the ground truth are less than 1%. Figures 86 and 87 visualize the errors in detecting the variability between the reference phantom, and the short and thin phantoms, respectively.

TABLE 17: The percentage error in the detected volumes of variability between the short and reference phantoms and between the thin and the reference phantom.

	Phantoms	
	Short and reference	Thin and reference
Ground truth volume of variability	33.0%	4.5%
Detected volume of variability	32.2%	4.1%
Percentage error	0.8%	0.4%

(a)   (b)   (c)
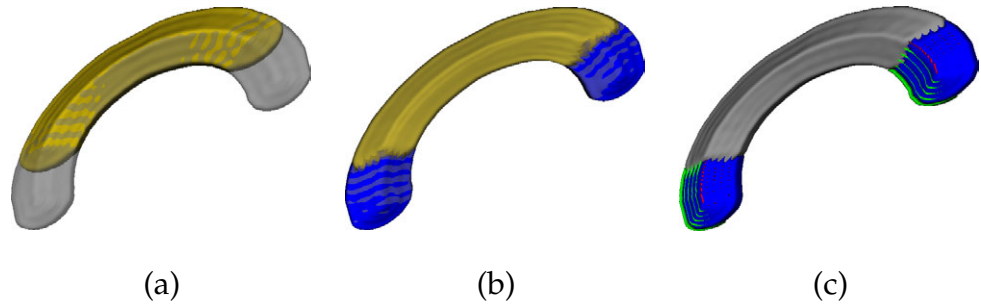
FIGURE 86: Accuracy of detecting the variability between the short and reference phantoms: (a) the short phantom superimposed on the reference phantom, (b) ground truth variability (blue) between the two phantoms, and (c) estimated variability using the proposed approach: blue represents the common detected area with the ground truth (true positive), red represents the missed points that were not detected (false negative), and green represents the introduced detected points that were not on the ground truth (false positive).

(a)   (b)   (c)
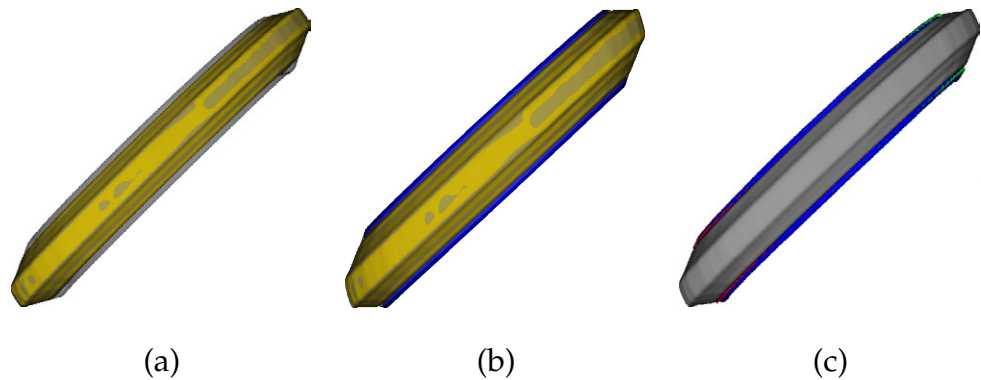
FIGURE 87: Accuracy of detecting the variability between the thin and reference phantoms: (a) the short phantom superimposed on the reference phantom, (b) ground truth variability between the two phantoms, and (c) estimated variability using the proposed approach: blue represents the common detected area with the ground truth (true positive), red represents the missed points that were not detected (false negative), and green represents the introduced detected points that were not on the ground truth (false positive).

F.   EXPERIMENTAL RESULTS

The proposed approach has been tested on in-vivo data collected from 16 right-handed dyslexic subjects aged 18 to 40 years, and a group of 14 controls who match for gender, age, educational level, socioeconomic background, handedness, and general intelligence. All the subjects were physically healthy, with no history of neurological diseases or head injury, and in brief have exactly the same psychiatric conditions. A summary of study participants is presented in Table 18. The images with voxel resolution $0.9375 \times 0.9375 \times 1.5$ mm^3 were acquired with the same GE 1.5T MRI scanner (Milwaukee, Wisconsin, USA) using a T1 weighted imaging sequence protocol. The "ground truth" diagnosis to evaluate the classification accuracy for each patient was given by clinicians. The CC segmentation results are illustrated in Figure 88. Comparative results with the known ground truth for the 15 data sets, which are not used in the training (manually segmented by an expert), have achieved a percentage error of $0.98 \pm 0.73\%$.

1.   3D Detection of CC Abnormalities of Dyslexia

Figures 89(a) and (b) present the average cylindrical maps r_{dyslexia} and r_{control} for 14 normal subjects and 16 dyslexic subjects. The difference $\Delta r = r_{\text{dyslexia}} - r_{\text{control}}$ is represented in Figure 90(a). As shown in Figure 90(a), some locations in these maps differ significantly for the normal and dyslexic subjects at the 95% confidence level. The inverse cylindrical mapping outlines the significant areas on the average CC of normal subjects (Figure 90(b)). These areas show that these significant differences (at the 95% confidence interval) exist in the four anatomical divisions of the CC, namely, splenium, rostrum, genu, and body. As shown in Figure 90(b), the white matter in dyslexic subjects was greater than controls, bilaterally along the body of the CC (i.e, the CC body for the dyslexic subjects is thicker than for the

TABLE 18: Summary of study participants. All participants were right handed, male, and Caucasian. Values are given as mean±SD. GFW stands for Goldman-Fristoe-Woodcock sound symbol test, GORT-3 stands for gray oral reading test, 3rd edition, WAIS-R atands for Wechsler adult intelligence scale, revised, and WRAT-3 stands for wide range achievement test, third edition

Feature	Dyslexic Subjects	Control Subjects
Number of Subjects	16	14
Age (years), *mean*	28.2	25.1
Range	18.5–40.4	17.8–40.6
Education (years)	14±3	14±2
Social Class	middle to upper middle	middle to upper middle
WAIS-R IQ	113±7	111±12
GORT-3 *Passage*	4±2	13±2
Comprehension	13±2	11±2
GFW *Reading*	41±4	51±4
Spelling	43±8	51±8
WRAT-3 *Reading*	91±11	107±7
Spelling	74±14	106±7
Arithmetic	97±13	112±11
LAC total	80±12	96±5

normal ones). Where differences attained statistical significance, the Δr achieved values up to 6.4 mm on the right and 7.0 mm on the left. There was, however, a reduction at the anterior and posterior extreme of the structure in dyslexia. In particular, significant values of Δr were observed as low as -6.5 mm in genu and -4.7 mm in splenium. There was otherwise no significant difference around the medial sagittal plane (Figure 90(b)).
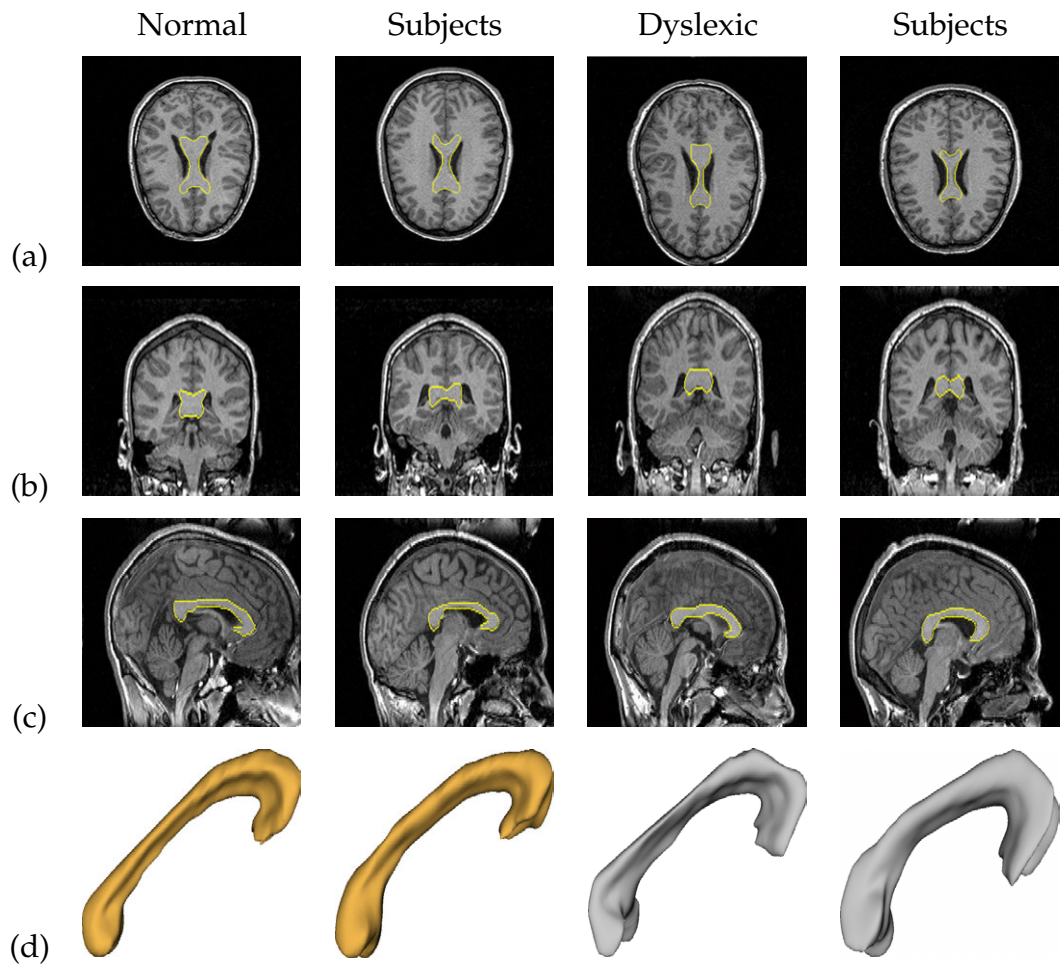
FIGURE 88: Automated 3D CC segmentation results projected onto the 2D (a) axial, (b) coronal, (c) sagittal planes, and (d) their 3D visualization.
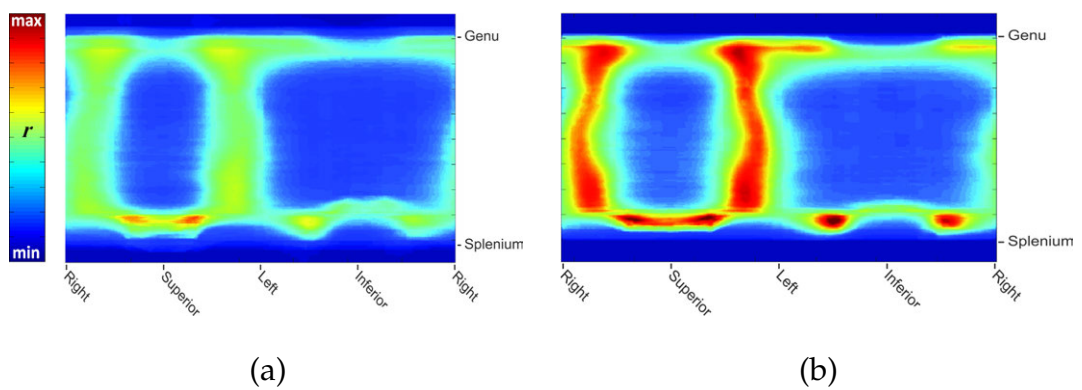
FIGURE 89: Average cylindric maps of (a) normal and (b) dyslexic subjects

(a)   (b)
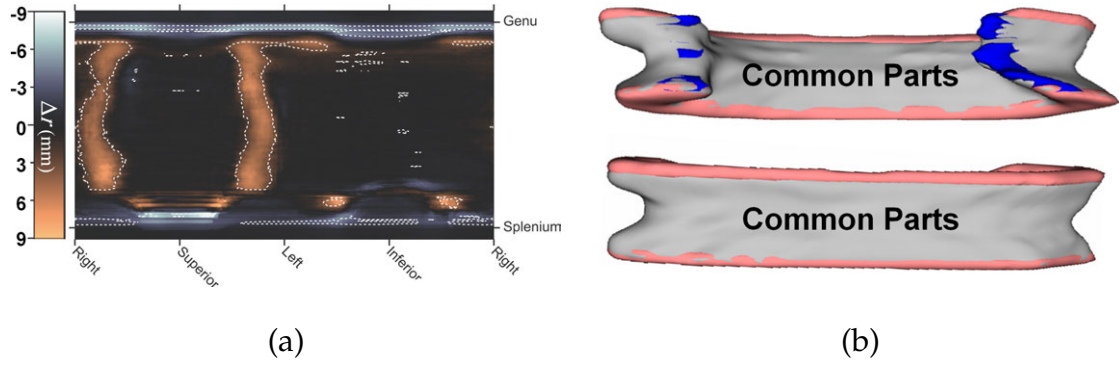
FIGURE 90: (a) Areas of the 95%-significant difference between normal and dyslexic subjects, and (b) color-coded anatomical differences between the CC for normal and dyslexic subjects: the common parts (gray), parts that exist in normal and do not exist in dyslexic subjects (blue), and parts that exist in dyslexic and do not exist in normal subjects (pink).

2. 3D Shape Analysis Diagnostic Results

Since the proposed results show a reduced length and a thicker body for the CC of dyslexic subjects, two features were selected to classify dyslexic and normal subjects, namely, the centerline length (CLL) and the CC thickness (CCT). The CCT for each subject is estimated as the mean thickness for each CC cross-section perpendicular to the centerline (see Figure 91). The differences in the mean length of the centerline of CCs and in the mean thickness of the CCs between dyslexic and control subjects are statistically significant according to the unpaired t-test (the two-tailed value P is less than 0.033 and 10^{-4}, respectively) as shown in Table 19.

The training subset for classification (14 persons used in the training) was arbitrarily selected among all the 30 subjects. The accuracy of classification based on using the k-nearest neighbor classifier for the test subjects (16 persons: nine dyslexic and seven control) was evaluated using the χ^2-test at 95% confidence level in order to examine significant differences in the Levy distances. Table 20 summarizes the diagnostic results for the test subjects at the 95% confidence interval
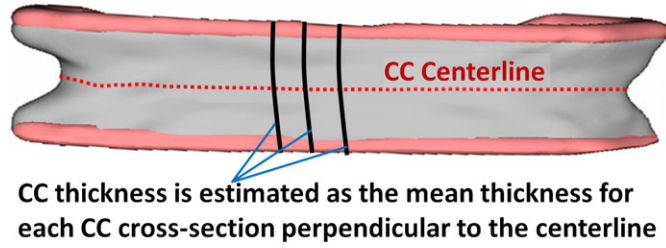
FIGURE 91: Features used to classify normal and dyslexic subject: the centerline length (CLL) and the mean CC thickness (CCT).

TABLE 19: Statistical analysis for the centerline length and the CC thickness for 16 dyslexic subjects and 14 control subjects.

	centerline length (CLL)		CC thickness (CCT)	
	Dyslexia	Control	Dyslexia	Control
Minimum (mm)	77.8	78.1	15.9	13.2
Maximum (mm)	90.9	105.4	57.3	50.0
Mean (mm)	86.4	90.6	37.6	27.9
Standard deviation	6.5	3.5	2.5	2.7
Significant difference, P-value	0.033		$< 10^{-4}$	

for the traditional white matter volumetric approach [11] and k-nearest neighbor classifiers based on the CLL, the CCT, and both the CLL and CCT. As shown in Table 20, the k-nearest neighbor classifier based on each of the two proposed extracted 3D shape features, i.e., CLL and CCT, achieves a higher accuracy than the traditional white matter volume-based approach. Moreover, combining the two features increases the accuracy from 75% (using the CLL alone)–88% (using CCT alone) to 94%. These results highlight the advantage of the proposed diagnostic approach and indicates that the CLL and CCT are promising supplements to current metrics that discriminate between normal and dyslexic subjects.

TABLE 20: Summary of diagnostic results for the test datasets (nine dyslexic subjects and seven control subjects) at 95% confidence interval for white matter volumetric approach (WMVA), Centerline Length (CLL) based approach, CC Thickness (CCT) based approach, and the combined CLL and CCT based approach.

	Dyslexic subjects	Control subjects	All subjects
WMVA	4 out of 9 (44%)	4 out of 7 (57%)	8 out of 16 (50%)
CLL	7 out of 9 (78%)	5 out of 7 (71%)	12 out of 16 (75%)
CCT	9 out of 9 (100%)	5 out of 7 (71%)	14 out of 16 (88%)
CLL & CCT	9 out of 9 (100%)	6 out of 7 (86%)	15 out of 16 (94%)

Another metric to test the performance of the system is to compute the Receiver Operating Characteristic (ROC). The ROC curve tests the sensitivity of the proposed diagnostic approach against the selection of the operating point (the classification threshold) by showing the relationship between the true positive and false positive fractions at different operating points. Each point on the graph is generated by using a different cut point (classification threshold). Figure 92 shows the ROC of four approaches; white matter volumetric approach [11], CLL based approach, CCT based approach, and the combined CLL and CCT diagnostic approach. Consistently, the combined CLL and CCT based classification approach achieves the highest performance, evidenced by the largest area under its ROC curve (Az=0.982, approaching the ideal value of 1).

G. DISCUSSION

Previous work has related dyslexia to a minicolumnopathy [155] and a bias in corticocortical connectivity that emphasizes longer connections at the expense of shorter ones [155, 179]. This is manifested as a decrease in the outer radiate white matter compartment (short arcuate connections) and an increase in the size of the
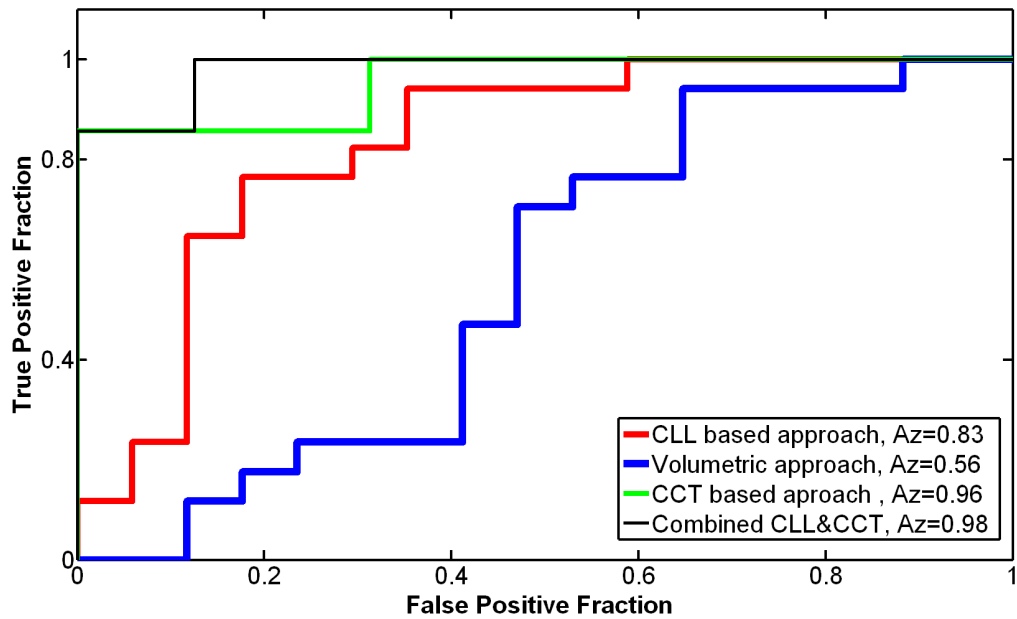
FIGURE 92: The ROC curves for white matter volumetric approach [11] (blue), CLL based approach (red), CCT based approach (green), and the combined CLL and CCT diagnostic approach (black). Note that 'Az' stands for the area under the curve.

CC (long commissural fibers) [275]. Corresponding changes have been found in gyral white matter depth when used as a proxy measurement for the gyral window [179].

The present study expands on previous findings by illustrating in a graphical manner the nature of the CC disturbance in dyslexia. Preliminary attempts at "conformal mapping" have measured straight-line distances from the axis to the boundary of the region of interest as a function of polar angle. This is not a conformal (angle-preserving) map, and more importantly, may not be invertible. The cross sections of many anatomical structures are not perfectly convex, or even star-shaped, so a ray from the axis may intersect the boundary at more than one point. These discontinuities may provide for spurious shape distortions within given segments of the analyzed outline.

The proposed implemented method measures the distance from a point on the boundary to the axis by the arc length of an electric field line, inside a CC-shaped conducting surface, with a point charge on the axis. Besides avoiding the problem of rays intersecting the boundary at more than one point, this approach can be used directly on three-dimensional volumes by solving the Laplace equation with a line charge on the axis of the two-dimensional boundary surface at zero potential. The point of intersection with the axis provides that point's z-coordinate in the projection space. Applying the method to the present series revealed abnormalities in CC size with an overall preservation of its general outline.

Previous studies suggest size differences of the CC in patients with dyslexia (e.g., in the study by Hydn et al. [23]). The nature of this abnormality has been variously ascribed to all major segments of this commissural tract [23, 193]. While comments on CC size difference abound in the dyslexia literature, references as to the shape of this structure are, by comparison, scant. A morphometric study by Robichon and Habib [25] indicated that the CC of dyslexic patients was more rounded and evenly thicker. The authors suggested that their finding, increased size of the CC and a corresponding increase in commissural connections, could explain reports of reduced cortical asymmetries in this condition [276]. Another study by Robichon et al. [277] showed significant differences in the angulation of the posterior segment of the CC. The finding was discussed in relation to parietal asymmetries and possible hormonal effects occurring in utero or during the early postnatal period in this patient population. The findings presented in this work are in agreement with those of Robichon and Habib [25]. Shape reconstruction using the proposed method indicates a generalized increase in size of the CC in patients with dyslexia (Figure 90). Size reductions at both poles may help average out any size increase and provide an explanation to negative studies of CC morphology in dyslexia [278]. In this regard, shape analysis offers complementary information to a real measurement in neuroimaging studies.

The shorter length of CC of dyslexic subjects (as shown in Table 19) is correlated with the results in [23] and with the results in more recent studies [26, 193]. Moreover, the proposed 3D mapping approach has the capability to demonstrate the whole anatomical differences (voxel-based) in the CC of normal and dyslexic brains instead of only differences in the CC divisions (area-based) as done by previous groups. Thus, the existing differences in all anatomical divisions of the CC (namely, splenium, rostrum, genu and body) were identified as shown in Figure 90.

H. SUMMARY

In total, the preliminary results in this chapter suggest that the proposed approach can detect significant differences in the four anatomical divisions of the CC. Moreover, it is able to demonstrate voxel-based anatomical differences between the CC of normal and dyslexic brains, rather than only area-based differences in the previous work. For evaluation, the proposed diagnostic system has been tested over subjects of ages that have well-known ground truth diagnosis. These experiments have confirmed that the 3D shape analysis of the CC, based on the centerline length and the CC thickness, is able to accurately discriminate between the dyslexic and normal subjects. These findings lead towards more efficient non-invasive computer assisted systems for diagnosis of dyslexia. The work presented in this chapter has been published in [9, 194–196]. Future work includes investigating the reliability of the proposed approach on MRI data of children at early ages, as well as infants, in order to investigate its usability in early dyslexia diagnostics. In addition, different brain structures will be investigated in order to quantitatively characterize the development and temporal changes of dyslexic brains.

CHAPTER VIII

CONCLUSIONS AND FUTURE WORK

Detecting abnormalities in medical structures is very challenging. This is due to a large and constantly growing number of different objects of interest and their associated abnormalities, large variations of their appearances and shapes in images, different medical imaging modalities, and associated changes of signal homogeneity and noise for each object. In this work, comprehensive mathematical models and novel advanced techniques are provided to analyze medical images and to automatically detect abnormalities in medical structures. The proposed models and techniques show promising results for solving difficult medical problems such as:

- Automatic segmentation of the left ventricle (LV) wall [122].

- Automatic delineation of the pathological tissues in the LV wall [132].

- Automatic quantification and follow-up of the LV dysfunction [127].

- Automatic estimation of the functional strain from cardiac images [146, 147].

- Automatic quantification of anatomical differences between the corpus callosum (CC) of dyslexic and control subjects [194, 195].

- Automated diagnosis of dyslexia based on analyzing brain images [9, 196].

In the following section, a summary of the most important contributions in this dissertation will be presented.

A. CONTRIBUTIONS

- Three novel models for the segmentation of medical structures have been
  proposed. The first model is a graph-cut optimization model that integrates
  both the appearance and shape of the object of interest for the purpose of seg-
  mentation. Experiments confirmed that this approach showed superior re-
  sults in segmenting the cavity of the heart. The second model is a fast march-
  ing level-set that evolves from an initial boundary with a speed function that
  is formed based on the intensity, spatial interaction, and object shape. Exper-
  iments confirmed the high capabilities of the proposed approach to evolve
  from the heart cavity and stop by the outer border of the LV, providing an
  accurate segmentation of the outer contour of the LV wall. The third seg-
  mentation approach makes full use of the intensity and spatial interaction de-
  scriptors, in a joint Markov-Gibbs random field (MGRF) model of the image
  signals and their region map, to identify the pathological tissue in the LV wall
  with high accuracy confirmed by both Dice similarity coefficient (DSC) and
  Bland Altman analyses. The intensity, spatial interaction, and shape descrip-
  tor are further extended to 3D to segment the corpus callosum (CC) structure
  from the magnetic resonance images (MRI) of the brain. The preliminary re-
  sults of the proposed segmentation approaches confirm the benefits of these
  models and encourage applying them in other applications.

- An accurate model to estimate the transmural extent, an important metric
  to quantify the myocardial wall of the heart, has been proposed. The model
  is based on solving the partial differential equation (PDE) to collocate the
  correspondence between two contours. Phantom validation showed that the
  PDE Laplace-based method outperforms the current methods in estimating
  the transmural extent, namely, the radial and centerline methods.

- A novel method for strain estimation from cine cardiac MRI is proposed. Unlike current methods that depend on the intensity and spatial information to track the wall motion, the proposed method sticks to the geometry of the heart to track its motion. To achieve this goal, the application of the proposed PDE method is extended to track the LV wall points by solving the Laplace equation between the LV contours of each two successive image frames over the cardiac cycle. The main advantage of the proposed tracking method over traditional texture-based methods is its ability to track the movement and rotation of the LV wall based on tracking the geometrical features of the inner, mid-, and outer walls of the LV. This overcomes noise sources that come from heart motion and that are associated with the scanning process. In addition, the proposed method showed accurate validation results on simulated phantoms with predefined point locations of the LV wall over the cardiac cycle.

- A novel mapping model to establish correspondences between two 3D surfaces is presented. Surfaces are mapped to a unified cylindrical domain for analysis. Validation on 3D simulated phantoms demonstrates the ability of the proposed approach to accurately detect the shape variability between two 3D surfaces. The model has been used to detect the abnormalities in the CC brain structure between the dyslexic and normal brains by analyzing the CCs in the cylindrical domain. This mapping leads to detect abnormalities in all divisions of the corpus callosum (i.e., splenium, rostrum, genu and body) and offers a whole 3D analysis of the CC abnormalities instead of only area based as done by the previous groups.

- A novel diagnostic framework for dyslexia detection is proposed, based on novel 3D features extracted by 3D shape analysis of the CC brain structure. Experiments have confirmed that the 3D shape analysis of the CC, based on the centerline length and the CC thickness, is able to accurately discriminate between the dyslexic and normal subjects. These findings lead toward

more efficient non-invasive computer assisted systems for the diagnosis of dyslexia.

B.   DIRECTIONS FOR FUTURE RESEARCH

Several possibilities of future work to further enhance the approaches proposed in this dissertation and to extend their use in other applications include, but are not limited to, the following:

- The spatial interaction model, which is used in the segmentation, is limited to pair-wise interactions. One of the trends is to develop higher-order MGRF models to more accurately define the spatial interaction between voxels. Future work includes investigating the powerful capabilities of these model to increase the accuracy of the proposed segmentation models.

- The shape model used in this dissertation is a probabilistic shape model, which may not be sufficient to describe complex shapes in case of limited number of training datasets. Future work includes investigating other shape models, such as a linear combinations of distance maps, in order to improve the efficiency of describing the object shape.

- The segmentation model is based on intensity, spatial interaction, and shape. One of the trends that is worth testing is the integration of the these features with other image features (e.g., scale space features, derivatives, etc). This might improve the segmentation accuracy.

- Since this dissertation proposed a method to estimates the functional strain from cardiac cine MRI. Future work includes estimating the correlation coefficients between the strain index and other performance indexes derived

from cine images, such as global (e.g., ejection fraction) and local (e.g., wall thickening) indexes. This will avoid the inter-slice variability problem since all these indexes will be derived from cardiac cine MRI data.

- The strain estimation method proposed in this dissertation is performed on 2D thick slices. Hence, a natural extension is to generalize the approach to be used for 4D (3D+time).

- A future work of this dissertation is to apply the developed models in other clinical applications such as the detection of cancerous cells in the prostate, the second leading cause of death for males in the United States. Most prostate images are often low contrast where the prostate boundaries are barely identified. To provide a more accurate segmentation of the prostate tissue and the cancerous region, more advanced mathematical models to accurately describe the visual appearance of the prostate images will be developed (e.g., higher-order MGRF models to better define the spatial interaction between the prostate voxels). The preliminary results of this work has been published in many conference proceedings and journal articles [279–287].

- A future work of this dissertation is to investigate the integration of the proposed work with the BioImaging lab work for the early detection of acute renal rejection [128, 129, 288–302].

- A future work of this dissertation is to investigate the integration of the proposed work with the BioImaging lab work for the early detection of lung cancer [143, 303–335].

- A future work of this dissertation is to investigate the integration of the proposed work with the BioImaging lab work for the detection of other brain disorders such as autism [313, 336–343].

REFERENCES

[1] A. Tsai, A. Yezzi, W. Wells, C. Tempany, D. Tucker, A. Fan, W. Grimson, and A. Willsky. A shape based approach to the segmentation of medical imagery using level sets. *IEEE Transactions on Medical Imaging*, 22:137–154, 2003.

[2] Medical skepticism, vol. 5. `http://glasshospital.com/2011/10/30/medical-skepticism-vol-5/`.

[3] A. G. Webb. *Introduction to Biomedical Imaging*. Wiley–IEEE Press, NJ, USA.

[4] M. D. Cerqueira, N. J. Weissman, V. Dilsizian, A. K. Jacobs, S. Kaul, W. K. Laskey, D. J. Pennell, J. A. Rumberger, T. Ryan, M. S. Verani, and American Heart Association Writing Group on Myocardial Segmentation and Registration for Cardiac Imaging. Standardized myocardial segmentation and nomenclature for tomographic imaging of the heart a statement for healthcare professionals from the cardiac imaging committee of the council on clinical cardiology of the american heart association. *Circulation*, 105:539–542, 2002.

[5] M. Nitzken, M. F. Casanova, G. Gimel'farb, A. Elnakib, F. Khalifa, A. Switala, and A. El-Baz. 3D shape analysis of the brain cortex with application to dyslexia. In *Proc. International Conference on Image Processing (ICIP'2011)*, pages 2657–2660. IEEE, 2011.

[6] A. El-Baz, M. Casanova, G. Gimel'farb, M. Mott, A. Switala, E. Vanbogaert, and R. McCracken. Dyslexia diagnostics by 3D texture analysis of cerebral white matter gyrifications. In *Proc. International Conference on Pattern Recognition (ICPR'2008)*, pages 1–4. IEEE, 2008.

[7] A. El-Baz, M. Casanova, G. Gimel'farb, M. Mott, A. Switala, E. Vanbogaert, and R. McCracken. A new CAD system for early diagnosis of dyslexic brains. In *Proc. International Conference on Image Processing (ICIP'2008)*, pages 1820–1823. IEEE, 2008.

[8] A. El-Baz, M. Casanova, G. Gimel'farb, M. Mott, and A. Switala. An MRI-based diagnostic framework for early diagnosis of dyslexia. *International Journal of Computer Assisted Radiology and Surgery*, 3(3-4):181–189, 2008.

[9] A. Elnakib, M. F. Casanova, G. Gimel'farb, A. E. Switala, and A. El-Baz. Dyslexia diagnostics by 3-D shape analysis of the corpus callosum. *IEEE Transactions on Information Technology in Biomedicine*, 16(4):700–708, 2012.

[10] T. Schultz. Estimating the crossing of nerve fibers in the human brain. In *Proc. SPIE on Electronic Imaging & Signal Processing (SPIE'2009)*, pages 1–3, 2009.

[11] M. Casanova, J. Araque, and J. Giedd. Reduced brain size and gyrification in the brains of dyslexic patients. *Journal of Child Neurology*, 9(4):275–281, 2004.

[12] P. Mansfield. Imaging by nuclear magnetic resonance. *Journal Physics E: Science Instrumentaion*, 21:18–30, 1984.

[13] P. Mansfield. Snapshot magnetic resonance imaging (nobel lecture). *Angewandte Chemie International Edition*, 43(41):5456–5464, 2004.

[14] E. M. Haacke. *Magnetic Resonance Imaging: Physical Principles and Sequence Design*. J. Wiley & Sons, New York, USA, 1999.

[15] F. W. Wehrli, J. MacFall, T. H. Newton, and D. G. Potts. *Advanced Imaging Techniques*. Clavadel Press, San Francisco, CA, USA, 1983.

[16] W. G. Bradley. Effect of magnetic relaxation times on magnetic resonance image interpretation. *Noninvasive Medical Imaging*, 1:193–204, 1984.

[17] H. Michaely, K. Herrmann, K. Nael, N. Oesingmann, M. Reiser, and S. Schoenberg. Functional renal imaging: Nonvascular renal disease. *Abdominal Imaging*, 32(1):1–16, 2007.

[18] F. Khalifa, A. El-Baz, G. Gimel'farb, and M. A. El-Ghar. Non-invasive image-based approach for early detection of acute renal rejection. In *Proc. International Conference on Medical Image Computing and Computer-Assisted Intervention (MICCAI'2010)*, pages 10–18, Beijing, China, September 20–24, 2010.

[19] L. Mechtler. Neuroimaging in neuro-oncology. *Neurologic Clinics*, 27(1):171–201, 2009.

[20] N. M. I. Noble, D. L. G. Hill, M. Breeuwer, and R. Razavi. The automatic identification of hibernating myocardium. In *Proc. International Conference on Medical Image Computing and Computer-Assisted Intervention (MICCAI'2004)*, pages 890–898, 2004.

[21] S. Nazarian, D. A. Bluemke, A. C. Lardo, M. M. Zviman, S. P. Watkins, T. L. Dickfeld, G. R. Meininger, A. Roguin, H. Calkins, G. F. Tomaselli, R. G. Weiss, R. D. Berger, J. A. Lima, and H. R. Halperin. Magnetic resonance assessment of the substrate for inducible ventricular tachycardia in nonischemic cardiomyopathy. *Circulation*, 112:2821–2825, 2005.

[22] M. Y. Henein. *Heart Failure in Clinical Practice*. Springer-Verlag, 2010.

[23] G. W. Hynd, J. Hall, E. S. Novey, D. Eliopulos, K. Black, J. J. Gonzalez, J. E. Edmonds, C. Riccio, and M. Cohen. Dyslexia and corpus callosum morphology. *Archives of Neurology*, 52(1):32–38, 1995.

[24] J. M. Rumsey, M. E. Casanova, G. B. Mannheim, N. Patronas, N. DeVaughn, S. D. Hamburger, and T. Aquino. Corpus callosum morphology, as measured with MRI, in dyslexic men. *Biological Psychiatry*, 39(9):769–775, 1996.

[25] F. Robichon and M. Habib. Abnormal callosal morphology in male adult dyslexics: Relationships to handedness and phonological abilities. *Brain and Language*, 62(1):127–146, 1998.

[26] J. G. Fine, M. Semrud-Clikeman, T. Z. Keith, L. M. Stapleton, and G. W. Hynd. Reading and the corpus callosum: An MRI family study of volume and area. *Neuropsychology*, 21(2):235–241, 2007.

[27] H. P. Kühl, A. M. Beek, A. P. van der Weerdt, M. B. Hofman, C. A. Visser, A. A. Lammertsma, N. Heussen, F. C. Visser, and A. C. van Rossum. Myocardial viability in chronic ischemic heart disease: Comparison of contrast-enhanced magnetic resonance imaging with (18)F-fluorodeoxyglucose positron emission tomography. *Journal of the American College of Cardiology*, 41(8):1341–1348, 2003.

[28] A. Elnakib, G. Gimel'farb, J. S. Suri, and A. El-Baz. Medical image segmentation: A brief survey. In A. El-Baz, R. Acharya, A. Laine, and J. Suri, editors, *Multi Modality State-of-the-Art Medical Image Segmentation and Registration Methodologies*, chapter 1, pages 1–39. Springer, New York, 2011.

[29] R. J. Kim, D. S. Fieno, T. B. Parrish, K. Harris, E.-L. Chen, O. Simonetti, J. Bundy, J. P. Finn, F. J. Klocke, and R. M. Judd. Relationship of MRI delayed contrast enhancement to irreversible injury, infarct age, and contractile function. *Circulation*, 100:1192–2002, 2009.

[30] D. S. Fieno, R. J. Kim, E. L. Chen, J. W. Lomasney, F. J. Klocke, and R. M. Judd. Contrast-enhanced magnetic resonance imaging of myocardium at risk: Distinction between reversible and irreversible injury throughout infarct healing. *Journal of the American College of Cardiology*, 36(6):1985–1991, 2000.

[31] R. M. Setser, D. G. Bexell, T. P. ODonnell, A. E. Stillman, M. L. Lieber, P. Schoenhagen, and R. D. White. Quantitative assessment of myocardial scar in delayed enhancement magnetic resonance imaging. *Journal of Magnetic Resonance Imaging*, 18(4):434–441, 2003.

[32] L. Amado, B. Gerber, S. Gupta, D. Rettmann, G. Szarf, R. Schock, K. Nasir, D. Kraitchman, and J. Lima. Accurate and objective infarct sizing by contrast-enhanced magnetic resonance imaging in a canine myocardial infarction model. *Journal of the American College of Cardiology*, 44:2383–2389, 2004.

[33] M. Neizel, M. Katoh, E. Schade, T. Rassaf, G. A. Krombach, M. Kelm, and H. P. Kühl. Rapid and accurate determination of relative infarct size in humans using contrast-enhanced magnetic resonance imaging. *Clinical Research in Cardiolog*, 98(5):319–324, 2009.

[34] A. M. Beek, O. Bondarenko, F. Afsharzada, and A. C. van Rossum. Quantification of late gadolinium enhanced CMR in viability assessment in chronic ischemic heart disease: A comparison to functional outcome. *Journal of Cardiovascular Magnetic Resonance*, 11(6):319–324, 2009.

[35] Q. Tao, J. Milles, K. Zeppenfeld, H. J. Lamb, J. J. Bax, J. H. Reiber, and R. J. van der Geest. Automated segmentation of myocardial scar in late enhancement MRI using combined intensity and spatial information. *Magnetic Resonance in Medicine*, 64(2):586–597, 2010.

[36] E. Heiberg, H. Engblom, J. Engvall, E. Hedström, M. Ugander, and H. Arheden. Semi-automatic quantification of myocardial infarction from delayed contrast enhanced magnetic resonance imaging. *Scandinavian Cardiovascular Journal*, 39(5):276–275, 2005.

[37] A. Hennemuth, A. Seeger, O. Friman, S. Miller, B. Klumpp, S. Oeltze, and H.-O. Peitgen. A comprehensive approach to the analysis of contrast enhanced cardiac MR images. *IEEE Transactions on Medical Imaging*, 27(11):1592–1610, 2008.

[38] A. Schenk, G. Prause, and H.-O. Peitgen. Efficient semiautomatic segmentation of 3D objects in medical images. In *Proc. International Conference on Medical Image Computing and Computer-Assisted Intervention (MICCAI'2000)*, pages 186–195, 2000.

[39] K. Elagouni, C. Ciofolo-Veit, and B. Mory. Automatic segmentation of pathological tissues in cardiac MRI. In *Proc. IEEE International Symposium on Biomedical Imaging: From Nano to Macro (ISBI'2010)*, pages 472–475. IEEE, 2010.

[40] C. Ciofolo, M. Frakin, B. Mory, G. Hautvast, and M. Breeuwer. Automatic myocardium segmentation in late-enhancement MRI. In *Proc. IEEE International Symposium on Biomedical Imaging: From Nano to Macro (ISBI'2008)*, pages 225–228. IEEE, 2008.

[41] E. C. Barbier, L. Johansson, L. Lind, H. Ahlstrom, and T. Bjerner. The exactness of left ventricular segmentation in cine magnetic resonance imaging and its impact on systolic function values. *Journal of Acta Radiologica*, 48(3):285–91, 2007.

[42] B. Sievers, S. Kirchberg, A. Bakan, U. Franken, and H.-J. Trappe. Impact of papillary muscles in ventricular volume and ejection fraction assessment by cardiovascular magnetic resonance. *Journal of Cardiovascular Magnetic Resonance*, 6(1):9–16, 2004.

[43] P. Thunberg, K. Emilsson, P. Rask, and A. Kahari. Estimation of ejection fraction and stroke volume using single- and biplane magnetic resonance imaging of the left cardiac ventricle. *Journal of Acta Radiologica*, 49(9):1016–1013, 2008.

[44] I. B. Ayed, S. Li, and I. Ross. Embedding overlap priors in variational left ventricle tracking. *IEEE Transactions on Medical Imaging*, 28(12):1902–1913, 2009.

[45] I. B. Ayed, Y. Lu, S. Li, and I. Ross. Left ventricle tracking using overlap priors. In *Proc. International Conference on Medical Image Computing and Computer-Assisted Intervention (MICCAI'2008)*, pages 1025–1033, New York, NY, USA, September 6–10, 2008.

[46] C. Li, X. Jia, and Y. Sun. Improved semi-automated segmentation of cardiac CT and MR images. In *Proc. IEEE International Symposium on Biomedical Imaging: From Nano to Macro (ISBI'2009)*, pages 25–28, Boston, MA, June 28–July 1, 2009. IEEE.

[47] W. Feng, H. Nagaraj, H. Gupta, S. G. Lloyd, I. Aban, G. J. Perry, D. A. Calhoun, L. J. Dell'Italia, and T. S. Denney Jr. A dual propagation contours technique for semi-automated assessment of systolic and diastolic cardiac function by CMR. *Journal of Cardiovascular Magnetic Resonance*, 11(1):1–13, 2009.

[48] T. Chen, J. Babb, P. Kellman, L. Axel, and D. Kim. Semiautomated segmentation of myocardial contours for fast strain analysis in cine displacement-encoded MRI. *IEEE Transactions on Medical Imaging*, 27(8):1084–1094, 2008.

[49] A. Pednekar, U. Kurkure, R. Muthupillai, S. Flamm, and I. A. Kakadiaris. Automated left ventricular segmentation in cardiac MRI. *IEEE Transactions on Biomedical Engineering*, 53(7):1425–1428, 2006.

[50] M. Uzümcü, R. van der Geest, C. Swingen, J. Reiber, and B. Lelieveldt. Time continuous tracking and segmentation of cardiovascular magnetic resonance images using multidimensional dynamic programming. *Investigative Radiology*, 41(1):52–62, 2006.

[51] C. Petitjean and J. N. Dacher. A review of segmentation methods in short axis cardiac MR images. *Medical Image Analysis*, 15(1):169–184, 2011.

[52] H. Zhang, A. Wahle, R. K. Johnson, T. D. Scholz, and M. Sonka. 4-D cardiac MR image analysis: Left and right ventricular morphology and function. *IEEE Transactions on Medical Imaging*, 29(2):350–364, 2010.

[53] M. Jolly, H. Xue, L. Grady, and J. Guehring. Combining registration and minimum surfaces for the segmentation of the left ventricle in cardiac cine MR images. In *Proc. International Conference on Medical Image Computing and Computer-Assisted Intervention (MICCAI'2009)*, pages 910–918, London, UK, September 20–24, 2009.

[54] U. Kurkure, A. Pednekar, R. Muthupillai, S. D. Flamm, and I. A. Kakadiaris. Localization and segmentation of left ventricle in cardiac cine-MR images. *IEEE Transactions on Biomedical Engineering*, 56(5):1360–1370, 2009.

[55] A. Schöllhuber. Fully automatic segmentation of the myocardium in cardiac perfusion MRI. In *Central European Seminar on Computer Graphics for Students*, pages 1360–1370, 2008.

[56] C. A. Cocosco, W. J. Niessen, T. Netsch, E. P. A. Vonken, G. Lund, A. Stork, and M. A. Viergever. Automatic image-driven segmentation of the ventricles in cardiac cine MRI. *Journal of Magnetic Resonance Imaging*, 28(2):366–374, 2008.

[57] M. Lynch, O. Ghita, and P. F. Whelan. Segmentation of the left ventricle of the heart in 3-D+t MRI data using an optimized nonrigid temporal model. *IEEE Transactions on Medical Imaging*, 27(2):195–203, 2008.

[58] J. Liang, G. Ding, and Y. Wu. Segmentation of the left ventricle from cardiac MR images based on radial GVF snake. In *Proc. International Conference on Biomedical Engineering Informatics (BMEI'2008)*, volume 2, pages 238–242, Sanya, Hainan, China, May 27–30, 2008.

[59] X. Zhuang, D. J. Hawkes, W. R. Crum, R. Boubertakh, S. Uribe, D. Atkinson, P. Batchelor, T. Schaeffter, R. Razavi, and D. L. G. Hill. Robust registration between cardiac MRI images and atlas for segmentation propagation. In *Proc. SPIE on Medical Imaging: Image Processing (SPIE'2007)*, pages 1–7, 2007.

[60] S. Zambal, J. Hladvka, and K. Bhler. Improving segmentation of the left ventricle using a two-component statistical model. In *Proc. International Conference on Medical Image Computing and Computer-Assisted Intervention (MIC-CAI'2006)*, pages 3151–158, Copenhagen, Denmark, September 22–26, 2006.

[61] M. Lynch, O. Ghita, and P. Whelan. Left-ventricle myocardium segmentation using a coupled level-set with a priori knowledge. *Computerized Medical Imaging and Graphics*, 30(4):255–262, 2006.

[62] A. Katouzian, A. Prakash, and E. Konofagou. A new automated technique for left- and right-ventricular segmentation in magnetic resonance imaging. In *Proc. Engineering in Medicine and Biology Society (EMBS'2006)*, pages 3074–3077, New York, NY, August 30–September 3, 2006.

[63] M. Jolly. Automatic segmentation of the left ventricle in cardiac MR and CT images. *International Journal of Computer Vision*, 70(2):151–163, 2006.

[64] M. Jolly, N. Duta, and G. Funka-Lea. Segmentation of the left ventricle in cardiac MR images. In *Proc. IEEE International Conference on Computer Vision (ICCV'2001)*, pages 501–508, Vancouver, British Columbia, Canada, July 7–14, 2006. IEEE.

[65] M. Lynch, O. Ghita, and P. Whelan. Automatic segmentation of the left ventricle cavity and myocardium in MRI data. *Computers in Biology and Medicine*, 6(4):389–1407, 2006.

[66] B. P. F. Lelieveldt, M. Üzümcü, R. J. van der Geest, J. H. C. Reiber, and M. Sonka. Multi-view active appearance models for consistent segmentation of multiple standard views: Application to long- and short-axis cardiac MR images. In *Proc. the 17th International Congress and Exhibition Computer Assisted Radiology and Surgery*, volume 1256, pages 1141–1146, 2003.

[67] J. C. Fu, J. W. Chai, and S. T. C. Won. Wavelet-based enhancement for detection of left ventricular myocardial boundaries in magnetic resonance images. *Magnetic Resonance Imaging*, 18(1):1135–1141, 2000.

[68] P. Yan, A. Sinusas, and J. S. Duncan. Boundary element method based regularization for recovering of LV deformation. *Medical Image Analysis*, 11(6):540–554, 2007.

[69] A. Lalande, L. Legrand, P. M. Walker, F. Guy, Y. Cottin, S. Roy, and F. Brunotte. Automatic detection of left ventricular contours from cardiac cine magnetic resonance imaging using fuzzy logic. *Investigative Radiology*, 34(3):211–217, 1999.

[70] S. O'Brien, O. Ghita, and P. F. Whelan. A novel model-based 3-D +time left ventricular segmentation technique. *IEEE Transactions on Medical Imaging*, 30(2):461–474, 2011.

[71] J. Cousty, L. Najman, M. Couprie, S. Clément-Guinaudeau, T. Goissen, and J. Garot. Segmentation of 4D cardiac MRI: Automated method based on spatio-temporal watershed cuts. *Image and Vision Computing*, 28(8):1229–1243, 2010.

[72] A. Andreopoulos and J. K. Tsotsos. Efficient and generalizable statistical models of shape and appearance for analysis of cardiac MRI. *Medical Image Analysis*, 12(3):335–357, 2008.

[73] X. Han, C. Xu, and J. L. Prince. A topology preserving level set method for geometric deformable models. *IEEE Transactions on Pattern Analysis and Machine Intelligence*, 25(6):61–79, 2009.

[74] N. Paragios. A variational approach for the segmentation of the left ventricle in cardiac image analysis. *International Journal of Computer Vision*, 50(3):345–362, 2002.

[75] P. Dendale, P. R. Franken, P. Block, Y. Pratikakis, and A. D. Roos. Contrast enhanced and functional magnetic resonance imaging for the detection of viable myocardium after infarction. *American Heart Journal*, 135:875–880, 1998.

[76] C. Klein, S. G. Nekolla, F. M. Bengel, M. Momose, A. Sammer, F. Haas, B. Schnackenburg, W. Delius, H. Mudra, D. Wolfram, and M. Schwaiger. Assessment of myocardial viability with contrast-enhanced magnetic resonance imaging: Comparison with positron emission tomography. *Circulation*, 105(2):162–167, 2002.

[77] B. L. Gerber, J. Garot, D. A. Bluemke, K. C. Wu, and J. A. Lima. Accuracy of contrast-enhanced magnetic resonance imaging in predicting improvement of regional myocardial function in patients after acute myocardial infarction. *Circulation*, 106:1083–1089, 2002.

[78] A. M. Beek, H. P. Kühl, O. Bondarenko, J. W. Twisk, M. B. Hofman, W. G. van Dockum, C. A. Visser, and A. C. van Rossum. Delayed contrast-enhanced magnetic resonance imaging for the prediction of regional functional improvement after acute myocardial infarction. *Journal of the American College of Cardiology*, 42(5):895–901, 2003.

[79] E. E. van der Wall and J. J. Bax. Late contrast enhancement by CMR: More than scar? *The International Journal of Cardiovascular Imaging*, 24(6):609–611, 2008.

[80] K. R. Hoffmann, D. P. Nazareth, L. Miskolczi, A. Gopal, Z. Wang, S. Rudin, and D. R. Bednarek. Vessel size measurements in angiograms: A comparison of techniques. *Medical Physics*, 29:1622–1633, 2002.

[81] N. Otsu. A threshold selection method from gray-level histograms. *IEEE Transactions on Systems, Man, and Cybernetics*, 9:62–66, 1979.

[82] F. h. Sheehan, F. L. Bolson, H. T. Dodge, D. G. Mathey, J. Schofer, and H. W. Woo. Advantages and applications of the centerline method for characterizing regional ventricular function. *Circulation*, 74(2):293–305, 1986.

[83] M. J. McGillem, G. B. Mancini, S. F. DeBoe, and A. J. Buda. Modification of the centerline method for assessment of echocardiographic wall thickening and motion: A comparison with areas of risk. *Journal of the American College of Cardiology*, 11(4):861–866, 1988.

[84] J. D. Schuijf, T. A. Kaandorp, H. J. Lamb, R. J. van der Geest, E. P. Viergever, E. E. van der Wall, A. de Roos, and J. J. Bax. Quantification of myocardial infarct size and transmurality by contrast-enhanced magnetic resonance imaging in men. *American Journal of Cardiology*, 94(3):284–288, 2004.

[85] F. P. van Rugge, E. E. van der Wall, S. J. Spanjersberg, A. de Roos, N. A. Matheijssen, A. H. Zwinderman, P. R. van Dijkman, J. H. Reiber, and A. V. Bruschke. Magnetic resonance imaging during dobutamine stress for detection and localization of coronary artery disease quantitative wall motion analysis using a modification of the centerline method. *Circulation*, 90(1):127–138, 1994.

[86] M. J. Ledesma-Carbayo, J. Kybic, M. Desco, A. Santos, M. Suhling, P. Hunziker, and M. Unser. Spatio-temporal nonrigid registration for ultrasound cardiac motion estimation. *IEEE Transactions on Medical Imaging*, 24(9):1113–1126, 2005.

[87] A. Elen, H. F. Choi, D. Loeckx, H. Gao, P. Claus, P. Suetens, F. Maes, and J. D'hooge. Three-dimensional cardiac strain estimation using spatio-temporal elastic registration of ultrasound images: A feasibility study. *IEEE Transactions on Medical Imaging*, 27(11):1580–1591, 2008.

[88] T. S. Denney and J. L. Prince. Reconstruction of 3-D left ventricular motion from planar tagged cardiac MR images: An estimation theoretic approach. *IEEE Transactions on Medical Imaging*, 14(4):625–635, 1995.

[89] W. S. Kerwin and J. L. Prince. Cardiac material markers from tagged MR images. *Medical Image Analysis*, 2:339–353, 1998.

[90] N. F. Osman and J. L. Prince. Visualizing myocardial function using HARP MRI. *Physics in Medicine and Biology*, 45:1665–1682, 2000.

[91] N. F. Osman, E. R. McVeigh, and J. L. Prince. Imaging heart motion using harmonic phase MRI. *IEEE Transactions on Medical Imaging*, 19(3):186–202, 2000.

[92] W. G. O'Dell, C. C. Moore, W. C. Hunter, E. A. Zerhouni, and E. R. McVeigh. Three-dimensional myocardial deformations: Calculation with displacement field fitting to tagged MR images. *Radiology*, 195:829–835, 1995.

[93] X. Liu and J. L. Prince. Shortest path refinement for motion estimation from tagged MR images. *IEEE Transactions on Medical Imaging*, 29(8):1560–1572, 2010.

[94] E. Maret, T. Todt, L. Brudin, E. Nylander, E. Swahn, J. L. Ohlsson, and J. E. Engvall. Functional measurements based on feature tracking of cine magnetic resonance images identify left ventricular segments with myocardial scar. *Cardiovascular Ultrasound*, 7(53), 2009.

[95] K. N. Hor, W. M. Gottliebson, C. Carson, E. Wash, J. Cnota, R. Fleck, J. Wansapura, P. Klimeczek, H. R. Al-Khalidi, E. S. Chung, W. Benson, and W. Mazur. Comparison of magnetic resonance feature tracking for strain calculation with harmonic phase imaging analysis. *JACC: Cardiovascular Imaging*, 3(3):144–151, 2010.

[96] K. N. Hor, R. Baumann, G. Pedrizzetti, G. Tonti, W. M. Gottliebson, M. Taylor, W. Benson, and W. Mazur. Magnetic resonance derived myocardial strain assessment using feature tracking. *Journal of Visualized Experiments*, 48:144–151, 2011.

[97] A. Schuster, S. Kutty, A. Padiyath, V. Parish, P. Gribben, D. A. Danford, M. R. Makowski, B. Bigalke, P. Beerbaum, and E. Nage. Cardiovascular magnetic resonance myocardial feature tracking detects quantitative wall motion during dobutamine stress. *Journal of Cardiovascular Magnetic Resonance*, 13(58), 2011.

[98] R. C. Dubes and A. K. Jain. Random field models in image analysis. *Journal of Applied Statistics*, 16:131–164, 1989.

[99] G. Gimel'farb. *Image Textures and Gibbs Random Fields*. Dordrecht: Kluwer Academic, 1999.

[100] A. A. Farag, A. S. El-Baz, and G. Gimel'farb. Precise segmentation of multimodal images. *IEEE Transactions on Image Processing*, 15(4):952–968, 2006.

[101] A. El-Baz. *Novel Stochastic Models for Medical Image Analysis*. PhD thesis, University of Louisville, Louisville, KY, USA, 2006.

[102] A. El-Baz and G. Gimel'farb. EM based approximation of empirical distributions with linear combinations of discrete Gaussians. In *Proc. International Conference on Image Processing (ICIP'2007)*, pages 373–376, San Antonio, Texas, 2007. IEEE.

[103] A. El-Baz, A. Elnakib, F. Khalifa, M. A. El-Ghar, R. Falk, and G. Gimel'farb. Precise segmentation of 3-D magnetic resonance angiography. *IEEE Transactions on Biomedical Engineering*, 59(7):2019–2029, 2012.

[104] A. Elnakib, G. Gimel'farb, T. Inanc, and A. El-Baz. Modified Akaike information criterion for estimating the number of components in a probability mixture model. In *Proc. IEEE International Conference on Image Processing (ICIP'2012)*, pages 2497–2500. IEEE, 2012.

[105] A. Elnakib, M. A. El-Ghar, G. Gimel'farb, R. Falk, J. Suri, and A. El-Baz. Modified Akaike information criterion for selecting the numbers of mixture components: An application to initial lung segmentation. In L. Saba and J. Suri, editors, *Multi-Detector CT Imaging: Abdomen, Pelvis, and CAD Applications*, chapter 28, pages 609–620. CRC Press: Taylor and Francis Group, 2014.

[106] A. Webb. *Statistical Pattern Recognition*. New York: Wiley, 2002.

[107] G. Gimel'farb, A. Farag, and A. El-Baz. Expectation–maximization for a linear combination of Gaussians. In *Proc. International Conference on Pattern Recognition (ICPR'2004)*, pages 422–425, Cambridge, UK, August 2004.

[108] A. A. Farag, A. El-Baz, and G. Gimel'farb. Density estimation using modified expectation-maximization algorithm for a linear combination of Gaussians. In *Proc. International Conference on Image Processing (ICIP'2004)*, volume 3, pages 1871–1874. IEEE, 2004.

[109] A. Farag, A. El-Baz, and G. Gimel'farb. Precise image segmentation by iterative EM-based approximation of empirical grey level distributions with linear combinations of Gaussians. In *Computer Vision and Pattern Recognition Workshop (CVPRW'2004)*, pages 121–129, Washington, D.C., USA, 2004. IEEE.

[110] A. A. Farag, A. El-Baz, and R. M. Mohamed. Density estimation using generalized linear model and a linear combination of Gaussians. *International Journal of Signal Processing*, 1:76–79, 2005.

[111] A. El-Baz, R. M. Mohamed, A. A. Farag, and G. Gimel'farb. Unsupervised segmentation of multi-modal images by a precise approximation of individual modes with linear combinations of discrete Gaussians. In *IEEE Computer Society Conference on Computer Vision and Pattern Recognition-Workshops (CVPRW'2005)*, pages 54–54. IEEE, 2005.

[112] A. El-Baz, A. A. Farag, and G. Gimel'farb. Iterative approximation of empirical grey-level distributions for precise segmentation of multimodal images. *EURASIP Journal on Applied Signal Processing*, 2005:1969–1983, 2005.

[113] P. Viola and W. M. Wells. Alignment by maximization of mutual information. In *Proc. IEEE International Conference on Computer Vision (ICCV'1995)*, pages 16–23. IEEE, 1995.

[114] Y. Boykov and V. Kolmogorov. An experimental comparison of min-cut/max-flow algorithms for energy minimization in vision. *IEEE Transactions on Pattern Analysis and Machine Intelligence*, 26(9):1124–1137, 2004.

[115] Y. Boykov and G. Funka-Lea. Graph cuts and efficient N-D image segmentation. *International Journal of Computer Vision*, 69(2):109–131, 2006.

[116] A. El-Baz and G. Gimel'farb. Image segmentation with a parametric deformable model using shape and appearance priors. In *Proc. IEEE Conference on Computer Vision and Pattern Recognition (CVPR'2008)*, pages 1–8. IEEE, 2008.

[117] A. El-Baz and G. Gimel'farb. Robust medical images segmentation using learned shape and appearance models. In *Proc. International Conference on Medical Image Computing and Computer-Assisted Intervention (MICCAI'2009)*, pages 281–288. Springer, 2009.

[118] A. El-Baz and G. Gimel'farb. Robust image segmentation using learned priors. In *Proc. IEEE International Conference on Computer Vision (ICCV'2009)*, pages 857–864. IEEE, 2009.

[119] D. Adalsteinsson and J. Sethian. A fast level set method for propagating interfaces. *Journal of Computational Physics*, 118(2):269–277, 1995.

[120] L. R. Dice. Measures of the amount of ecologic association between species. *Ecological society of America*, 26:279–302, 1945.

[121] R. J. Kim, D. J. Shah, and R. M. Judd. How we perform delayed enhancement imaging. *Journal of Cardiovascular MR*, 5:505–514, 2003.

[122] A. Elnakib, G. M. Beache, G. Gimel'farb, and A. El-Baz. A new framework for automated segmentation of left ventricle wall from contrast enhanced cardiac magnetic resonance images. In *Proc. International Conference on Image Processing (ICIP'2011)*, pages 2289–2292. IEEE, 2011.

[123] J. Besag. On the statistical analysis of dirty pictures. *Journal of the Royal Statistical Society*, pages 259–302, 1986.

[124] R. J. Kim, E. Wu, A. Rafael, E.-L. Chen, M. A. Parker, O. Simonetti, F. J. Klocke, R. O. Bonow, and R. M. Judd. The use of contrast-enhanced magnetic resonance imaging to identify reversible myocardial dysfunction. *The New England Journal of Medicine*, 43(20):1445–1453, 2000.

[125] K. M. Choi, R. J. Kim, G. Gubernikoff, J. D. Vargas, M. Parker, and R. M. Judd. Transmural extent of acute myocardial infarction predicts long-term improvement in contractile function. *Circulation*, 104(10):1101–1107, 2001.

[126] S. Jones, B. R. Buchbinder, and I. Aharon. Three-dimensional mapping of cortical thickness using Laplace's equation. *Human Brain Mapping*, 11, 2000.

[127] A. Elnakib, G. M. Beache, G. Gimel'farb, and A. El-Baz. New automated Markov–Gibbs random field based framework for myocardial wall viability quantification on agent enhanced cardiac magnetic resonance images. *The International Journal of Cardiovascular Imaging*, 28(7):1683–1698, 2012.

[128] F. Khalifa, M. A. El-Ghar, B. Abdollahi, H. Frieboes, T. El-Diasty, and A. El-Baz. A comprehensive non-invasive framework for automated evaluation of acute renal transplant rejection using DCE-MRI. *NMR in Biomedicine*, 26(11):1460–1470, 2013.

[129] F. Khalifa, G. M. Beache, M. A. El-Ghar, T. El-Diasty, G. Gimel'farb, M. Kong, and A. El-Baz. Dynamic contrast-enhanced MRI-based early detection of acute renal transplant rejection. *IEEE Transactions on Medical Imaging*, 32(10):1910–1927, 2013.

[130] J. M. Bland and R. W. Martin. Statistical methods for assessing agreement between two methods of clinical measurement. *Lancet*, 327(8476):307–310, 1986.

[131] A. El-Baz, G. Gimel'farb, R. Falk, M. A. El-Ghar, V. Kumar, and D. Heredia. A novel 3D joint Markov–Gibbs model for extracting blood vessels from PC-MRA images. In *Proc. International Conference on Medical Image Computing and Computer-Assisted Intervention (MICCAI'2009)*, pages 943–950, 2009.

[132] A. Elnakib, G. M. Beache, M. Nitzken, G. Gimel'farb, and A. El-Baz. A new framework for automated identification of pathological tissues in contrast enhanced cardiac magnetic resonance images. In *Proc. IEEE International Symposium on Biomedical Imaging: From Nano to Macro (ISBI'2011)*, pages 1272–1275. IEEE, 2011.

[133] R. Bolli, A. R. Chugh, D. D'Amario, J. H. Loughran, M. F. Stoddard, S. Ikram, G. M. Beache, S. G. Wagner, A. Leri, T. Hosoda, F. Sanada, J. B. Elmore, P. Goichberg, D. Cappetta, N. K. Solankhi, I. Fahsah, D. G. Rokosh, M. S. Slaughter, J. Kajstura, and P. Anversa. Cardiac stem cells in patients with ischaemic cardiomyopathy (SCIPIO): Initial results of a randomised phase 1 trial. *Lancet*, 378(9806):1847–1857, 2011.

[134] F. Khalifa, G. M. Beache, G. Gimel'farb, G. A. Giridharan, and A. El-Baz. Accurate automatic analysis of cardiac cine images. *IEEE Transactions on Biomedical Engineering*, 59(2):445–455, 2012.

[135] F. Khalifa, G. Beache, A. El-Baz, and G. Gimel'farb. Deformable model guided by stochastic speed with application in cine images segmentation.

In *Proc. International Conference on Image Processing (ICIP'2010)*, pages 1725–1728, Hong Kong, September 26–29, 2010.

[136] F. Khalifa, G. M. Beache, G. Gimel'farb, and A. El-Baz. A novel approach for accurate estimation of left ventricle global indexes from short-axis cine MRI. In *Proc. International Conference on Image Processing (ICIP'2011)*, pages 2645–2649, Brussels, Belgium, September 11–14, 2011.

[137] F. Khalifa, G. M. Beache, M. Nitzken, G. Gimel'farb, G. A. Giridharan, and A. El-Baz. Automatic analysis of left ventricle wall thickness using short-axis cine CMR images. In *Proc. IEEE International Symposium on Biomedical Imaging: From Nano to Macro (ISBI'11)*, pages 1306–1309, Chicago, Illinois, March 30–April 2, 2011.

[138] F. Khalifa, G. M. Beache, G. Gimel'farb, G. A. Giridharan, and A. El-Baz. A new image-based framework for analyzing cine images. In A. El-Baz, U. R. Acharya, M. Mirmedhdi, and J. S. Suri, editors, *Handbook of Multi Modality State-of-the-Art Medical Image Segmentation and Registration Methodologies*, volume 2, chapter 3, pages 69–98. Springer, New York, 2011.

[139] J. Bonet and R. D. Wood. *Nonlinear Continuum Mechanics for Finite Element Analysis*. Cambridge University Press, 1997.

[140] M. Nitkzen, G. Beache, A. Elnakib, F. Khalifa, G. Gimel'farb, and A. El-Baz. Improving full-cardiac cycle strain estimation from tagged CMR by accurate modeling of 3D image appearance characteristics. In *Proc. IEEE International Symposium on Biomedical Imaging: From Nano to Macro (ISBI'2012)*, pages 462–465, Barcelona, Spain, 2012. IEEE.

[141] T. Arts, W. C. Hunter, A. Douglas, A. M. Muijtjens, and R. S. Reneman. Description of the deformation of the left ventricle by a kinematic model. *Journal of Biomechanics*, 25:1119–1127, 1992.

[142] T. E. Waks, J. L. Prince, and A. S. Douglas. Cardiac motion simulator for tagged MRI. In *Proc. Workshop on Mathematical Methods in Biomedical Image Analysis*, pages 182–191, 1996.

[143] A. Soliman, F. Khalifa, A. Alansary, G. Gimel'farb, and A. El-Baz. Segmentation of lung region based on using parallel implementation of joint MGRF: Validation on 3D realistic lung phantoms. In *Proc. IEEE International Symposium on Biomedical Imaging: From Nano to Macro (ISBI'2013)*, pages 852–855. IEEE, 2013.

[144] G. M. Beache, S. F. Kulke, H. L. Kantor, P. Niemi, T. A. Campbell, D. A. Chesler, H. Gewirtz, B. R. Rosen, T. J. Brady, and R. M. Weisskoff. Imaging perfusion deficits in ischemic heart disease with susceptibility-enhanced T2-weighted MRI: Preliminary human studies. *Magnetic Resonance Imaging*, 16(1):19–27, 1998.

[145] G. M. Beache, V. J. Wedeen, R. M. Weisskoff, P. T. O'Gara, B. P. Poncelet, D. A. Chesler, T. J. Brady, B. R. Rosen, and R. E. Dinsmore. Intramural mechanics in hypertrophic cardiomyopathy: Functional mapping with strain-rate MR imaging. *Radiology*, 197(1):117–124, 1995.

[146] A. Elnakib, G. M. Beache, H. Sliman, G. Gimel'farb, T. Inanc, and A. El-Baz. A novel laplace-based method to estimate the strain from cine cardiac magnetic resonance images. In *Proc. International Conference on Image Processing (ICIP'2013)*. IEEE, 2013. (In press).

[147] A. Elnakib, G. M. Beache, T. I. G. Gimel'farb, and A. El-Baz. Validating a new methodology for strain estimation from cardiac cine MRI. In *Proc. International Symposium on Computational Models for Life Science (CMLS'13)*, pages 277–286, 2013.

[148] V. Blau, N. van Atteveldt, M. Ekkebus, R. Goebel, and L. Blomert. Reduced neural integration of letters and speech sounds links phonological and reading deficits in adult dyslexia. *Current Biology*, 19(6):503–508, 2009.

[149] K. Pugh, W. Mencl, A. Jenner, L. Katz, S. Frost, J. Lee, S. Shaywitz, and B. Shaywitz. Functional neuroimaging studies of reading and reading disability (developmental dyslexia). *Mental Retardation and Developmental Disabilities Research Reviews*, 6(3):61–79, 2000.

[150] F. Vellutino and D. Scanlon. Phonological coding, phonological awareness, and reading ability: Evidence from a longitudinal and experimental study. *Merrill Palmer Quarterly*, 33(3):321–363, 1987.

[151] J. Torgesen. Lessons learned from research on interventions for students who experience difficulty learning to read. In P. McCardle and V. Chabra, editors, *The Voice of Evidence in Reading Research*, pages 338–355. Paul H Brookes Publishing, Berlin, 1994.

[152] M. Wolf. *Proust and the Squid: The Story and Science of the Reading Brain*. New York: Harper Collins, 2007.

[153] M. Casanova and C. R. Tillquist. Encephalization, emergent properties, and psychiatry: A minicolumnar perspective. *Merrill Palmer Quarterly*, 14(1):101–118, 2008.

[154] V. B. Mountcastle. *Perpetual Neuroscience: The Cerebral Cortex*. MA: Harvard University Press, 1988.

[155] M. Casanova, D. P. Buxhoeveden, M. Cohen, A. E. Switala, and E. L. Roy. Minicolumnar pathology in dyslexia. *Annals of Neurology*, 52(1):108–110, 2002.

[156] E. L. Williams and M. F. Casanova. Autism and dyslexia: A spectrum of cognitive styles as defined by minicolumnar morphometry. *Medical Hypotheses*, 74(1):59–62, 2010.

[157] Y.-F. Sun, J.-S. Lee, and R. Kirby. Brain imaging findings in dyslexia. *Pediatrics & Neonatology*, 51(2):89–96, 2010.

[158] M. Eckert. Neuroanatomical markers for dyslexia: A review of dyslexia structural imaging studies. *The Neuroscientist*, 10(4):362–371, 2004.

[159] S. Eliez, J. M. Rumsey, J. N. Giedd, J. E. Schmitt, A. J. Patwardhan, and A. L. Reiss. Morphological alteration of temporal lobe gray matter in dyslexia: An MRI study. *Journal of Child Psychology and Psychiatry*, 41(5):637–644, 2000.

[160] M. Kronbichler, H. Wimmer, W. Staffen, F. Hutzler, A. Mair, and G. Ladurner. Developmental dyslexia: Gray matter abnormalities in the occipitotemporal cortex. *Human Brain Mapping*, 29(5):613–625, 2008.

[161] W. E. Brown, S. Eliez, V. Menon, J. M. Rumsey, C. D. White, and A. L. Reiss. Preliminary evidence of widespread morphological variations of the brain in dyslexia. *Neurology*, 56(6):781–783, 2001.

[162] S. M. Brambati, C. Termine, M. Ruffino, G. Stella, F. Fazio, S. F. Cappa, and D. Perani. Regional reductions of gray matter volume in familial dyslexia. *Neurology*, 63(4):742–745, 2004.

[163] G. Silani, U. Frith, J. F. Demonet, F. Fazio, D. Perani, C. Price, C. D. Frith, and E. Paulesu. Brain abnormalities underlying altered activation in dyslexia: A voxel based morphometry study. *Brain*, 128(10):2453–2461, 2005.

[164] M. A. Eckert, C. M. Leonard, M. Wilke, M. Eckert, T. Richards, A. Richards, and V. Berninger. Anatomical signatures of dyslexia in children: Unique information from manual and voxel based morphometry brain measures. *Cortex*, 41(3):304–315, 2005.

[165] E. Vinckenbosch, F. Robichon, and S. Eliez. Gray matter alteration in dyslexia: Converging evidence from volumetric and voxel-by-voxel MRI analyses. *Neuropsychologia*, 43(3):324–331, 2005.

[166] F. Hoeft, A. Meyler, A. Hernandez, C. Juel, H. Taylor-Hill, J. L. Martindale, G. McMillon, G. Kolchugina, J. M. Black, A. Faizi, G. K. Deutsch, W. T. Siok, A. L. Reiss, S. Whitfield-Gabrieli, and J. D. E. Gabrieli. Functional and morphometric brain dissociation between dyslexia and reading ability. *Proc. National Academy of Sciences*, 104(10):4234–4239, 2007.

[167] D. Menghini, G. E. Hagberg, L. Petrosini, M. Bozzali, E. Macaluso, C. Caltagirone, and S. Vicari. Structural correlates of implicit learning deficits in subjects with developmental dyslexia. *Annals of the New York Academy of Sciences*, 1145(1):212–221, 2008.

[168] C. Steinbrink, K. Vogt, A. Kastrup, H.-P. Müller, F. D. Juengling, J. Kassubek, and A. Riecker. The contribution of white and gray matter differences to developmental dyslexia: Insights from DTI and VBM at 3.0 T. *Neuropsychologia*, 46(13):3170–3178, 2008.

[169] C. Pernet, J. Andersson, E. Paulesu, and J. F. Demonet. When all hypotheses are right: A multifocal account of dyslexia. *Human Brain Mapping*, 30(7):2278–2292, 2009.

[170] R. T. Schultz, N. K. Cho, L. H. Staib, L. E. Kier, J. M. Fletcher, S. E. Shaywitz, D. P. Shankweiler, L. Katz, J. C. Gore, J. S. Duncan, and B. A. Shaywitz. Brain morphology in normal and dyslexic children: The influence of sex and age. *Annals of Neurology*, 35(6):732–742, 1994.

[171] T. M. Evans, D. L. Flowers, E. M. Napoliello, and G. F. Eden. Sex-specific gray matter volume differences in females with developmental dyslexia. *Brain Structure and Function*, pages 1–14, 2013.

[172] K. Jednoróg, N. Gawron, A. Marchewka, S. Heim, and A. Grabowska. Cognitive subtypes of dyslexia are characterized by distinct patterns of grey matter volume. *Brain Structure and Function*, pages 1–11, 2013.

[173] A. J. Krafnick, D. L. Flowers, E. M. Napoliello, and G. F. Eden. Gray matter volume changes following reading intervention in dyslexic children. *Neuroimage*, 57(3):733–741, 2011.

[174] N. M. Raschle, M. Chang, and N. Gaab. Structural brain alterations associated with dyslexia predate reading onset. *Neuroimage*, 57(3):742–749, 2011.

[175] E. L. Williams, A. El-Baz, M. Nitzken, A. E. Switala, and M. F. Casanova. Spherical harmonic analysis of cortical complexity in autism and dyslexia. *Translational Neuroscience*, 3(1):36–40, 2012.

[176] I. Altarelli, K. Monzalvo, S. Iannuzzi, J. Fluss, C. Billard, F. Ramus, and G. Dehaene-Lambertz. A functionally guided approach to the morphometry of occipitotemporal regions in developmental dyslexia: Evidence for differential effects in boys and girls. *The Journal of Neuroscience*, 33(27):11296–11301, 2013.

[177] A. M. Dale, B. Fischl, and M. I. Sereno. Cortical surface-based analysis: I. segmentation and surface reconstruction. *Neuroimage*, 9(2):179–194, 1999.

[178] B. Fischl and A. M. Dale. Measuring the thickness of the human cerebral cortex from magnetic resonance images. *Proc. National Academy of Sciences*, 97(20):11050–11055, 2000.

[179] M. F. Casanova, A. S. El-Baz, J. Giedd, J. M. Rumsey, and A. E. Switala. Increased white matter gyral depth in dyslexia: Implications for corticocortical connectivity. *Journal of Autism and Developmental Disorders*, 40(1):21–29, 2010.

[180] A. A. Beaton. The relation of planum temporale asymmetry and morphology of the corpus callosum to handedness, gender, and dyslexia: A review of the evidence. *Brain and Language*, 60(2):255–322, 1997.

[181] M. A. Eckert and C. M. Leonard. Structural imaging in dyslexia: The planum temporale. *Mental Retardation and Developmental Disabilities Research Reviews*, 6(3):198–206, 2000.

[182] C. Rae, J. A. Harasty, T. E. Dzendrowskyj, J. B. Talcott, J. M. Simpson, A. M. Blamire, R. M. Dixon, M. A. Lee, C. H. Thompson, P. Styles, A. J. Richardson, and J. F. Stein. Cerebellar morphology in developmental dyslexia. *Neuropsychologia*, 40(8):1285–1292, 2002.

[183] C. J. Stoodley and J. F. Stein. Cerebellar function in developmental dyslexia. *The Cerebellum*, pages 1–10, 2012.

[184] A. Kushch, K. Gross-Glenn, B. Jallad, H. Lubs, M. Rabin, E. Feldman, and R. Duara. Temporal lobe surface area measurements on MRI in normal and dyslexic readers. *Neuropsychologia*, 31(8):811–821, 1993.

[185] J. P. Larsen, T. Høien, I. Lundberg, and H. Ødegaard. MRI evaluation of the size and symmetry of the planum temporale in adolescents with developmental dyslexia. *Brain and Language,* 39(2):289–301, 1990.

[186] C. M. Leonard, K. K. S. Voeller, L. J. Lombardino, M. K. Morris, G. W. Hynd, A. W. Alexander, H. G. Andersen, M. Garofalakis, J. C. Honeyman, J. Mao, F. Agee, and E. V. Staab. Anomalous cerebral structure in dyslexia revealed with magnetic resonance imaging. *Archives of Neurology*, 50(5):461–469, 1993.

[187] J. S. Bloom, M. A. Garcia-Barrera, C. J. Miller, S. R. Miller, and G. W. Hynd. Planum temporale morphology in children with developmental dyslexia. *Neuropsychologia*, 51(9):1684–1692, 2013.

[188] J. M. Rumsey, B. C. Donohue, D. R. Brady, K. Nace, J. N. Giedd, and P. Andreason. A magnetic resonance imaging study of planum temporale asymmetry in men with developmental dyslexia. *Archives of Neurology*, 54(12):1481, 1997.

[189] J. M. Rumsey, K. Nace, B. Donohue, D. Wise, J. M. Maisog, and P. Andreason. A positron emission tomographic study of impaired word recognition and phonological processing in dyslexic men. *Archives of Neurology*, 54(5):562–573, 1997.

[190] M. A. Eckert, C. M. Leonard, T. L. Richards, E. H. Aylward, J. Thomson, and V. W. Berninger. Anatomical correlates of dyslexia: Frontal and cerebellar findings. *Brain*, 126(2):482–494, 2003.

[191] V. G. Fernandez, K. Stuebing, J. Juranek, and J. M. Fletcher. Volumetric analysis of regional variability in the cerebellum of children with dyslexia. *The Cerebellum*, pages 1–10, 2013.

[192] J. D. Schmahmann, J. Doyon, M. Petrides, A. C. Evans, and A. W. Toga. *MRI Atlas of the Human Cerebellum*. Academic Press, 2000.

[193] K. von Plessen, A. Lundervold, N. Duta, E. Heiervang, F. Klauschen, A. I. Smievoll, L. Ersland, and K. Hugdahl. Less developed corpus callosum in dyslexic subjects – A structural MRI study. *Neuropsychologia*, 40(7):1035–1044, 2002.

[194] M. F. Casanova, A. El-Baz, A. Elnakib, J. Giedd, J. M. Rumsey, E. L. Williams, and A. E. Switala. Corpus callosum shape analysis with application to dyslexia. *Translational Neuroscience*, 1(2):124–130, 2010.

[195] A. Elnakib, A. El-Baz, M. F. Casanova, G. Gimel'farb, and A. E. Switala. Image-based detection of corpus callosum variability for more accurate discrimination between dyslexic and normal brains. In *Proc. IEEE International Symposium on Biomedical Imaging: From Nano to Macro (ISBI'2010)*, pages 109–112. IEEE, 2010.

[196] A. Elnakib, A. El-Baz, M. F. Casanova, and A. E. Switala. Dyslexia diagnostics by centerline-based shape analysis of the corpus callosum. In *Proc. International Conference on Pattern Recognition (ICPR'2010)*, pages 261–264. IEEE, 2010.

[197] D. L. Bihan, J. F. Mangin, C. Poupon, C. A. Clark, S. Pappata, N. Molko, and H. Chabriat. Diffusion tensor imaging: Concepts and applications. *Journal of Magnetic Resonance Imaging*, 13(4):354–546, 2001.

[198] R. Bammer. Basic principles of diffusion-weighted imaging. *European Journal of Radiology*, 45(23):169–184, 2003.

[199] P. C. Sundgren, Q. Dong, a. S. K. M. D. Gomez-Hassan, P. Maly, and R. Welsh. Diffusion tensor imaging of the brain: Review of clinical applications. *Neuroradiology*, 46(5):339–250, 2004.

[200] T. Klingberg, M. Hedehus, E. Temple, T. Salz, J. D. Gabrieli, M. E. Moseley, and R. A. Poldrack. Microstructure of temporo-parietal white matter as a basis for reading ability: Evidence from diffusion tensor magnetic resonance imaging. *Neuron*, 25(2):493–500, 2000.

[201] S. N. Niogi and B. D. McCandliss. Left lateralized white matter microstructure accounts for individual differences in reading ability and disability. *Neuropsychologia*, 44(11):2178–2188, 2006.

[202] T. Richards, J. Stevenson, J. Crouch, L. C. Johnson, K. Maravilla, P. Stock, R. Abbott, and V. Berninger. Tract-based spatial statistics of diffusion tensor imaging in adults with dyslexia. *American Journal of Neuroradiology*, 29(6):1134–1139, 2008.

[203] J. C. Carter, D. C. Lanham, L. E. Cutting, A. M. Clements-Stephens, X. Chen, M. Hadzipasic, J. Kim, M. B. Denckla, and W. E. Kaufmann. A dual DTI approach to analyzing white matter in children with dyslexia. *Psychiatry Research: Neuroimaging*, 172(3):215–219, 2009.

[204] T. N. Odegard, E. A. Farris, J. Ring, R. McColl, and J. Black. Brain connectivity in non-reading impaired children and children diagnosed with developmental dyslexia. *Neuropsychologia*, 47(8):1972–1977, 2009.

[205] M. Vandermosten, B. Boets, H. Poelmans, S. Sunaert, J. Wouters, and P. Ghesquière. A tractography study in dyslexia: Neuroanatomic correlates of orthographic, phonological and speech processing. *Brain*, 135(3):935–948, 2012.

[206] M. Vandermosten, B. Boets, H. Poelmans, S. Sunaert, P. Ghesquière, and J. Wouters. White matter lateralization and interhemispheric coherence to auditory modulations in normal reading and dyslexic adults. *Neuropsychologia*, 51(11):2087–2099, 2013.

[207] K. M. Hasan, D. L. Molfese, I. S. Walimuni, K. K. Stuebing, A. C. Papanicolaou, P. A. Narayana, and J. M. Fletcher. Diffusion tensor quantification and cognitive correlates of the macrostructure and microstructure of the corpus callosum in typically developing and dyslexic children. *NMR in Biomedicine*, 25(11):1263–1270, 2012.

[208] C. Beaulieu, C. Plewes, L. A. Paulson, D. Roy, L. Snook, L. Concha, and L. Phillips. Imaging brain connectivity in children with diverse reading ability. *Neuroimage*, 25(4):1266–1271, 2005.

[209] S. L. Rimrodt, D. J. Peterson, M. B. Denckla, W. E. Kaufmann, and L. E. Cutting. White matter microstructural differences linked to left perisylvian language network in children with dyslexia. *Cortex*, 46(6):739–749, 2010.

[210] S. Ogawa, T. M. Lee, A. S. Nayak, and P. Glynn. Oxygenation–sensitive contrast in magnetic resonance image of rodent brain at high magnetic fields. *Magnetic Resonance in Medicine*, 14(1):68–78, 1990.

[211] B. A. Shaywitz, G. R. Lyon, and S. E. S. E. Shaywitz. The role of functional magnetic resonance imaging in understanding reading and dyslexia. *Developmental Neuropsychology*, 30(1):613–632, 2006.

[212] S. L. Rimrodt, A. M. Clements-Stephens, K. R. Pugh, S. M. Courtney, P. Gaur, J. J. Pekar, and L. E. Cutting. Functional MRI of sentence comprehension in children with dyslexia: Beyond word recognition. *Cerebral Cortex*, 19(2):402–413, 2009.

[213] H. Baillieux, E. J. M. Vandervliet, M. Manto, P. M. Parizel, P. Deyn, and P. Mariën. Developmental dyslexia and widespread activation across the cerebellar hemispheres. *Brain and Language*, 108(2):122–132, 2009.

[214] C. Reilhac, C. Peyrin, J.-F. Démonet, and S. Valdois. Role of the superior parietal lobules in letter-identity processing within strings: FMRI evidence from skilled and dyslexic readers. *Neuropsychologia*, 51(4):601–612, 2012.

[215] O. A. Olulade, J. W. Gilger, T. M. Talavage, G. W. Hynd, and C. I. McAteer. Beyond phonological processing deficits in adult dyslexics: Atypical fMRI activation patterns for spatial problem solving. *Developmental Neuropsychology*, 37(7):617–635, 2012.

[216] S. E. Shaywitz, B. A. Shaywitz, K. R. Pugh, R. K. Fulbright, R. T. Constable, W. E. Mencl, D. P. Shankweiler, A. M. Liberman, P. Skudlarski, J. M. Fletcher, L. Katz, C. L. K. E. Marchione, C. Gatenby, and J. C. Gore. Functional disruption in the organization of the brain for reading in dyslexia. *Proc. National Academy of Sciences*, 95(5):2636–2641, 1998.

[217] B. A. Shaywitz, S. E. Shaywitz, K. R. Pugh, W. E. Mencl, R. K. Fulbright, P. Skudlarski, R. T. Constable, K. E. Marchione, J. M. Fletcher, G. R. Lyon, and J. C. Gore. Disruption of posterior brain systems for reading in children with developmental dyslexia. *Biological Psychiatry*, 52(2):101–110, 2002.

[218] P. Georgiewa, R. Rzanny, C. Gaser, U.-J. Gerhard, U. Vieweg, D. Freesmeyer, H.-J. Mentzel, W. A. Kaiser, and B. Blanz. Phonological processing in dyslexic children: A study combining functional imaging and event related potentials. *Neuroscience Letters*, 318(1):5–8, 2002.

[219] K. Groth, T. Lachmann, A. Riecker, I. Muthmann, and C. Steinbrink. Developmental dyslexics show deficits in the processing of temporal auditory information in German vowel length discrimination. *Reading and Writing*, 24(3):285–303, 2011.

[220] C. Steinbrink, K. Groth, T. Lachmann, and A. Riecker. Neural correlates of temporal auditory processing in developmental dyslexia during German vowel length discrimination: An fMRI study. *Brain and Language*, 121(1):1–11, 2012.

[221] B. Díaz, F. Hintz, S. J. Kiebel, and K. V. Kriegstein. Dysfunction of the auditory thalamus in developmental dyslexia. *Proc. National Academy of Sciences*, 109(34):13841–13846, 2012.

[222] I. Kovelman, E. S. Norton, J. A. Christodoulou, N. Gaab, D. A. Lieberman, C. Triantafyllou, M. Wolf, S. Whitfield-Gabrieli, and J. D. E. Gabrieli. Brain basis of phonological awareness for spoken language in children and its disruption in dyslexia. *Cerebral Cortex*, 22(4):754–764, 2012.

[223] V. Blau, J. Reithler, N. van Atteveldt, J. Seitz, P. Gerretsen, R. Goebel, and L. Blomert. Deviant processing of letters and speech sounds as proximate cause of reading failure: A functional magnetic resonance imaging study of dyslexic children. *Brain*, 133(3):868–879, 2010.

[224] G. F. Eden, J. W. VanMeter, J. M. Rumsey, J. M. Maisog, R. P. Woods, and T. A. Zeffiro. Abnormal processing of visual motion in dyslexia revealed by functional brain imaging. *Nature*, 382(6586):66–69, 1996.

[225] J. B. Demb, G. M. Boynton, and D. J. Heeger. Functional magnetic resonance imaging of early visual pathways in dyslexia. *The Journal of Neuroscience*, 18(17):6939–6951, 1998.

[226] C. Peyrin, M. Lallier, J.-F. Demonet, C. Pernet, M. Baciu, J. F. L. Bas, and S. Valdois. Neural dissociation of phonological and visual attention span

disorders in developmental dyslexia: FMRI evidence from two case reports. *Brain and Language*, 120(3):381–394, 2012.

[227] R. B. H. Tootell, J. B. Reppas, A. M. Dale, R. B. Look, M. I. Sereno, R. Malach, T. J. Brady, and B. R. Rosen. Visual motion aftereffect in human cortical area MT revealed by functional magnetic resonance imaging. *Nature*, 375(6527):139–141, 1995.

[228] M.-L. Bosse and S. Valdois. Influence of the visual attention span on child reading performance: A cross-sectional study. *Journal of Research in Reading*, 32(2):230–253, 2009.

[229] R. C. Wolf, F. Sambataro, C. Lohr, C. Steinbrink, C. Martin, and N. Vasic. Functional brain network abnormalities during verbal working memory performance in adolescents and young adults with dyslexia. *Neuropsychologia*, 48(1):309–318, 2010.

[230] H. Beneventi, F. E. TØnnessen, L. Ersland, and K. Hugdahl. Executive working memory processes in dyslexia: Behavioral and fMRI evidence. *Scandinavian Journal of Psychology*, 51(3):192–202, 2010.

[231] K. R. Pugh, W. E. Mencl, B. A. Shaywitz, S. E. Shaywitz, R. K. Fulbright, R. T. Constable, P. Skudlarski, K. E. Marchione, A. R. Jenner, J. M. Fletcher, A. M. Liberman, D. P. Shankweiler, L. Katz, C. Lacadie, and J. C. Gore. The angular gyrus in developmental dyslexia: Task-specific differences in functional connectivity within posterior cortex. *Psychological Science*, 11(1):51–56, 2000.

[232] S. van der Mark, P. Klaver, K. Bucher, U. Maurer, E. Schulz, S. Brem, E. Martin, and D. Brandeis. The left occipitotemporal system in reading: Disruption of focal fMRI connectivity to left inferior frontal and inferior parietal language areas in children with dyslexia. *Neuroimage*, 54(3):2426–2436, 2011.

[233] L. Cohen, S. Dehaene, L. Naccache, S. Lehéricy, G. Dehaene-Lambertz, M.-A. Hénaff, and F. Michel. The visual word form area spatial and temporal characterization of an initial stage of reading in normal subjects and posterior split-brain patients. *Brain*, 123(2):291–307, 2000.

[234] E. Temple, G. K. Deutsch, R. A. Poldrack, S. L. Miller, P. Tallal, M. M. Merzenich, and J. D. E. Gabrieli. Neural deficits in children with dyslexia ameliorated by behavioral remediation: Evidence from functional MRI. *Proc. National Academy of Sciences*, 100(5):2860–2865, 2003.

[235] E. H. Aylward, T. L. Richards, V. W. Berninger, W. E. Nagy, K. M. Field, A. C. Grimme, A. L. Richards, J. B. Thomson, and S. C. Cramer. Instructional treatment associated with changes in brain activation in children with dyslexia. *Neurology*, 61(2):212–219, 2003.

[236] T. L. Richards and V. W. Berninger. Abnormal fMRI connectivity in children with dyslexia during a phoneme task: Before but not after treatment. *Journal of Neurolinguistics*, 21(4):294–304, 2008.

[237] H. Wimmer, M. Schurz, D. Sturm, F. Richlan, J. Klackl, M. Kronbichler, and G. Ladurner. A dual-route perspective on poor reading in a regular orthography: An fMRI study. *Cortex*, 46(10):1284–1298, 2010.

[238] A. Seki, T. Koeda, S. Sugihara, M. Kamba, Y. Hirata, T. Ogawa, and K. Takeshita. A functional magnetic resonance imaging study during sentence reading in Japanese dyslexic children. *Brain and Development*, 23(5):312–316, 2001.

[239] Y. Kita, H. Yamamoto, K. Oba, Y. Terasawa, Y. Moriguchi, H. Uchiyama, A. Seki, T. Koeda, and M. Inagaki. Altered brain activity for phonological manipulation in dyslexic Japanese children. *Brain*, 2013. [Epub ahead of print].

[240] F. Richlan, M. Kronbichler, and H. Wimmer. Structural abnormalities in the dyslexic brain: A meta-analysis of voxel-based morphometry studies. *Human Brain Mapping*, 34(11):3055–3065, 2013.

[241] J. R. Binder. Neuroanatomy of language processing studied with functional MRI. *Clinical Neuroscience*, 4(2):87–94, 1996.

[242] K. R. Pugh, B. A. Shaywitz, S. E. Shaywitz, R. T. Constable, P. Skudlarski, R. K. Fulbright, R. A. Bronen, D. P. Shankweiler, L. Katz, J. M. Fletcher, and J. C. Gore. Cerebral organization of component processes in reading. *Brain*, 119(4):1221–1238, 1996.

[243] F. Hoeft, B. D. McCandliss, J. M. Black, A. Gantman, N. Zakerani, C. Hulme, H. Lyytinen, S. Whitfield-Gabrieli, G. H. Glover, A. L. Reiss, and J. D. E. Gabrieli. Neural systems predicting long-term outcome in dyslexia. *Proc. National Academy of Sciences*, 108(1):361–366, 2011.

[244] J. M. Maisog, E. R. Einbinder, D. L. Flowers, P. E. Turkeltaub, and G. F. Eden. A meta-analysis of functional neuroimaging studies of dyslexia. *Annals of the New York Academy of Sciences*, 1145(1):237–259, 2008.

[245] F. Richlan, M. Kronbichler, and H. Wimmer. Functional abnormalities in the dyslexic brain: A quantitative meta-analysis of neuroimaging studies. *Human Brain Mapping*, 30(10):3299–3308, 2009.

[246] J. Linkersdörfer, J. Lonnemann, S. Lindberg, M. Hasselhorn, and C. J. Fiebach. Grey matter alterations co-localize with functional abnormalities in developmental dyslexia: An ALE meta-analysis. *PloS one*, 7(8):e43122, 2012.

[247] F. Richlan, M. Kronbichler, and H. Wimmer. Meta-analyzing brain dysfunctions in dyslexic children and adults. *Neuroimage*, 56(3):1735–1742, 2011.

[248] A. Elnakib, M. Nitzken, M. F. Casanova, H.-Y. Park, G. Gimel'farb, and A. El-Baz. Quantification of age-related brain cortex change using 3D shape analysis. In *Proc. International Conference on Pattern Recognition (ICPR'2012)*, pages 41–44. IEEE, 2012.

[249] S. Belongie, J. Malik, and J. Puzicha. Shape matching and object recognition using shape contexts. *IEEE Transactions on Pattern Analysis and Machine Intelligence*, 24(4):509–522, 2002.

[250] J. Duchon. Splines minimizing rotation-invariant semi-norms in sobolev spaces. In W. Schempp and K. Zeller, editors, *Constructive Theory of Functions of Several Variables*. 1977.

[251] S. Belongie, J. Malik, and J. Puzicha. A universal prior for integers and estimation by minimum description length. *The Annals of Statistics*, 11(2):416–431, 1982.

[252] S. Haker, S. Angenent, A. Tannenbaum, and R. Kikinis. Nondistorting flattening maps and the 3-D visualization of colon CT images. *IEEE Transactions on Medical Imaging*, 19(7):665–670, 2000.

[253] Y. Wang, B. S. Peterson, and L. H. Staib. Shape-based 3D surface correspondence using geodesics and local geometry. In *Proc. IEEE Conference on Computer Vision and Pattern Recognition (CVPR'2000)*, pages 644–641. IEEE, 2000.

[254] D. Zhang and M. Hebert. Harmonic maps and their applications in surface matching. In *Proc. IEEE Conference on Computer Vision and Pattern Recognition (CVPR'1999)*, pages 524–530, Fort Collins, CO, USA, 1999. IEEE.

[255] W. Zeng, J. Marino, A. Kaufman, and X. D. Gu. Volumetric colon wall unfolding using harmonic differentials. *Computers & Graphics*, 35(3):726–732, 2011.

[256] L. Gorelick, M. Galun, E. Sharon, R. Basri, and A. Brandt. Shape representation and classification using the poisson equation. *IEEE Transactions on Pattern Analysis and Machine Intelligence*, 28(12):1991–2005, 2006.

[257] Q. He, Y. Duan, J. Miles, and N. Takahashi. Statistical shape analysis of the corpus callosum in subtypes of autism. In *Proc. IEEE International Conference on Bioinformatics and Bioengineering (BIBE'2007)*, pages 1087–1091. IEEE, 2007.

[258] C. N. Vidal, R. Nicolson, T. J. DeVito, K. M. Hayashi, J. A. Geaga, D. J. Drost, P. Williamson, N. Rajakumar, Y. Sui, R. A. Dutton, A. W. Toga, and P. M. Thompson. Mapping corpus callosum deficits in autism: An index of aberrant cortical connectivity. *Biological Psychiatry*, 60(3):218–225, 2006.

[259] Q. He, S. Christ, K. Karsch, D. Peck, and Y. Duan. Shape analysis of corpus callosum in phenylketonuria using a new 3D correspondence algorithm. In *Proc. SPIE on Medical Imaging (SPIE'2010)*, pages 1087–1091, San Diego, CA, 2010.

[260] R. Schinzinger. *Conformal Mapping: Methods and Applications*. Courier Dover Publications, 2003.

[261] A. Pitiot, H. Delingette, P. M. Thompson, and N. Ayache. Expert knowledge guided segmentation system for brain MRI. *Neuroimage*, 3(1):S85–S96, 2004.

[262] R. A. Heckemann, J. V. Hajnal, P. Aljabar, D. Rueckert, and A. Hammers. Automatic anatomical brain MRI segmentation combining label propagation and decision fusion. *Neuroimage*, 33(1):115–126, 2006.

[263] Y. Zhou and A. W. Toga. Efficient skeletonization of volumetric objects. *IEEE Transactions on Visualization and Computer Graphics*, 5(3):196–209, 1999.

[264] I. Bitter, A. E. Kaufman, and M. Sato. Penalized-distance volumetric skeleton algorithm. *IEEE Transactions on bVisualization and Computer Graphics*, 7(3):195–206, 2001.

[265] S. Svensson, I. Nyström, and G. S. di Baja. Curve skeletonization of surface-like objects in 3D images guided by voxel classification. *Pattern Recognition Letters*, 23(12):1419–1426, 2002.

[266] S. Bouix, K. Siddiqi, and A. Tannenbaum. Flux driven fly throughs. In *Proc. IEEE Conference on Computer Vision and Pattern Recognition (CVPR'2003)*, pages 449–454, Madison, Wisconsin, 2003. IEEE.

[267] D. Attali and A. Montanvert. Computing and simplifying 2D and 3D continuous skeletons. *Computer Vision and Imag Understanding*, 67(3):261–273, 1997.

[268] L. Cohen and R. Kimmel. Global minimum for active contour models: A minimal path approach. *International Journal of Computer Vision*, 24(1):57–78, 1997.

[269] A. Elnakib, A. El-Baz, M. F. Casanova, G. Gimel'farb, and A. E. Switala. Image-based detection of corpus callosum variability for more accurate discrimination between autistic and normal brains. In *Proc. IEEE International Conference on Image Processing (ICIP'2010)*, pages 4337–4340. IEEE, 2010.

[270] M. F. Casanova, A. El-Baz, A. Elnakib, A. E. Switala, E. L. Williams, D. L. Williams, N. J. Minshew, and T. E. Conturo. Quantitative analysis of the shape of the corpus callosum in patients with autism and comparison individuals. *Autism*, 15(2):223–238, 2011.

[271] A. El-Baz, A. Elnakib, M. F. Casanova, G. Gimel'farb, A. E. Switala, D. Jordan, and S. Rainey. Accurate automated detection of autism related corpus callosum abnormalities. *Journal of Medical Systems*, 35(5):929–939, 2011.

[272] A. Elnakib, M. F. Casanova, G. Gimel'farb, A. E. Switala, and A. El-Baz. Autism diagnostics by centerline-based shape analysis of the corpus callosum. In *Proc. IEEE International Symposium on Biomedical Imaging: From Nano to Macro (ISBI'2011)*, pages 1843–1846. IEEE, 2011.

[273] A. Elnakib, M. F. Casanova, G. Gimel'farb, and A. El-Baz. Autism diagnostics by 3D shape analysis of the corpus callosum. In K. Suzuki, editor, *Machine Learning in Computer-aided Diagnosis: Medical Imaging Intelligence and Analysis*, chapter 15, pages 315–335. IGI Global, 2012.

[274] Y. Benjamini and Y. Hochberg. Controlling the false discovery rate: A practicle and powerful appraoch to multiple testing. *Journal of the Royal Statistical Society*, B57(1):289–300, 1995.

[275] H. A. E. Munim, R. Fahmi, N. Y. El-Zehiry, A. A. Farag, and M. F. Casanova. Volumetric MRI aanalysis of dyslexic subjects using a level-set framework. In J. S. Suri and A. Farag, editors, *Deformable Models Theory and Biomaterial Applications*, pages 461–492. Springer, New York, 2007.

[276] M. Habib. The neurological basis of developmental dyslexia: An overview and working hypothesis. *Brain*, 123(12):2373–2399, 2000.

[277] F. Robichon, P. Bouchard, J.-F. Dmonet, and M. Habib. Developmental dyslexia: Re-evaluation of the corpus callosum in male adults. *European Neurology*, 43(4):233–237, 2000.

[278] B. F. Pennington, P. A. Filipek, D. Lefly, J. Churchwell, D. N. Kennedy, J. H. Simon, C. M. Filley, A. Galaburda, M. Alarcon, and J. C. DeFries. Brain morphometry in reading-disabled twins. *Neurology*, 53(4):723–729, 1999.

[279] A. Firjany, A. Elnakib, A. El-Baz, G. Gimel'farb, M. A. El-Ghar, and A. Elmagharby. Novel stochastic framework for accurate segmentation of prostate in dynamic contrast enhanced MRI. In *Prostate Cancer Imaging. Computer-Aided Diagnosis, Prognosis, and Intervention*, pages 121–130. Springer, 2010.

[280] A. Firjani, A. Elnakib, F. Khalifa, A. El-Baz, G. Gimel'farb, M. A. El-Ghar, and A. Elmaghraby. A novel 3D segmentation approach for segmenting the prostate from dynamic contrast enhanced MRI using current appearance and learned shape prior. In *Proc. IEEE International Symposium on Signal Processing and Information Technology (ISSPIT'2010)*, pages 137–143. IEEE, 2010.

[281] A. Firjani, A. Elnakib, F. Khalifa, G. Gimel'farb, M. A. El-Ghar, J. Suri, A. Elmaghraby, and A. El-Baz. A new 3D automatic segmentation framework for accurate segmentation of prostate from DCE-MRI. In *Proc. IEEE International Symposium on Biomedical Imaging: From Nano to Macro (ISIB'2011)*, pages 1476–1479. IEEE, 2011.

[282] A. Firjani, F. Khalifa, A. Elnakib, G. Gimel'farb, M. A. El-Ghar, A. Elmaghraby, and A. El-Baz. 3D automatic approach for precise segmentation of the prostate from diffusion-weighted magnetic resonance imaging. In *Proc. IEEE International Conference on Image Processing (ICIP'2011)*, pages 2285–2288. IEEE, 2011.

[283] A. Firjani, F. Khalifa, A. Elnakib, G. Gimel'farb, M. A. El-Ghar, A. Elmaghraby, and A. El-Baz. Non-invasive image-based approach for early detection of prostate cancer. In *Proc. Fourth International Conference on Developments in eSystems Engineering (DeSE'2011)*, pages 172–177, Dubai, UAE, December 6–8, 2011.

[284] A. Firjani, A. Elnakib, F. Khalifa, G. Gimel'farb, M. A. El-Ghar, A. El-maghraby, and A. El-Baz. A new 3D automatic segmentation framework for accurate extraction of prostate from diffusion imaging. In *Proc. Biomedical Sciences and Engineering Conference (BSEC'2011)*, pages 1–4. IEEE, 2011.

[285] A. Firjani, F. Khalifa, A. Elnakib, G. Gimel'farb, A. Elmaghraby, and A. El-Baz. A novel image-based approach for early detection of prostate cancer. In *Proc. IEEE International Conference on Image Processing (ICIP'2012)*, pages 2849–2852, 2012.

[286] A. Firjani, A. Elnakib, F. Khalifa, G. Gimel'farb, M. A. El-Ghar, A. El-maghraby, and A. El-Baz. A diffusion-weighted imaging based diagnostic system for early detection of prostate cancer. *Journal of Biomedical Science and Engineering (JBiSE)*, 6:346–356, 2013.

[287] A. Firjani, F. Khalifa, A. Elnakib, G. Gimel'farb, M. A. El-Ghar, A. El-maghraby, and A. El-Baz. A novel image-based approach for early detection of prostate cancer using DCE-MRI. In K. Suzuki, editor, *Computational Intelligence in Biomedical Imaging*, chapter 3, pages 55–85. Springer Science and Business Media, 2014.

[288] S. E. Yuksel, A. El-Baz, A. A. Farag, M. Abo El-Ghar, T. A. Eldiasty, and M. A. Ghoneim. Automatic detection of renal rejection after kidney transplantation. In *International Congress Series*, volume 1281, pages 773–778, 2005.

[289] S. E. Yuksel, A. El-Baz, and A. A. Farag. A kidney segmentation framework for dynamic contrast enhanced magnetic resonance imaging. In *Proc. International Symposium on Mathematical Methods in Engineering (MME'2006)*, pages 55–64, Ankara, Turkey, April, 27-29, 2006.

[290] S. E. Yuksel, A. El-Baz, A. A. Farag, M. El-Ghar, T. Eldiasty, and M. A. Ghoneim. A kidney segmentation framework for dynamic contrast enhanced magnetic resonance imaging. *Journal of Vibration and Control*, 13(9-10):1505–1516, 2007.

[291] A. M. Ali, A. A. Farag, and A. El-Baz. Graph cuts framework for kidney segmentation with prior shape constraints. In *Proc. International Conference on Medical Image Computing and Computer-Assisted Intervention (MICCAI'2007)*, volume 1, pages 384–392, Brisbane, Australia, October 29–November 2, 2007.

[292] A. El-Baz, A. A. Farag, S. E. Yuksel, M. E. A. El-Ghar, T. A. Eldiasty, and M. A. Ghoneim. Application of deformable models for the detection of acute renal rejection. In A. A. Farag and J. S. Suri, editors, *Deformable Models*, volume 1, chapter 10, pages 293–333. 2007.

[293] A. El-Baz, A. Farag, R. Fahmi, S. Yuksel, W. Miller, M. A. El-Ghar, T. El-Diasty, and M. Ghoneim. A new CAD system for the evaluation of kidney diseases using DCE-MRI. In *Proc. International Conference on Medical Image Computing and Computer-Assisted Intervention (MICCAI'2006)*, pages 446–453, Copenhagen, Denmark, October 1-6, 2006.

[294] A. El-Baz, A. Farag, R. Fahmi, S. Yuksel, M. A. El-Ghar, and T. Eldiasty. Image analysis of renal DCE MRI for the detection of acute renal rejection. In *Proc. International Conference on Pattern Recognition (ICPR'2006)*, pages 822–825, Hong Kong, August 20-24, 2006.

[295] A. Farag, A. El-Baz, S. Yuksel, M. A. El-Ghar, and T. Eldiasty. A framework for the detection of acute rejection with dynamic contrast enhanced magnetic resonance imaging. In *Proc. IEEE International Symposium on Biomedical Imaging: From Nano to Macro (ISBI'2006)*, pages 418–421, Arlington, Virginia, USA, April 69, 2006. IEEE.

[296] A. El-Baz, G. Gimel'farb, and M. A. El-Ghar. New motion correction models for automatic identification of renal transplant rejection. In *Proc. International Conference on Medical Image Computing and Computer-Assisted Intervention (MICCAI'2007)*, pages 235–243, Brisbane, Australia, October 29 - November 2, 2007.

[297] A. El-Baz, G. Gimel'farb, and M. A. El-Ghar. Image analysis approach for identification of renal transplant rejection. In *Proc. International Conference on Pattern Recognition (ICPR'2008)*, pages 1–4, Tampa, Florida, USA, December 8-11, 2008.

[298] A. El-Baz, G. Gimel'farb, and M. A. El-Ghar. A novel image analysis approach for accurate identification of acute renal rejection. In *Proc. International Conference on Image Processing, (ICIP'2008)*, pages 1812–1815, San Diego, California, USA, October 12–15, 2008.

[299] F. Khalifa, G. Gimel'farb, M. A. El-Ghar, G. Sokhadze, S. Manning, P. McClure, R. Ouseph, and A. El-Baz. A new deformable model-based segmentation approach for accurate extraction of the kidney from abdominal CT images. In *Proc. International Conference on Image Processing (ICIP'2011)*, pages 3393–3396, Brussels, Belgium, September 11–14, 2011.

[300] F. Khalifa, A. Elnakib, G. M. Beache, G. Gimel'farb, M. A. El-Ghar, G. Sokhadze, S. Manning, P. McClure, and A. El-Baz. 3D kidney segmentation from CT images using a level set approach guided by a novel stochastic speed function. In *Proc. International Conference on Medical Image Computing and Computer-Assisted Intervention (MICCAI'2011)*, pages 587–594, Toronto, Canada, Sept. 18–22, 2011.

[301] M. Mostapha, F. Khalifa, A. Alansary, A. Soliman, G. Gimel'farb, and A. El-Baz. Dynamic MRI-based computer aided diagnostic systems for early detection of kidney transplant rejection: A survey. In *Proc. International Symposium on Computational Models for Life Sciences (CMLS'2013)*, volume 1559, pages 297–306, 2013.

[302] M. Mostapha, F. Khalifa, A. Alansary, A. Soliman, J. Suri, and A. El-Baz. Computer-aided diagnosis systems for acute renal transplant rejection: Challenges and methodologies. In A. El-Baz and L. saba J. Suri, editors, *Abdomen and Thoracic Imaging*, chapter 1, pages 1–35. Springer, 2014.

[303] A. El-Baz, A. A. Farag, R. Falk, and R. La Rocca. Automatic identification of lung abnormalities in chest spiral CT scans. In *Proc. IEEE International Conference on Acoustics, Speech, and Signal Processing, (ICASSP'2003)*, volume 2, pages II–261. IEEE, 2003.

[304] A. El-Baz, A. A. Farag, R. Falk, and R. La Rocca. A unified approach for detection, visualization, and identification of lung abnormalities in chest spiral CT scans. In *International Congress Series*, volume 1256, pages 998–1004. Elsevier, 2003.

[305] A. El-Baz, A. A. Farag, R. Falk, and R. La Rocca. Detection, visualization and identification of lung abnormalities in chest spiral CT scan: Phase-I. In *Proc. International conference on Biomedical Engineering, Cairo, Egypt*, volume 12, 2002.

[306] A. A. Farag, A. El-Baz, G. Gimel'farb, and R. Falk. Detection and recognition of lung abnormalities using deformable templates. In *Proc. International Conference on Pattern Recognition (ICPR'2004)*, volume 3, pages 738–741. IEEE, 2004.

[307] A. A. Farag, A. El-Baz, G. G. Gimelfarb, R. Falk, and S. G. Hushek. Automatic detection and recognition of lung abnormalities in helical CT images using deformable templates. In *Proc. International Conference on Medical Image Computing and Computer-Assisted Intervention (MICCAI'2004)*, pages 856–864. Springer, 2004.

[308] A. El-Baz, S. E. Yuksel, S. Elshazly, and A. A. Farag. Non-rigid registration techniques for automatic follow-up of lung nodules. In *Proc. Computer Assisted Radiology and Surgery (CARS'2005)*, volume 1281, pages 1115–1120. Elsevier, 2005.

[309] A. A. Farag, A. El-Baz, G. Gimelfarb, M. Abou El-Ghar, and T. Eldiasty. Quantitative nodule detection in low dose chest CT scans: New template modeling and evaluation for CAD system design. In *Proc. International Conference on Medical Image Computing and Computer-Assisted Intervention (MICCAI'2005)*, pages 720–728. Springer, 2005.

[310] A. El-Baz, A. Farag, G. Gimel'farb, R. Falk, M. Abou El-Ghar, and T. Eldiasty. A framework for automatic segmentation of lung nodules from low dose chest CT scans. In *Proc. International Conference on Pattern Recognition (ICPR'2006)*, volume 3, pages 611–614. IEEE, 2006.

[311] A. M. Ali, A. S. El-Baz, and A. A. Farag. A novel framework for accurate lung segmentation using graph cuts. In *Proc. IEEE International Symposium on Biomedical Imaging: From Nano to Macro (ISBI'2007)*, pages 908–911. IEEE, 2007.

[312] A. El-Baz, G. Gimel'farb, R. Falk, and M. Abou El-Ghar. A novel approach for automatic follow-up of detected lung nodules. In *Proc. International Conference on Image Processing (ICIP'2007)*, volume 5, pages 501–504. IEEE, 2007.

[313] A. El-Baz, G. Gimel'farb, R. Falk, and M. Abou El-Ghar. A new CAD system for early diagnosis of detected lung nodules. In *Proc. International Conference on Image Processing (ICIP'2007)*, volume 2, pages II–461. IEEE, 2007.

[314] A. A. Farag, A. El-Baz, G. Gimel'farb, R. Falk, M. A. El-Ghar, T. Eldiasty, and S. Elshazly. Appearance models for robust segmentation of pulmonary nodules in 3D LDCT chest images. In *Proc. International Conference on Medical Image Computing and Computer-Assisted Intervention (MICCAI'2006)*, pages 734–741, Copenhagen, Denmark, October 1-6, 2006.

[315] A. M. Ali and A. A. Farag. Automatic lung segmentation of volumetric low-dose CT scans using graph cuts. In *Advances in Visual Computing*, pages 258–267. Springer, 2008.

[316] A. El-Baz, G. L. Gimel'farb, R. Falk, M. Abou El-Ghar, T. Holland, and T. Shaffer. A new stochastic framework for accurate lung segmentation. In *Proc. International Conference on Medical Image Computing and Computer-Assisted Intervention (MICCAI'2008)*, pages 322–330, 2008.

[317] A. El-Baz, G. L. Gimel'farb, R. Falk, D. Heredis, and M. Abou El-Ghar. A novel approach for accurate estimation of the growth rate of the detected lung nodules. In *Proc. International Workshop on Pulmonary Image Analysis*, pages 33–42, 2008.

[318] A. El-Baz, G. L. Gimel'farb, R. Falk, T. Holland, and T. Shaffer. A framework for unsupervised segmentation of lung tissues from low dose computed tomography images. In *Proc. British Machine Vision (BMVC'2008)*, pages 1–10, 2008.

[319] A. El-Baz, G. Gimel'farb, R. Falk, and M. Abou El-Ghar. A new approach for automatic analysis of 3D low dose CT images for accurate monitoring the detected lung nodules. In *Proc. International Conference on Pattern Recognition (ICPR'2008)*, pages 1–4. IEEE, 2008.

[320] A. El-Baz, G. Gimel'farb, R. Falk, M. Abou El-Ghar, and H. Refaie. Promising results for early diagnosis of lung cancer. In *Proc. IEEE International Symposium on Biomedical Imaging: From Nano to Macro (ISBI'2008)*, pages 1151–1154. IEEE, 2008.

[321] A. El-Baz, G. Gimelfarb, R. Falk, and M. Abo El-Ghar. Automatic analysis of 3D low dose CT images for early diagnosis of lung cancer. *Pattern Recognition*, 42(6):1041–1051, 2009.

[322] A. El-Baz, G. Gimelfarb, R. Falk, M. Abou El-Ghar, S. Rainey, D. Heredia, and T. Shaffer. Toward early diagnosis of lung cancer. In *Proc. International Conference on Medical Image Computing and Computer-Assisted Intervention (MICCAI'2009)*, pages 682–689. Springer, 2009.

[323] A. El-Baz, G. Gimel'farb, R. Falk, and M. El-Ghar. Appearance analysis for diagnosing malignant lung nodules. In *Proc. IEEE International Symposium*

on Biomedical Imaging: From Nano to Macro (ISBI'2010), pages 193–196. IEEE, 2010.

[324] A. El-Baz, P. Sethu, G. Gimel'farb, F. Khalifa, A. Elnakib, R. Falk, and M. Abo El-Ghar. Elastic phantoms generated by microfluidics technology: Validation of an imaged-based approach for accurate measurement of the growth rate of lung nodules. *Biotechnology Journal*, 6(2):195–203, 2011.

[325] A. El-Baz, G. Gimelfarb, R. Falk, M. Abo El-Ghar, and J. Suri. Appearance analysis for the early assessment of detected lung nodules. In *Lung Imaging and Computer Aided Diagnosis*, chapter 17, pages 395–404. 2011.

[326] A. El-Baz, P. Sethu, G. Gimelfarb, F. Khalifa, A. Elnakib, R. Falk, A. M. El-Ghar, and J. Suri. Validation of a new imaged-based approach for the accurate estimating of the growth rate of detected lung nodules using real computed tomography images and elastic phantoms generated by state-of-theart microfluidics technology. In *Lung Imaging and Computer Aided Diagnosis*, chapter 18, pages 405–420. 2011.

[327] A. El-Baz, M. Nitzken, G. Gimelfarb, E. Van Bogaert, R. Falk, M. Abo El-Ghar, and J. Suri. Three-dimensional shape analysis using spherical harmonics for early assessment of detected lung nodules. In *Lung Imaging and Computer Aided Diagnosis*, chapter 19, pages 421–438. 2011.

[328] A. El-Baz, G. Gimelfarb, R. Falk, and M. Abo El-Ghar. 3D MGRF-based appearance modeling for robust segmentation of pulmonary nodules in 3D LDCT chest images. In *Lung Imaging and Computer Aided Diagnosis*, chapter 3, pages 51–63. 2011.

[329] B. Abdollahi, A. Soliman, A. Civelek, X.-F. Li, G. Gimelfarb, and A. El-Baz. A novel 3D joint MGRF framework for precise lung segmentation. In *Machine Learning in Medical Imaging*, pages 86–93. Springer, 2012.

[330] A. El-Baz, F. Khalifa, A. Elnakib, M. Nitzken, A. Soliman, P. McClure, M. Abou El-Ghar, and G. Gimelfarb. A novel approach for global lung registration using 3D Markov-Gibbs appearance model. In *Proc. International Conference on Medical Image Computing and Computer-Assisted Intervention (MICCAI'2012)*, pages 114–121. Springer, 2012.

[331] A. El-Baz, G. Gimel'farb, M. Abou El-Ghar, and R. Falk. Appearance-based diagnostic system for early assessment of malignant lung nodules. In *Proc. International Conference on Image Processing (ICIP'2012)*, pages 533–536. IEEE, 2012.

[332] A. El-Baz, A. Soliman, P. McClure, G. Gimel'farb, M. Abou El-Ghar, and R. Falk. Early assessment of malignant lung nodules based on the spatial analysis of detected lung nodules. In *Proc. IEEE International Symposium on Biomedical Imaging: From Nano to Macro (ISBI'2012)*, pages 1463–1466. IEEE, 2012.

[333] A. El-Baz, A. Elnakib, M. Abou El-Ghar, G. Gimel'farb, R. Falk, and A. Farag. Automatic detection of 2D and 3D lung nodules in chest spiral CT scans. *International Journal of Biomedical Imaging*, 2013, 2013.

[334] A. El-Baz, G. M. Beache, G. Gimel'farb, K. Suzuki, K. Okada, A. Elnakib, A. Soliman, and B. Abdollahi. Computer-aided diagnosis systems for lung cancer: Challenges and methodologies. *International Journal of Biomedical Imaging*, 2013, 2013.

[335] A. Soliman, F. Khalifa, A. Alansary, G. Gimel'farb, and A. El-Baz. Performance evaluation of an automatic MGRF-based lung segmentation approach. In *Proc. International Symposium on Computational Models for Life Sciences (CMLS'2013)*, volume 1559, pages 323–332, 2013.

[336] M. F. Casanova, A. Farag, E.-B. Ayman, M. Meghan, H. Hassan, R. Fahmi, and A. E. Switala. Abnormalities of the gyral window in autism: A macroscopic correlate to a putative minicolumnopathy. *Journal of Special Education and Rehabilitation*, 7(1-2), 2006.

[337] R. Fahmi, A. S. El-Baz, H. Abd El Munim, A. A. Farag, and M. F. Casanova. Classification techniques for autistic vs. typically developing brain using MRI data. In *Proc. IEEE International Symposium on Biomedical Imaging: From Nano to Macro (ISBI'2007)*, pages 1348–1351. IEEE, 2007.

[338] A. A. Farag, R. Fahmi, M. F. Casanova, A. E. Abdel-Hakim, H. A. El-Munim, and A. El-Baz. Robust neuroimaging-based classification techniques of autistic vs. typically developing brain. In *Deformable Models*, chapter 16, pages 535–566. Springer, 2007.

[339] R. Fahmi, A. Elbaz, H. Hassan, A. A. Farag, and M. F. Casanova. Structural MRI-based discrimination between autistic and typically developing brain. In *Proc. Computer Assisted Radiology and Surgery (CARS'2007)*, pages 24–26, 2007.

[340] A. El-Baz, M. F. Casanova, G. Gimel'farb, M. Mott, and A. E. Switala. Autism diagnostics by 3D texture analysis of cerebral white matter gyrifications. In *Proc. International Conference on Medical Image Computing and Computer-Assisted Intervention (MICCAI'2007)*, pages 882–890. Springer, 2007.

[341] M. F. Casanova, A. El-Baz, M. Mott, G. Mannheim, H. Hassan, R. Fahmi, J. Giedd, J. M. Rumsey, A. E. Switala, and A. Farag. Reduced gyral window and corpus callosum size in autism: Possible macroscopic correlates of a minicolumnopathy. *Journal of Autism and Developmental Disorders*, 39(5):751–764, 2009.

[342] M. F. Casanova, A. El-Baz, E. Vanbogaert, P. Narahari, and A. Switala. A topographic study of minicolumnar core width by lamina comparison between autistic subjects and controls: Possible minicolumnar disruption due to an anatomical element in-common to multiple laminae. *Brain Pathology*, 20(2):451–458, 2010.

[343] M. F. Casanova, A. S. El-Baz, S. S. Kamat, B. A. Dombroski, F. Khalifa, A. El-nakib, A. Soliman, A. Allison-McNutt, and A. E. Switala. Focal cortical dys-plasias in autism spectrum disorders. *Acta Neuropathologica Communications*, 1(1):67, 2013.

APPENDIX I

NOMENCLATURE

The following convention is used throughout the dissertation.

- Q is the number of gray levels.

- $\mathbf{Q} = \{0, \ldots, Q - 1\}$ denote sets of gray levels q.

- $\mathbf{L} = \{ob, bg\}$ denote a set of region labels (i.e., object "ob" and background "bg" labels).

- $\mathbf{U} = [0, 1]$ denote the unit interval $[0, 1]$.

- (x, y) – 2D Cartesian coordinates of points (pixels) in the image plane.

- $\mathbf{R} = \{(x, y) : 1 \leq x \leq X, 1 \leq y \leq Y\}$ is a finite arithmetic grid supporting gray level images $\mathbf{g} : \mathbf{R} \to \mathbf{Q}$ and their region maps $\mathbf{m} : \mathbf{R} \to \mathbf{L}$.

- $\mathbf{g} = [g_{x,y} : (x, y) \in \mathbf{R}; g_{x,y} \in \mathbf{Q}]$ – a gray level digital image taking gray values from a finite set $\mathbf{Q} = \{0, \ldots, Q - 1\}$.

- $\mathbf{m} = [m_{x,y} : (x, y) \in \mathbf{R}; m_{x,y} \in \mathbf{L}]$ – a region map taking labels from a finite set $\mathbf{L} = \{ob, bg\}$.

- $\mathbf{s} = [S_{m_{x,y}} : (x, y) \in \mathbf{R}; S_{m_{x,y}} \in \mathbf{U}]$ – a positive probabilistic shape for the object and background region map taking values from the unit interval $\mathbf{U} = [0, 1]$.

- $P(\mathbf{g}, \mathbf{m})$ is a joint MGRF model of the image $\mathbf{g}$ and its region map $\mathbf{m}$.

- $P(\mathbf{g}|\mathbf{m})$ is a conditional distribution of images, given the map (the lower level of the model).

- $P(\mathbf{m})$ is an unconditional Gibbs probability distribution of maps with shape prior (the higher level).

- $P_{\mathrm{s}}(\mathbf{m})$ is a prior shape probability distribution of maps.

- $P_{\mathrm{h}}(\mathbf{m})$ is an unconditional Gibbs probability distribution of maps.

- $\mathbf{N}_a$ is a neighborhood system of pixels (or voxels) at absolute distance a.

- $\mathbf{A} = [a : a \in \{1, \sqrt{2}, ..\}]$ is a set of the absolute distances a between the pixel (or voxel) and its neighbors in the neighborhood system.

- $\mathbf{V}_a = \{V_{a,\mathrm{eq}}, V_{a,\mathrm{ne}}\}$ denote the Gibbs potential values for pixels at distance a with equal (i.e., $V_{a,\mathrm{eq}}$) or non equal (i.e., $V_{a,\mathrm{ne}}$) labels.

- ξ is the shift in x–direction.

- η is the shift in y–direction.

- $f_{a,\mathrm{eq}}(\mathbf{m})$ denotes the relative frequency of the equal label pairs in the equivalent pixel pairs $\{((x, y), (x+\xi, y+\eta)): (x, y) \in \mathbf{R}; (x+\xi, y+\eta) \in \mathbf{R}; (\xi, \eta) \in \mathbf{N}_a\}$.

- λ denotes an object ("ob") or background ("bg") region label (i.e., $\lambda \in \mathbf{L}$).

- $p_\lambda = [p_\lambda(q) : q \in \mathbf{Q}; \lambda \in \mathbf{L}]$ denote pixel-wise probability distributions for the object and its background.

- $p_{\mathrm{LCDG}}(q)$ is the estimated density for the mixed gray level distribution using LCDG approximation.

- $w_{\mathrm{p},.}$ is the mixed weight of positive Gaussian kernel.

- $w_{\mathrm{n},.}$ is the mixed weight of negative Gaussian kernel.

- C_n is the number of negative Gaussian kernel for the estimated mixed density.

- C_p is the number of positive Gaussian kernel for the estimated mixed density.

- μ denotes the mean of a population.

- σ denotes the standard deviation of a population.

- $\rho \equiv (\mu, \sigma^2)$ shorthand notation for mean, μ, and variance, σ^2.

- $\psi(q|\rho)$ is a Gaussian density with ρ denoting its mean and variance.

- $\Phi(\rho)$ is a cumulative Gaussian probability function with ρ denoting its mean and variance.

- $\Psi_\rho = (\psi(q|\rho) : q \in \mathbf{Q})$ is a Discrete Gaussian (DG) density distribution; $\psi(q|\rho) = \Phi_\rho(q + 0.5) - \Phi_\rho(q - 0.5)$ for $q = 1, \ldots, Q - 2$, $\psi(0|\rho) = \Phi_\rho(0.5)$, and $\psi(Q - 1|\rho) = 1 - \Phi_\rho(Q - 1.5)$ [102].

- $\alpha \in \{p, n\}$ an index specifies whether the DG is positive or negative.

- $E(.)$ is the Gibbs energy function.

- t is a discrete time instance, i.e., $t \in \{0, 1, ..\}$.

- ν denotes a point coordinates; in 2D $\nu = (x, y)$ and in 3D $\nu = (x, y, z)$.

- $D(\nu)$ is the normalized minimum Euclidian distance between every point $\nu = (x, y)$ in the outer area of an object and the object edge.

- $F(\nu)$ is a speed function of a level set function.

- $T(\nu)$ is the time at which the level set front crosses the point (x, y).

- β is a constant to control the evolution of a level set function.

- $|\mathbf{C}|$, $|\mathbf{G}|$, and $|\mathbf{g}|$ denote areas (by the number of pixels) of the segmented object $\mathbf{C}$, its ground truth $\mathbf{G}$, and the image data $\mathbf{g}$.

- $P_{\texttt{area}}$ is the percentage area of the pathological tissue in the left ventricle wall of the heart.

- A_i denotes the area of pathology of a segment i, $i \in \{1, 2, .., 17\}$, in the 17-segment myocardial model [4] of the left ventricle wall of the heart.

- B_i denotes the area of a segment i, $i \in \{1, 2, .., 17\}$, in the 17-segment myocardial model [4] of the left ventricle wall of the heart.

- $P_{\texttt{path}}$ is the transmural extent of the pathological tissue in the left ventricle wall of the heart.

- T_j is the LV width in the line j.

- d_j is the extent of pathology in the line j.

- Υ is a scaler potential field between two potential surfaces.

- $\mathbf{B_a} = [B_{a1}, B_{a2}, .., B_{am}]$ denote a potential surface $\mathbf{a}$ of m points $B_{a1}, B_{a2}, .., and B_{am}$.

- $\mathbf{B_b} = [B_{b1}, B_{b2}, .., B_{bn}]$ denote a potential surface $\mathbf{b}$ of n points $B_{b1}, B_{b2}, .., and B_{bn}$.

- E_x, E_y denote the electrical filed vectors of the potential field Υ in x and y directions, respectively.

- S_L denotes the Lagrangian strain for finitely small displacement.

- X_1, X_2 denote the circumferential and radial directions for an element on the left ventricle (LV) wall, respectively.

- x_1, x_2 denote the dimensions of an element on the LV wall.

- $\varepsilon_{x_1}, \varepsilon_{x_2}$ denote the normal components of the strain S_L in the circumferential and radial directions, respectively.

- $\varepsilon_{x_1 x_2}, \varepsilon_{x_2 x_1}$ denote the shearing components of the strain S_L.

- $\Delta x_1, \Delta x_2$ denote the displacement of an element on the LV wall in the circumferential and radial directions, respectively.

- A, B denote a start point and an end point, respectively.

- r(GT) denote the correlation coefficient between a measurement ant its ground truth (GT) value.

- C_{AB} is a set of all possible paths linking A, and B.

- $C(l)$ is a path in the set C_{AB}.

- $W(\nu)$ is a cost point at the point ν inside the object of interest.

- L is the path length.

- (i, j, k) denotes an object boundary point in a 3D image.

- (i_0, j_0, k) denotes the center on the slicing plane k.

- (x, y, z) – Cartesian coordinates of points (voxels) for a 3D image.

- (r, θ, z) – Polar coordinates of points.

- $r_{\text{dyslexia}}, r_{\text{normal}}$ denote the mean corpus callosum shape maps for dyslexic and normal subjects, respectively.

- $\Delta r = r_{\text{dyslexia}} - r_{\text{control}}$ denotes the absolute difference between the mean corpus callosum shape maps of dyslexic and normal subjects.

- $q*$ denotes a false discovery rate.

- V_{Ref}, V_{Short}, and V_{Thin} denote volumes of CC (number of voxels times the voxel volume) for the reference, short, and thin phantoms, respectively.

- A_z denotes the area under the curve.

CURRICULUM VITAE

Ahmed Elnakib

BioImaging Lab
Department of Bioengineering
Paul C. Lutz Hall, Rm 304
University of Louisville, Louisville, KY 40292
E-mail: aaelna02@louisville.edu
Tel: (502) 852-4032
Cell: (502) 851-0573

Education

Degree	Date	School	Area
Ph.D.	2013	University of Louisville	Electrical Engineering
M. Sc.	2007	Mansoura University, Egypt	Electrical Engineering
B. Sc.	2003	Mansoura University, Egypt	Electrical Engineering

Thesis/Dissertation:

Ph.D. Dissertation: *Developing Advanced Mathematical Models for Detecting Abnormalities in 2D/3D Medical Structures*– Dr. Ayman S. El-Baz, Thesis Advisor.

M.S. Thesis: *Intrusion Detection Systems using FPGA*– Dr. Mohy Eldin A. Abou-Elsoud and Dr. Ahmad A. Hassan, Thesis Advisors.

Teaching Experience

Assist in teaching, laboratory demonstration, conducting tutorials, grading, and assisting in projects of the following undergraduate courses for Electrical Engineering students:

Place	Course Subject	Semester/Year
Mansoura University	Microprocessor Architecture Computer Networks Advanced Electronics III	2007-2008
Mansoura University	Linear Network Analysis and Synthesis Advanced Electronics I Advanced Electronics II	2005-2006
Mansoura University	Integrated Circuits Layout & Design Artificial Neural Networks Basic Electronics Electronic circuits laboratory	2003-2004

Employment

- 2008-2013 Research Assistant, Bioimaging Lab, Bioengineering Department, University of Louisville, USA.

- 2004-2008 Research Assistant, Department of Electronics and Communications Engineering, Mansoura University, Egypt.

Scientific and Honor Societies

- Member, Institute of Electrical and Electronics Engineers (IEEE).

- Member of The Egyptian Engineers Syndicate, Electrical Engineering License No. 8239/49.

Selected Awards and Recognition

- Participant in the BioImaging Lab team that ranked the first place award in *the international MRBrainS challenge at MICCAI conference* among 56 teams submitted their results and 12 teams invited for the onsite competition, September 2013.

- *Theobald Scholarship Award* in recognition of valuable contribution to the Department of Electrical and Computer Engineering (ECE), University of Louisville, April 2013.

- ECE *Outstanding student*, April 2012.

- *Who's Who* Among Students in American Universities, 2011.

- Reviewer, *IEEE International Symposium on Biomedical Imaging Conference*.

- Reviewer, *IEEE Transactions on Image processing*.

- Reviewer, *IEEE Transactions on Medical Imaging*.

- Reviewer, *International Journal of Biomedical Imaging*.

- University Travel Awards in *2011 and 2012* to attend the ISBI and ICIP conferences.

- Sponsored Research Tuition Award in *Summer 2012, Fall 2012, Spring 2013, Summer 2013, and Fall 2013*.

Research Activities

- Image modeling, image segmentation algorithms, 2-D and 3-D registration, and texture and shape analysis of human organs.

- Development of computer aided diagnosis (CAD) systems for prostate cancer, dyslexia, autism, and cardiac diseases.

- Analysis of cardiac images to follow up the treatment of cardiac diseases.

- Analysis of brain images to detect developmental brain disorders.

- Assisted in grants writing and preparing primary results for the Bioimaging Lab, University of Louisville.

Class work Grade

A total of 34 credit hours in ECE, Math and CS subjects - GPA is 3.872. Particular course concentration has been in statistical modeling, medical imaging, and machine learning. Relevant courses include: digital image processing, intro to biometrics, foundation of optimization, artificial intelligence, pattern recognition and machine intelligence, introduction to medical imaging, graph cut algorithms, introduction to random process and estimation theory, and medical image analysis.

Skills

- *Programming Language*: C++, VHDL, Visual Basic, Java Script.

- *Systems*: Windows, Linux.

- *Utilities*: Matlab, Simulink, Pspice, L-Edit, Mentor Graphic Tools, MS Excel, MS Word, Latex.

Publications

During the PhD (Fall 2008- Fall 2013), I have authored or co-authored 15 journal articles, 7 book chapters, and 30 peer-reviewed conference papers. The articles have appeared in world-renown journals including The International Journal of Cardiovascular Imaging (impact factor 2.648), Autism (5-years impact factor 3.166), Journal of Biotechnology (5-years impact factor 3.34), Medical Physics (impact factor 2.83), IEEE Transactions on Biomedical Engineering (impact factor 2.348), IEEE Transactions on Information Technology in Biomedicine (impact factor 1.98), Journal of Medical Systems (impact factor 1.783), and Pattern Recognition Letters (5-years impact factor 1.529). The conference papers were reported as top-rank international conferences in image processing, and medical imaging, e.g. MICCAI, ISBI, ICIP, and IPMI with acceptance rate less than 30%.

Journal Papers

1. M. F. Casanova, A. S. EL-Baz, S. S Kamat, B. A. Dombroski, F. Khalifa, **A. Elnakib**, A. soliman, A. Allison-McNutt, and A. E. Switala, "Focal Cortical Dysplasias in Autism Spectrum Disorders," *Acta Neuropathologica Communications,* vol. 1, issue 1, pp. 1-11, October, 2013. DOI: 10.1186/2051-5960-1-67.

2. A. Alansary, A. Soliman, F. Khalifa, **A. Elnakib**, M. Mostapha, M. Nitzken, M. Casanova, and A. El-Baz, "MAP-Based Framework for Segmentation of MR Brain Images Based on Visual Appearance and Prior Shape," MIDAS Journal, vol. 1, pp. 1-13, Oct 2013. Available: http://hdl.handle.net/10380/3440.

3. A. Firjani, **A. Elnakib**, F. Khalifa, G. Gimel'farb, M. Abou El-Ghar, A. Elmaghraby, and A. El-Baz, "A Diffusion-weighted Imaging Based diagnostic System for Early Detection of Prostate Cancer," *J. Biomedical Science and Engineering (JBiSE),* vol. 6, 99. 346-356, 2013.

4. H. Sliman, F. Khalifa, **A. Elnakib**, A. Soliman, A. El-Baz, G. M. Beache, A. Elmaghraby, and G. Gimel'farb. "Myocardial Borders Segmentation from Cine MR Images using Bidirectional Coupled Parametric Deformable Models," *Medical physics,* vol. 40, no. 9:092302, 2013.

5. A. El-Baz, **A. Elnakib**, M. Abou El-Ghar, G. Gimel'farb, and R. Falk, "Automatic Detection of 2D and 3D Lung Nodules in Chest Spiral CT Scans," *International Journal of Biomedical Imaging,* vol. 2013, Article ID 517632, 11 pages, 2013.

6. A. El-Baz, G. Beache, G. Gimel'farb, K. Suzuki, K. Okada, **A. Elnakib**, A.Soliman and B. Abdollahi, "Computer Aided Diagnosis Systems for Lung Cancer: Challenges and Methodologies," *International Journal of Biomedical Imaging,* vol. 2013, Article ID 942353, 46 pages, 2013.

7. A. Rudra, A. Chowdhury, **A. Elnakib**, F. Khalifa, A. Soliman, G. Beache, and A. El-Baz, "Kidney Segmentation using Graph Cuts and Pixel Connectivity," *Pattern Recognition Letters,* vol. 34, no. 13, pp. 170-1475, 2013.

8. **A. Elnakib**, M. F. Casanova, G. Gimel'farb, A. E. Switala, and A. El-Baz, "Dyslexia Diagnostics by 3D Shape Analysis of the Corpus Callosum," *IEEE Transactions on Information Technology in Biomedicine (TITB),* vol. 16, no. 4, pp. 700-708, July 2012.

9. **A. Elnakib**, G. M. Beache, G. Gimel'farb, and A. El-Baz, "New Automated Markov-Gibbs Random Field Framework for Myocardial Wall Viability Quantification in Agent Contrast Enhanced Cardiac Magnetic Resonance Images," *The International Journal of Cardiovascular Imaging,* vol. 28, no. 7, pp. 1683-1698, October 2012.

10. A. El-Baz, **A. Elnakib**, F. Khalifa, M. Abou El-Ghar, R. Falk, and G. Gimel'farb, "Precise Segmentation of 3D Magnetic Resonance Angiography," *IEEE Transaction on Biomedical Engineering (TBME),* vol. 59, no. 7, pp. 2019-2029, July 2012.

11. A. El-Baz, **A. Elnakib**, M. F. Casanova, G. Gimel'farb, A. E. Switala, D. Jordan, and S. Rainey, "Accurate Automated Detection of Autism Related Corpus Callosum Abnormalities," *International Journal of Medical Systems (JMS),* vol. 35, no. 5, pp. 929-939, October 2011.

12. A. Rudra, M. Sen, A. Chowdhury, **A. Elnakib**, and A. El-Baz, "3D Graph Cut with New Edge Weights for Cerebral White Matter Segmentation," *Pattern Recognition Letters,* vol. 32, no. 7, pp. 941–947, May 2011.

13. M. Casanova, A. El-Baz, **A. Elnakib**, J. Giedd, J. Rumsey, E. Williams, A. Switala, "Quantitative Analysis of the Shape of the Corpus Callosum in Autistic Individuals," *Autism,* vol. 15, no. 2, pp. 223-238, March 2011.

14. A. El-Baz, P. Sethu, G. Gimel'farb, F. Khalifa, **A. Elnakib**, R. Falk, and M. Abo El-Ghar, "Elastic Phantoms Generated by Microfluidics Technology: Validation of an Imaged-Based Approach for Accurate Measurement of the Growth Rate of Lung Nodules," *Biotechnology Journal,* vol.6, no.2, pp.195-203, February 2011.

15. M. Casanova, A. El-Baz, **A. Elnakib**, J. Giedd, J. Rumsey, E. Williams, A. Switala, "Corpus Callosum Shape Analysis with Application to Dyslexia," *Journal of Translational Neuroscience,* vol. 1, no. 2, pp. 124-130, June 2010.

Book Chapters

1. **A. Elnakib**, M. Abou El-Ghar, G. Gimel'farb, R. Falk, J. Suri, and A. El-Baz, "Modified Akaike Information Criterion for Selecting the Numbers of Mixture Components: An Application to Initial Lung Segmentation," In *Multi-Detector CT Imaging: Abdomen, Pelvis, and CAD Applications (L. Saba and J. Suri, Editors),* CRC Press: Taylor and Francis Group, 2014, Chapter 28, pp. 609-620.

2. A. Firjani, F. Khalifa, **A. Elnakib**, G. Gimel'farb, M. Abou El-Ghar, A. Elmaghraby, and A. El-Baz, "A Novel Image-based Approach for Early Detection of Prostate Cancer using DCE-MRI," In *Handbook of Computational Intelligence in Biomedical Imaging,* (K. Suzuki Editor), Springer-Verlag, New York, 2014, Chapter 3, pp. 55-82.

3. **A. Elnakib**, M Casanova, G. Gimel'farb, A. Switala, and A. El-Baz, "Autism Diagnostics by 3D Shape Analysis of the Corpus Callosum," In *Machine Learning in Computer-Aided Diagnosis: Medical Imaging Intelligence and Analysis*, IGI Global (Hershey, PA), 2011, Chapter 15, pp. 315-335.

4. **A. Elnakib**, A. El-Baz, G. Gimel'farb, and J. Suri, "Medical Image Segmentation: A Brief Survey," In *Handbook of Multi-Modality Medical Image Segmentation and Registration Techniques: Volume 2,* (A. El-Baz, R. Acharya, M. Mirmedhdi, and J. Suri, Editors), Springer-Verlag, New York, 2011, Chapter 1, pp. 1-39.

5. El-Baz, G. Gimel'farb, **A. Elnakib**, R. Falk, and M. Abou El-Ghar, "Fast Accurate Unsupervised Segmentation of 3D Magnetic Resonance Angiography," In *Handbook of Atherosclerosis Disease Management*, (J. S. Suri, Editor), Springer, 2011, Chapter 14, pp. 411-432.

6. A. El-Baz, P. Sethu, G. Gimel'farb, F. Khalifa, **A. Elnakib**, R. Falk, M. Abo El-Ghar, and J. Suri, "Validation of a New Image-Based Approach for the Accurate Estimating of the Growth Rate of Detected Lung Nodules Using Real Computed Tomography Images and Elastic Phantoms Generated by State-of-the-Art Microfluidics Technology," In *Handbook of Lung Imaging and Computer Aided Diagnosis,* (A. El-Baz and J. Suri, Editors), Taylor & Francis, October 2011, Chapter 18, pp. 405-420.

7. M. Sen, A. Rudra, A. Chowdhury, **A. Elnakib**, A. El-Baz, "Cerebral White Matter Segmentation using Probabilistic Graph Cut Algorithm," In *Handbook of Recent Advances in Medical Segmentation and Registration Technologies*, (A. El-Baz, R. Acharya, M. Mirmedhdi, and J. Suri, Editors), Springer-Verlag, New York, March 2011, Chapter 2, pp. 41-67.

Refereed Conference Papers

1. H. Sliman, F. Khalifa, **A. Elnakib**, A. Soliman, G. M. Beache, A. Elmaghraby, and A. El-Baz, "A New Segmentation-Based Tracking Framework For Extracting The Left Ventricle Cavity From Cine Cardiac MRI," *Proc. IEEE International Conference on Image Processing (ICIP'13),* Melbourne, Australia, September 15-18, 2013, (in press), (selected for oral presentation).

2. **A. Elnakib**, G. M. Beache, H. Sliman, G. Gimel'farb, T. Inanc, and A. El-Baz, "A Novel Laplace-Based Method to Estimate the Strain from Cine Cardiac Magnetic Resonance Images," *Proc. IEEE International Conference on Image Processing (ICIP'13),* Melbourne, Australia, September 15-18, 2013, (in press), (selected for oral presentation).

3. **A. Elnakib**, G. M. Beache, G. Gimel'farb, T. Inanc, and A. El-Baz, "Validating a New Methodology for Strain Estimation from Cardiac Cine MRI," *Proc. International Symposium on Computational Models for Life Science (CMLS'13),* Sydney, Australia, November 27-29, 2013.

4. H. Sliman, F. Khalifa, **A. Elnakib**, A. Soliman, G. M. Beache, G. Gimel'farb, A. Emam, A. Elmaghraby, and A. El-Baz, " Accurate Segmentation Framework for the Left VentricleWall from Cardiac Cine MRI," *Proc. International Symposium on Computational Models for Life Science (CMLS'13),* Sydney, Australia, November 27-29, 2013.

5. **A. Elnakib**, M. Nitzken, M. F. Casanova, H.-Y. Park, G. Gimel'farb, and A. El-Baz, "Quantification of Age-related Brain Cortex Change using 3D Shape Analysis," *Proc. IEEE International Conference on Pattern Recognition (ICPR'12),* Tsukuba, Japan, November 11-15, 2012, pp.41-44.

6. **A. Elnakib**, G. Gimel'farb, T. Inanc, and A. El-Baz, "Modified Akaike Information Criterion for Estimating the Number of Components in a Probability Mixture Model," *Proc. IEEE International Conference on Image Processing (ICIP'12),* Orlando, Florida, USA, September 30-October 3, 2012, pp. 2497-2500.

7. A. El-Baz, F. Khalifa, **A. Elnakib**, M. Nitkzen, A. Soliman, P. McClure, G. Gimel'farb, and M. Abou El-Ghar, "A Novel Approach for Global Lung Registration using 3D Markov Gibbs Appearance Model," *Proc. International Conference on Medical Image Computing and Computer-Assisted Intervention (MICCAI'12),* Nice, France, October 1-5, 2012, pp. 114-121.

8. M. Nitzken, G. Beache, **A. Elnakib**, F. Khalifa, G. Gimel'farb, and A. El-Baz, "Accurate Modeling of Tagged CMR 3D Image Appearance Characteristics to Improve Cardiac Cycle Strain Estimation," *Proc. IEEE International Conference on Image Processing (ICIP'12),* Orlando, Florida, USA, September 30-October 3, 2012, pp. 521-524.

9. A. Firjani, F. Khalifa, **A. Elnakib**, G. Gimel'farb, M. Abou El-Ghar, A. Elmaghraby, and A. El-Baz, "A Novel Image-Based Approach for Early Detection of Prostate Cancer," *Proc. IEEE International Conference on Image Processing (ICIP'12),* Orlando, Florida, USA, September 30-October 3, 2012, pp. 2849-2852.

10. M. Nitkzen, G. Beache, **A. Elnakib**, F. Khalifa, G. Gimel'farb, and A. El-Baz, "Improving Full-Cardiac Cycle Strain Estimation from Tagged CMR by Accurate Modeling of 3D Image Appearance Characteristics," *Proc. IEEE International Symposium on Biomedical Imaging: From Nano to Macro (ISBI'12),* Barcelona, Spain, May 2-5, 2012, pp. 462-465 (selected for oral presentation).

11. A. S. Chowdhury, R. Roy, S. K. Bose, F. Khalifa, **A. Elnakib**, and A. El-Baz, "Non-rigid Biomedical Image Registration using Graph Cuts with a Novel Data Term," *Proc. IEEE International Symposium on Biomedical Imaging: From Nano to Macro (ISBI'12),* Barcelona, Spain, May 2-5, 2012, pp. 446-449. (Selected for oral presentation).

12. **A. Elnakib**, G. M. Beache, G. Gimel'farb, and A. El-Baz, "A New Framework for Automated Segmentation of Left Ventricle Wall from Contrast Enhanced Cardiac Magnetic Resonance Images," *Proc. IEEE International Conference on Image Processing (ICIP'11),* Brussels, Belgium, September 11-14, 2011, pp. 2337-2340.

13. **A. Elnakib**, G. M. Beache, G. Gimel'farb, and A. El-Baz, "A New Framework for Automated Identification of Pathological Tissues in Contrast Enhanced Cardiac Magnetic Resonance Images," *Proc. IEEE International Symposium on Biomedical Imaging: From Nano to Macro (ISBI'11),* Chicago, Illinois, USA, 30 March-2 April 2011, pp. 1272-1275.

14. **A.Elnakib**, M. Casanova, G. Gimel'farb, A. Switala, and A. El-Baz, "Autism Diagnostics by Centerline-based Shape Analysis of the Corpus Callosum," *Proc. IEEE International Symposium on Biomedical Imaging: From Nano to Macro (ISBI'11),* Chicago, Illinois, USA, 30 March- 2 April, 2011, pp. 1843-1846.

15. F. Khalifa, **A. Elnakib**, G. M. Beache, G. Gimel'farb, M. Abo El-Ghar, G. Sokhadze, S. Manning, P. McClure, and A. El-Baz, "3D Kidney Segmentation from CT Images using a Level Set Approach Guided by a Novel Stochastic Speed Function," *Proc. International Conference on Medical Image Computing and Computer-Assisted Intervention (MICCAI'11),* Toronto, Canada, September 18-22, 2011, pp. 587-594.

16. A. Firjani, **A. Elnakib**, F. Khalifa, G. Gimel'farb, M. Abo El-Ghar, A. Elmaghraby, and A. El-Baz, " A New 3D Automatic Segmentation Framework for Accurate Extraction of Prostate from Diffusion Imaging," *Proc. Biomedical Science and Engineering Conference - Image Informatics and Analytics in Biomedicine,* Knoxville, Tennessee, March-15-17, 2011, pp. 1-4.

17. A. Firjani, **A. Elnakib**, F. Khalifa, G. Gimel'farb, M. Abo El-Ghar, J. Suri, A. Elmaghraby, and A. El-Baz, " A New 3D Automatic Segmentation Framework for Accurate Extraction of Prostate from DCE-MRI," *Proc. IEEE International Symposium on Biomedical Imaging: From Nano to Macro (ISBI'2011),* Chicago, Illinois, USA, 30 March-2 April, 2011, pp. 1476-1479.

18. A. Firjani, F. Khalifa, **A. Elnakib**, G. Gimel'farb, M. Abo El-Ghar, A. Elmaghraby, and A. El-Baz, "Non-Invasive Image-based Approach for Early Detection of Prostate Cancer," *Proc. The Fourth International Conference on Developments in eSystems Engineering (DeSE'11),* Dubai, UAE, December 6-8, 2011.

19. A. Firjani, F. Khalifa, **A. Elnakib**, G. Gimel'farb, M. Abo El-Ghar, A. Elmaghraby, and A. El-Baz, "3D Automatic Approach for Precise Segmentation of the Prostate from Diffusion-Weighted Magnetic Resonance Imaging," *Proc. IEEE International Conference on Image Processing (ICIP'11),* Brussels, Belgium, September 11-14, 2011, pp. 2333-2337.

20. A. El-Baz, M. Nitzken, F. Khalifa, **A. Elnakib**, G. Gimel'farb, R. Falk, and M. Abo El-Ghar, "3D Shape Analysis for Early Diagnosis of Malignant Lung Nodules," *Proc. International Conference on Information Processing)in Medical Imaging (IPMI'11),* Monastery Irsee, Germany (Bavaria), July 3-8, 2011, pp. 772-783. (Selected for oral presentation. Oral acceptance rate is 5% and the overall acceptance rate is 20%).

21. A. El-Baz, M. Nitzken, F. Khalifa, **A. Elnakib**, G. Gimel'farb, R. Falk, and M. Abo El-Ghar, "3D Shape Analysis for Early diagnosis of Malignant Lung Nodules," *Proc.*

International Conference on Medical Image Computing and Computer-Assisted Intervention (MICCAI'11), Toronto, Canada, September 18-22, 2011, pp. 175-182.

22. M. Nitzken, M. F. Casanova, G. Gimel'farb, **A. Elnakib**, F. Khalifa, A. Switala, and A. El-Baz, " 3D Shape Analysis of the Brain Cortex with Application to Dyslexia," *Proc. IEEE International Conference on Image Processing (ICIP'11),* Brussels, Belgium, September 11-14, 2011, pp. 2713-2716. (Selected for oral presentation).

23. M. Nitzken, M. Casanova, G. Gimel'farb, F. Khalifa, **A. Elnakib**, A. Switala, and A. El-Baz, " 3D Shape Analysis of the Brain Cortex with Application to Autism," *Proc. IEEE International Symposium on Biomedical Imaging: From Nano to Macro (ISBI'11),* Chicago, Illinois, USA, 30 March- 2 April, 2011, pp. 1847-1850.

24. **A. Elnakib**, A. El-Baz, M. Casanova, G. Gimel'farb, A. Switala, "Image-Based Detection of Corpus Callosum Variability for More Accurate Discrimination Between Autistic and Normal Brains," *Proc. IEEE International Conference on Image Processing (ICIP'10),* Hong Kong, September 26-29, 2010, pp. 4381-4384.

25. **A. Elnakib**, A. El-Baz, M. Casanova, G. Gimel'farb, and A. Switala, "Dyslexia Diagnostics by Centerline-Based Shape Analysis of the Corpus Callosum," *Proc. International Conference on Pattern Recognition (ICPR'10),* Istanbul, Turkey, August 23-26, 2010, pp. 261-264. (Selected for oral presentation. Oral acceptance rate is 9% and the overall acceptance rate is 35%).

26. **A. Elnakib**, M. Casanova, A. El-Baz, G. Gimel'farb, and A. Switala, "Image-Based Detection of Corpus Callosum Variability For More Accurate Discrimination Between Dyslexic and Normal Brains," *Proc. IEEE International Symposium on Biomedical Imaging: From Nano to Macro (ISBI'10),* Rotterdam, The Netherlands, April 14-17, 2010, pp. 109-112.

27. A. Firjani, **A. Elnakib**, F. Khalifa, A. El-Baz, G. Gimel'farb, M. Abo El-Ghar, and A. Elmaghraby, "A Novel 3D Segmentation Approach for Segmenting the Prostate from Dynamic Contrast Enhanced MRI using Current Appearance and Learned Shape Prior," *Proc. IEEE International Symposium on Signal Processing and Information Technology,* Luxor, Egypt, December 15-18, 2010, pp. 137-143.

28. A. Firjany, **A. Elnakib**, A. El-Baz, G. Gimel'farb, M. Abo El-Ghar, A. Elmaghraby, "Novel Stochastic Framework for Accurate Segmentation of Prostate in Dynamic Contrast Enhanced MRI," *Proc. The First International Workshop on Prostate Cancer Imaging: Computer Aided Diagnosis, Prognosis, and Intervention,* Beijing, China, September 20 - 24, 2010, pp. 123-130.

29. A. El-Baz, P. Sethu, G. Gimel'farb, F. Khalifa, **A. Elnakib**, R. Falk, and M. Abo El-Ghar, "A New Validation Approach for the Growth Rate Measurement using Elastic Phantoms Generated By State-of-the-Art Microfluidics Technology," *Proc. IEEE International Conference on Image Processing (ICIP'10),* Hong Kong, September 26-29, 2010, pp. 4381-4384.

30. A. Chowdhury, A. Rudra, M. Sen, **A. Elnakib**, A. El-Baz,, "Cerebral White Matter Segmentation from MRI using Probabilistic Graph Cuts and Geometric Shape Priors," *Proc. IEEE International Conference on Image Processing (ICIP'10),* Hong Kong, China, Sept. 26-29, 2010, pp. 3649-3652.

Abstract Published in Proceedings

1. M. Abou El-Ghar, A. El-Baz, F. Khalifa, **A. Elnakib**, A. Firjani, and T. El-Diasty, "Non-invasive Image-based Approach for Early Diagnosis of Prostate Cancer," *18th Symposium of the European Society of Urogenital Radiology (ESUR'11),* Dubrovnik, Croatia, October 13-16, 2011.

2. M. Casanova, A. El-Baz, **A. Elnakib**, J. Giedd, J. Rumsey, E. Williams, A. Switala, "Corpus Callosum Shape Analysis with Application to Dyslexia," *Book of Scientific Proceedings, AACAP 57th Annual Meeting,* October 28, 2010; 57, NRPOSTER-2.25.

Graduate Advisor

Dr. Ayman El-Baz, Department of Bioengineering Department, University of Louisville, KY.